University of Wollongong

Research Online

University of Wollongong Thesis Collection 2017+

University of Wollongong Thesis Collections

2018

Characteristics of Aerosol Particles: Concentration, Particle Size and Formation Mechanisms in Urban-Marine Environments

Doreena Dominick
University of Wollongong

Follow this and additional works at: https://ro.uow.edu.au/theses1

University of Wollongong

Copyright Warning

You may print or download ONE copy of this document for the purpose of your own research or study. The University does not authorise you to copy, communicate or otherwise make available electronically to any other person any copyright material contained on this site.

You are reminded of the following: This work is copyright. Apart from any use permitted under the Copyright Act 1968, no part of this work may be reproduced by any process, nor may any other exclusive right be exercised, without the permission of the author. Copyright owners are entitled to take legal action against persons who infringe their copyright. A reproduction of material that is protected by copyright may be a copyright infringement. A court may impose penalties and award damages in relation to offences and infringements relating to copyright material. Higher penalties may apply, and higher damages may be awarded, for offences and infringements involving the conversion of material into digital or electronic form.

Unless otherwise indicated, the views expressed in this thesis are those of the author and do not necessarily represent the views of the University of Wollongong.

Recommended Citation

Dominick, Doreena, Characteristics of Aerosol Particles: Concentration, Particle Size and Formation Mechanisms in Urban-Marine Environments, Doctor of Philosophy thesis, School of Chemistry, University of Wollongong, 2018. https://ro.uow.edu.au/theses1/527

Research Online is the open access institutional repository for the University of Wollongong. For further information contact the UOW Library: research-pubs@uow.edu.au

Characteristics of Aerosol Particles: Concentration, Particle Size and Formation Mechanisms in Urban-Marine Environments

Doreena Dominick

Supervisors:
Associate Professor Dr Stephen Wilson
Co-supervisor:
Professor Dr Clare Murphy (Paton-Walsh)

This thesis is presented as part of the requirements for the conferral of the degree:

Doctor of Philosophy

The University of Wollongong
School of Chemistry

December 2018

Declaration

I, Doreena Dominick, declare that this thesis submitted in partial fulfilment of the requirements for the conferral of the degree Doctor of Philosophy, from the University of Wollongong, is wholly my own work unless otherwise referenced or acknowledged. This document has not been submitted for qualifications at any other academic institution.

Doreena Dominick
Friday, 12nd December, 2018

Abstract

Atmospheric particle properties were measured in the South Eastern coastal city of Wollongong, Australia, during an intensive field campaign known as Measurement of Urban, Marine and Biogenic Air (MUMBA), between 15th January and 16th February 2013. A scanning mobility particle sizer (SMPS) was operated to measure particle number size distributions ranging from 14 nm to 660 nm in diameter. Principal component analysis was applied to the entire data measured by SMPS and, based on strong component loadings (value ≥ 0.75), three size fractions (i) Small (N_S) :15 nm $<$ Dp $<$ 50 nm, (ii) Medium (N_M) :60 nm $<$ Dp $<$ 150 nm and (iii) Large (N_L) :210 nm $<$ Dp $<$ 450 nm were revealed. The three size fractions described 89% of the dataset cumulative variance. The daily pattern of particle number size distribution revealed morning, afternoon and night peaks. Traffic emissions and marine aerosols were the major contributors of particles observed in the morning, when the N_S fraction dominated. A mixture of marine aerosols and secondary aerosols from photochemical oxidation was the main contributor during the afternoon. The Port Kembla Steel Works and the urban areas were the major contributors of particles at night. Secondary organic aerosols were identified by a mass ratio of organic carbon to elemental carbon (OC/EC) of greater than 1, and this was commonly observed. A weak correlation ($R^2 = 0.3$) between OC and EC indicated that there were multiple sources of both OC and EC.

Particle formation and growth events were observed from particle number size distribution data in the range of 14 nm to 660 nm. Eight particle formation and growth event days were observed (four Class I and four Class II), which is equivalent to 25% of the total observation days (15th January to 16th February, 2013). The events occurred during the day, starting after 8:00 Australian Eastern Standard time with an average duration of five hours. The events also appeared to be positively linked to the prevailing easterly to north easterly sea breezes that carry pollutants from sources in and around Sydney. This suggests that photochemical reactions and a combination of oceanic and anthropogenic air masses are among the factors that influenced these events. However, no single factor could be identified that directly influenced these particle formation and growth events.

Differential Slant Column Densities (DSCDs) and aerosol extinction were successfully retrieved using ultra-violet spectral measurements from a ground-based instrument configured for Multi-Axis Differential Optical Absorption Spectroscopy (MAX-DOAS). The oxygen collisional complex (O_4) absorption in the ultra-violet (UV) spectra region was used to retrieve the aerosol extinction profile using the Heidelberg Profile (HEIPRO) algorithm. Measurements from the MAX-DOAS instrument give information on the marine environment compared to the rest of the instruments deployed during the MUMBA campaign. A strong correlation ($R^2 = 0.77$) was observed between the vertical profile of aerosol extinctions retrieved from MAX-DOAS and Light Detection and Ranging (LIDAR) on a chosen "clear day" on the 7th February, 2013. Both instruments derived a significant scattering layer (higher aerosol concentration) at a height of 300 m on this "clear day". Surface aerosol extinctions (of 200 m height and below) retrieved from MAX-DOAS were uncorrelated with the *in-situ* $PM_{2.5}$ mass concentrations ($R^2 = 0.12$). This result is due in part to the low $PM_{2.5}$ concentrations observed during the aerosol measurement period.

Together, the analysis of aerosol size fractions, particle formation events and vertical profile of aerosol distribution in this thesis provide one of the most detailed characterisations of atmospheric aerosols in an urban-marine environment ever presented for an Australian city.

Acknowledgments

I would like to express my most sincere thanks and appreciation to my supervisors Associate Professor Dr Stephen Wilson and Associate Professor Dr Clare Murphy for their relentless encouragement, patience, trust, advice and guidance throughout the research and completion of my work. I would like to thank the University of Wollongong for accepting me as a PhD candidate with scholarship support. Thank you to the Australian Government′s National Environmental Science Program through the Clean Air and Urban Landscapes Hub for the top-up scholarship and for all the funding required to complete this work. Thanks also to the Australian Research Council (for funding the campaign as part of the Discovery Project DP110101948).

A special note of gratitude goes to all other members of the Centre for Atmospheric Chemistry, University of Wollongong who were always at hand to help and support in many different ways. I thank the scientists at CSIRO Climate Science Centre, Aspendale, Victoria, Australia, the Australian Nuclear Sciences and Technology Organisation (ANSTO), New South Wales, and the researchers at GNS Sciences, Avalon, Lower Hutt, New Zealand that helped in the MUMBA campaign and throughout my research work.

My special appreciation and thanks to Dr. Ruhi Humphries, Dr. Melita Keywood and Paul Selleck from CSIRO, to Robert George Ryan of the University of Melbourne, to Dr. Ben Marwick of the University of Wollongong and to Dr. Alan Griffiths from ANSTO for all the help and knowledge that they shared with me throughout my work. Special thanks also goes to Dr. Mahendrea Bhujel for helping in the carbonaceous aerosol data analysis.

I also express my heartfelt appreciation and thanks to the Office of Environment and Heritage, New South Wales, to the Bureau of Meteorology, Australia and the Roads and Maritime Services, New South Wales. These authorities were very helpful in providing datasets which were used to support the results and discussion in this work. I also acknowledge the NOAA Air Resources Laboratory (ARL) for the provision of the HYSPLIT transport and dispersion model and/or READY website (http://www.arl.noaa.gov/ready.html) as well as to David Carslaw who was involved in the development of the great and useful OpenAir package for analysis of air quality data and the relevant R code for public access. A big thank you to the

Kids Uni and the Science Centre for their assistance and for providing the location for the instruments during the MUMBA campaign.

Last but not least, my gratitude beyond measure goes to my friends for their guidance and for their kindness in sharing useful knowledge and to my lovely family for their unfailing love, relentless encouragement, support and prayers that have contributed towards the accomplishment of this thesis.

Contents

Chapter 1

Introduction and Literature Review

A campaign known as the Measurements of Urban, Marine and Biogenic Air took place in the coastal city of Wollongong, New South Wales during summer 2013 (details are discussed in Chapter 2). A large range of measurements was made during the campaign. Intensive analyses on trace gases were done and published by *Paton-Walsh et al.* [2017] *Guérette et al.* [2017] and *Guérette* [2016].

However, analysis on the aerosol measurement obtained during the campaign was still lacking. Therefore, this thesis focuses on the aerosol measurements in order to provide a detailed characterisation of the atmospheric composition during the campaign.

1.1 Description of the Air Pollution Issues

Air pollution is the presence of diverse pollutants in the atmosphere and is responsible for adverse effects on health and the environment [*Brauer et al.*, 2012; *Kim et al.*, 2013; *Kinney*, 2008]. A 2018 report by the World Health Organisation (WHO) states that air pollution is now the world′s largest environmental factor affecting human health. The global estimate of total deaths caused by ambient air pollution and household air pollution in 2016 was 4.2 and 3.8 million people, respectively [*WHO*, 2018]. These deaths were mainly caused by aerosols and ozone, where aerosols were the biggest single factor [*WHO et al.*, 2013, 2016]. Approximately 7 million people, in total, die every year from cardiovascular diseases caused by exposure to fine particles (particles of diameter of 2.5 µm or less ($PM_{2.5}$)) [*WHO*, 2018]. The estimate of total deaths from cardiovascular diseases attributable to ozone exposure was 254 000 (95% uncertainty interval of 97 000 - 422 000) globally in 2015 [*Cohen et al.*, 2017]. The estimated adult deaths globally due to cardiovascular disease resulting from exposure to ozone were 1.23 million in 2015 [*Malley et al.*, 2017]. These estimated values indicate that reducing air pollution could provide very significant population scale health benefits. In addition to effects on human health, ambient aerosols influence climate, cause visibility degradation and damage building materials [*Brimblecombe*, 2015; *IPCC*, 2013; *Seinfeld and Pandis*, 2016].

Since air pollutants, especially aerosol particles, significantly impact on human health and climate, research on these air pollutants is being intensively carried out around the world to understand the sources of pollutants, their composition, their formation mechanisms and their detrimental effects. The characteristics of aerosols vary depending on their sources as well as meteorological, geographical and topographical conditions. Studies on aerosol particle size in Australia include the work of *Cheung et al.* [2011]; *Mejia et al.* [2007]; *Pushpawela et al.* [2018]; *Salimi et al.* [2017], which focuses on sub-micron particles in the urban environment in the north-eastern part of Australia. There have been similar studies in natural environments in Australia. Particle size in Eucalyptus forests *Ristovski et al.* [2010] and particle formation associated with natural emissions from the Eucalyptus forest in south-east Australia *Suni et al.* [2008], as well as particle size in a sub-tropical clean marine site in the coastal area of Eastern Australia *Modini et al.* [2009] and the characteristics of particle size at a clean marine mid-latitude site *Cainey et al.* [2007] have been investigated. *Guo et al.* [2008] conducted a study in the rural environment of Eastern Australia.

Ultrafine particles (particles with diameters less than 100 nanometre (nm)) contribute to a large fraction of the total particle number concentration globally [*Kulmala et al.*, 2004; *Spracklen et al.*, 2006]. New particle formation is one of the sources of ultrafine particles [*Kulmala et al.*, 2013; *Wahlina et al.*, 2001]. *Kulmala et al.* [2004] report that many studies have been conducted globally in order to investigate particle formation processes in different environmental settings such as urban, industrial, coastal and boreal polar regions. However, most of the studies have been conducted in the Northern Hemisphere, at various locations from clean, remote sites to polluted environments including *Dada et al.* [2017]; *Dall′Osto et al.* [2018]; *de España et al.* [2017]; *Mohr et al.* [2017]; *Németh et al.* [2018]; *Vehkamäki et al.* [2004]. The Northern Hemisphere includes the large continents of Asia, Europe and North America, while the Southern Hemisphere mainly consists of oceans. This means that the approximately 68% of the Earth′s land mass is in the Northern Hemisphere. The Northern Hemisphere also has approximately 90% of the global population and more industrial activity than the Southern Hemisphere. For that reason, there is a much higher level of pollution in the Northern Hemisphere [Pirie, 2018]. Many first-world countries, however, have cleaned up their atmosphere through mitigation policies. These differences are likely to result in the different aerosol properties experienced in the Southern Hemisphere. Hence more studies are required to understand the characteristics of aerosols in the Southern Hemisphere [*Mitchell et al.*, 2017; *Rotstayn et al.*, 2013].

1.2 Characteristics of Aerosols

Aerosols are suspended solid or liquid particles in the atmosphere [*Boucher*, 2015; *Seinfeld and Pandis*, 2012]. Typically, the size of atmospheric particles can range from 1 nanometre (nm) to 100 micrometre (µm)[*Boucher*, 2015; *Hendricks et al.*, 2012]. Aerosols are also referred to as particulate matter (PM) by the air quality community *Fuzzi et al.* [2015].

There are several ways to classify the characteristics of aerosols. They include size distribution, formation mechanisms and sources, which are discussed in sections 1.2.1 and 1.2.2.

1.2.1 Aerosol Size Distribution

The particle number size distribution is one of the important characteristics for studying aerosol properties. Aerosol particles evolve continuously in the atmosphere, therefore, their sources and transformation processes during the evolution period provide information on aerosol properties [*Birmili et al.*, 2010; *Hinds*, 2012; *Seinfeld and Pandis*, 2016]. The general classification of particle size fractions includes coarse particles (PM_{10}), fine particles ($PM_{2.5}$) and ultrafine particles as indicated along the top of Fig.1.1. PM_{10} refers to particles with diameters of 10 µm or less. $PM_{2.5}$ are particles with diameters of 2.5 µm or less and ultrafine particles are particles with diameters less than 0.1 µm.

Particle size distribution is usually illustrated in the form of a log-normal distribution, because particle diameter (Dp) typically varies over several orders of magnitude. Particle number normalized by range of log-transformed particle diameter (dlogDp) of the interval is used in the y-axis of Fig. 1.1. The distribution of particle size *n(r)* can be represented by a differential radius number density distribution *(dN)* which represents the number of particles with radii between r and $r + dr$ per unit volume (Eq. 1.1) [*MacCartney*, 1976]:

$$n(r) = \frac{dN(r)}{dr} \tag{1.1}$$

It is possible to use this distribution of particle number with radius to describe particle volume. The distribution of particle volume *V(r)* can be represented by a differential volume density *(dV)*, which represents the volume contained in particles whose radii lie between $r + dr$ per unit volume (Eq. 1.2) [*MacCartney*, 1976]:

$$V(r) = \frac{dV}{dr} \tag{1.2}$$

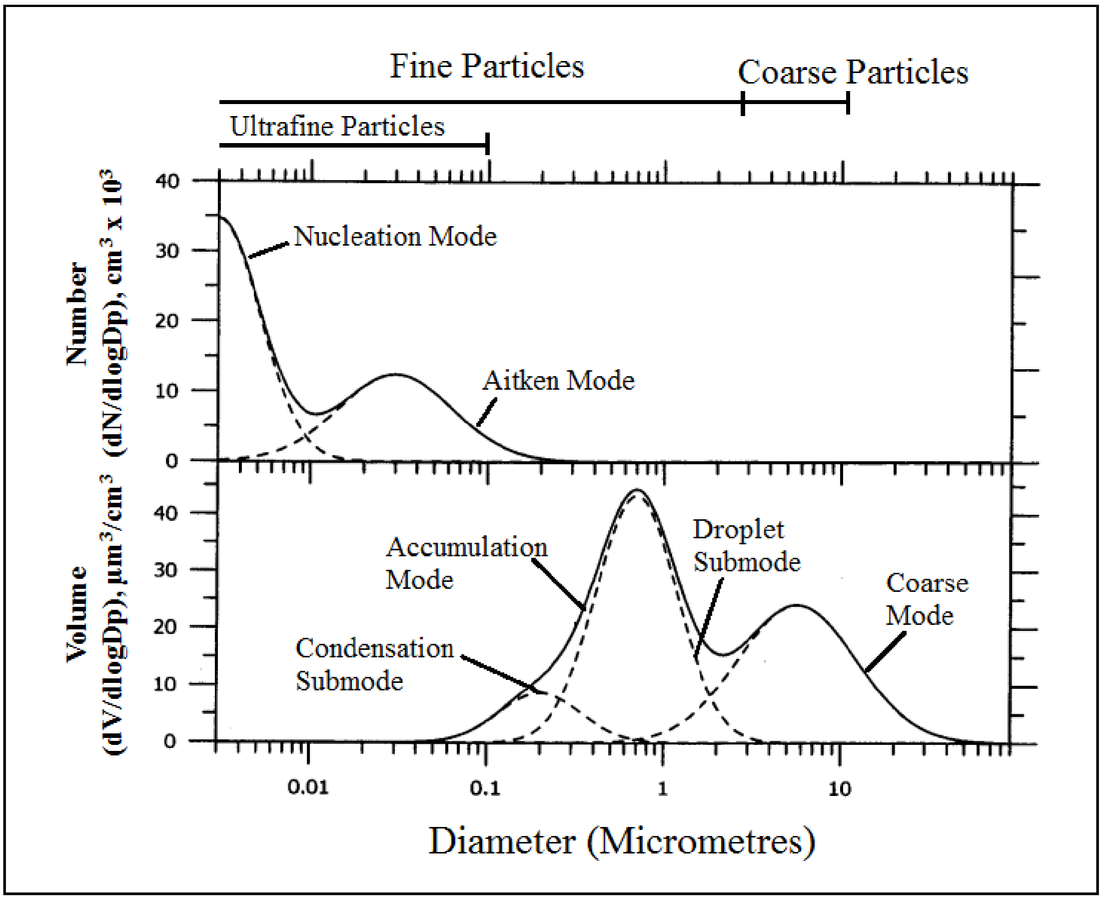

Fig. 1.1: Particle size distribution plotted as number and volume distribution for different modes. (Source: *Seinfeld and Pandis* [2016]).

Fine particles attract more attention because of the awareness of their negative effects on health [*Collins et al.*, 2014; *Lee et al.*, 2018; *Pope III and Dockery*, 2006]. Generally, the composition of fine particles includes sulfate, nitrate and ammonium salts as well as elemental and organic carbon. Fine particles also contain trace metals such as lead, nickel and copper. Coarse particles generally contain dust, crustal elements, nitrate, sodium, chloride and biogenic organic particles such as pollen and spores [*Harrison et al.*, 2011; *Seinfeld and Pandis*, 2016]. As shown in this figure, the number concentration is dominated by ultrafine aerosols, while the volume or mass concentration is dominated by larger aerosols. Most of the mass is found in the size range between 0.1 µm and 10 µm.

Particles in the atmosphere in terms of number are generally dominated by particles less than one micrometre (< 1 µm in diameter) [*Petäjä et al.*, 2006; *Seinfeld* *and Pandis*, 2016]. Particles with a diameter of less than 1 µm are made up of three modes: Nucleation mode, Aitken mode and Accumulation mode. Nucleation and Aitken modes correspond to ultrafine particles. Other than these three modes, there is a mode known as Coarse mode (Fig. 1.1). Each mode is characterised by a diameter associated with the maximum value of the mode′s frequency function curve [*Hinds*, 1999]. These modes are described below.

(a) Nucleation Mode

The nucleation mode includes particles with Dp less than 0.01 µm. Particles in this mode are usually newly formed particles that are generated through gas-to-particle conversion [*Fuzzi et al.*, 2015; *USEPA*, 2004]. Gas-to-particle is a process involving condensation of vapours which leads to either the nucleation conversion of new aerosols or the condensation growth of existing particles [*Tomasi and Lupi*, 2017]. These particles are formed from either biogenic or anthropogenic emissions in many different environments including forests [*Kulmala and Kerminen*, 2008] and coastal environments [*O'Dowd et al.*, 2007, 2002].

(b) Aitken Mode

Particles in this mode have Dp in the range from 0.01 µm to 0.1 µm. Aitken mode particles are also recently formed particles that are still actively undergoing condensation of gases and water vapour. Initially this process is relatively fast [*Shen et al.*, 2011; *USEPA*, 2004]. These particles act as nuclei for the condensation of low vapour pressure gaseous species causing them to grow towards the accumulation mode.

(c) Accumulation Mode

The accumulation mode includes particles with Dp between 0.1 µm and 1.0 µm. Particles in this mode are generated mainly through coagulation (two particles combining to form one) of existing smaller diameter particles and from condensation (gas molecules condensing on a particle) of vapours onto existing particles which induces particle growth [*Fuzzi et al.*, 2015; *Shen et al.*, 2011; *USEPA*, 2004]. Accumulation mode particles can also be introduced into the atmosphere through the incomplete combustion of wood, oil, coal, gasoline and other fuels [*Shen et al.*, 2011].

(d) Coarse Mode

The coarse mode includes particles with Dp between 10 µm and 2.5 µm[*OEH*, 2005]. Coarse mode particles are introduce into the atmosphere from minerals, crustal material and organic debris by mechanical processes (breaking up of large particles) through crushing, grinding and abrasion of surfaces [*Fuzzi et al.*, 2015; *USEPA*, 2004]. These particles are also emitted into the atmosphere from both natural and anthropogenic sources [*WHO et al.*, 2013]. The coarse mode may also include sea salt and nitrates formed from the reaction of nitric acid with sodium chloride. The evaporation of sprays and bursting of bubbles in the ocean produce coarse particles of sea salt [*Rasool*, 2012]. The wind also picks up dust, soil and biological particles and suspends them in the atmosphere [*Wilson and Suh*, 1997]. Anthropogenic coarse particles are introduced into the atmosphere through dust from road surfaces, traffic emissions, and industrial and agricultural activities.

1.2.2 Primary and Secondary Aerosols

Sources and sinks of aerosols in the atmosphere is show in Fig. 1.2. Aerosols in the atmosphere can be divided into primary and secondary aerosols. Primary aerosols are those that are emitted directly from the emission source [*Fuzzi et al.*, 2015; *Harrison et al.*, 2011; *Seinfeld and Pandis*, 2012]. Primary aerosols can be emitted into the atmosphere by natural/biogenic and anthropogenic sources (Fig. 1.2). Primary aerosols from natural sources include sea spray/sea salt, biomass-burning particles, wind-blown mineral dust and volcanic emissions, whereas those of biogenic sources include plant fragments, micro organisms and pollen. Anthropogenic sources include combustion emissions (from transportation and industrial activities), fugitive emissions (from wind erosion of storage piles, unpaved plant roads, materials handling, loading and transfer operations) and non-industrial fugitive emissions (traffic entrainment of dust from public roads, agricultural operations and constructions) [*Kim et al.*, 2015; *Kumar et al.*, 2010; *Pöschl*, 2005; *Seinfeld and Pandis*, 2012; *Tomasi and Lupi*, 2017].

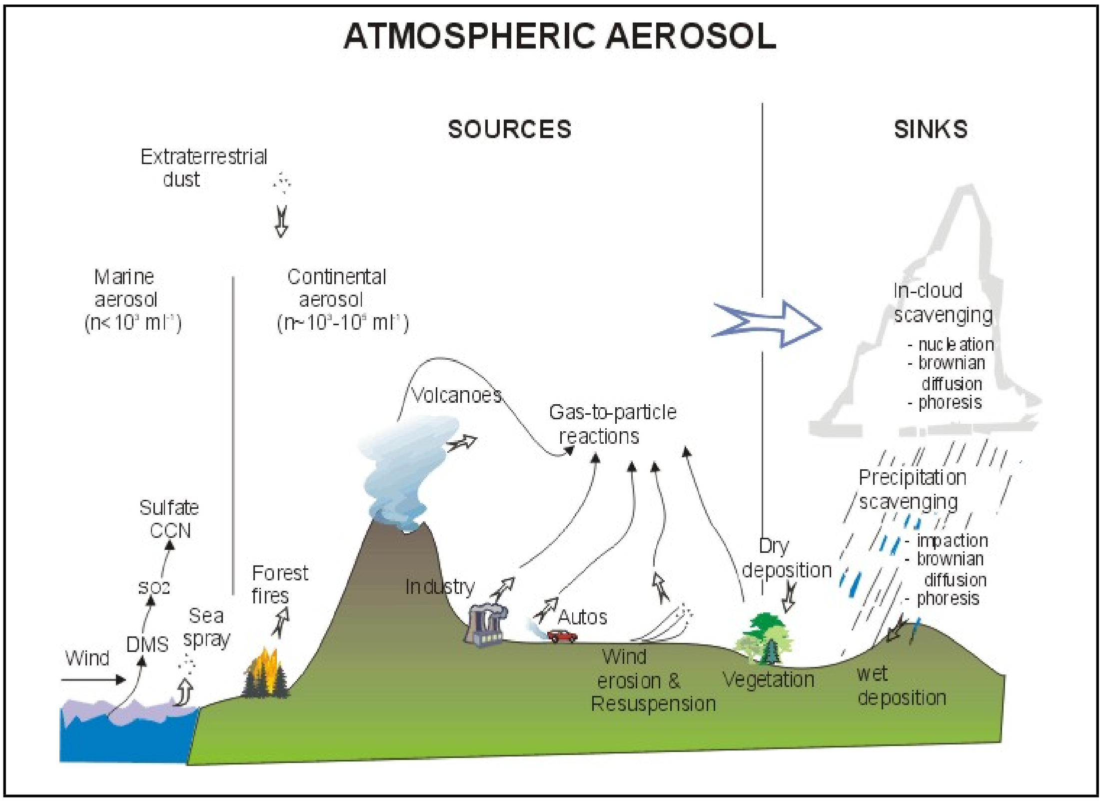

Fig. 1.2: Life cycle of aerosols in the atmosphere: emission, transport and sink processes. (Source: Lecture notes on METEO 437: ATMOSPHERIC PHYSICS II - Physics and Chemistry of Clouds (https://www.ems.psu.edu/ lno/Meteo437/Aerosol.jpg)).

Once airborne, aerosol particles may undergo chemical transformation to form secondary aerosols. These processes change the particle size, structure and composition [*Pöschl*, 2005; *Seinfeld and Pandis*, 2012]. There are two types of secondary aerosols. The first type refers to aerosols that are formed through the condensation/reaction of gases on pre-existing particles. This leads to an increase in mass concentration. The second type involves the formation of new nanometre particles. This mechanism is known as new particle formation [*Duh et al.*, 2008; *Harrison et al.*, 2011; *Seinfeld and Pandis*, 2012]. Examples of gaseous precursors that are involved in the formation of secondary aerosols are sulfur dioxide (SO_2) and nitrogen oxides (NO_x) which are primarily emitted from the combustion of fossil fuels [*Hawkins and Russell*, 2010]. Volatile organic compounds are also involved in the formation of secondary aerosols [*Carlton et al.*, 2006; *Holzinger et al.*, 2007]. Several processes make the transformation into secondary aerosols possible. They include condensation of gases on the surface of aerosols, coagulation of aerosols and chemical modification of the aerosol surface, which allows water to condense generating cloud condensation nuclei which then form cloud droplets [*Seinfeld et al.*, 2016]. Examples of secondary products are sulfates (e.g. from SO_2), nitrates (e.g. from NO_x)

and aerosol organic carbon species [*Kim et al.*, 2015]. Secondary aerosols are found mostly in the fine particle fraction [*WHO et al.*, 2013].

1.3 Atmospheric Lifetime of Aerosols

The atmospheric lifetime of aerosols in the atmospheric boundary layer is often on the order of a day depending, not only on their size, but also on aerosol chemistry and meteorological conditions. Aerosols masses are removed from the atmosphere through deposition on the Earth′s surface (dry deposition) and incorporation into cloud droplets during the formation of precipitation (wet deposition) (Fig. 1.2) [*Mohan*, 2016].

Ultrafine particles, in terms of particle number, experience short atmospheric lifetimes ranging from minutes to hours [*Chang et al.*, 2004; *Seinfeld and Pandis*, 2012]. Nucleation mode particles have the shortest lifetimes (minutes). These particles grow via coagulation and condensation. Accumulation mode particles experience atmospheric lifetimes ranging from days to weeks, significantly longer than that of Nucleation and Aitken mode particles. Longer lifetimes result from less efficient removal mechanisms as the particles slowly grow to reach the Coarse mode. Particles in the Coarse mode accumulate, form cloud droplets and are lost through wet and also dry deposition. The lifetime of coarse particles in the atmosphere is reasonably short (minutes to hours). Their relatively large size causes them to settle out of the atmosphere by dry deposition, by fall out and scavenging by falling rain drops [*Seinfeld and Pandis*, 2012; *Selvam*, 2010].

1.4 Effects of Aerosols

1.4.1 Effects of Aerosols on Human Health

Exposure to aerosol particles can cause health problems even when a small amount of particles enters the lungs. These effects are often more pronounced in children and the elderly. Several studies on epidemiology and toxicology identified a the correlation between fine particulate matter and various health conditions, particularly respiratory and cardiovascular health problems [*Lee et al.*, 2018; *Parker et al.*, 2018; *Xing et al.*, 2016]. Recently, *Cohen et al.* [2017] reported that ambient $PM_{2.5}$ was the fifth ranking mortality risk factor in 2015. The global estimate of mortality due to ambient $PM_{2.5}$ in 2015 was 4.2 million people (95% uncertainty interval of 3.7 - 4.8 million per year). These estimated values are based on the global burden of disease attributable to ambient fine particulate matter exposure reported by *Forouzanfar et al.* [2016] which included lower respiratory infections, cerebrovascular disease, ischaemic heart disease, chronic obstructive pulmonary disease and lung cancer. In addition to outdoor air pollution, a study by *Lim et al.* [2012] reported an estimated 3.5 million deaths per year due to indoor air pollution, which includes the use of solid fuels for cooking and heating. *Dadvand et al.* [2013] compared air pollution across 14 sites in 9 countries and found that there were positive correlations between high levels of air pollution and low birth weights. *Hoy et al.* [2016] and *Begg et al.* [2007] reported that about 3000 deaths in Australia are attributable to urban air pollution each year. Among the studied diseases, coronary heart diseases was the highest percentage (70%) of the total deaths due to air pollution in Australia.

Studies from the multi-country European Study of Cohorts for Air Pollution Effects (ESCAPE) project have reported that long term exposure to particulate matter has a negative impact on lung function [*Adam et al.*, 2015; *Gehring et al.*, 2013] and resulted in an increase in chronic obstructive pulmonary disease [*MacIntyre et al.*, 2013]. Similar findings have been observed in Taiwan by *Guo et al.* [2018]). Other health effects that associated with exposure to particulate matter reported from ESCAPE project include acute coronary events [*Cesaroni et al.*, 2014], stroke [*Stafoggia et al.*, 2014], childhood pneumonia [*MacIntyre et al.*, 2013], low birth weight [*Pedersen et al.*, 2013] and lung cancer [*Raaschou-Nielsen et al.*, 2013].

1.4.2 Effects of Aerosols on Earth Climate

Atmospheric aerosols play crucial direct and indirect roles in the energy balance of the atmosphere.

Direct effect: The radiative forcing due to the interaction of aerosol (both natural and anthropogenic) with radiation before any environmental adjustment takes place is known as the "direct effect" [*Boucher et al.*, 2013]. Generally, bright-coloured aerosols reflect radiation in all directions and scatter sunlight back to space which cools the Earth. However, darker-coloured aerosols absorb significant amounts of light. This phenomenon both warms and cools the Earth′s surface. The warming effect is caused by the absorbing properties of the aerosols. The cooling effect is experienced because aerosols can also scatter and provide shade to the Earth′s surface [*IPCC*, 2013; *Voiland*, 2010].

Indirect effect: The radiative forcing from aerosol-cloud interactions encompasses instantaneous effect on cloud characteristics due to changing concentrations of cloud condensation and ice nuclei. All subsequent changes contribute to the "indirect effect" [*Boucher et al.*, 2013]. This effect is caused by the impact of aerosols on clouds due to some aerosols′ hydrophilic properties. These hydrophilic properties mean that these aerosols can act as cloud condensation nuclei (CCN). CCN affect the characteristics of clouds by modifying the cloud droplet number concentration, the cloud droplet size, the cloud lifetime as well as the precipitation processes [*Boucher et al.*, 2013; *Rosenfeld et al.*, 2008]. The interaction between aerosol particles and clouds is among the greatest of the uncertainties related to the quantification of aerosol effects on climate [*IPCC*, 2013]. Indirect effects usually provide cooling. Clouds in clean environments consist of a relatively high number of large droplets as there is a low number of water soluble particles. As a result of the large droplets, the clouds look dark and translucent (Fig. 1.3 (a)). Clouds in polluted air consist of a high number of small droplets, because generally there is a high concentration of water soluble particles. This makes polluted clouds look brighter (Fig. 1.3 (b)). Brighter coloured clouds block sunlight from reaching the Earth′s surface which then shades the planet and provides a cooling effect (which is also known as "cloud albedo effect") [*IPCC*, 2013; *Voiland*, 2010]. Smaller cloud droplets also reduce precipitation efficiency [*Lohmann and Feichter*, 2005].

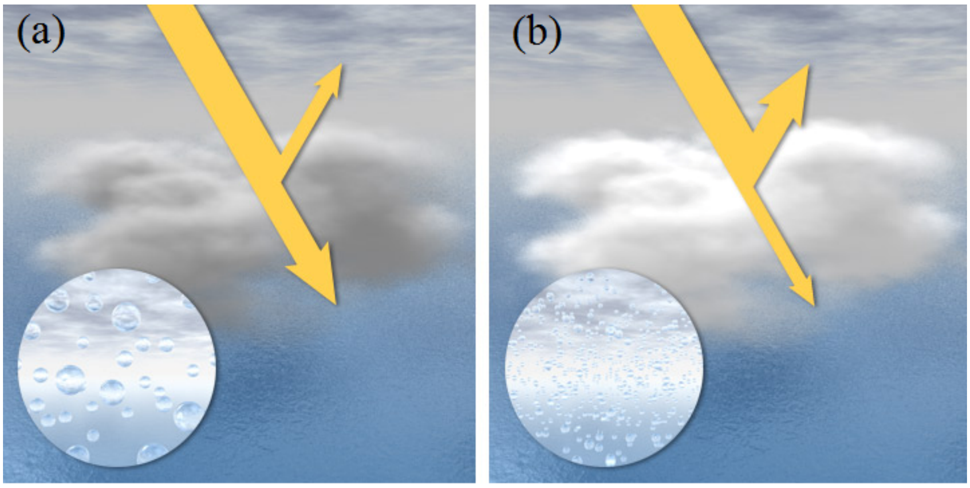

Fig. 1.3: Effects of aerosols particles on cloud properties: (a) low particle loading (clean air) (b) high particles loading (polluted air). (Source: *Voiland* [2010]).

Owing to these radiative properties, aerosol are a major component of the energy budget of the Earth. Hence, changes in aerosol population contribute to climate change as detailed in the Synthesis Report of Fifth Assessment Report (AR5) by Intergovernmental Panel on Climate Change (IPCC). The energy budget of the Earth refers to the flow of energy into and out of the Earth′s atmosphere. The major emitted pollutants that have changed since pre-industrial time (1750) that impact upon the energy budget are shown in Fig. 1.4. Radiative forcing is the change in energy flux caused by a driver and is calculated at the tropopause or at the top of the atmosphere relative to pre-industrial conditions (defined as 1750) [*IPCC et al.*, 2014]. Radiative forcing is expressed in Watts per square meter (Wm^{-2}) and can be positive or negative. Positive radiative forcing refers to the Earth's receiving more incoming energy than it radiates out to space relative to 1750. This net gain of energy will cause warming. Negative radiative forcing means that Earth loses more energy to space relative to 1750 (Fig. 1.4). Aerosols are the most uncertain component of radiative forcing, which limits the ability to quantify and predict the global climate [*IPCC*, 2013]. Aerosols are the second largest factor after CO_2 influencing global radiative forcing, with the estimated value of 0.9 [uncertainty from 0.1 to 1.9] Wm^{-2} [*IPCC*, 2013].

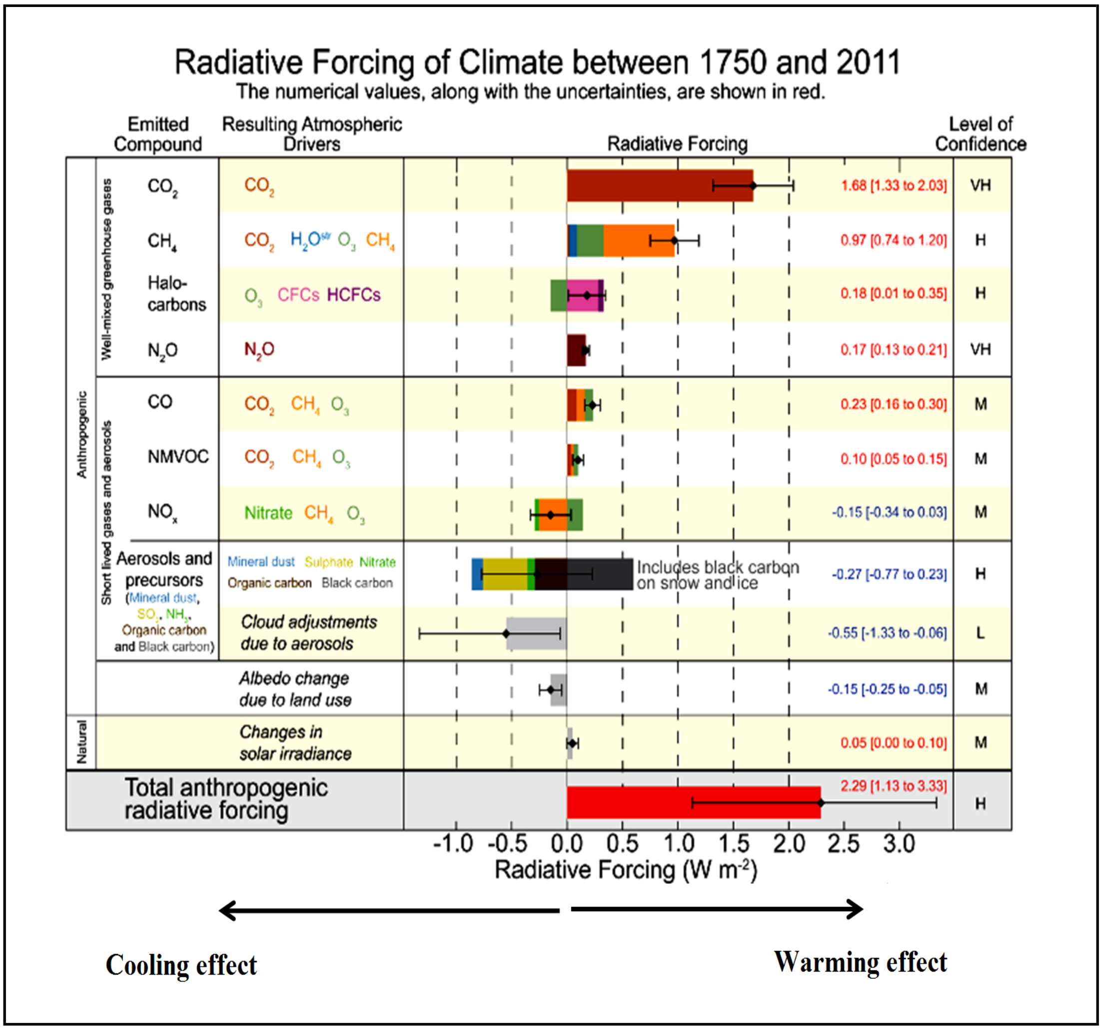

Fig. 1.4: Global radiative forcing of atmospheric drivers from pre-industrial times until 2011 (1750 to 2011). The radiative forcing is shown with bars. Atmospheric drivers are illustrated in different colors. The letters VH = Very High; H = High; M = Moderate; and L = Low (refer to the level of confidence that exists in our qualification of the processes). Modified from *IPCC* [2013].

1.5 Optical Properties

Aerosols have optical properties which provide aerosols with the ability to interact with the propagation of radiation by scattering and absorption. The optical properties depend on the aerosol chemical and physical characteristics and the wavelength of the light. The interaction of radiation with particles by scattering, absorption or both, leads to extinction of the incident light [*Brasseur and Jacob*, 2017; *Toon and Pollack*, 1980]. Extinction is the fraction depletion of radiance per unit path length [*Barry and Hall-McKim*, 2014]. The resulting attenuation of radiation along a path through the atmosphere is described by the Beer-Lambert law [*Brasseur and Jacob*, 2017] (Eq. 1.3).

$$I = I_o e^{-\beta_{ext} L} \tag{1.3}$$

In Equation 1.3, I_o represents the initial light intensity. I is the light intensity after it passes through the sample. L is the path length of the light through the aerosols and β_{ext} is the extinction coefficient characteristic of the aerosol which is the sum of scattering and absorption coefficients ($\beta_{ext} = \beta_{scattering} + \beta_{absorption}$).

Aerosol optical depth (AOD) is the integrated extinction coefficient over a column of air from the Earth′s surface to the top of the atmosphere. The values of AOD reveal how much direct sunlight is prevented from reaching the ground by particles in the atmosphere (i.e. dust, smoke, pollution). AOD is a dimensionless number that is related to the number of aerosol particles in the vertical column of atmosphere over the observation location. Low and high AOD correspond to clear skies and hazy-cloudy skies, respectively [*Barry and Hall-McKim*, 2014; *Brasseur and Jacob*, 2017; *Khor et al.*, 2014; *Toon and Pollack*, 1980].

1.6 Particle Formation and Growth

As noted before, aerosol nucleation refers to the formation of stable particle clusters (with diameters of approximately 1 nm) [*Dall′Osto et al.*, 2018]. When a nucleated particle grows to a detectable size this is known as a new particle formation event. This differentiates it from nucleation as it is instrumentally defined, and depending on the instrument used, the detectable particle size ranges from 1 nm to 10 nm [*Dall′Osto et al.*, 2018; *Kulmala et al.*, 2004]. New particle formation is an important source of atmospheric aerosols, and is a key factor for influencing the properties of aerosol particles [*Peng et al.*, 2017].

Both natural and anthropogenic sources contribute to new particle formation processes [*Kristensson et al.*, 2008]. New particles are generally formed via homogeneous or heterogeneous nucleation. Heterogeneous nucleation which is also known as "nucleated condensation", is the process of nucleation that takes place on already existing stable particle clusters [*Kulmala and Kerminen*, 2008]. Homogeneous nucleation is the process of nucleation that forms a new stable particle cluster [*Kulmala and Kerminen*, 2008].

Sulfuric acid (H_2SO_4) plays a significant role in new particle formation in the atmosphere [*Brus et al.*, 2017] for both binary and ternary nucleation *Kürten et al.* [2015]. This is because H_2SO_4 has a low vapour pressure and has a strong affinity for water [*Duplissy et al.*, 2016]. H_2SO_4 originates in the atmosphere from the oxidation of SO_2. A binary reaction is a two-component system; an example is the reaction between H_2SO_4 and water. A ternary reaction is a three-component system, such as the reaction between H_2SO_4, water and the third chemical species [*Kulmala and Kerminen*, 2008]. Examples of the third chemical species that are involved in ternary reactions are ammonia *Kirkby et al.* [2011]; *Merikanto et al.* [2007]; *Schobesberger et al.* [2015] and amines [*Kürten et al.*, 2014].

These nucleation processes are then followed by particle growth processes. Mechanisms involved in particle growth include condensation and coagulation [*O'Dowd et al.*, 1998]. Condensation growth is the next most important process for particle growth after nucleation [*Leppä et al.*, 2011]. Condensation occurs when vapour molecules adhere to the particle′s surface, enhancing the particle size [*Hinds*, 2011]. Aerosol particles collide, forming larger particles [*Hinds*, 2011] and reduces the total particle number concentration but does not affect the total volume of particles.

1.6.1 Classification of New Particle Formation

Surface plots, also known as contour plots of particle size distribution over time are commonly used to illustrate these new particle formation events. In these plots, the y-axis represents Dp, the x-axis represents time and the z-axis represents particle number concentration which is often plotted in different colours (Fig. 1.5). Visually, from these plots, new particle formation events are defined by the appearance of a typical shape called a “banana shape” (seen inside the rectangular box presented in Fig. 1.5). According to the classification developed by *Dal Maso et al.* [2005], new particle formation events are generally classified as either Class I or Class II.

(i) Class I is the event where the “banana shape” can be observed and the growth and information rate can be determined.

(ii) Class II is the event where the particle formation is still observable but due to fluctuation in particle diameter, the growth is not clearly observed and information rate is difficult to quantify.

Class I events can be sub-grouped into Class Ia and Class Ib. Class Ia occurs in an environment with very few or no pre-existing particles. A very clear new particle formation event is observed. Class Ib contains the rest of Class I events (Fig 1.5).

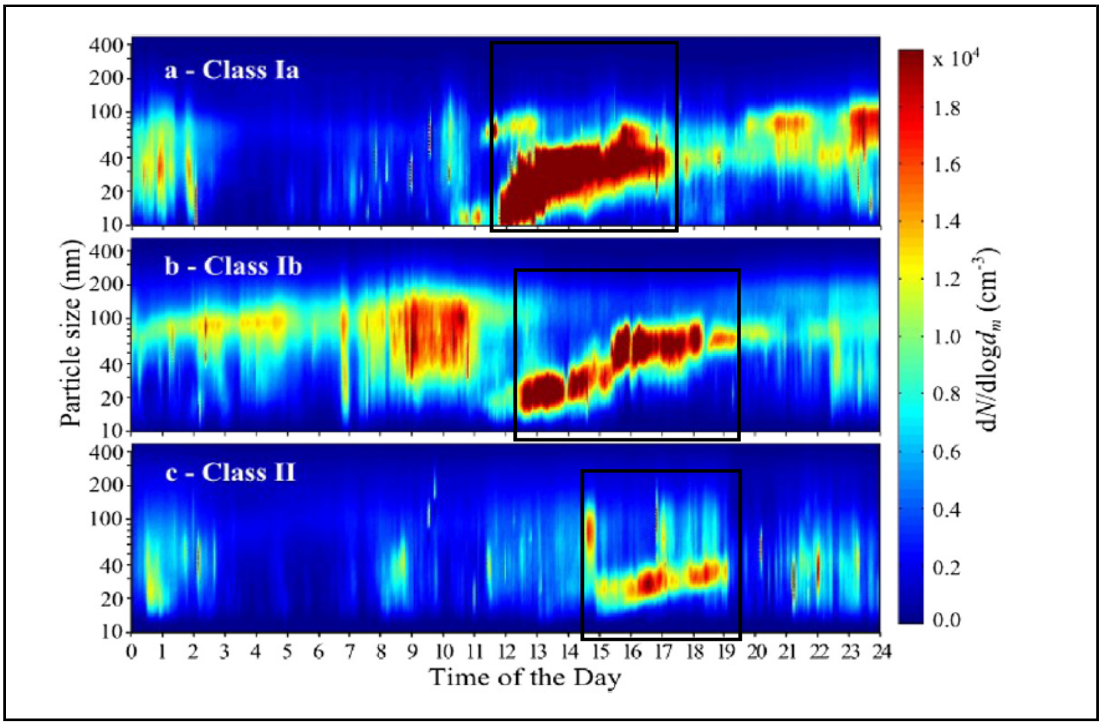

Fig. 1.5: Example of contour plots of particle number size distribution.(a) Class Ia event, (b) Class Ib event and (c) Class II event. The y- axis represents particle diameter and note that the y-axis is in log format. The x-axis represents time and the colour bar represents particle number concentration. The rectangular box delineates the events (Source:*Siakavaras et al.* [2016])

1.7 Overview of Air Quality With A Focus on New South Wales, Australia

Air quality in Australia is comparatively good, by global standards [*Butler and Whelan*, 2018]. However, there are people living in certain areas of Australia that still experience health problems due to high levels of air pollution, especially from the combustion of fossil fuels from coal-burning power stations, wood for heating during winter and vehicles in the large cities [*Butler and Whelan*, 2018]. A report by the NSW Office of Environment and Heritage *OEH* [2017] states that the annual average $PM_{2.5}$ concentration in all the cities studied in Australia were below the advisory reporting standard by the Australian National Environment Protection Measure for Ambient Air Quality (Air NEPM, 8 $\mu g\,m^{-3}$) and the World Health Organisation guidelines (WHO,10 $\mu g\,m^{-3}$) (Fig. 1.6). In comparison with many other places studied in Europe, United States and Asian countries, Australia recorded a low annual average $PM_{2.5}$ concentration (Fig. 1.6).

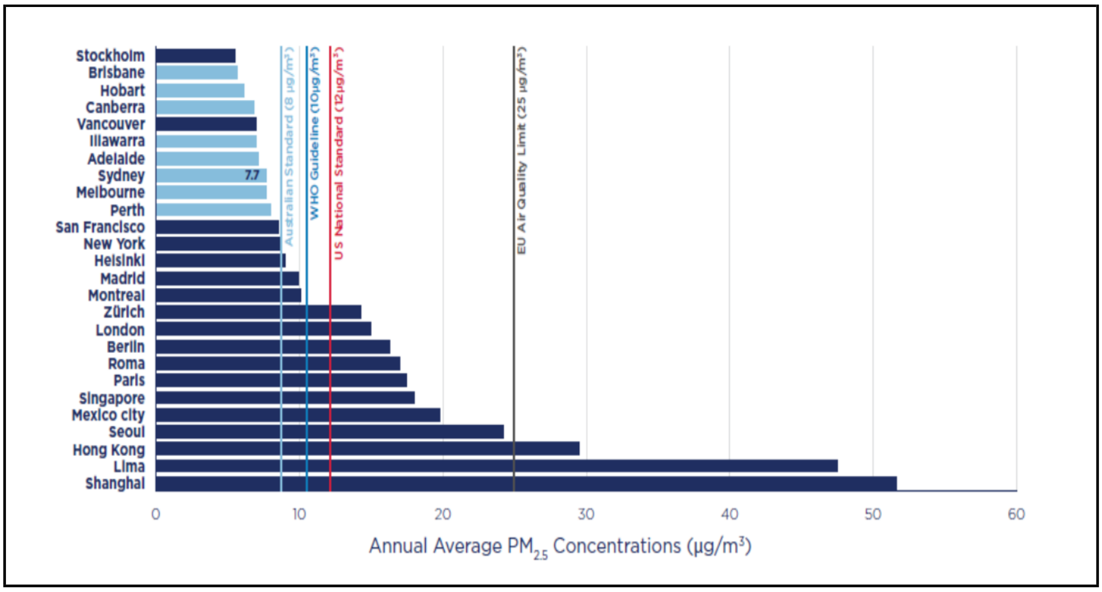

Fig. 1.6: Comparison of the annual average $PM_{2.5}$ concentration between cities in Australia and other cities globally. The comparison is based on 2014 measurements. (Source: *OEH* [2017]).

In this work, Wollongong in the Illawarra, New South Wales, Australia was the focus region. The NSW Office of Environment and Heritage reported that the recent air quality (2012-2016) was generally good by world standards. The Air Quality Index (AQI) was between the "very good or good" and "fair" categories for 83% to 91% of days in the Illawarra (Fig. 1.7). The AQI is a scale of air pollution used in summarising air quality level in Australia. An AQI of 100 triggers an air pollution health alert. A lower value of AQI (less that 100) indicates better air quality and a higher value of AQI (more than 100) indicates unhealthy air quality.

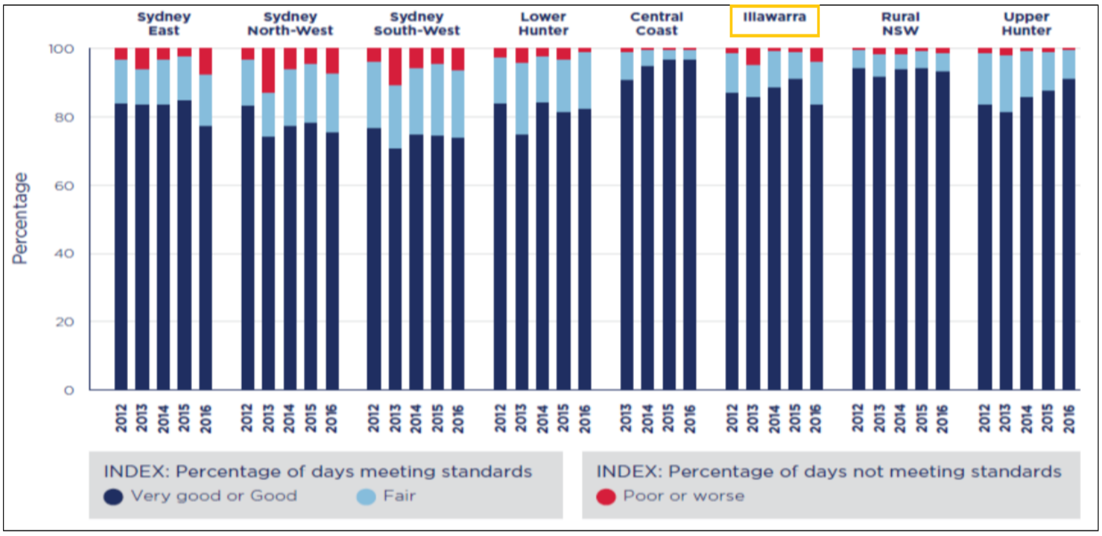

Fig. 1.7: Air Quality Index categories as a percentage of time in New South Wales sub-regions, between 2012 and 2016. (Source: *OEH* [2017]).

The *OEH* [2017] reported that the "poor or worse" air quality index experienced in NSW was due to particles and ozone. A study by *Broome et al.* [2015] reported that $PM_{2.5}$ and ozone were responsible for 2.1% and 0.8%, respectively of total deaths per year in Sydney, Australia′s largest and rapidly growing city.

Generally, particle concentrations in the Illawarra are comparable with the levels measured in other cities in Australia. However, these pollutants do exceed national standards from time to time [*OEH*, 2015]. The maximum value for daily and annual averages of $PM_{2.5}$ sometimes exceeds the Australian Air NEPM, which is 25 $\mu g\,m^{-3}$ and 8 $\mu g\,m^{-3}$ respectively (Fig. 1.8). Frequent daily exceedences are observed especially during bushfires and dust storms events (2002, 2003, 2006, 2009 and 2013). The exceedences observed in the annual average $PM_{2.5}$ are contributed by several events including the dry El Nino season (2002-2007), regional dust storms (2009) and bushfires (2013) [*OEH*, 2015]. The Office of Environment and Heritage, NSW reported exceedences without exceptional events in order to account for natural events in the air quality statement 2016 [*OEH*, 2016]. Exceptional events are those events related to bush fires, hazard reduction burning and dust storms. All three air quality monitoring stations in Illawarra met the $PM_{2.5}$ daily goal in 2016 when exceptional events are excluded.

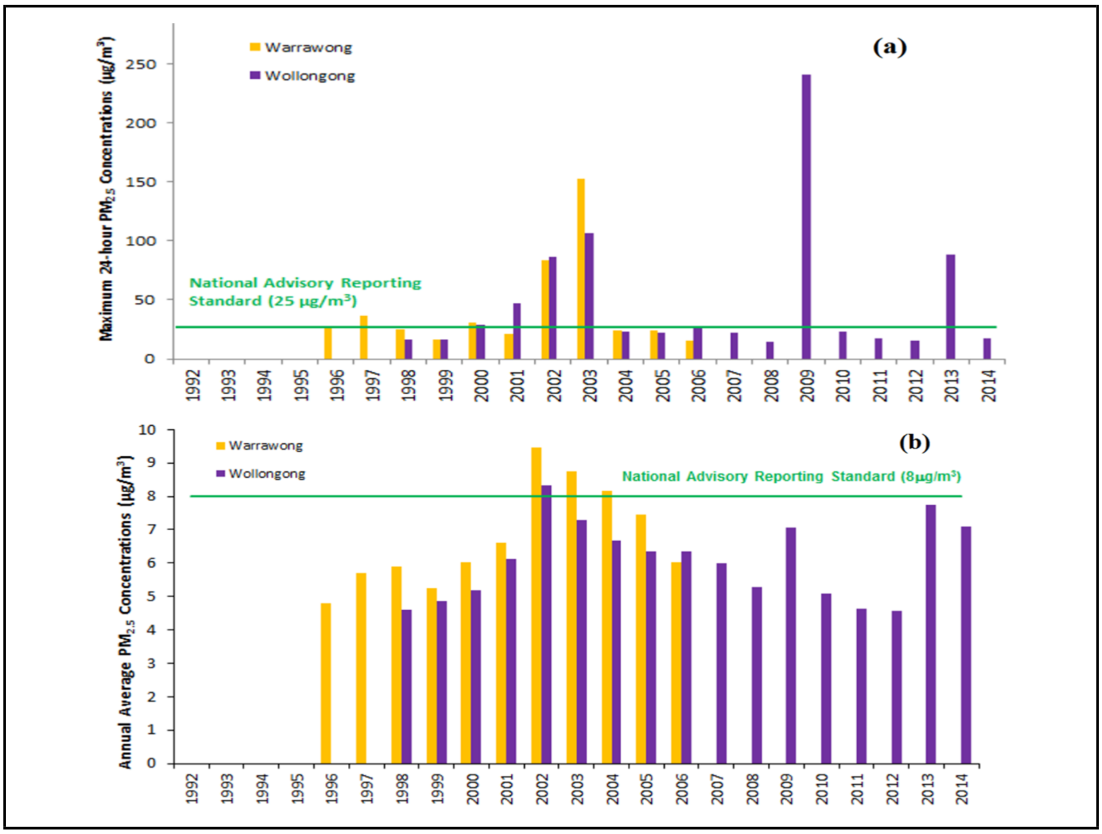

Fig. 1.8: (a) Daily average and (b) Annual average of $PM_{2.5}$ concentration in Illawarra (Wollongong and Warrawong) 1992 to 2014. (Source: *OEH* [2015]).

Air quality categorized as “poor” on the basis of the AQI in NSW in 2013 was generally poorer relative to several previous years of very good air quality across much of the State. The “poor” air quality was mainly related to warmer and drier conditions and severe bushfires. January 2013 recorded the warmest maximum temperatures on record in Sydney and across the State. During the months July to October, dry conditions with above-average temperatures were recorded. The warm and dry period that was accompanied by windy conditions between September and October led to bushfire activity in western Sydney, the Blue Mountains, Wollondilly and the Hunter Valley [*OEH*, 2015].

Major sources of $PM_{2.5}$ and PM_{10} in the Illawarra region reported by *OEH* [2015] included: (a) industrial activities contributing 70% of $PM_{2.5}$ and 81% of PM_{10}, iron and steel production as well as mining and extractive activities were major contributors. (b) domestic and/or commercial sectors contributed 12% of $PM_{2.5}$ and 20% of PM_{10}, with wood heating in residential areas accounting for over 90% of particle emissions. Other sources of aerosol particles included on-road and non-road mobile sources. The air quality experienced in the Illawarra region is also influenced by inter-regional transport of air pollutants, particularly from air movement from the Sydney basin. At night, cold air and low vertical mixing conditions allow pollutants to accumulate in the Sydney basin. In the early morning, the south-westerly winds blow the accumulated air pollutants from Sydney inland to the Sydney basin, picking up pollution from industrial and housing areas and from transportation. In the presence of a north easterly wind (sea breeze), the accumulated air pollutants in Sydney basin are blown down to the Illawarra region [*OEH*, 2015].

1.8 General Climate Conditions During Summer in NSW, Australia

The climate in Australia varies considerably. The Bureau of Meteorology, Australia *BOM* [2009], reported that Northern Australia encompasses equatorial and tropical savannah climates. Southern Australia has a Mediterranean climate with warm, dry summers and mild winters. Climates in the Western regions of Australia are hot arid and semi-arid with dry summers followed by mild, rainy winters. East Australia experiences a temperate climate. The automatic weather station at Bellambi, operated by the Australian Bureau of Meteorology, is the nearest alternative site to the MUMBA campaign site (Fig. 2.1(b)). The climate record from the nearest long-term meteorological measurement site (Bellambi) shows that during the campaign months, monthly averaged temperatures ranged from 19 ^{o}C to 26 ^{o}C. Wind direction is primarily from the southern sector in the morning and from the north-east sector in the afternoon. Monthly average wind speed ranged from 16 km h^{-1} to 18 km h^{-1} in the morning and from 24 km h^{-1} to 25 km h^{-1} in the afternoon [*BOM*, 2018].

1.9 Objectives and Significance of the Research

The overall aim of this research is to understand the changeable atmospheric aerosols resulting from an interaction between the urban, marine and biogenic environments. Measurements used in this research are from a field measurement campaign known as the Measurements of Urban, Marine and Biogenic Air (MUMBA) campaign, which occurred during summer in the coastal city of Wollongong, Australia. Whilst the trace gas compositions observed during this campaign have been analysed [*Guérette*, 2016; *Guérette et al.*, 2017; *Paton-Walsh et al.*, 2017, 2018], the characteristics of the aerosol population had not be studied.

The results obtained from this research are also necessary to add to the current understanding of atmospheric pollution and to fill the gap in knowledge of the characteristics of aerosol populations in the Illawarra region (south east coast of Australia). The conditions in the south east coast are similar to those on much of the east coast of Australia, but less affected by local sources than those of more densely populated regions such as Sydney. Therefore, the impact of other sources, such as the large-scale eucalyptus forest and the ocean could be significant. Additionally, the study of the aerosol vertical distribution is the first undertaken in the Illawarra region. Therefore, this research has high potential for use as a basis for planning improvements in air quality in the region, as well as a reference point for any future studies.

This work uses the aerosol measurements made during MUMBA along with measurements of the mole fraction of trace gases (including NO_x, CO, O_3 and volatile organic compounds), the meteorological state and traffic volumes. The specific objectives of this research are to analyse data from MUMBA campaign to:

(1) Interpret the characteristics of aerosol particle number size distribution.

(2) Interpret particle formation mechanisms.

(3) Assess the retrieval of aerosol properties by remote sensing techniques.

1.10 Outline of the Thesis

This thesis comprises six chapters. Chapter 1 describes the background and the objectives of the study. Chapter 2 describes the various methods applied, including instrumentation and computational techniques used. Chapter 3 presents the overview of the characteristics of aerosol populations observed from the aerosol measurements (16th January to 15th February, 2013) during the campaign. This chapter forms the framework to the published work: *Dominick, D., S. R. Wilson, C. Paton-Walsh, R. Humphries, E.-A. Gurette, M. Keywood, D. Kubistin, and B. Marwick (2018), Characteristics of airborne particle number size distributions in a coastal-urban environment, Atmos. Environ., 186, 256-265.* Chapter 4 presents the particle formation and growth events, which explains the frequency of occurrence of the events and the factors that influenced the new particle formation events in the complex coastal-urban-biogenic site. Chapter 5 presents the observation of aerosol populations by a remote sensing technique provided by the Multi-Axis Differential Optical Absorption Spectroscopy (MAX-DOAS) instrument. This instrument provides information on the aerosol vertical distribution. Finally, chapter 6 summarises all the findings obtained from this study and suggests recommendations for future research work.

Chapter 2

Materials and Method

2.1 Background of the Measurement Site

The MUMBA Campaign ran for approximately two months (21st December 2012 to 15th February 2013). This campaign was made possible by collaboration between the Centre for Atmospheric Chemistry, University of Wollongong (UOW) and several other teams of scientists from organisations and institutes including (i) CSIRO Climate Science Centre, Aspendale, Victoria, Australia, (ii) Australian Nuclear Sciences and Technology Organisation (ANSTO), New South Wales, Australia and (iii) GNS Sciences, Avalon, Lower Hutt, New Zealand.

The study area was the seaside city of Wollongong located in the Illawarra region of New South Wales, Australia, approximately 80 km south of Sydney (Fig. 2.1(a)). Wollongong is New South Wales' 3rd largest city after Sydney and Newcastle. Wollongong is also the 10th largest city in Australia. The estimated resident population in 2013 in Wollongong council region and Ilawarra region reported by the Australian Bureau of Statistics was 205,157 people and 295,957 people, respectively.

There were two measurement sites during the MUMBA campaign, the main measurement site (labelled as "A") was at University-based child care facility "Kids Uni" (34.397 °S and 150.900 °E) and the secondary site (labelled as "Second site") was at the University of Wollongong East Campus (34.401 °S and 150.899 °E) (Fig. 2.1(b)). The distance between these two sites was approximately 400 meters. Other measurement sites used in this study were located at the University of Wollongong, main campus (34.405 °S and 150.878 °E) and at the Wollongong air quality monitoring station operated by the Office of Environmental and Heritage (OEH) (34.419 °S and 150.886 °E) (Fig. 2.1(b)). This OEH air quality monitoring station is in a residential area and located approximately 3 km from the campaign site.

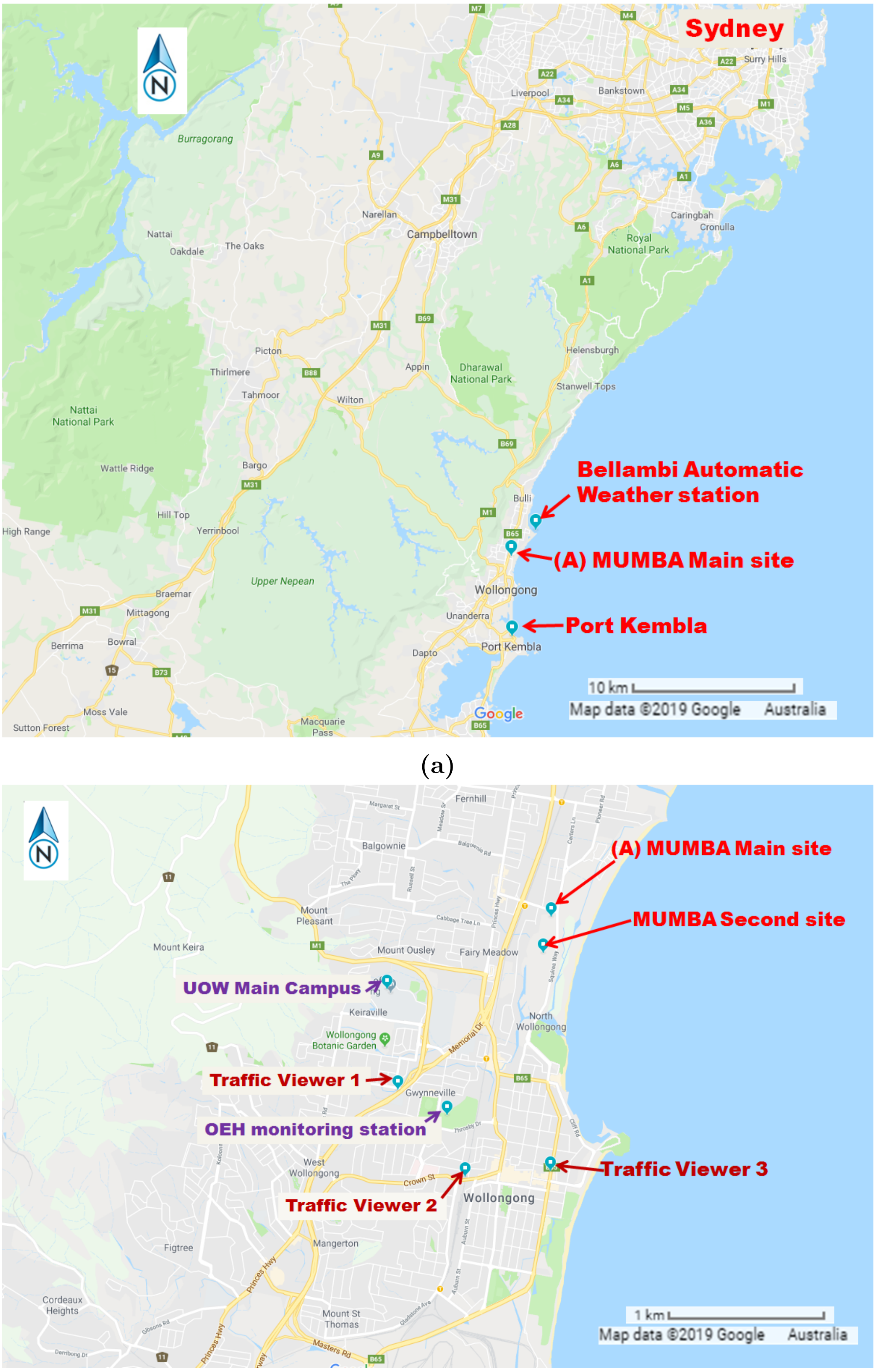

Fig. 2.1: (a) Main MUMBA measuring site (labelled as "A") and Bellambi Automatic Weather station and (b) Second MUMBA monitoring site, traffic viewer stations, University of Wollongong (UOW) main campus and Office of Environment and Heritage (OEH) air monitoring station.

The MUMBA campaign sites represented an urban area located near highways, train lines and housing. To the northwest of the main site there is a suburban area known as Fairy Meadow which contains a large strip for commercial and industrial activities. A coastal nature reserve called Puckey's Estate Reserve that is dominated by wetland areas located to the east of the site. Thomas Dalton Park is located to the northeast. Port Kembla, an industrial suburb and harbour with a large local steel works industry is located approximately 10 km south of the site. The Wollongong central business district is located 3 km south of the site. There is also a large scale forest nature reserve known as the Illawarra Escarpment State Conservation Area on a steep escarpment which begins approximately 3 km to the west of the site. The forest covers 20 km east to west and 60 km north to south and consists of diverse forest types including sub-tropical rainforest, eucalypts and indigenous cedars [*NSW*, 2017].

2.2 Instrumentation

2.2.1 Aerosol Sampling

A wide variety of instruments was used during the MUMBA campaign. Instruments used in this work can be divided into five categories (Table 2.1). Details of all instruments deployed during the campaign as well as the data processing are given in *Paton-Walsh et al.* [2017] and *Guérette et al.* [2017]. Data obtained from this campaign have been published online at PANGAEA *Guérette et al.* [2017].

Two main instruments were relevant to this work. They were the Scanning Mobility Particle Sizer (SMPS) and the Multi-Axis Differential Optical Absorption Spectrometer (MAX-DOAS). They will be discussed in detail in Section 2.3 and Section 2.4, respectively.

Table 2.1: Summary of instruments and measured parameter(s) used in this study

Category	Measured parameter(s)	Instruments	Measurement time resolution
In-situ Aerosol	Particle number size concentration with particle diameters ranging from $\sim$ 14 nm to $\sim$ 660 nm	Scanning Mobility Particle Sizer (Model: TSI 3080 for electrostatic classifier, TSI 3081 for differential mobility analyser and TSI 3772 for condensation particle counter)	$\sim$ 5 min
	Total particle number concentrations of diameter largers than 3 nm (CN_3)	Ultrafine Condensation Particle Counter (Model: TSI 3776)	$\sim$ 1 s
	Total number concentration of cloud condensation nuclei (CNN)	Cloud Condensation Nuclei Counter (Longmont, CO, USA)	$\sim$ 1 s
	$PM_{2.5}$ mass concentration	eSampler aerosol monitor (Model: Met One, 9800)	1 h
	Carbonaceous aerosols in $PM_{2.5}$ fraction	Thermal Optical Carbon analyser (Model: Met One, 2001A)	Daily: 04:00-09:00 10:00-18:00
In-situ Reactive Gases	O_3	Thermoelectron dual cell UV Ozone Analyser (Model: Thermo 49i)	1 min
	NO, NO_2^+	Chemiluminescence, Molybdenum converter (Model: Thermo 42i)	1 min
	VOCs	Proton Transfer Reaction-Mass Spectrometry (PTR-MS)(Model: Ionicon)	$\sim$ 3min
In-Situ GreenHouseGasses (GHG)	CO_2, CO, CH_4, N_2O	Fourier Transfer Infrared Spectroscopy (FTIR) Analyser (Model: UOW/Ecotech Spectronus)	$\sim$3 min
Optical Measurements	Integrated slant column and vertical profile of NO_2, O_3, O_4, BrO, H_2CO,H_2O, IO and aerosol loading and dominant size mode in the lower troposphere and stratosphere.	Multi-Axis Differential Optical Absorption Spectroscopy (MAX-DOAS) (Model: Avantes Avaspec, ULS3648)	$\sim$ 20 min
	Aerosol Optical depth	Direct beam solar radiation at 500 nm Sun Photometer (Model: Middleton, serial number: 1059 and 1029)	1 min
	Boundary layer height	Elastic backscatter at 355 nm Light Detection and Ranging (LIDAR) (Model: Leosphere ALS-400)	$\sim$ 30 s
Meteorological parameters	Wind speed, wind direction, temperature, relative humidity and pressure	Weather Station,Campbell Scientific, Easy weather	1 min, 5 min

In addition to SMPS and MAX-DOAS, an Ultrafine Condensation Particle Counter (TSI model 3776, USA) was used to measure total particle number concentrations for particles with a diameter larger than 3 nm (CN_3). Fine particle mass (with an aerodynamic diameter of less than 2.5 µm, $PM_{2.5}$) was measured by an eSampler aerosol monitor (Met One Instruments model 9800, USA). The Droplet measurement Technologies cloud condensation nuclei counter (Longmont, CO, USA) was used to measure cloud condensation nuclei (CCN). The eSampler made duplicates of measurements. Continuous real-time particle loadings were obtained by light scattering measurements, calibrated using a gravimetric measurement of the cumulative particle loading on filters which were changed weekly. Carbonaceous aerosol measurements (elemental carbon (EC) and organic carbon (OC)) and ionic substances were obtained from filter samples of total $PM_{2.5}$ which were collected using an Ecotech High Volume Air Sampler (model 3000). EC and OC were analysed after the campaign using a Thermal Optical Carbon Analyser (model 2001A, Met One Instruments, USA). Two Middleton Solar SP02 Sunphotometers (with serial numbers # 1059 and # 1029) were deployed at the University of Wollongong, ≈ 2 km southwest of the campaign site to measure aerosol optical depth of the atmosphere. An elastic backscatter aerosols Light Detection and Ranging (LIDAR) (model: ALS-400, Leosphere, Orsay, France) was used to measure range-resolved backscatter at 355 nm. The Klett inversion method *Ansmann and Muller* [2005]; *Klett* [1985] was used to derive range-resolved aerosol extinction at 355 nm from the LIDAR signal under the assumption of a constant backscatter-to-extinction ratio, known as the lidar ratio, of 25 steradian (sr). This value is within the range typical for marine aerosols of 20-26 sr [*Müller et al.*, 2007]. The particular implementation of the Klett inversion was from the Single Calculus Chain software [*Mattis et al.*, 2016].

2.2.2 Trace Gases, Traffic Data and Physical Parameters

A range of measurements was used to assist in the interpretation of the aerosol observations. Gas phase composition measurements, including the concentration of NO_x, CO, O_3 and volatile organic compounds were used. Details of these supporting data were reported by *Paton-Walsh et al.* [2017] and *Guérette et al.* [2017]. SO_2 was measured by OEH using a pulsed fluorescence spectrophotometer type Teledyne API model T100. Traffic volume (number of vehicles per hour) was obtained from the Road and Maritime Department, New South Wales, Australia. The traffic data were recorded with hourly resolution (00:00 to 23:00 h) and collected from three nearby traffic volume viewer sites as shown in Fig. 2.1 (b). Two meteorological datasets were used in this study. The first set was measured on site during the MUMBA campaign and the second set was measured by the Automatic Weather Station operated by the Australian Bureau of Meteorology at Bellambi (34.37°S, 150.93°E) (about 4 km northeast of the MUMBA campaign site)(Fig. 2.1(a)). Wind data from the MUMBA campaign site and from the Bellambi weather stations demonstrated that both stations experienced similar meteorological conditions [*Guérette*, 2016]. Meteorological parameters including temperature (°C), relative humidity (%), wind speed (m s^{-1}) and wind direction (°) together with global irradiance (W m^{-2}) were studied. It should be noted that global irradiance was measured using a solar radiation sensor (Davis Instruments, Vintage Pro2, USA) located at the University of Wollongong (Fig. 2.1(b)). The time zone used throughout this work was Australian Eastern Standard Time, AEST (UTC +10).

2.2.3 Data Analysis and Air Masses

Descriptive and statistical analyses were carried out using R statistical analysis version 3.3.1, 3.3.2, 3.3.3 and 3.5.1 [*R Core Team*, 2016]. The main package used in R statistical analysis was "openair" version 2.4.2 [*Carslaw and Ropkins*, 2012]. A built- in function in "openair" was used to average wind data. In this function, vector and scalar averaging are used for wind direction and wind speed, respectively. In addition to R statistical analysis, the Statistical Package for the Social Sciences (SPSS) software version 21 (IBM, USA) was used for multivariate analysis: Principal Component Analysis (PCA) and Hierarchical agglomerative cluster analysis (HACA).

Principal Component Analysis (PCA): PCA was used to determine the most significant particle diameter ranges that accounted for the variance in the observed particle size distributions. PCA is capable of reducing the dimensionality of the dataset, by transforming a set of inter-correlated variables into a set of uncorrelated variables. In this present work, PCA with eigenvalues of more than one are used in the varimax rotation to obtain the significant factors [*Kim and Mueller*, 1987]. The variables are particle size distributions. The principal components can be expressed as in Eq. 2.1 below:

$$Z_{ij} = a_{1i}x_{1j} + a_{2i}x_{2j} + ... + a_{ni}x_{nj} \tag{2.1}$$

where "Z_{ij}" is component score for component "i" for sample "j", "a" is component loading and "x" is the measured value of the variable. There are a total of "n" variables.

Hierarchical agglomerative cluster analysis (HACA): Hierarchical clustering is a method of building a hierarchy of clusters. A cluster is a group with similar objects. Hierarchical Agglomerative clustering is an approach that starts with each point in the dataset as a separate cluster. Then, two clusters that are closest together are identified and merged into a new cluster. This step continues until all the clusters are merged together [*Kaushik*, 2016; *Madhulatha*, 2012; *Wilks*, 2011]. The final product from HACA is a set of clusters where each cluster is different (heterogeneity) from the other cluster, and the objects within each cluster are similar (homogeneity) to each other [*McKenna*, 2003]. In this work, objects/variables are concentration of trace gases and meteorological parameters. HACA was performed using Ward's method and the Euclidean distance was used to measure any similarities [*Lau et al.*, 2009]. The Euclidean distance is based on a single linkage (also known as nearest neighbour). The distance between two clusters was computed as the distance between the two closest elements in the two clusters [*Ibarra-Berastegi et al.*, 2009].

Air masses: The path of air masses arriving at the monitoring site was studied using the Hybrid-Single Particle Lagrangian Integrated Trajectory (HYSPLIT) model [*Draxler and Rolph*, 2003; *Draxler et al.*, 2018]. The Global Data Assimilation System (GDAS) analysis product, a ready formatted meteorological dataset was used as the model data input. This dataset is publicly available from the National Oceanic and Atmospheric Administration (NOAA) at ftp://ftpprd.ncep.noaa.gov//pub/data/nccf/com/hysplit/prod/, the National Centre for Environmental Prediction (NCEP)[*Stein et al.*, 2015] and at www.ready.noaa.gov/archives.php for NOAA Air Resources Laboratories (NOAA ARL). Back-trajectory calculations are one of the most widely used features in HYSPLIT [*Fleming et al.*, 2012].

Bivariate polar plots were also generated to study the dependence of measurements on the local wind characteristics. Wind speed and wind direction data were measured during the campaign at the height of approximately 10 m above ground level [*Guérette et al.*, 2017; *Paton-Walsh et al.*, 2017].

2.3 Scanning Mobility Particle Sizer (SMPS)

The measurement of the particle number size distribution of the aerosol particles was performed with a scanning mobility particle sizer (SMPS) spectrometer (TSI 3936). This instrument measures the number of particles within 64 size bins with diameters from 14 nm to 660 nm with a measurement time resolution of approximately five minutes. The three major components of the SMPS spectrometer are: (i) an electrostatic classifier (TSI 3080), (ii) a differential mobility analyser (TSI 3081) and (iii) a condensation particle counter (TSI 3772). The explanation of the SMPS system is based on the operation and service manual reports (*TSI* [2010, 2012, 2014]) and also on a previous study by *Pettibone* [2009]. Size distribution inversions were performed using the Aerosol Instrument Management software, version 10.2.0.11 by TSI.

A basic schematic of how this instrument works is shown in Fig. 2.2. Polydisperse particles (a collection of non-uniform particles) enter the system and pass through an inertial impactor. The inertial impactor is a filter which removes all particles that are larger than a particular size. After passing through this filter, the particles pass through the bipolar ion neutralizer, which replaces the unknown charge distribution with a known charge distribution by creating positive and negative ions in the air with well-defined concentration using a Krypton-85 (Kr-85) radioactive source. The aerosol charge distribution is converted to the Fuch's charge equilibrium distribution [*Fuchs*, 1963] as the particles pass through the ionized air.

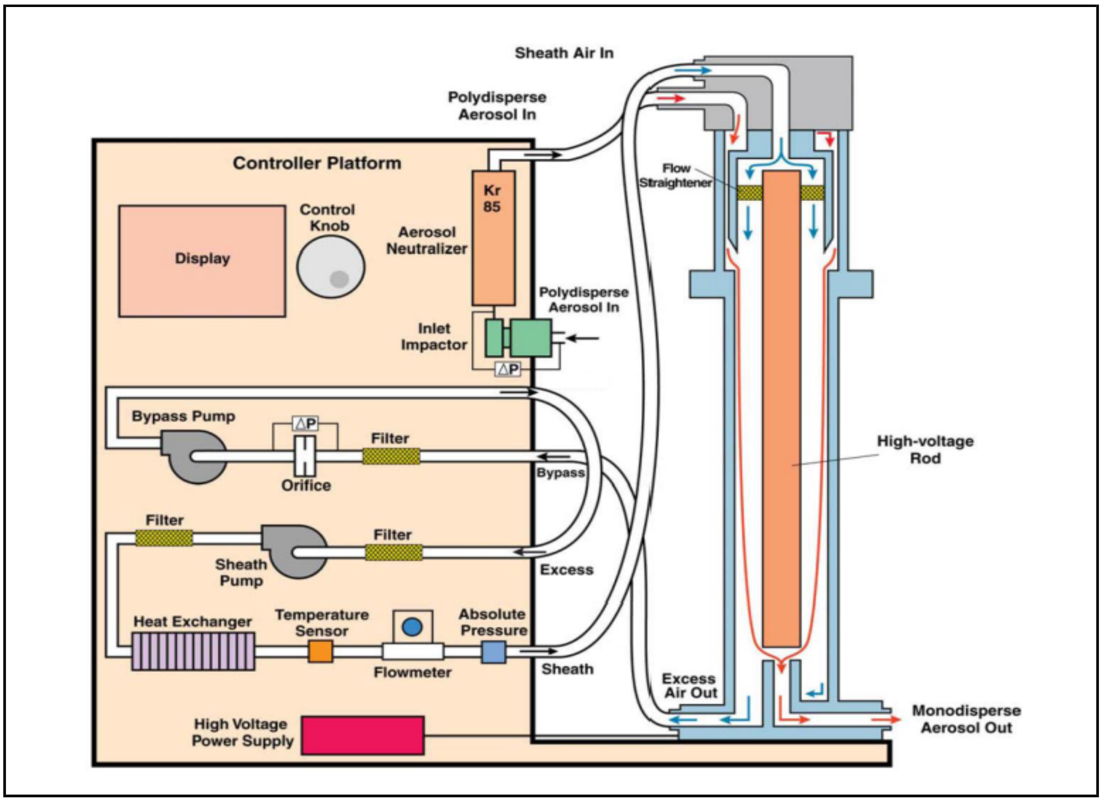

Fig. 2.2: Basic schematic of SMPS working principle. Source *TSI* [2010].

Then the polydisperse aerosol particles enter the differential mobility analyser (DMA) which operates on the principle of the mobility of a charged particle in an electric field, hence particles are separated according to their electrical mobility. The DMA is made up of two concentric metal cylinders: an inner cylinder (centre rod/electrode) and an outer cylinder. The inner cylinder is maintained at a controlled negative voltage and the outer cylinder is electrically grounded thus creating an electric field between the two cylinders. The aerosol particles are separated from the control electrode by the particle free sheath air flow (a laminar flow of particle-free air which is injected around the centre electrode). Positively charged particles move rapidly across the clean sheath air layer towards the negatively charged inner electrode while, negatively charged particles are deposited on the outer wall. In this stage, particles with high electrical mobility at the chosen voltage will be deposited on the electrode. Neutral particles and those with low electrical mobility flow to exit the DMA with the excess air. Only particles with the narrow range of electrical mobility will pass through the output opening. After exiting the DMA, the classified aerosols (monodisperse aerosols) flow on to the condensation particle counter.

The particles are counted in the condensation particle counter by growing them to larger sizes and then detecting them using a light scattering technique. The schematic of the basic working principle of a condensation particle counter is illustrated in Fig. 2.3. An aerosol sample is drawn into the sample inlet and passed through a region which is supersaturated using an external fluid source. In this study, butanol was used. As the vapour molecules condense on the aerosol particles, they grow and form liquid droplets. The particles then pass through a laser beam and the scattered light is detected by a photodetector, which counts the individual particles as flashes of light. The entire particle size distribution and number concentration are measured by exponentially increasing the voltage of the inner electrode in the DMA over a user-selected period of time.

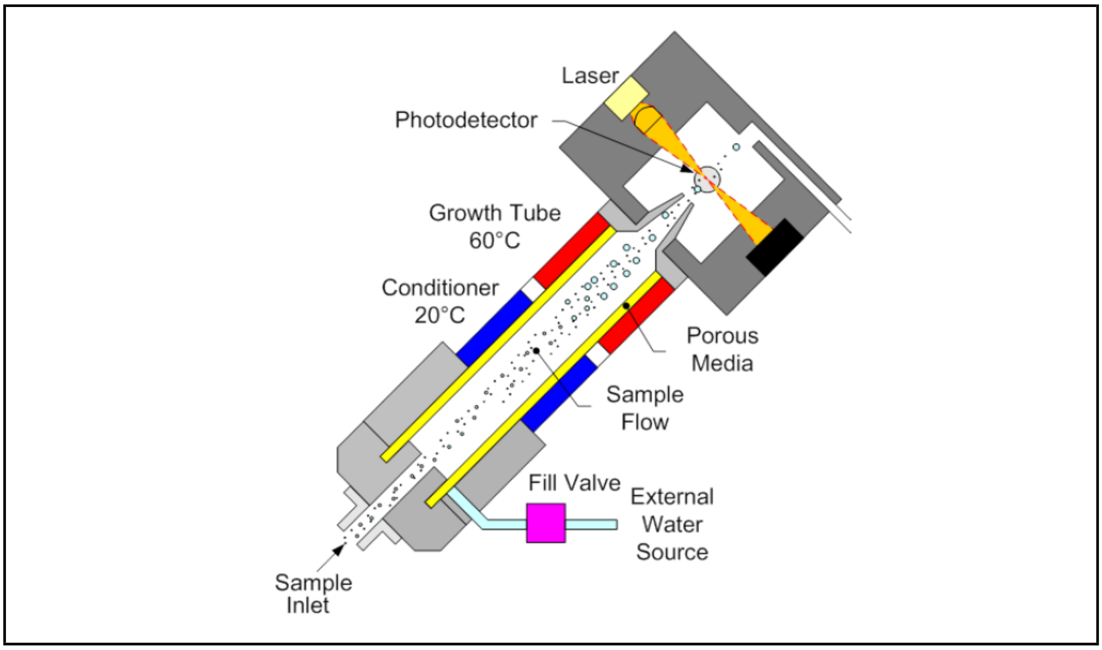

Fig. 2.3: Schematic of basic the condensation particle counter (CPC) working principle. Source *TSI* [2014].

2.3.1 Particle Number Concentration Calculation

An equation to normalize particle number concentration over the width of the bin (Eq. 2.2) has been proposed by *TSI* [2012]. This equation is used to re-calculate total particle number concentration at certain bin sizes.

$$\frac{dN}{dlogD_p} = \frac{dN}{logD_{p,u} - logD_{p,l}} \tag{2.2}$$

Where dN is the particle number, D_p is the midpoint of the particle diameter for the bin, $logD_{p,u}$ is the upper channel diameter and $logD_{p,l}$ is the lower channel diameter.

2.4 Multi-Axis Differential Optical Absorption Spectroscopy (MAX-DOAS)

The MAX-DOAS is a passive remote sensing technique which measures scattered sunlight in the ultraviolet and visible wavelengths (UV-VIS) at different elevation angles. The experimental setup is simple as it detects a natural light source scattered (sunlight) and can be fully automated for long-term deployment. Used together with forward radiative transfer calculations, MAX-DOAS measurements can provide vertical distribution information of aerosol extinction and trace gases concentration in the lower troposphere [*Hönninger and Platt*, 2002; *Hönninger et al.*, 2004; *Wang et al.*, 2016b]. MAX-DOAS analyses use the oxygen collisional complex (O_4) absorption to retrieve aerosol properties. This is because O_4 has a very well known vertical concentration profile and numerous absorption bands observable over ultraviolet and visible wavelengths, making it easy to detect [*Frieß et al.*, 2006; *Wagner et al.*, 2004]. The O_4 concentration has a well defined relationship with atmospheric pressure and temperature as it is determined by the equilibrium of $2O_2 \leftrightarrows O_4$.

Aerosols change the average observation path through the atmosphere. In an atmosphere with low aerosol loading, light scattering is predominantly due to Rayleigh (molecular) processes occurring meaning that the average scattering point is at a distance from the observer. At a low observation angle, this gives a long path length close to the ground. Therefore, a significant O_4 retrieval amount is observed. When there is a high aerosol loading, more scattering occurs so the scattering point on average is closer to the observer, which creates a shorter observation path length. Therefore, the O_4 retrieval amount is decreased [*Wagner et al.*, 2004]. The ability of aerosols to change the average photon path length through the atmosphere for MAX-DOAS observations is presented in Fig. 2.4. Once the aerosol scattering profile has been estimated, the average path through the atmosphere is known. Absorption features of other species can then be used to estimate their vertical concentration distribution.

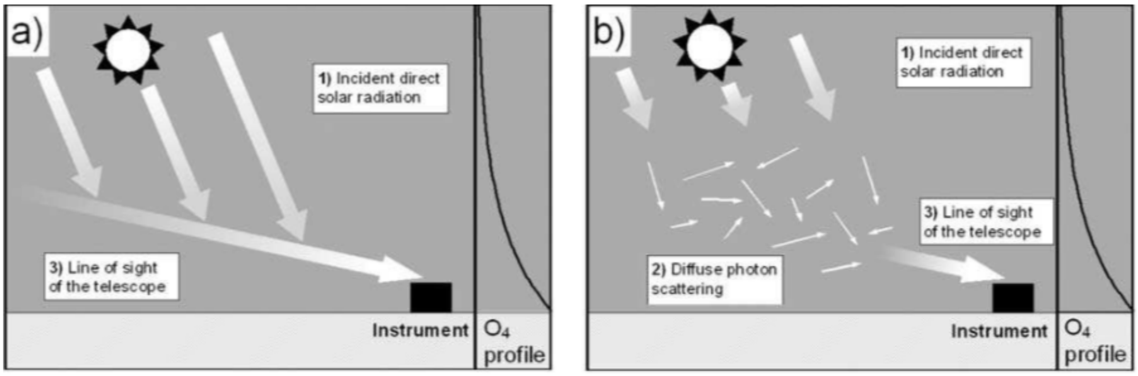

Fig. 2.4: Diagram of the ability of aerosol loading to change the average observation path length for MAX-DOAS observations. (a) In an atmosphere with low aerosol loading, the observed photons are mainly single scattered and more sunlight penetrates to the ground surface because of less/no aerosol scattering effect. The penetration depth of the direct sunlight is large and therefore the observation path length (line of sight of the telescope) is longer. (b) In an atmosphere with a high aerosol loading, mainly diffused photon scattering is observed and less sunlight penetrates to the ground. The penetration depth of the incident direct solar radiation is smaller and the observation path length (line of sight of the telescope) is shorter. Adapted from *Wagner et al.* [2004].

There have been several studies of measurements of aerosols and trace gases using MAX-DOAS. For example the work by *Ryan et al.* [2018] measured daytime HONO, NO_2 and aerosol distributions in Melbourne, Australia reported midday peaks in the diurnal cycle of HONO surface concentrations and the source distribution of HONO, NO_2 and aerosol. *Chan et al.* [2018] measured aerosols and NO_2 in Hong Kong over five years. The retrieved aerosols from MAX-DOAS showed a good correlation with aerosol optical depth (AOD) of sun photometer observations. Ground level NO_2 mixing ratios from a long path DOAS measurement agreed well with the MAX-DOAS NO_2. *Garcia-Nieto et al.* [2018] retrieved the vertical distribution of O_4 and nitrous acid (HONO) in Madrid, Spain. They also studied the temporal pattern of HONO and the contribution of HONO to the OH formation through photolysis.. *Wang et al.* [2016b] in Madrid, Spain reported a good correlation between the surface aerosol extinction coefficient as measured by MAX-DOAS and in-situ $PM_{2.5}$ concentrations. *Gratsea et al.* [2016] measured NO_2, HCHO, glyoxal (CHOCHO) and O_4 in the urban environment of Athens. Not only did they obtain information on the temporal and spatial distribution as well as the diurnal, weekly and seasonal variation of aerosols and the measured reactive trace gases, but they were also able to determine the pollutant sources. *Frieß et al.* [2016] studied the intercomparison of aerosol extinction profiles retrieved from a number of MAX-DOAS measurements. They reported that the time series of aerosol optical thickness retrieved from MAX-DOAS showed a good match with the co-located sun photometer measurements.

2.4.1 Instrument Specification and Retrieval Settings

A MAX-DOAS instrument based on an Avantes Avaspec ULS3648 spectrometer was deployed during this campaign. The MAX-DOAS instrument consisted of three main parts, including a telescope, a spectrometer and a computer as the control unit. The MAX-DOAS instrument made measurements from 266 nm to 538 nm of scattered solar radiation at a range of elevations. The spectrometer used has a Symmetrical Czerny-Turner design with a 75 mm focal length. A prism acted as the vertical (elevation) scanning device which was driven by a stepper motor. The scattered sunlight is then focused on to the optical fibre. The optical fibre is connected to the spectrometer for spectral analysis. The MAX-DOAS schematic diagram of the experimental setup is illustrated in Fig. 2.5.

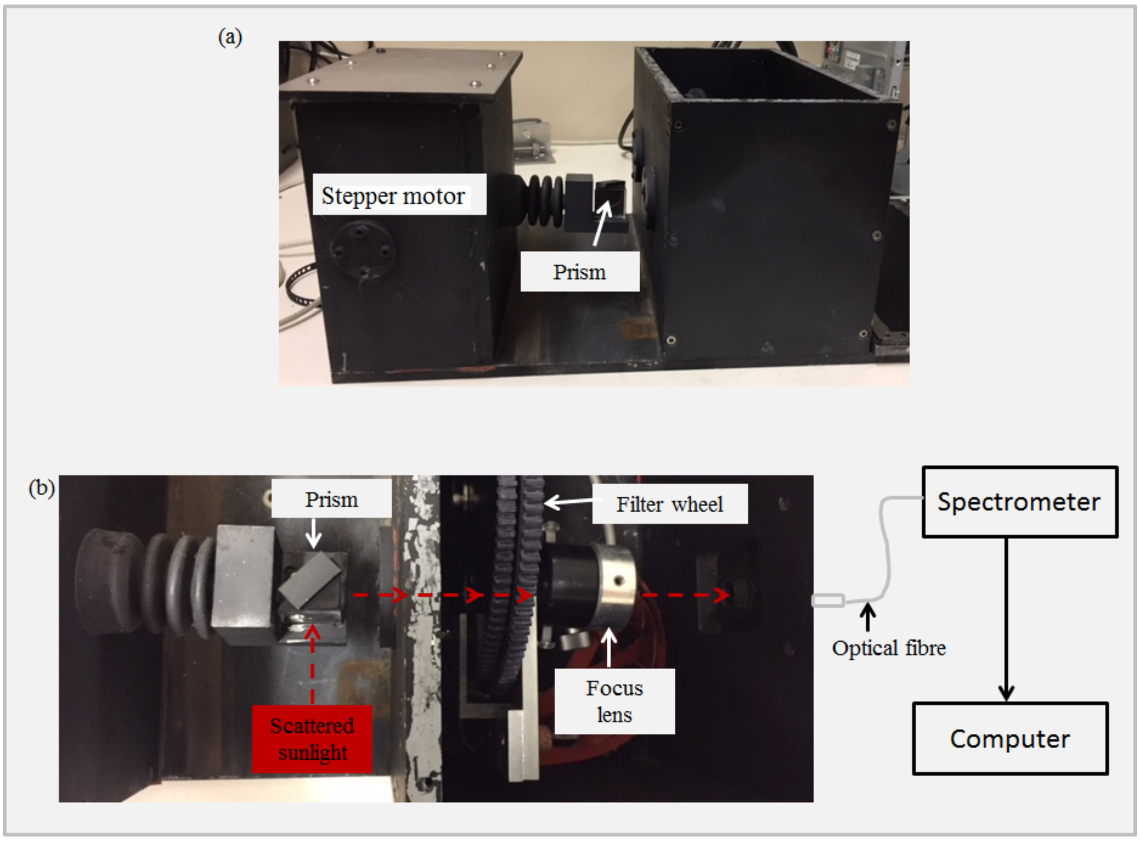

Fig. 2.5: Schematic diagram of the MAX-DOAS setup during the MUMBA campaign. (a) A stepper motor connected to a prism to collect scattered sunlight from different elevation angles. (b) The sequence of the spectra measurements from prism to the computer.

The telescope scanning system was mounted on the roof of a building, approximately 20 m above ground level at the University of Wollongong East Campus (34.401 °S and 150.899 °E) which is labelled as “Second site” in Fig. 2.1(b). The telescope was pointed at a fixed azimuth angle (68°), facing the open ocean (Fig. 2.6). A full measurement sequence consisted of elevation viewing angles of 1°, 2°, 4°, 8°, 16°, 30°, 60° and 90°. The full measurement sequence was preformed consecutively taking 20 min on average.

Fig. 2.6: Photo of MAX-DOAS taken during the campaign. The instrument was positioned towards the open ocean looking towards the north-east (68°).

MAX-DOAS measurement: A sketch of MAX-DOAS measurement is shown in Fig. 2.7. Sunlight enters the Earth′s atmosphere at an angle (solar zenith angle, (ϑ)) from the zenith and the instrument views the scattered light at angles between the horizon (α). Scattered light at different elevation angles is collected by the telescope and the signal is detected in the form of a spectrum by the spectrometer. The light path through the upper atmosphere depends little on the viewing direction, while in the lowest atmospheric layers, the light path increases as the viewing direction approaches the horizon. The smaller the elevation, the larger the sensitivity for species located near the ground [*Hönninger et al.*, 2004; *Sinreich*, 2007].

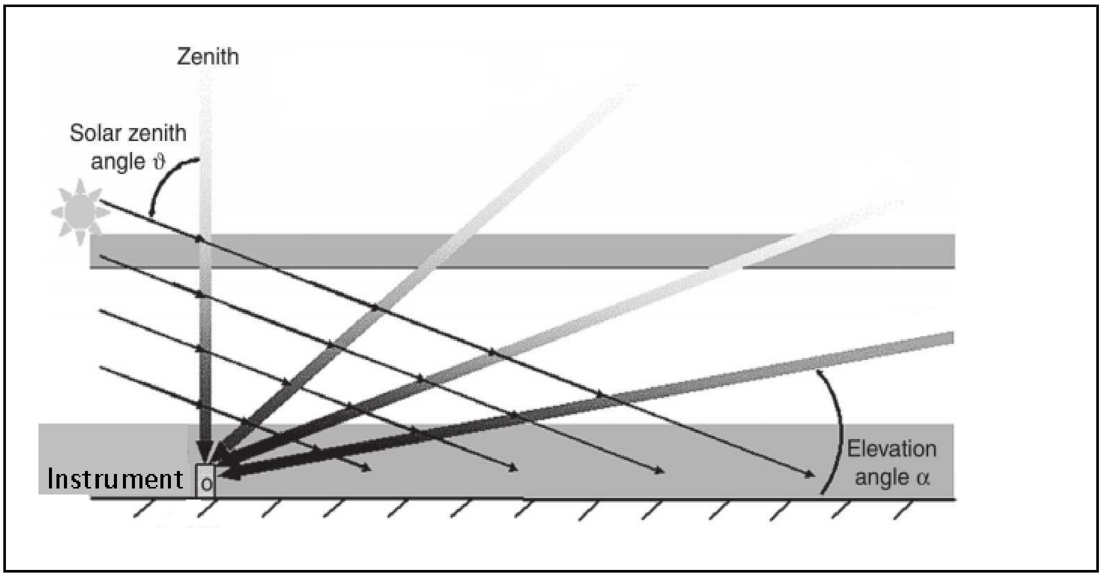

Fig. 2.7: Sketch of a MAX-DOAS measurement geometry. Adapted from *Platt and Stutz* [2008].

Spectral analysis: The measured spectra were analysed using the DOAS technique which is based on the Beer-Lambert law and can be used to describe the attenuation of scattered sunlight along its atmospheric light path through the atmosphere [*Platt and Stutz*, 2008]. The attenuation of the initial light intensity (I_o) due to absorption by an absorber with the concentration (c) along the light path (L) can be expressed as in Eq. 2.3, where λ is the wavelength of interest, I is the light intensity after passing through an absorber and $\sigma(\lambda)$ is the wavelength-dependent absorption cross-section of the absorber. A detailed description of the DOAS method and its applications can be found in *Platt and Stutz* [2008]. The QDOAS software (version 2.108) used in these analyses was developed by BIRA_IASB (http://uv-vis.aeronomie.be/software/QDOAS). The configuration setup can be found in QDOAS software user manual by *Danckaert et al.* [2014].

$$I(L, \lambda) = I_o e^{(-c.\sigma(\lambda).L)} \tag{2.3}$$

The wavelength interval between 350 nm and 389 nm was used here. There were two O_4 absorption bands in this range (360 nm and 380 nm). The selected molecular spectral cross-sections chosen for this work have been used successfully in previous studies. The temperatures were chosen based on what is available that would be relevant for the lower troposphere at this site. The molecular absorption cross-section files fitted were O_4 at 298 K (*Hermans et al.* [1999]), O_3 at 293 K (*Bogumil et al.* [2003]), NO_2 at 298 K (*Vandaele et al.* [1996]), HCHO at 297 K

(*Meller and Moortgat* [2000]) and BrO at 298 K (*Wilmouth et al.* [1999]). A 5^{th} order polynomial was included in the fit. The effect of Raman scattering by the atmosphere, the so-called "Ring effect" [*Grainger and Ring*, 1962], was included by fitting a calculated Ring spectrum as an additional absorber. The Ring spectrum file was based on the method introduced by *Chance and Spurr* [1997], as implemented in the QDOAS software.

DSCDs and Vertical profile retrieval: The MAX-DOAS measurements provide indirect information on the aerosol vertical profile. Therefore, inverse methods are necessary for the retrieval procedure [*Frieß et al.*, 2006]. The QDOAS retrieval results are labelled as DSCDs denoting the difference between the slant column densities of atmospheric trace gases measured at an elevation angle (α) and a reference measurement [*Xing et al.*, 2017]. A zenith sky (90°) measurement of the same elevation sequence has been used as reference measurement in this work. These DSCDs are then converted to aerosol vertical profiles by using a radiative transfer model known as the Heidelberg profile (HEIPRO) developed by the Institute of Environmental Physics (IUP) Heidelberg, Germany [*Frieß et al.*, 2006, 2011, 2016].

The inversion algorithm was developed based on the Optical Estimation Method [*Rodgers*, 2000] which employs the radiation transfer model SCIATRAN as the forward model [*Rozanov et al.*, 2005]. The Optical Estimation Method is based on Bayesian statistics. Briefly, the maximum a posteriori (MPA) solution ($\widehat{x}$) is determined by minimizing the cost function (χ^2), as is illustrated in Eq. 2.4:

$$X^2(x) = [y - F(x,b)]^T S\epsilon^{-1}[y - F(x,b)] + [x - x_a]^T S_a^{-1}[x - x_a] \tag{2.4}$$

The function *F(x,b)* is the radiative transfer model or forward function that describes the measurement vector (y) (the DSCDs at different elevation angles) as a function of atmospheric state (x) (aerosol vertical profile). The vector b represents additional forward model parameters including meteorological parameters (for example pressure and temperature), aerosol single scattering albedo as well as the aerosol scattering phase function. The a priori atmospheric state vector, (x_a) serves as an additional constraint. Sϵ and S_a denote the diagonal measurement covariance matrices, representing the uncertainties in the measurements and of the *a priori* state, respectively. The vertical resolution of the retrieval is quantified by the averaging kernel matrix (**A**), shown in Eq. 2.5:

$$\mathbf{A} = \frac{\delta\widehat{x}}{\delta x} \tag{2.5}$$

The variable **A** represents the sensitivity of the retrieved profile ($\widehat{x}$) to the atmospheric state (x). The retrieved profile ($\widehat{x}$) can be smoothed by the averaging kernel matrix ($\mathbf{A}$), as illustrated in Eq. 2.6:

$$\widehat{x} = x_a + \mathbf{A}(x - x_a) \tag{2.6}$$

Aerosol inversion: In the forward radiative transfer model, the employed atmospheric pressure and temperature profiles were adapted from a climatology database employed in SCIATRAN, which contains various monthly and latitude dependent trace gases vertical profiles [*Hendrick et al.*, 2014; *Wang et al.*, 2016b, 2014]. For the scattering process the aerosols were assumed to have an asymmetry parameter of 0.72 and single scattering albedo of 0.93. Surface albedo was set at 0.05. The *a priori* a priori profile used in the aerosol retrieval was linearly decreasing from the surface to higher altitude.

Chapter 3

Characterisation of Aerosol Particle Number Size Distribution

3.1 Introduction

This chapter provides an overview of particle populations measured during the MUMBA campaign. The main objectives of this chapter are to analyse the characteristics of the observed particle size and their temporal changes as well as, to identify the potential particle sources. Measurements used in this chapter can be divided into three categories: (i) aerosol particle data, (ii) trace gases and volatile organic compound concentrations, and (iii) meteorological and traffic data. Aerosol particle properties considered are the particle number concentration for particles ranging in size from 14 nm to 660 nm ($\text{PNC}_{14nm-660nm}$), the total particle number concentration range from 3 nm to 2.5 µm (CN_3) , the fine particle mass (with an aerodynamic diameter of less than 2.5 µm, $\text{PM}_{2.5}$), the carbonaceous aerosol composition (elemental carbon (EC) and organic carbon (OC)) and the secondary organic aerosol concentration (SOA). Trace gas data include the mole fraction (ppb) of NO_x, CO, O_3 and selected volatile organic compounds (benzene, toluene, isoprene). The meteorological datasets include temperature, global irradiance, wind speed,wind direction and relative humidity. This chapter focuses on four major topics. It begins with an overview of the meteorological conditions experienced during the campaign (Section 3.2). Second, the particle number concentration (cm^{-3}) and particle mass concentration ($\mu\text{g}\,\text{m}^{-3}$) are characterised (Section 3.3). Third, the identification of potential emission sources of the particles (Section 3.4) is considered and finally, the variability (temporal changes) of particle number is presented in Section 3.5 and 3.6. The work presented in this chapter forms the basis of the published paper *Dominick et al.* [2018] entitled “Characteristics of Airborne Particle Number Size Distribution in a Coastal-Urban Environment” in the journal of Atmospheric Environment.

3.2 Meteorological Conditions

As mentioned in Chapter 2, the MUMBA campaign was run during the local Australian summer. Fig. 3.1 (a-e) shows the diurnal cycle of temperature, global irradiance, wind speed, wind direction and relative humidity. The mean diurnal temperature ranged between 20 °C and 24 °C. Overall, clear days were experienced during the campaign which resulted in a mean global irradiance of 700 W m^{-2} at noon. Wind speed increased steadily and it reached the maximum reading at noon. In terms of wind direction during the campaign, westerly winds were observed overnight and early in the morning (breeze blowing from the land to sea (i.e. land breeze)) and easterly winds occurred in the middle of the day (breeze blowing from the sea to land (i.e. sea breeze)). Full details of the meteorological conditions during the campaign are given in the study by *Paton-Walsh et al.* [2017]. Overall, most of the time during the measurement period, the site experienced air masses blown in from the ocean with little input from the free troposphere. This is illustrated by the four clusters of 48-h backward trajectories at 100 m (Fig. 3.1 (f)) and 48-h backward trajectories at 500 m (Fig. 3.1(g)). This implies that oceanic air masses were one of the sources that contributed to the atmospheric composition at the monitoring site during the campaign.

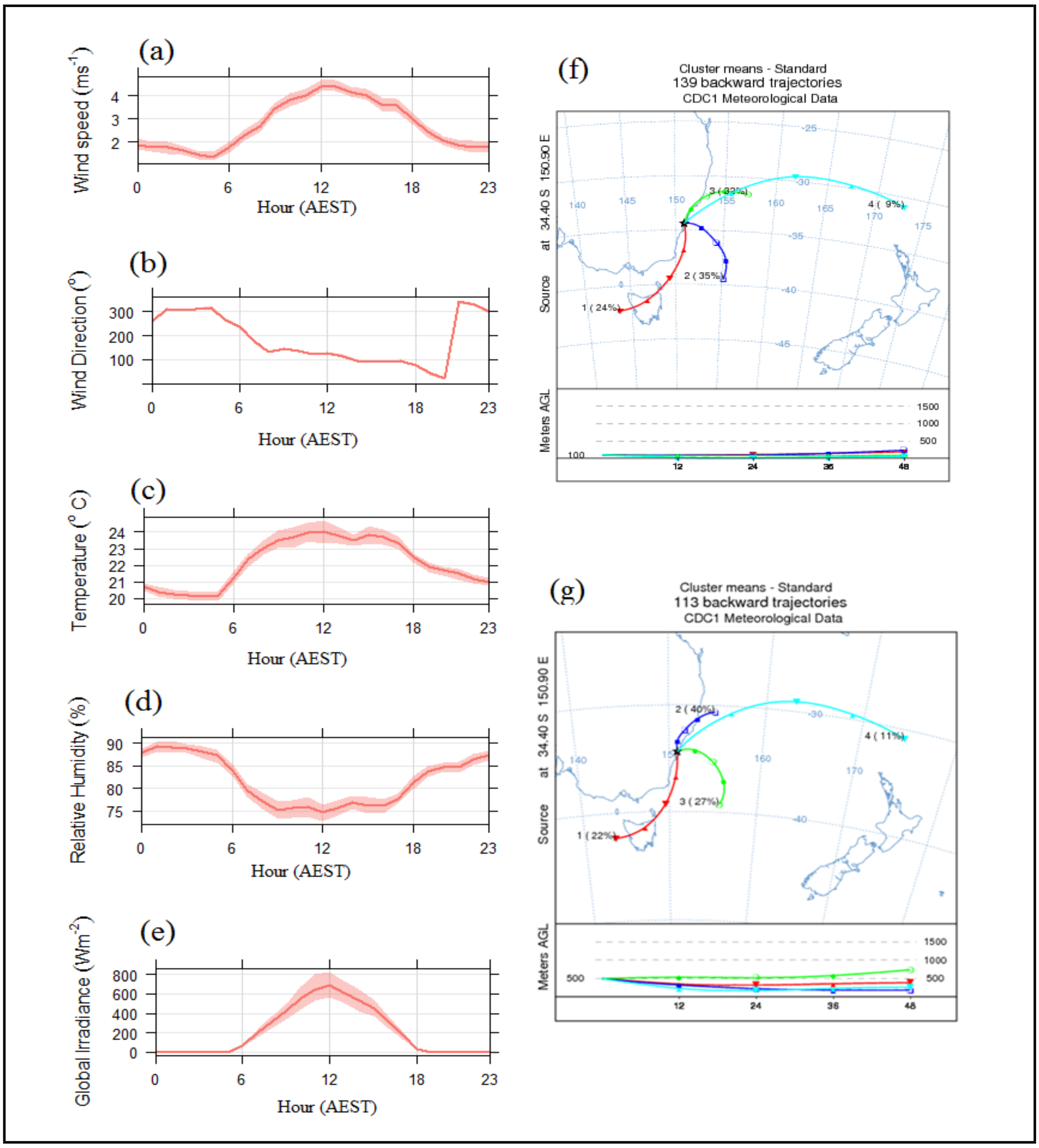

Fig. 3.1: The mean diurnal variation of meteorological parameters measured at the site including global irradiance (a-e). The shaded area is the 95 % confidence level. Figures (a-e) were plotted using R statistical analysis packaged ”openair” (*Carslaw and Ropkins* [2012]). Fig. (f) and Fig. (g) created using the Hybrid-Single Particle Lagrangian Integrated Trajectory (HYSPLIT) model and show four mean clusters of 48-h backward trajectories at 100 m and 500 m, respectively. The data used for these plots covered the aerosol measurements for the time period (16th January to 15th February 2013).

3.2.1 Variation of Particle Number Concentration in Relation to Wind Direction

The monitoring station experienced air masses from the ocean and inland over the campaign period as shown by HYSPLIT backward trajectories. Air masses from different wind directions were considered to be generally representative of the area and important for the understanding of their effects on particle number concentration and potential particle sources. Wind data (10-min averages) and aerosol measurements were reviewed. Wind directions were divided into eight wind sectors (Fig. 3.2 (a)) to get an overall idea on the variability of wind direction. By studying the number of observations within each wind sector, the eight wind sectors (W1 to W8) were then condensed into four major wind sectors S1 to S4 (Fig. 3.2 (b)). Sector 2 (S2) will be used as an example of how the four wind sectors were obtained. S2 covered the wind sector of $46° \leq x \leq 180°$ which is a combination of W2, W3 and W4 of the eight wind sectors (Fig. 3.2 (a)). W2, W3 and W4 have similar characteristics in terms of frequency of occurrence. Distributions of particle number concentration ($PNC_{14nm-660nm}$) from the four wind sectors are illustrated in Fig. 3.2 (c). The highest occurrence of particle distribution was observed in Sector 2 (34%), followed by Sector 4 (23%) and Sector 1 (23%). The lowest was in Sector 3 (19%).

The aerosol sources expected in the four wind sectors can be summarised as follows:

(i) Sector 1 ($0° < x \leq 45°$): Air masses were transported by wind down the coast from other regions including Sydney.

(ii) Sector 2 ($46° \leq x \leq 180°$): Air masses approaching from this direction were generally from the open ocean (Pacific Ocean). There could also be biogenic input from the small coastal strip to the east of the measurement site.

(iii) Sector 3 ($181° \leq x \leq 225°$): Anthropogenic sources were from urban areas and industrial activities. In the southern direction, approximately 10 km from the campaign site are an active industrial suburb and a harbour (Port Kembla) with a large local steel works industry. Approximately 3 km to the south of the campaign site is also the Wollongong central business district.

(iv) Sector 4 ($226° \leq x \leq 360°$): Emissions from anthropogenic sources include commercial and industrial properties, as well as main highways, roads and the South Coast train line. Biogenic emissions from this direction were generally from a large scale forest nature reserve known as the Illawarra Escarpment conservation area, approximately 3 km from the site.

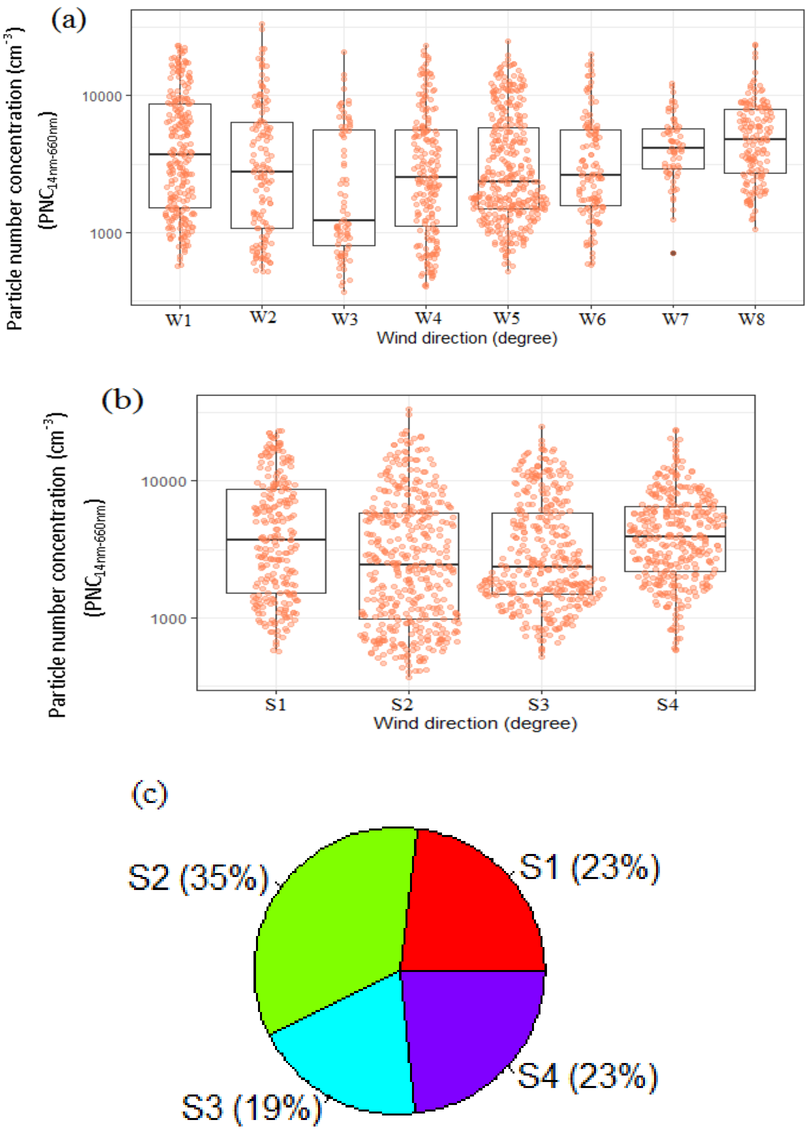

Fig. 3.2: (a) Distribution of particle number concentrations (PNC$_{14nm-660nm}$) in the eight wind sectors. W1, W2, W3, W4, W5, W6, W7 and W8 covered wind sectors of 0°< x ≤ 45°, 46°≤ x ≤ 90°, 91°≤ x ≤ 135°, 136°≤ x ≤ 180°, 181°≤ x ≤ 225°, 226°≤ x ≤ 270°, 271°≤ x ≤ 315° and 316°≤ x ≤ 360°, respectively. (b) Distribution of PNC$_{14nm-660nm}$ in the four wind sectors. S1, S2, S3, S4 covered wind sectors of 0°< x ≤ 45°, 46°≤ x ≤ 180°, 181°≤ x ≤ 225° and 226°≤ x ≤ 360°, respectively. Box and whisker statistical information summarise the particle distribution in each wind sector. The central line of each box is the median. The lower and upper edges of each box are the 25% quartile and 75% quartile, respectively. Whisker extended to the smallest of either the furthest data point or 1.5 times the quartile value. Note that the y-axis is in log format. (c) The occurrence frequency of particle number concentration (PNC$_{14nm-660nm}$) at each wind sector is shown. The figures are based on 10-min averaged data collected at the MUMBA site covering the whole time frame of aerosol measurement (16th January 2013 to 15th February 2013).

3.3 Overview of Particle Populations

The daily variation of the total particle number concentration ($Dp_{14nm-660nm}$) and the total particle number concentration (3 nm to 2.5 µm (CN_3)) over the period of the campaign are shown in Fig. 3.3 (a)). There was evidence of morning, afternoon and night peaks in both $PNC_{14nm-660nm}$ and CN_3. The morning peak was around 6:00 to 7:00 AEST, while the afternoon and night peaks were observed from around 12 noon to 14:00 AEST and 22:00 to 23:00 AEST, respectively. The greatest contributor to particle number size distribution ranged from 14 nm to 660 nm over the measurement period was ultrafine particle ($<$ 100 nm) (Fig. 3.3 (b)). Bivariate polar plot shows the relationship between wind direction and wind speed (Fig. 3.3 (c)). During the campaign, high particle number concentrations were observed in the south and northeast sectors at high wind speed. Under low wind speed conditions, high particle number concentrations were observed in the south west and southeast. Factors that contributed to this observation are discussed in Section 3.5.

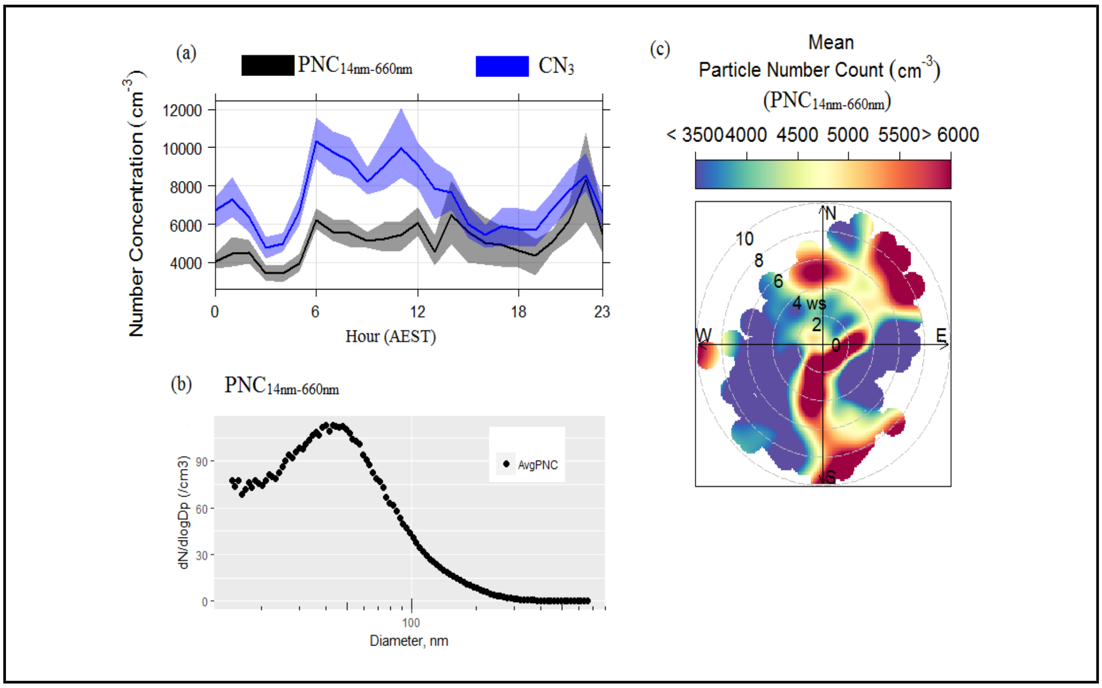

Fig. 3.3: Total particle number concentration (measured from 16th January 2013 to 15th February 2013; (a) average diurnal variation of total particle number concentration ($PNC_{14nm-660nm}$) and total particle number concentration range from 3 nm to 2.5 µm (CN_3) with the 95 % confidence level shaded, (b) average particle number size distributions from 14 nm to 660 nm and (c) dependence of total particle number concentration ($PNC_{14nm-660nm}$) on wind speed and wind direction. Wind speed and wind direction are represented by the concentric circles and coloured shape, respectively. Average particles counts are illustrated by the colour bar. Note that 10-min averaged data were used.

3.3.1 $PM_{2.5}$

The daily mean mass concentration of $PM_{2.5}$ from 24th January 2013 to 15th February 2013 during the aerosol phase of the MUMBA campaign was 6.1 $\mu g\,m^{-3}$. The maximum daily average was 22.1 $\mu g\,m^{-3}$ (Fig. 3.4). The daily mean $PM_{2.5}$ measured at the nearby Office of Environment and Heritage (OEH) for the same time period was 6.2 $\mu g\,m^{-3}$. The OEH station is located approximately 3 km from the MUMBA campaign site (Fig. 2.1(b)). This suggests that the two sites were exposed to similar sources. The daily mean of $PM_{2.5}$ obtained in this study was always below the maximum allowable daily mean as specified by the Australian National Environment Protection (Ambient Air Quality) Measure (Air NEPM) of 25 $\mu g\,m^{-3}$ (not to be exceeded) and by the United States Environmental Protection Agency, US EPA (35 $\mu g\,m^{-3}$, 98^{th} percentile, averaged over 3 years).

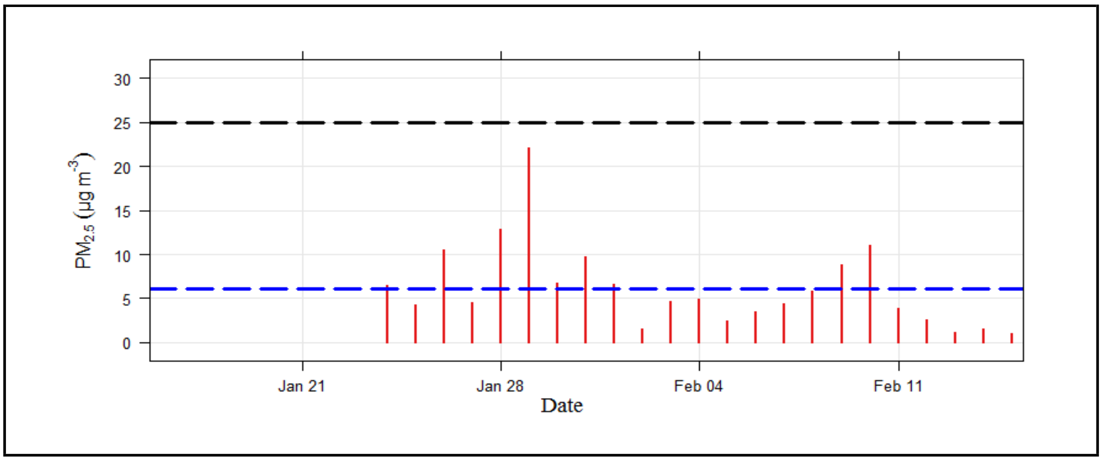

Fig. 3.4: Time series of daily average mass concentration of $PM_{2.5}$ measured from 24th January 2013 to 15th February 2013. The blue dashed line is daily mean mass concentration of $PM_{2.5}$. The black dashed line is the maximum allowable daily mean as specified in the Australian National Environment Protection (Ambient Air Quality) Measure (Air NEPM) which is (25 $\mu g\,m^{-3}$).

3.3.2 Characteristics of Particle Number Concentration

Particle size distribution is an important way of understanding aerosol properties and their sources [*Charron et al.*, 2008; *Harrison et al.*, 2011]. While fine particle (particle with diameter < 2.5 µm) are considered to be of a significant concern for health, there is also an emerging focus on ultrafine particles (particle with a diameter <100 nm) [*Harrison and Yin*, 2000; *WHO et al.*, 2013]. The focus of this study is on $PNC_{14nm-660nm}$, CN_3 and particle number ranged from 3 nm to 100 nm ($PNC_{3nm-100nm}$). Figure 3.5 (a) illustrates the time series of the 10-minute averaged particle number concentration of $PNC_{14nm-660nm}$ and CN_3. Number concentration of $PNC_{14nm-660nm}$ ranged between 3.6 x 10^2 cm^{-3} and 1.8 x 10^5 cm^{-3}, while CN_3

ranged from 4.6 x 10^2 cm^{-3} to 6.5 x 10^4 cm^{-3}.

An extreme event was observed on the 16th of January 2013 (Fig. 3.5 (a)) at approximately 22:00 (Fig. 3.5 (b)). The 10-minute averaged particle number concentration of $PNC_{14nm-660nm}$ at 22:00 was 1.8 x 10^5 cm^{-3}. The monitoring site experienced increase in wind speed between 18:30 and 21:00 (Fig. 3.5 (d)) and wind blowing from the southwest sector (Fig. 3.5 (c)). After 21:00, wind speed started to ease and this could have reduced the dilution of particle number number concentration which then resulted in the extreme event.

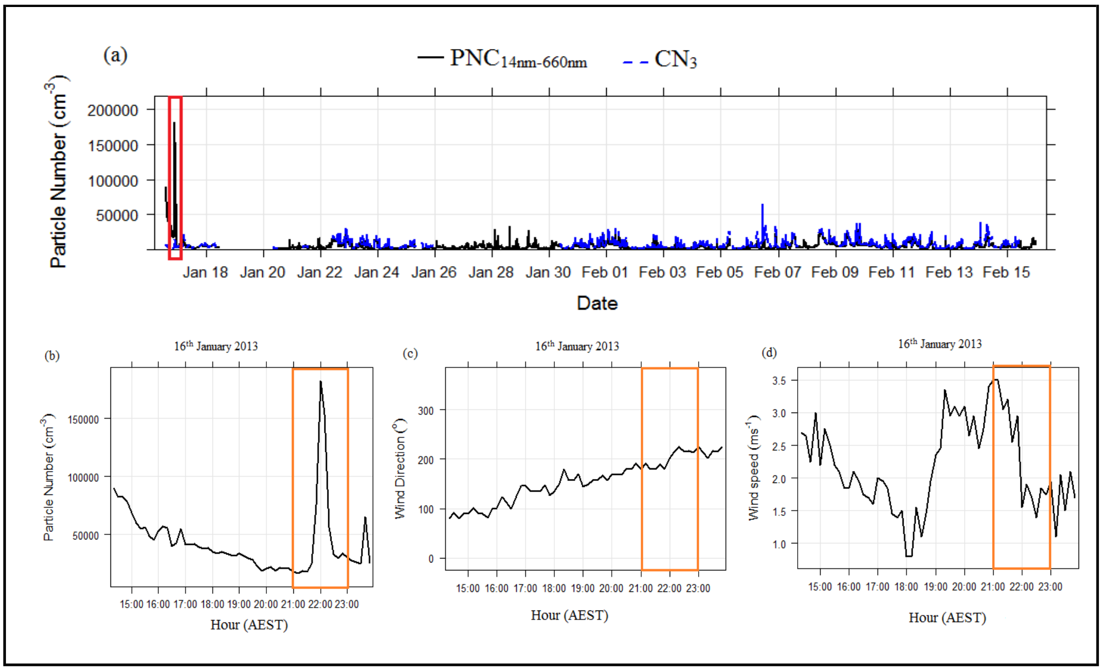

Fig. 3.5: (a) Time series of $PNC_{14nm-660nm}$ and total particle number concentration range from 3 nm to 2.5 µm (CN_3) from 16th January 2013 to 15th February 2013 and (b) time series of $PNC_{14nm-660nm}$ on 16th January 2013. Figure (c) and (d) are wind direction and wind speed on 16th January 2013, respectively. The rectangular orange box delineates the extreme event. Note that 10-min averaged data was used.

The mean of CN_3 over the period of 16th January 2013 to 15th February 2013 was 7.4 x 10^3 cm^{-3} with a median value of 5.5 x 10^3 cm^{-3}. During the aerosol measurement period, aerosol populations were dominated by the ultrafine particles (particle with a diameter <100 nm) as shown in Fig. 3.3(b). On that account, there are a few assumptions made in this work including particle numbers with size diameter ranging from 660 nm to 2.5 µm nm are negligible. Another assumption was CN_3 provides information on ultrafine particles ($PNC_{3nm-100nm}$). Therefore, the ultrafine particles concentrations in this study were calculated using Eq. 3.1 to 3.3. Particles from 3 nm to 14 nm (abbreviated as "$a_{3nm-14nm}$") were obtained by subtracting $PNC_{14nm-660nm}$ from total CN_3. Then "$a_{3nm-14nm}$" was added to the sum of particle number from 14 nm to 100 nm (abbreviated as"$b_{14nm-100nm}$") to obtain PNC between 3 nm and 100 nm (abbreviated as "$c_{3nm-100nm}$").

$$a_{3nm-14nm} = \text{Total CN}_3 - \text{PNC}_{14nm-660nm} \tag{3.1}$$

$$b_{14nm-100nm} = \text{Sum of PNC from PNC}_{14nm} \text{ to PNC}_{100nm} \tag{3.2}$$

$$c_{3nm-100nm} = a_{3nm-14nm} + b_{14nm-100nm} \tag{3.3}$$

The observation of particle concentration over the size range of 14 nm to 660 nm measured by the SMPS in this study was compared with other studies at coastal environments (Table 3.1). The mean and median of the 10-minute averaged particle number concentration between 14 nm and 660 nm measured during the aerosol measurements period were 5.2 x 10^3 cm^{-3} and 3.1 x 10^3 cm^{-3}, respectively. The mean value reported in this study was comparable to studies by *Peng et al.* [2014] on a particle number ranging from 15 nm to 660 nm at a sub-urban coastal site in China and by *Sorribas et al.* [2011] on particle number between 14 nm and 673 nm at a coastal-rural environment in Spain. However, the mean value of particle number ranging from 14 nm to 660 nm in this study was lower than the study by *Pey et al.* [2008] on particle number ranging from 13 nm to 800 nm at a coastal-urban environment in Barcelona, with a mean value of 16.9 x 10^3 cm^{-3}. One can conclude that the particle number concentrations observed during this campaign fell within range of the particle number concentration observed elsewhere in marine and urban environments.

Table 3.1: Comparison between this study and other studies. PNC is particle number concentration. NA is not available.

			PNC x 10^3 (cm^{-3})			
Study	Site	Size (nm)	Mean	Median	Quartile, Q1 (25% percentile)	Quartile, Q3 (75% percentile)
This study	Urban-marine	3-100	7.0	5.2	2.7	9.5
This study	Urban-marine	14-660	5.2	3.1	1.6	6.2
This study	Urban-marine	3-2500	7.4	5.5	3.0	9.9
Cheung et al.(2011)	Urban	4-110	9.3	NA	NA	NA
Peng et al. (2014)	Coastal	15-660	5.7	3.9	NA	NA
Sorribas et al. (2011)	Coastal-rural	14-673	8.7	7.1	NA	NA

The mean and median of ultrafine particles ($PNC_{3nm-100nm}$) over the period of 16th January 2013 to 15th February 2013 were 7.0 x 10^3 cm^{-3} and 5.2 x 10^3 cm^{-3}, respectively which is comparable to the value reported by *Cheung et al.* [2011] for a sub-tropical urban environment in Australia (Table 3.1). The calculated mean total CN_3 and $PNC_{3nm-100nm}$ shows that the particle population observed in this study was dominated by ultrafine particles.

3.3.3 Classification of Particle Number Concentration

Principal component analysis (PCA) (details in Section 2.2.3) was performed on the total PNC$_{14nm-660nm}$ and the distribution of component loadings is illustrated in Fig. 3.6. Component loadings (factor loadings), reflect the correlation between the factors and variables (particle population in the individual size bins). In this study, strong component loadings (value ≥ 0.75, [*Liu et al.*, 2003] as dashed line in Figure 3.6) were chosen for result interpretation. That is, particle numbers were summed across the size ranges "above the dashed line" and identified as Factor 1, Factor 2 and Factor 3 (Fig. 3.6).

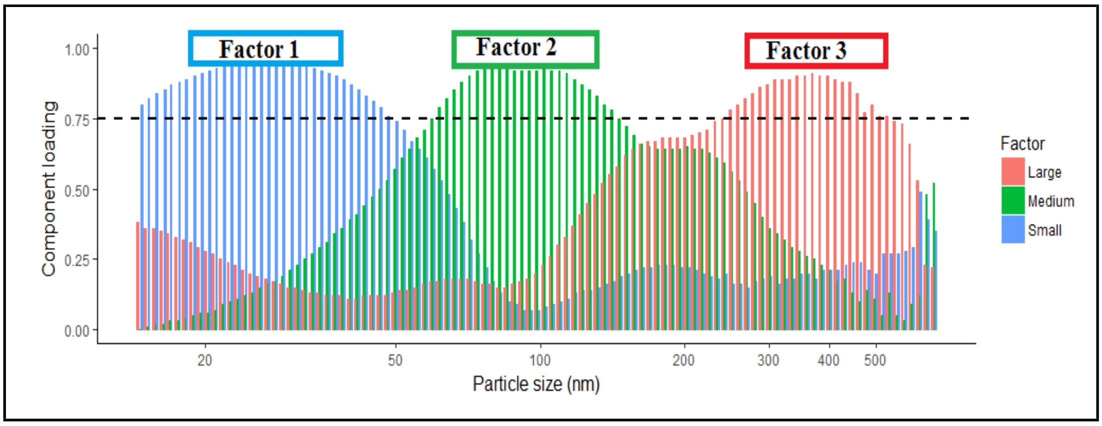

Fig. 3.6: Distribution of component loadings on the entire 10-minute averaged particle number concentration. Only component loadings that were equal to and greater than 0.75 were used to interpret the results. Note: x-axis is in log scale.

Given their distribution, Factor 1 is labelled as the Small Factor (N$_S$) (14 nm $<$ Dp $<$ 50 nm), Factor 2 is labelled as the Medium Factor (N$_M$) (60 nm $<$ Dp $<$ 150 nm) and Factor 3 is labelled as the Large Factor (N$_L$) (210 nm $<$ Dp $<$ 450 nm). Factor 1 and Factor 2 described 31% of the variability, respectively meanwhile, Factor 3 described 27% and all three size fractions described 89% of the cumulative variance. The Small, Medium and Large factors used in this study are approximately equivalent to Nucleation mode, Aitken mode and Accumulation mode, respectively. It is worth mentioning that Nucleation mode sizes (Dp $<$ 10 nm) were actually not within the dataset used in this study (PNC$_{14nm-660nm}$). The temporal variations in these factors are discussed in Section 3.5.

3.4 Identification of Emission Sources

Probable sources were identified by relating the particle number concentrations to carbonaceous aerosols concentrations. The characteristics of carbonaceous aerosols can be generally interpreted by considering organic carbon (OC), elemental carbon

(EC) and the sum of these, Total Carbon (TC = OC + EC). OC contains light reflective species whereas, EC is the least reflective and most light absorbing component [*Pöschl*, 2005]. Organic carbon includes all organic compounds, formed from both primary sources and formed through secondary formation pathways. Elemental carbon is a primary pollutant released into the atmosphere mainly during the incomplete combustion of fossil fuels and biomass [*Tian et al.*, 2013].

Measurements of OC and EC were made during the campaign using a $PM_{2.5}$ high volume sampler (details in *Paton-Walsh et al.* [2017]). The high volume sampling times were morning (4:00 to 9:00) and afternoon (10:00 to 18:00). Overall, the mean masses of $PM_{2.5}$ collected in the morning and afternoon were comparable (although the measurement durations were different). The percentage of total carbon in $PM_{2.5}$ was higher in the morning compared to the afternoon (Table 3.2 (a) and (b)). This observation is due to the higher concentrations of EC measured, presumably due to the morning traffic and low atmospheric mixing. This coincided with the clear morning maximum observed in combustion products, such as CO, NO_x, benzene and toluene as well as the motor vehicle movement diurnal patterns (Fig. 3.7). The low percentage of total carbon in $PM_{2.5}$ in the afternoon was due to the low concentration of combustion products as well as increased modulation from vertical mixing and increases in wind speed.

Table 3.2: (a) Morning and (b) Afternoon mean mass concentrations of organic carbon (OC), elemental carbon (EC), total carbon (TC), $PM_{2.5}$, OC/EC and secondary organic aerosols (SOA).

(a)	(Morning, AM = 4:00 - 9:00)						
Date	OC	EC	TC	$PM_{2.5}$	OC/EC	% of TC in $PM_{2.5}$*	SOA
27-01-13	1.30	0.20	1.50	3.50	6.50	24.10	1.50
28-01-13	0.70	0.10	0.80	22.90	7.00	12.86	1.10
29-01-13	4.70	2.70	7.40	NA	1.74	118.91	1.00
30-01-13	3.00	1.50	4.50	NA	2.00	72.31	1.00
31-01-13	1.30	0.10	1.40	NA	13.00	22.50	1.60
1-02-13	1.90	0.50	2.40	9.30	3.80	38.57	0.90
3-02-13	2.00	0.10	2.10	0.80	20.00	33.75	2.60
4-02-13	2.60	1.60	4.20	3.80	1.63	67.49	1.00
7-02-13	2.30	0.60	2.90	3.10	3.83	46.60	0.90
8-02-13	3.00	0.60	3.60	4.70	5.00	57.85	2.20
9-02-13	4.20	0.80	5.00	6.70	5.25	80.35	3.40
10-02-13	3.20	0.20	3.40	14.20	16.00	54.64	4.30
11-02-13	1.10	0.30	1.40	3.70	3.67	22.50	0.60
12-02-13	3.60	1.60	5.20	3.70	2.25	83.56	1.00
13-02-13	1.00	0.50	1.50	1.40	2.00	24.10	1.00
14-02-13	2.20	2.90	5.10	3.10	0.76	81.95	1.00
Mean	2.38	0.89	3.28	6.22	5.90	52.63	1.57
Median	2.25	0.55	3.15	3.70	3.82	50.62	1.00

Note: *The mean value of $PM_{2.5}$ measured in the morning was used to calculate the percentage of TC in $PM_{2.5}$ ((TC/6.22) x 100). NA = Not available. OC, EC, $PM_{2.5}$ and SOA data presented in the unit of µg m^{-3}.

(b)	(Afternoon, PM = 10:00 - 18:00)						
Date	OC	EC	TC	$PM_{2.5}$	OC/EC	% of TC in $PM_{2.5}$*	SOA
24-01-13	1.70	0.10	1.80	5.30	17.00	31.47	2.30
27-01-13	1.50	0.10	1.60	5.40	15.00	27.97	2.00
30-01-13	2.00	0.20	2.20	NA	10.00	38.46	2.60
31-01-13	2.30	0.20	2.50	8.40	11.50	43.71	2.60
1-02-13	1.50	1.00	2.50	5.20	1.50	43.71	1.00
2-02-13	1.20	0.20	1.40	2.60	6.00	24.48	1.00
3-02-13	2.60	0.20	2.80	8.60	13.00	48.95	3.40
4-02-13	0.80	0.20	1.00	7.30	4.00	17.48	1.20
7-02-13	3.00	0.60	3.60	6.30	5.00	62.94	2.40
8-02-13	4.10	1.00	5.10	7.20	4.10	89.16	2.10
9-02-13	2.90	0.30	3.20	8.30	9.67	55.94	3.10
10-02-13	1.60	0.20	1.80	10.30	8.00	31.47	1.60
11-02-13	2.60	0.80	3.40	5.60	3.25	59.44	0.80
12-02-13	1.80	0.20	2.00	2.50	9.00	34.97	1.90
13-02-13	1.40	0.10	1.50	1.30	14.00	26.22	1.70
14-02-13	1.80	0.40	2.20	1.50	4.50	38.46	1.30
Mean	2.05	0.36	2.41	5.72	8.47	42.18	1.94
Median	1.80	0.20	2.20	5.60	8.50	38.46	1.95

Note: *The mean value of $PM_{2.5}$ measured in the afternoon was used to calculate the percentage of TC in $PM_{2.5}$ ((TC/5.72) x 100). NA = Not available. OC, EC, $PM_{2.5}$ and SOA data presented in the unit of µg m^{-3}.

According to a study by *Turpin and Huntzicker* [1995], the sources of carbonaceous particles can be qualitatively estimated by determining the relationship between the OC and EC concentrations. The correlation between OC and EC should be higher when a major fraction of both OC and EC are emitted by a dominant primary source (e.g., biomass burning, coal combustion or motor vehicular exhaust). *Lin et al.* [2009] used measurements at a coastal and urban area in Taiwan to define a good correlation between OC and EC when R^2 value is ≥ 0.80. They defined a weak correlation for R^2 as ≤ 0.40. In the present study, the R^2 value obtained for OC to EC was 0.3 (n=35) for the aerosol measurement period. This value suggests that OC and EC are not from a dominant primary source. Similar observations were made by *Na et al.* [2004] in a semi-rural area in California. However, *Cao et al.* [2007] observed good correlation between OC and EC at Qingdao and Xiamen (both developing coastal cities in China) with R^2 value of 0.78 and 0.87, respectively.

The mass ratio of OC to EC (OC/EC) provides information about the emission sources of aerosols. The mean (± standard deviation) value of all OC/EC (n=35) calculated for the MUMBA campaign is 6.9 (± 5.2) with a median of 5.0. The mean value obtained during the MUMBA campaign is comparable to the mean value of 6.1 (± 1.3) for a semi-rural area in California [*Na et al.*, 2004] and the mean value of 6.5 (± 3) for a coastal site in the Southern Italy [*Dinoi et al.*, 2017]. There was significant variability in OC/EC values as presented in the standard deviation obtained during the MUMBA campaign. The variation can be due to the multiple sources of OC and EC.

Studies at urban and rural sites in North-Western Europe and north central part of India, concluded that if the OC/EC ratio exceeds 1.0 or 2.0, respectively, there is formation of SOA [*Weijers and Schaap*, 2013], *Pachauri et al.* [2013] and *Pani et al.* [2017]. All OC/EC ratios (excluding the ratio on 14^{th} February 2013 in the morning) obtained at MUMBA ranged from 1.5 to 20.0 (Table 3.2(a) and (b)), indicating the dominance of OC and hence the presence of SOA. The OC obtained at MUMBA is therefore derived from both SOA and various combustion processes including fossil fuel.

The amount of SOA has also been calculated using the method of *Turpin and Huntzicker* [1995] with modification by *Lim et al.* [2003], as shown in Eq. 3.4.

$$\text{SOA} = 1.6[OC - (\frac{OC}{EC_{primary}}) \times EC] \tag{3.4}$$

where, OC/$\text{EC}_{primary}$ is the average of OC/EC in freshly emitted combustion aerosols, which in this analysis is the average of OC/EC in the morning. More details about the OC/$\text{EC}_{primary}$ calculation can be found in *Keywood et al.* [2011]. The calculated SOA are presented in Table 3.2(a) and (b)). The concentration of calculated SOA was higher in the afternoon than in the morning. As reported by *Ding et al.* [2016], isoprene is an important volatile organic compound that plays a key role in the formation of SOA. Isoprene is mainly emitted by biogenic sources (i.e. vegetation) [*Claeys et al.*, 2004; *Guenther et al.*, 2006]. In addition to biogenic sources, isoprene is also emitted by anthropogenic sources (i.e. traffic emissions) [*Borbon et al.*, 2001; *Kansal*, 2009]. The correlation between the isoprene (as measured by the proton transfer reaction-mass spectrometry) and SOA (as derived above) was determined and the results are illustrated in Table 3.3. The isoprene concentration used was the average of observations taken during the aerosol collection period.

Table 3.3: Comparison of the relationship between SOA and isoprene in the morning (4:00 to 9:00) and in the afternoon (10:00 to 18:00). Details of the separation of sources for isoprene are given in Eq. 3.5 and 3.6. AnthroIso = anthropogenic isoprene and BioIsop = biogenic isoprene. Anthropogenic isoprene (AnthroIso), biogenic isoprene (BioIso) data are presented in the unit of mole fraction (ppb). SOA data are presented in the unit of $\mu g\,m^{-3}$. Definitions are given in the text.

Isoprene	SOA	R^2	Variables		Morning	Afternoon
					R^2	
Morning	Morning	0.6	SOA	BioIso	0.6	0.1
Morning	Afternoon	0.02	SOA	AnthroIso	0.02	0.08
Afternoon	Afternoon	0.1				
Afternoon	Morning	0.007				

The R^2 values observed between SOA and isoprene ranged from 0.007 to 0.6 (Table 3.3). The largest R^2 was observed between isoprene and SOA which was measured in the morning, which indicated the significant correlation of isoprene concentrations to morning SOA. The relationship between SOA and other volatile organic compounds measured by the proton transfer reaction-mass spectrometry (i.e. monoterpene and formaldehyde) was examined for both the morning and in the afternoon. Weak to moderate relationships were obtained ($R^2 < 0.5$, details not included in this work). To determine the sources that influenced the SOA formation, biogenic and anthropogenic isoprene concentrations were calculated using equations as shown in Eq. 3.5 and Eq. 3.6:

$$\text{Anthropogenic isoprene} = \text{Benzene} \times 0.05 \tag{3.5}$$

$$\text{Total Isoprene} = \text{Biogenic Isoprene} + \text{Anthropogenic Isoprene} \tag{3.6}$$

The anthropogenic isoprene contribution calculation (Eq. 3.5) was determined by using the method proposed by *Borbon et al.* [2001] and *Duane et al.* [2002] in which assumes that the anthropogenic isoprene concentration is 5% of that of benzene. The study by *Borbon et al.* [2001] was in Lille, France while the study *Duane et al.* [2002] was in Insubria, Northern Italy. The results of this calculation of biogenic and anthropogenic isoprene are presented in Table 3.4(a) and (b). The percentages of the average anthropogenic contribution to isoprene in the morning and in the afternoon were 3.2% and 1.6%, respectively, indicating a dominance of isoprene. *Paton-Walsh et al.* [2017] reported on the biogenic influences on the high levels of isoprene and monoterpenes observed which are important for both O_3 formation and secondary organic aerosol formation in the region. The biogenic sources (e.g. isoprene and monoterpenes) were from the nearby Illawarra escarpment conservation area which is dominated by eucalypts forest. Studies by *Emmerson et al.*

[2016] and *Emmerson et al.* [2018], which focused on estimates of biogenic emission from eucalypts for south eastern Australia, highlight the potential for eucalypt forests to emit isoprene and monoterpenes.

Table 3.4: (a) Morning and (b) Afternoon mean values of benzene, isoprene, anthropogenicisoprene (AnthroIso), biogenic isoprene (BioIso), and secondary organic aerosols (SOA).

(a)	(Morning, AM = 4:00 - 9:00)				
Date	Isoprene	Benzene	AnthroIsop	BioIsop	SOA
27-01-2013	0.23	0.08	0.004	0.22	1.50
28-01-2013	0.12	0.13	0.007	0.12	1.10
29-01-2013	0.34	0.19	0.010	0.33	1.00
30-01-2013	0.16	0.15	0.008	0.15	1.00
31-01-2013	0.32	0.15	0.008	0.32	1.60
1-02-2013	0.23	0.27	0.013	0.21	0.90
3-02-2013	0.10	0.04	0.002	0.10	2.60
4-02-2013	0.22	0.18	0.009	0.21	1.00
7-02-2013	0.27	0.07	0.003	0.27	0.90
8-02-2013	0.47	0.18	0.009	0.46	2.20
9-02-2013	0.64	0.23	0.012	0.62	3.40
10-02-2013	0.63	0.32	0.016	0.62	4.30
11-02-2013	0.07	0.14	0.007	0.07	0.60
12-02-2013	0.14	0.20	0.010	0.13	1.00
13-02-2013	0.17	0.14	0.007	0.17	1.00
14-02-2013	0.37	0.46	0.023	0.35	1.00
Mean	0.28	0.18	0.009	0.27	1.57

Note: Benzene, isoprene, anthropogenic isoprene (AnthroIso), biogenic isoprene (BioIso) data are presented in the unit of mole fraction (ppb). SOA data presented in the unit of $\mu\mathrm{g\,m^{-3}}$.

(b)	(Afternoon, PM = 10:00 - 18:00)				
Date	Isoprene	Benzene	AnthroIsop	BioIsop	SOA
24-01-2013	0.68	0.11	0.006	0.67	2.30
27-01-2013	0.79	0.18	0.009	0.78	2.00
30-01-2013	0.41	0.08	0.004	0.41	2.60
31-01-2013	0.41	0.18	0.009	0.41	2.60
1-02-2013	0.07	0.13	0.006	0.06	1.00
2-02-2013	0.11	0.07	0.003	0.10	1.00
3-02-2013	0.20	0.06	0.003	0.20	3.40
4-02-2013	0.24	0.06	0.003	0.23	1.20
7-02-2013	0.38	0.15	0.008	0.37	2.40
8-02-2013	0.49	0.28	0.014	0.47	2.10
9-02-2013	0.41	0.26	0.013	0.40	3.10
10-02-2013	0.44	0.12	0.006	0.43	1.60
11-02-2013	0.13	0.16	0.008	0.12	0.80
12-02-2013	0.31	0.05	0.003	0.31	1.90
13-02-2013	0.42	0.05	0.002	0.42	1.70
14-02-2013	0.51	0.10	0.005	0.51	1.30
Mean	0.38	0.13	0.006	0.37	1.94

Note: Benzene, isoprene, anthropogenic isoprene (AnthroIso), biogenic isoprene (BioIso) data are presented in the unit of mole fraction (ppb). SOA data presented in the unit of $\mu g\,m^{-3}$.

3.5 Temporal Variation of Particle Number

The diurnal patterns of the particle number concentration for the Small (N_S), Medium (N_M) and Large (N_L) size fractions are presented in Figure 3.7. For reference, several trace gas species have also been included. Three different time frames were created based on the observed particles′ temporal variation (Fig. 3.7) which were also chosen to match the high volume sampler time periods. The three time frames used were: (i) morning (4:00 to 9:00); (ii) afternoon (10:00 to 18:00) and (iii) night (21:00 to 23:00). These time period definitions will be used for further analyses.

Bivariate polar plots are a useful way to show the variation of a variable′s concentration with wind speed and wind direction in polar coordinates. Wind direction together with wind speed can effectively cluster and discriminate different emission sources. Hence, together with the time series, bivariate polar plots have been used to study the sources of the particle number (Fig. 3.8, Fig. 3.10 and Fig. 3.11). In a bivariate polar plot, wind speed is plotted as the distance from origin and wind direction as the angle. The colour is the average value of the variable [*Carslaw and Ropkins*, 2012; *Uria-Tellaetxe and Carslaw*, 2014].

3.5.1 Morning (4:00 to 9:00)

Concentration of all size fractions (N_L, N_M and N_S) increased around 6:00 to 7:00 AEST. N_M and N_S show show a smaller increase in concentration, whereas N_L has a clear maximum in concentration (although the differences in number concentration for the fractions should be noted). The increase in particle concentration probably influenced by the morning local traffic emission (7:00 to 8:00 Australian Eastern Daylight Time (UTC + 11)). A morning peak is also observed in the products of combustion such as CO, NO_x, benzene and toluene as well as in the number of motor vehicles (Fig. 3.7). This agrees with the inference drawn from the EC observations, where higher EC concentrations are observed in the morning compared to those in the afternoon (Table 3.2 (a) and (b)), presumably due to the fossil fuel used. A study by *Mejia et al.* [2007] observed a similar morning peak around 6:00 to 10:00 in the subtropical city of Brisbane, Australia.

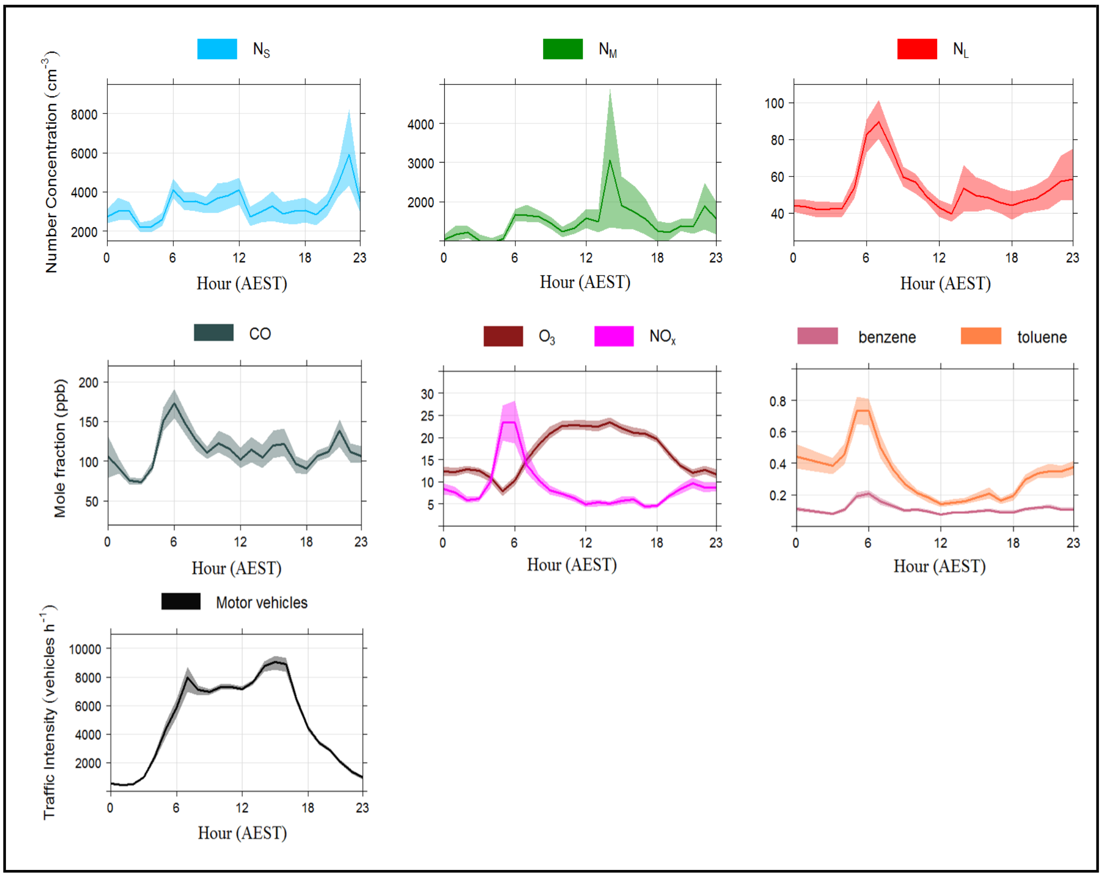

Fig. 3.7: Hourly diurnal variation derived from 10-minute average of particle number concentration data measured from 16th January 2013 to 15th February 2013. Small (N_S), Medium (N_M) and Large (N_L) size fractions are in the unit of cm^{-3}. CO is measured in mole fraction (ppb) of dry air. Benzene, toluene, NO_x, O_3 are measured in mole fraction (ppb) of ambient air. Motor vehicles data are presented in number of vehicles per hour. The shaded area is the 95 % confidence level.

Overall, it is concluded that all three size fractions were influenced by combustion emissions, presumably from traffic. The obvious peak observed in N_L can be attributed to road traffic as well as growth of N_M into bigger size particles. A clear maximum concentration followed by a significant decrease in N_L and combustion products in the morning which were not observed in the N_S and N_M factors, indicated that the N_S and N_M factors were influenced by other undefined sources.

Earlier studies including *Morawska et al.* [2008], reported that particles in the size range 20 nm to 130 nm in suburban Brisbane, Queensland came from vehicle emission. *Ristovski et al.* [2006] found that particles ranging from 20 nm to 60 nm and 20 nm to 130 nm are related to petrol and diesel engine exhaust, respectively. *Harris and Maricq* [2001] concluded that particle mean size diameters in the range of 40 nm to 80 nm correspond to petrol fuelled engines, while 60 nm to 120 nm particles correspond to diesel fuelled engines. Other studies including *Kittelson et al.* [2000]

reported that particles of sizes ranging from 50 nm to 300 nm are related to vehicle emissions. Using these observations, one of the sources of particles < 1 µm is motor vehicles.

The dependence of N_S, N_M and N_L on wind speed and direction in the morning (4:00 to 9:00) is presented in Fig. 3.8. N_L reveals a high particle number concentration in the northwest and southeast. Observations in the northwest coincide with the location of commercial and industrial properties, main highways, roads and the South Coast train line. High particle number concentrations in the northwest are not clear in N_S and N_M and this may be caused by additional sources masking the traffic pattern. Observations in the southeast were due to the location of the active industrial suburb and the Wollongong central business district which are located to the south of the campaign site. The wind direction between 4:00 and 9:00 was from the southwest and southeast (Fig. 3.9).

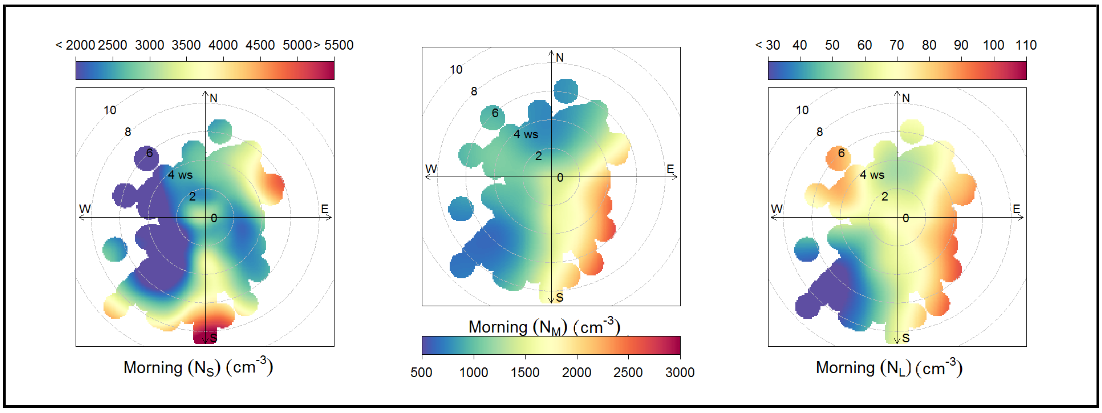

Fig. 3.8: Dependence of mean particle number concentration (cm^{-3}), wind speed and wind direction of Small (N_S), Medium (N_M) and Large (N_L) size fractions in the morning (4:00 to 9:00). Wind speed and wind direction are represented by the concentric circles and coloured shape, respectively. Average particles counts are illustrated by the colour bar. Note that the colour scale varies between plots.

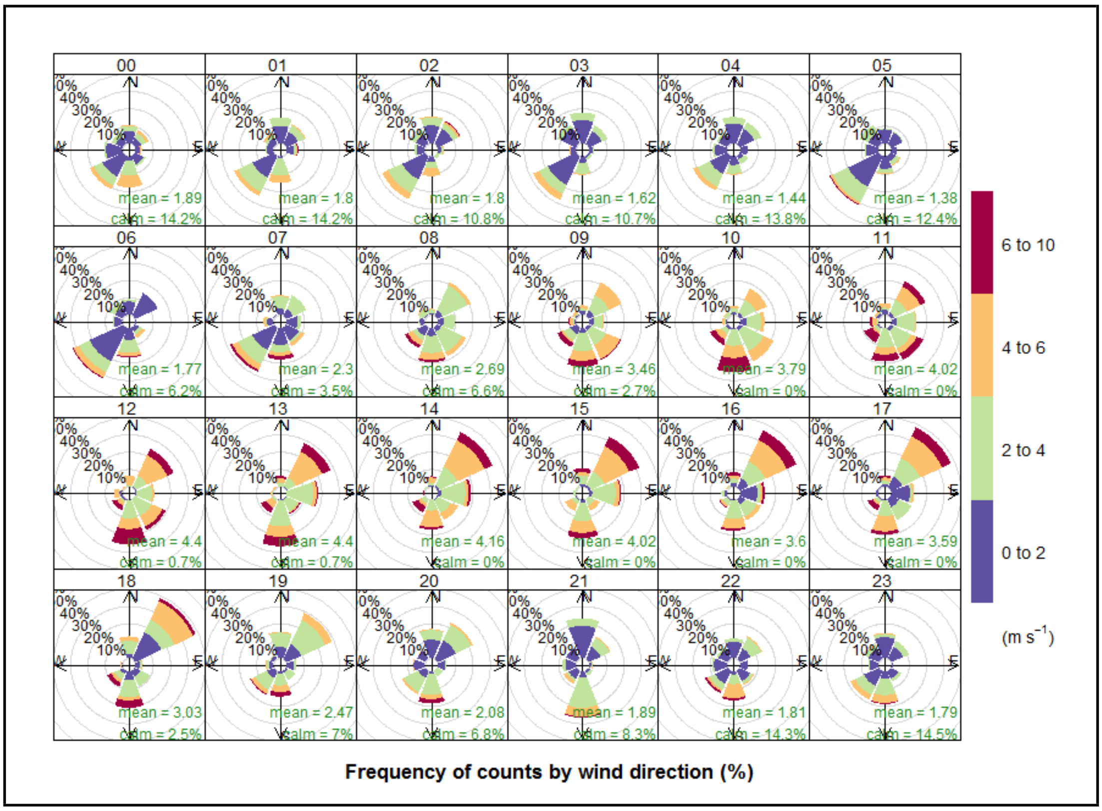

Fig. 3.9: Hourly wind roses during the aerosol measurements which covers the period of 16th January to 15th February 2013. Wind directions are represented by the coloured "wedge" shape. The percentages of occurrence of the winds represented by the concentric circles. The strength of the wind speed is represented by the colour bar.

3.5.2 Afternoon (10:00 to 18:00)

Afternoon peaks (≈ 11:00 - 14:00) coincided with the peak in global irradiance and ground level ozone concentration and so may be associated with photochemistry. This is also consistent with the observed increased concentrations of secondary organic aerosols (SOA) in the afternoon. The median SOA concentration in the afternoon was approximately double the magnitude observed in the morning (Table 3.2 (a) and (b)). The generation of SOA is often photochemically initiated [*Wang et al.*, 2016a].

Meteorological conditions also played a role in the variability of the observed afternoon peaks. Overall, the monitoring site experienced strong wind speed during the afternoon (Fig. 3.1) with north easterly sea breezes capable of carrying particles down from Sydney region (Fig. 3.9). This can contribute to the observed particle number concentration variability. At the same time, the sea breezes can dilute the concentration of particles if there is little urban influence in the incoming air. Decreases in the particle number concentration can also be caused by the greater vertical mixing due to greater solar heating.

The distribution of N_S, N_M and N_L shows relatively high particle number concentrations coming from the northwest during this time (Fig. 3.10). This is consistent with the particle sources being near busy highways, roads and also the commercial and industrial areas located in the northwest of the monitoring station. Another potential source that could contribute to particle concentrations is biogenic emissions released from the Illawarra escarpment. The Illawarra escarpment is dominated by Eucalyptus species. Eucalypts are among the highest emitters of biogenic volatile organic compounds in southeastern Australia [*Emmerson et al.*, 2016; *Winters et al.*, 2009]. Although the measurement site rarely experienced northwest winds during the aerosol campaign period (Fig. 3.9), high particle numbers were measured when these conditions occurred. However, the limited data set hinders analysis. All size fractions show reasonably high particle number concentrations at low wind speed from the southeast as well as from the southwest for small and medium factors. These observations were likely driven by local sources of particles.

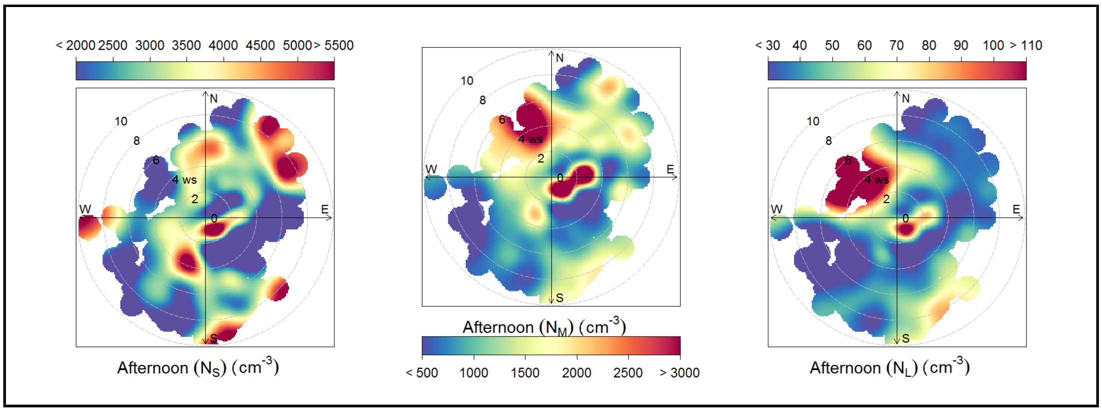

Fig. 3.10: Dependence of mean particle number concentration (cm^{-3}), wind speed and wind direction of Small (N_S), Medium (N_M) and Large (N_L) size fractions in the afternoon (10:00 to 18:00). Wind speed and wind direction are represented by the concentric circles and coloured shape, respectively. Average particles counts are illustrated by the colour bar. Note that the colour scale varies substantially between plots.

3.5.3 Night (21:00 to 23:00)

The night peak (22:00 - 23:00) which is clearly observed in N_S, but is also evident in N_M and N_L (Fig. 3.7), is probably linked to the accumulation of particles from traffic and industrial activities. Increase in the particle number concentration can also be caused by the stable conditions and low vertical mixing. High particle number concentrations were observed in winds from the south for all three size factors as illustrated in the distribution plots (Fig. 3.11). The source is likely to be from Port Kembla, an active industrial area, and the Wollongong central business district.

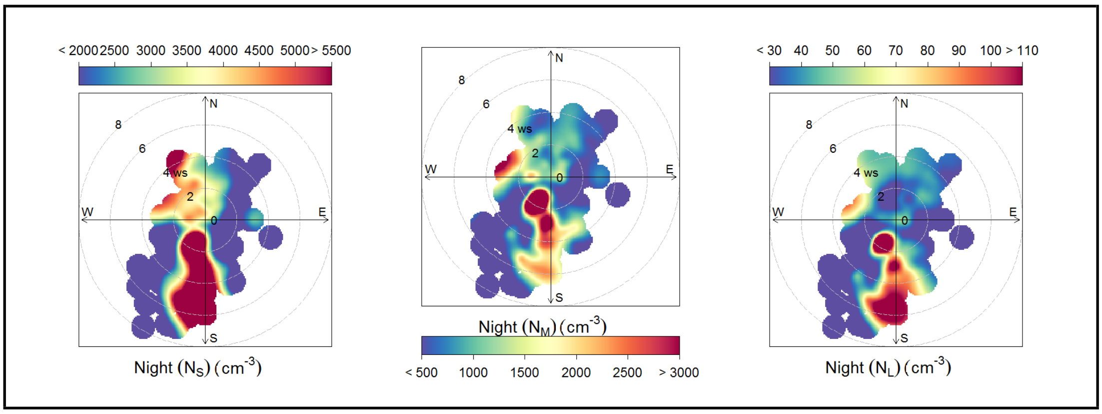

Fig. 3.11: Dependence of mean particle number concentration (cm^{-3}), wind speed and wind direction of Small (N_S), Medium (N_M) and Large (N_L) size fractions in the night (21:00 to 23:00). Wind speed and wind direction are represented by the concentric circles and coloured shape, respectively. Average particles counts are illustrated by the colour bar. Note that the colour scale varies between plots.

3.6 Particle Size Distribution

Particle size distribution in the four wind sectors was also investigated (Section 3.2.1). The average particle size distribution for the four wind sectors is illustrated in Fig. 3.12. The maxima were observed in Sector 1 and Sector 2 at particle size ranging from 43 nm to 48 nm and from 48 nm to 50 nm, respectively. Meanwhile, the maxima were observed in Sector 3 and Sector 4 at particle sizes between 40 nm and 43 nm (Fig. 3.12). T-test has showed that there is no significant correlation in the size distributions for the four wind sectors however, Sectors 1 and 2 contained slightly bigger particle sizes compared to particle populations in Sectors 3 and 4. This is because Sectors 1 and 2 were influenced by marine air masses which contain marine aerosols (i.e. sea salt aerosols). The pollution sources can be other regions including Sydney and the open ocean. Meanwhile, Sectors 3 and 4 were influenced by inland air masses. Pollution sources for these two sectors include industrial activities, traffic emissions and local particle sources.

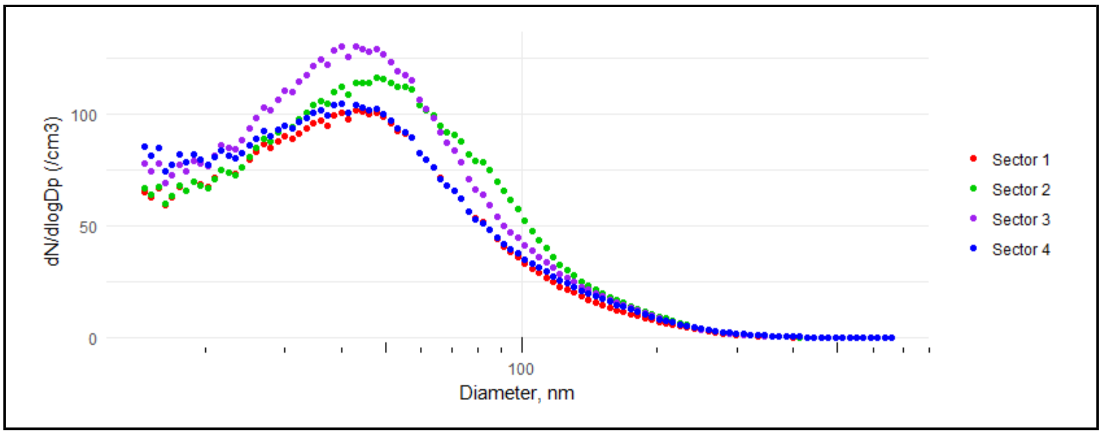

Fig. 3.12: Particle size distribution of average particle number concentration at four wind sectors: Sector 1 (0°< x ≤ 45°), Sector 2 (46°≤ x ≤ 180°), Sector 3 (181°≤ x ≤ 225°) and Sector 4 (226°≤ x ≤ 360°). Note that 10-min averaged data measured from 16th January 2013 to 15th February 2013 were used. The x-axis is in log format.

Size distribution was also classified by time of day. This is illustrated using the average of particle number size distribution at three time frames as stated in Section 3.5: morning (4:00 to 9:00), afternoon (10:00 to 18:00) and night (21:00 to 23:00) for the whole aerosol measurement period (Fig. 3.13).

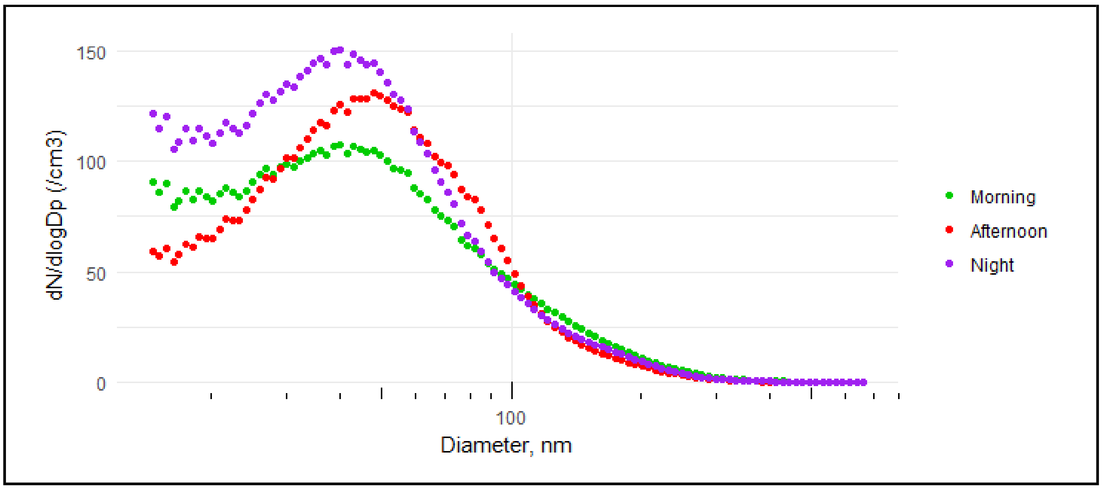

Fig. 3.13: Particle size distribution of average particle number concentration at different times: Morning (4:00 to 9:00), Afternoon (10:00 to 18:00) and Night (21:00 to 23:00) to illustrate the effects of different sources on number size distribution. Note that 10-min averaged data measured from 16th January 2013 to 15th February 2013 was used and the x-axis is in log format.

In general, the afternoon data showed maxima at slightly different size ranges compared to the morning and night data. Using a t-test it was concluded that only the afternoon and morning data had a difference significant at the 95% confidence level. Particles size maxima in the morning and night ranged from 40 nm to 43 nm and 39 nm to 40 nm, respectively (Fig 3.13). Meanwhile, concentration maxima for particles of a diameter between 48 nm and 50 nm were observed in the afternoon. Slightly bigger particles observed in the afternoon can be caused by air masses experienced by the monitoring site in the afternoon (Fig. 3.9) which were generally from the ocean which carried marine aerosols including sea salt aerosols.

Particle size distribution on the 22nd of January 2013 at specific times ("key hours") was also studied. The 22nd of January 2013 was used because larger particles (Dp > 150 nm) were also observed on this day. The "key hours" were chosen based on the diurnal variation of the three size fractions as illustrated in Fig. 3.7. Morning is represented by data observed at 5:00 and 6:00. Midday/afternoon and night are represented by data observed at 12:00 and 13:00 and 22:00 and 23:00, respectively.

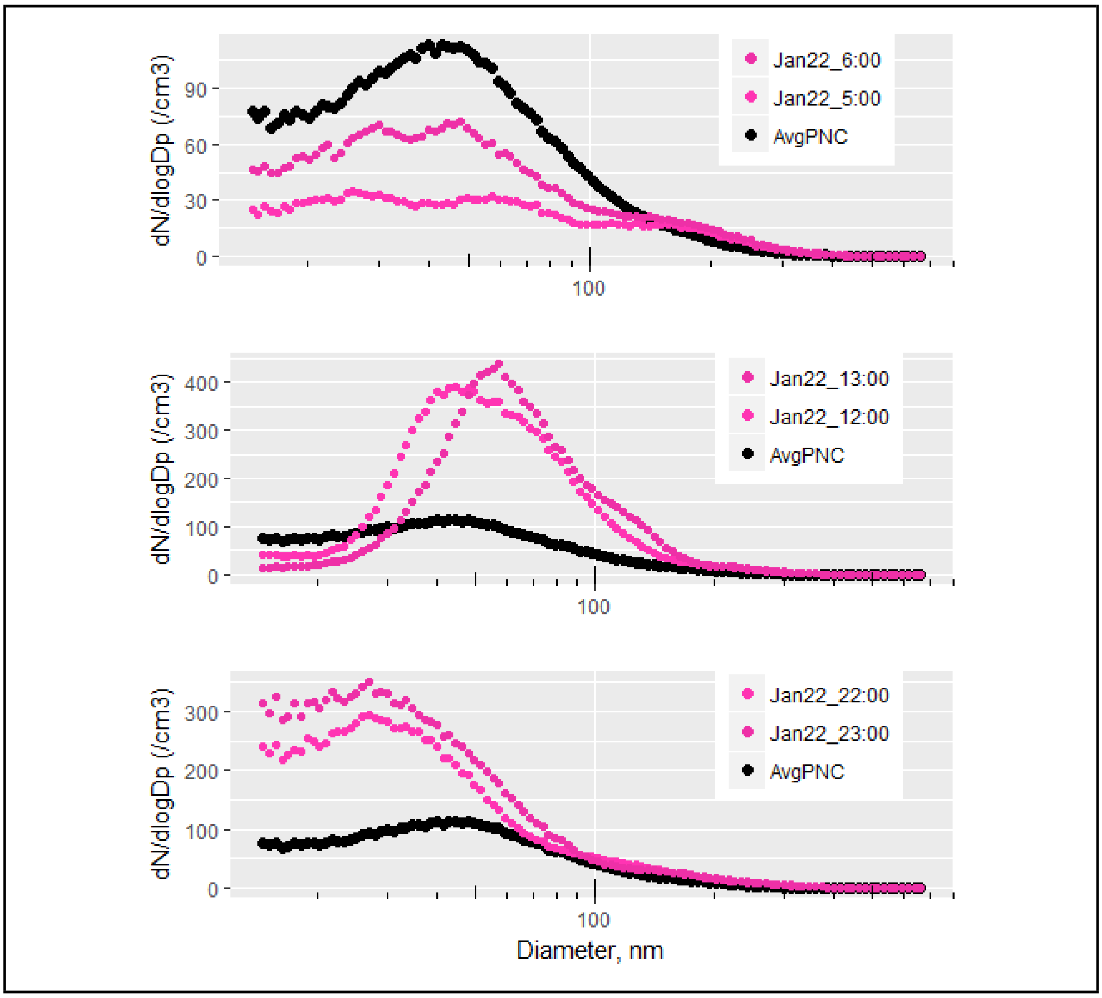

Fig. 3.14: Effects of different sources on the particle size distribution. Average particle number, AvgPNC presented in black dots. Particle number size distribution on 22nd January 2013 at the "key hours" presented in purple dots. Note that 10-min averaged data are used and the x-axis is in log format.

The particle concentration was maxima for particles ranging from 25 nm to 50 nm on the 22nd January 2013 at 5:00 and 6:00 as demonstrated by particle number distribution shown in Fig. 3.14. Observed peaks were probably driven by morning traffic. Large particles in the size distribution were also measured on this day, however at much lower concentrations than for the smaller particles. Midday/afternoon (12:00 and 13:00) peaks were approximately from 45 nm to 60 nm (Fig. 3.14). Observed peaks were probably influenced by SOA as well as sea breezes. Peaks from 25 nm to 27 nm were observed at night (22:00 and 23:00) (Fig. 3.14). This was fit with the diurnal pattern of 10-min averaged data measured between 16th January 2013 and 15th February 2013, where there was a clear peak observed in N_S (Fig. 3.7). Overall, different sources have been observed to influence the particle number size distribution. The monitoring site experienced slightly bigger particle size populations from oceanic air masses compared with inland air masses. In daily variation terms (morning, midday/afternoon and night), slightly bigger particle size populations were observed in the midday/afternoon compared to morning and night time frames.

Aerosols derived from ocean air particles (sea spray) are produced at the ocean surface from the interaction between wind and waves. Ocean-derived aerosols are also produced through secondary processes involving the interaction between ocean and atmosphere or through the interaction between the ocean and anthropogenic combustion emission over the ocean [*de Leeuw et al.*, 2014; *Grythe et al.*, 2014]. On average, the monitoring station experienced increases in wind speed with north easterly winds able to carry sea salt aerosols related to the transport of pollutants down the coast from in and around Sydney in the midday/afternoon time frames (Fig. 3.9). This is one of the factors that can explain the observation of a slightly larger particle size population in the midday/afternoon and when the monitoring site experienced oceanic air mass.

3.7 Summary and Conclusions

This chapter presents an analysis of the characteristics of aerosol populations as measured during the MUMBA campaign. It also discusses the potential sources of these aerosol populations at the time of the research. The findings are as follows:

(i) Particle number concentrations ranging from 14 nm to 660 nm showed an unimodal distribution, dominated by ultrafine particles (particle diameter from 3 nm to 100 nm). The mean value of particle diameter ranging from 3 nm to 100 nm was 7.0 x 10^3 cm^{-3} ;

(ii) The monitoring site experienced low daily mass concentration of fine particles ($PM_{2.5}$). The mean daily mass of $PM_{2.5}$ obtained during the aerosol measurements period was 6.1 $\mu g\,m^{-3}$ with a daily mass that was always below the maximum allowable daily mean as specified in the Australian National Environment Protection (Ambient Air Quality) Measure (Air NEPM) which is (25 $\mu g\,m^{-3}$, not to be exceeded);

(iii) Three size fractions were obtained from particle number size distributions ranging from 14 nm to 660 nm in diameter using Principal Component Analysis. Those three size fractions described 89% of the cumulative variance. The three size fractions were Small Factor (14 nm $<$ Dp $<$ 50 nm), Medium Factor (60 nm $<$ Dp $<$ 150 nm) and Large Factor (210 nm $<$ Dp $<$ 450 nm);

(iv) Potential sources of particle populations measured during the aerosol phase of MUMBA campaign were marine and forest environments which interacted with urban air. The particles observed in the morning were found to be influenced by traffic emissions. A mixture of marine sources, local sources and secondary aerosols production initiated by photochemical oxidation were the main sources of particles in the afternoon. Industrial emissions such as from local steel works and the urban environment were the major contributors of particles at night; and

(v) Concentrations of carbonaceous aerosols were contributed by multiple sources including combustion processes (for example fossil fuel) and secondary formation processes (secondary organic aerosols).

Chapter 4

Observation of Particle Formation Mechanisms

4.1 Introduction

New particle formation and growth involves the formation of stable molecular clusters (new particles) and the growth of this cluster to detectable sizes [*Kerminen et al.*, 2018]. New particle formation takes place almost anywhere and any time in the atmosphere, and varies depending upon the surrounding environment [*Kulmala et al.*, 2004, 2014]. To investigate the new particle formation mechanisms, aerosol data obtained from the MUMBA campaign were analysed (refer to Chapter 2). Aerosol data included the particle number concentration ranging from 14 nm to 660 nm ($\mathrm{PNC}_{14nm-660nm}$) and the total concentrations of particles ranging from 3 nm to 2.5 µm (CN_3). Auxiliary data included concentration (dry air) mixing ratio of CO, concentrations (ambient air) mixing ratio for NO_x,O_3, SO_2 and volatile organic compounds (such as isoprene, benzene, toluene, xylenes) and meteorological dataset included temperature, global irradiance, wind speed, wind direction and relative humidity.

Until this study, there were little research on new particle formation conducted in a mixed environment setting where the air quality depends on the interplay between different sources. This chapter presents the occurrence frequency, characteristics and the factors that enhance new particle formation processes. A multivariate statistical technique known as hierarchical agglomerative cluster analysis (HACA) was applied to cluster the factors that correlated to the new particle formation events.

4.2 Particle Formation Event Characteristics

Particle formation events are identified as a burst of particles growing from small (< 10 nm) into larger size particles by the processes of condensation and/or coagulation [*Kulmala et al.*, 2004]. The particle formation events observed in this work focus on Class I events. The criteria for Class 1 events used in this study as proposed by *Dal Maso et al.* [2005] are (i) a new mode of particles (30 nm) must be observed, (ii) the event must occur over a time span of hours and (iii) the new mode must show signs of growth. The Class I type events as indicated in Chapter 1 were investigated. Contour plots of particle number size distribution during the aerosol measurements period during the MUMBA campaign are illustrated in Fig. 4.1 and 4.2.

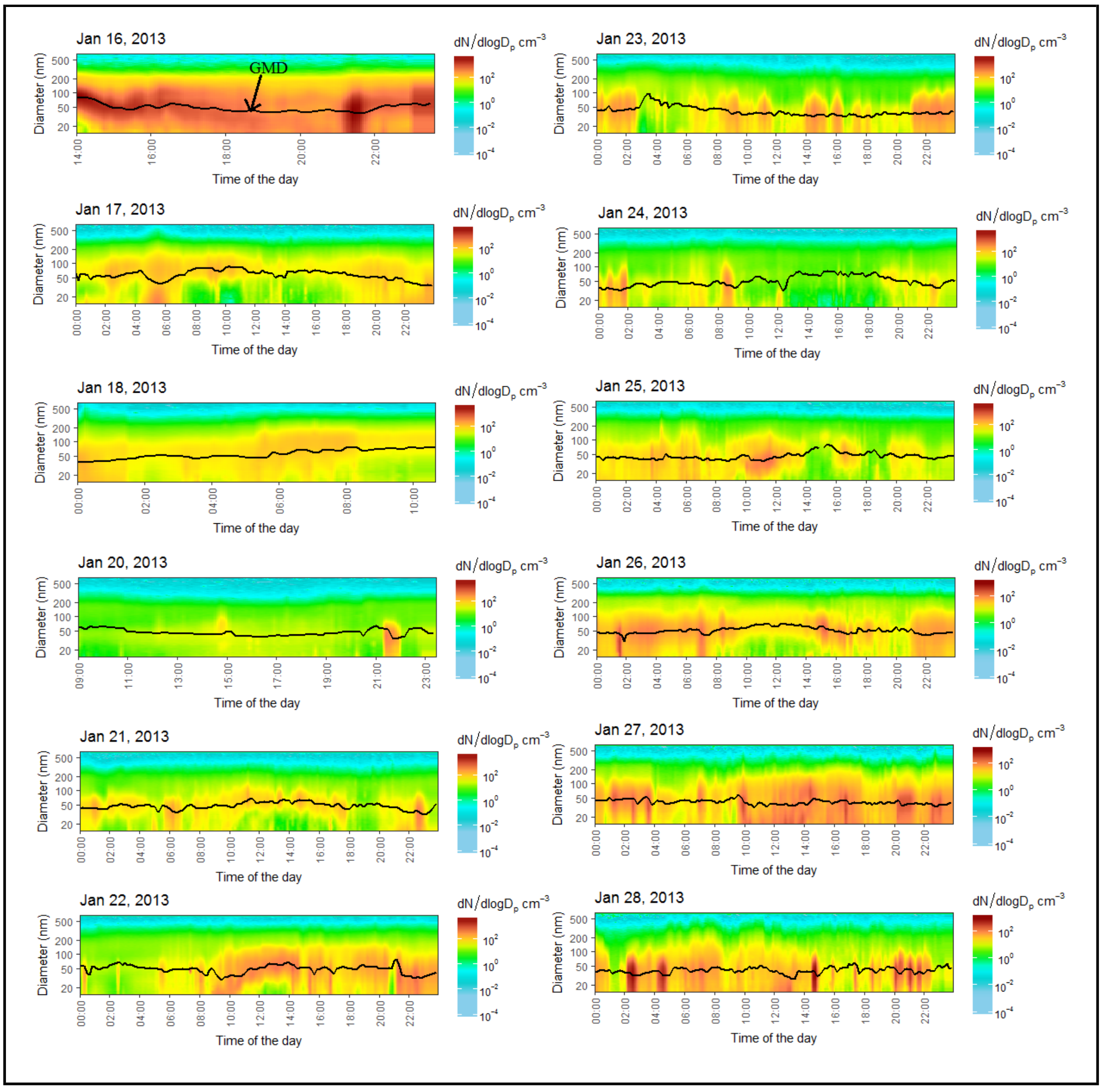

Fig. 4.1: Contour plots of particle number size distribution during the aerosol measurements period. Note that the y-axis is in log format. GMD is geometric mean diameter. Ten-minute averaged data were used.

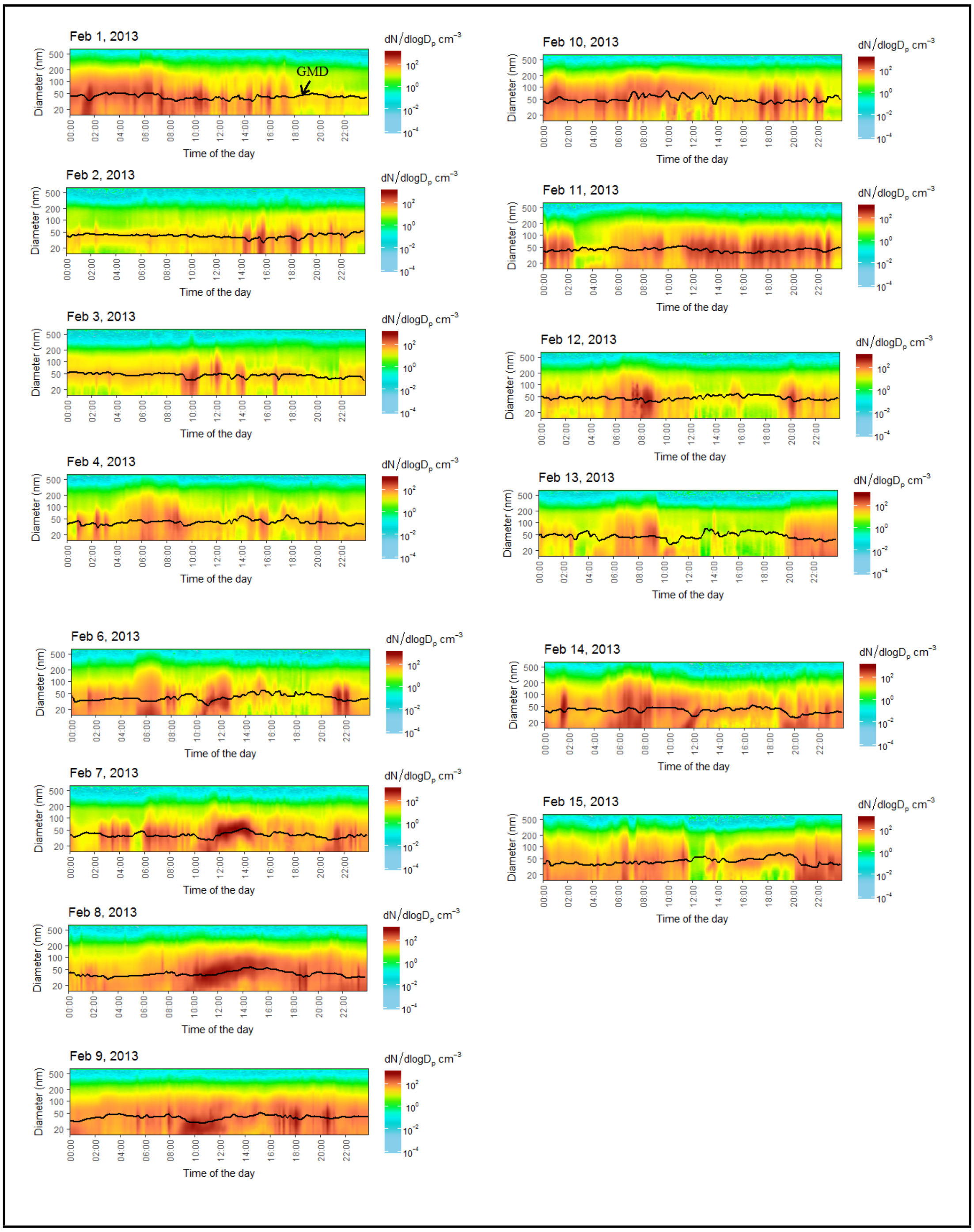

Fig. 4.2: Continued from Fig. 4.1. Contour plots of particle number size distribution during the aerosol measurements period. Note that the y-axis is in log format. GMD is geometric mean diameter. Ten-minute averaged data were used.

A significant increase in the small particle number concentration over time is a useful marker for new particle formation events. With the limitation of the available SMPS instrument, it was not possible to measure particles with a diameter less than 14 nm in this campaign. To overcome this problem, the method reported by *Mejía and Morawska* [2009] was used, by assuming that the new particles were formed earlier and grew until reaching a measurable size. In this present study,

CN_3 and $PNC_{14nm-660nm}$ were used to test this assumption. The total particle number concentration above 660 nm was taken as negligible because the particle populations measured at aerosol phase of the MUMBA campaign were dominated by ultrafine particles (particle diameter from 3 nm to 100 nm) as discussed in Chapter 3. The difference between these two measurements provided information on small particles (3 nm $< Dp <$ 14 nm) which were involved in the newly formed particles through gas-to-particle conversion. This method was used in a study by *Humphries et al.* [2015] for similar purposes. The concentration of small particles (3 nm $<$ $Dp <$ 14 nm) can be illustrated by the ratio of CN_3 and total particle number measured by SMPS ($PNC_{14nm-660nm}$). An increase in the ratio value relative to the CN_3 indicates a higher number concentration of small particles relative to the total particles population and a marker of particle growth.

Growth rate is one of the most relevant variables in identifying particle formation events and it is defined as the change in particle diameter due to particle population growth [*Sorribas et al.*, 2015]. This growth rate was computed using Eq. 4.1 as used in studies of *Kulmala et al.* [2004]; *Modini et al.* [2009]; *Pushpawela et al.* [2018]. The geometric mean diameter (GMD) is used to define a "characteristic size". Changes in GMD are used to calculate growth rate. The GMD values were retrieved using the Aerosol Instrument Management software, version 10.2.0.11 by TSI.

$$\text{Growth rate} = \frac{(D_{pg_{end}} - D_{pg_{start}})}{(t_{end} - t_{start})} \tag{4.1}$$

Where D_{pgend} and $D_{pgstart}$ represent the geometric mean diameter at time t_{end} and t_{start}, respectively when a clear particle formation pattern is observed.

4.3 Results and Discussion

The characteristics of Class I event were compared with several other events to identify the factors that contribute to the occurrence of new particle formation and growth. Several other events used for comparison are discussed in Section 4.3.4.

4.3.1 General Characteristics and Occurrence of Particle Formation Events

Four Class I particle formation events were identified visually during the 31 sampling days of this campaign. The occurrence frequency of particle formation events was therefore 13% of the total number of days. There was one event observed in January 2013 (22nd January) and three more observed in February 2013 (6th, 7th and 8th February) (Table 4.1). All Class I events occurred during the day, approximately between 8:30 and 14:30 with an average time duration of 5 hours (Fig. 4.3). During the Class I event days, total particle number concentration increased from about 3000 cm^{-3} to 15 000 cm^{-3}, on average.

A study on new particle formation during the Sydney Particle Study campaign at Sydney *Cope et al.* [2014], identified 50% of the days displaying new particle formation events (Class I and Class II) under summer conditions. For a more meaningful comparison, the Class II new particle formation events (refer to definition in Chapter 1) were included in this analysis. There were four Class II new particle formation events identified during MUMBA (17th, 27th, 29th January and 9th February, 2013) (Fig. 4.1 and Fig. 4.2), which gave a total of eight new particle formation events identified in this study. These eight days therefore show an occurrence of 25% over the total number of days. The 24-hr backward trajectories calculated for the entire aerosol measurement period revealed that 50% of the sampled air masses arriving at 10:00 AEST were from north and northeast sectors. The 10:00 AEST was chosen because the particle formation and growth event days (Class I and Class II) were observed at this time. This observation indicates that air mass from the north and northeast sectors correlate with the Class I and Class II event days identified during the MUMBA campaign.

Table 4.1: Summary of particle formation events during the MUMBA aerosol measurement period. GMD is geometric mean diameter and GR is growth rate

Date	Time (Start)	Time (End)	Duration (hours)	Primary (GMD) (nm)	Final GMD (nm)	GR (nm/hr)
22-Jan-2013	8:30	14:00	6.3	30.0	70.0	6.3
6-Feb-2013	10:00	13:00	3.0	25.0	50.0	8.3
7-Feb-2013	10:00	14:00	4.0	24.0	55.0	7.8
8-Feb-2013	8:30	14:30	6.0	30.0	60.0	5.0
Average			4.8	27.2	58.8	6.9 (± 1.5)

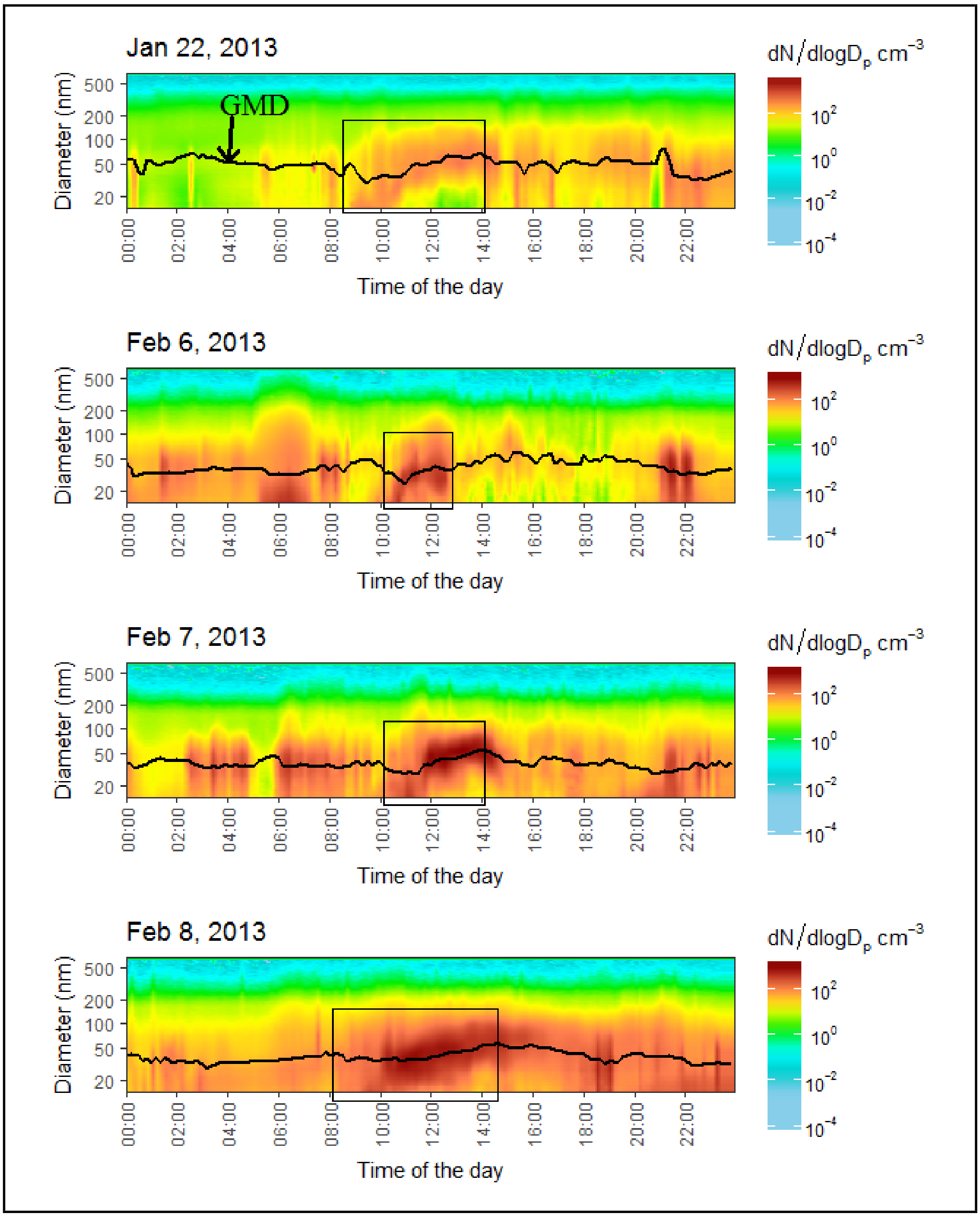

Fig. 4.3: Contour plots of particle number size distribution on Class I event days (Jan 22nd, Feb 6th, Feb 7th and Feb 8th, 2013). The rectangular box represents the relevant time of particle formation events. Note that the y-axis is in log scale. GMD is geometric mean diameter. Ten-minute averaged data were used.

[*Zhang et al.*, 2004] described the classification of particle formation and growth events using the rate of change of total particle number concentration (dN/dt), where N is the number of particles in the nucleation mode (i.e. particles of diameter of less than 10 nm). In this study, particles in the size range of PNC$_{3nm-14nm}$ were used (Table 4.2) as the nucleation mode. A "strong" particle formation event is an event with $N > 10\ 000$ cm^{-3} for at least one hour and $dN/dt > 10\ 000$ cm^{-3} hr^{-1}. A "weak" particle formation event is typically classified as an event with $5000 < N < 10\ 000$ cm^{-3} for at least one hour and $5000 < dN/dt < 10\ 000$ cm^{-3} hr^{-1}. There were missing CN$_3$ data on the 22th of January and on the 8th of February, 2013 which made the classification of the event difficult. On the 6th of February, 2013, there were times that particle number for PNC$_{3nm-14nm}$ were more than 10 000 cm^{-3}, however it lasted for less than an hour. The events on February 6th and 7th, 2013 were classified as "weak" particle formation events.

Table 4.2: Summary of particle number concentration ranging from 3 nm to 14 nm (PNC$_{3nm-14nm}$) on the Class I event days during the MUMBA aerosol measurement phase.

Date (Time of the Class I event observed)	PNC$_{3nm-14nm}$, (cm^{-3}) (Minimum to maximum)
22-Jan-2013 (8:30 - 14:00)	1323 to 5174
6-Feb-2013 (10:00 - 13:00)	1587 to 56 915
7-Feb-2013 (10:00 - 14:00)	1937 to 6436
8-Feb-2013 (8:30 - 14:30)	2229 to 6062

Next, the growth rates of these new particles and the possibility that the new particles were activated as cloud condensation nuclei were studied. *Kulmala et al.* [2004] reported that particle diameter growth rates differed according to environmental conditions and varied from 1 nm hr^{-1} to 20 nm hr^{-1}. In this study, particle growth rates were between 5.0 nm hr^{-1} and 8.3 nm hr^{-1} with an average value of 6.9 nm hr^{-1}. These observed growth rates were within the range reported for other urban environments of between 0.5 nm hr^{-1} to 9.0 nm hr^{-1} *Kulmala et al.* [2004] and similar to those for a remote, sub-tropical coastal environment in Australia of 1.8 nm hr^{-1} to 8.2 nm hr^{-1} with a average value of 6.4 nm hr^{-1} [*Modini et al.*, 2009]. Overall, the growth rates in this study are comparable with the growth rates obtained in other studies within urban and coastal environments.

The possibility that in this study the new particles formed on particle formation and growth event days were activated as CCN was investigated using CCN data, particle number size distributions and particles' GMD. The CCN data were measured by Droplet measurement Technologies (Longmont, CO, USA) and were activated at a supersaturation of 0.55% (details in *Paton-Walsh et al.* [2017]). The particle size range of 14 nm to 150 nm was used because particle formation and growth events were observed in this particle size range (Fig. 4.3). Figure 4.4 illustrates the comparison of CCN, GMD and particle number size distributions from 14 nm to 150 nm on Class I event days. Particles that are less than 50 nm are inefficient as cloud condensation nuclei [*Dusek et al.*, 2006; *Petters and Kreidenweis*, 2007]. Studies by *Dusek et al.* [2006] and *Seinfeld and Pandis* [2012] report that particles of a diameter of 50 nm - 100 nm have a high potential to be activated and act as CCN. A study by *Lihavainen et al.* [2003] in Finland noted that the formation of CCN was related to particle growth and ceased when particle growth stopped. Overall, particles formed on Class I event days identified during the aerosol measurements of the MUMBA campaign could increase and/or decrease the number of CCN (Fig. 4.4). In terms of particle diameter, there is no clear pattern that particles with GMD equal to and larger than 50 nm observed on Class I event days were activated as cloud condensation nuclei (Fig. 4.4). One can conclude that particles of diameter ranging from 50 nm to 100 nm observed during the Class I event days inefficiently contribute to the concentration of CCN during the MUMBA campaign.

Fig. 4.4: Time series of cloud condensation nuclei (CCN), geometric mean diameter (GMD) and particle number size distributions from 14 nm to 150 nm ($PNC_{14nm-150nm}$) on Class I event days (Jan 22nd, Feb 6th, Feb 7th and Feb 8th, 2013). The rectangular box represents time of the particle formation and growth events. Ten-minute averaged data were used.

4.3.2 Particle growth from smaller size particles

Measurements of CN_3 were used to study whether there was evidence that smaller particles emerged earlier and grew until reaching a detectable size by SMPS. CN_3 was compared with $PNC_{14nm-660nm}$. Presuming that particle numbers > 600 nm are small, the ratio of CN_3 to $PNC_{14nm-660nm}$ (CN_3 / $PNC_{14nm-660nm}$) is useful in quantifying the proportion of the smaller particles in the sample. A high value of CN_3 / $PNC_{14nm-660nm}$ indicates a large proportion of small particles (3 nm $< Dp <$ 14 nm) in the particle population. The time series observations of $PNC_{14nm-660nm}$ and CN_3 / $PNC_{14nm-660nm}$ on Class I event days are illustrated in Fig. 4.5. As there were missing CN_3 data on the 22^{th} of January 2013 and on the 8^{th} of February 2013 (Fig. 4.5(a) and (d), respectively), the growth of smaller sizes could not be studied on these days.

On the 6^{th} of February 2013 (Fig. 4.5 (b)), no peak was observed in the CN_3 / $PNC_{14nm-660nm}$ ratio before 7:00. There was also no particle growth observed in the contour plot (Fig. 4.3). This suggests that particle formation and growth processes did not occur for sizes > 3 nm at this time. However, from 8:00, the CN_3 / $PNC_{14nm-660nm}$ ratio did increase, then followed by a decrease in the CN_3 / $PNC_{14nm-660nm}$ ratio at 10:00 due to a relative decrease in smaller particle concentration. Subsequently, a particle growth process was observed in the contour plot after 10:00 (Fig. 4.3).

On the 7^{th} of February 2013 (Fig. 4.5 (c)), there were peaks observed in the CN_3 / $PNC_{14nm-660nm}$ ratio before 7:00. However, there was no particle growth observed in the contour plot (Fig. 4.3). This suggests that there was a high concentration of smaller particle (> 3 nm) but growth processes did not occur for sizes > 3 nm at this time. After 7:00, the CN_3 / $PNC_{14nm-660nm}$ ratio increased again and slowly decreased at around 10:00 due to a relative decrease in smaller particle concentration. Subsequently, a particle growth process was observed in the contour plot after 10:00 (Fig. 4.3).

These observations illustrate that particle growth can be observed in the size range 3 nm to 14 nm prior to being a detectable by SMPS.

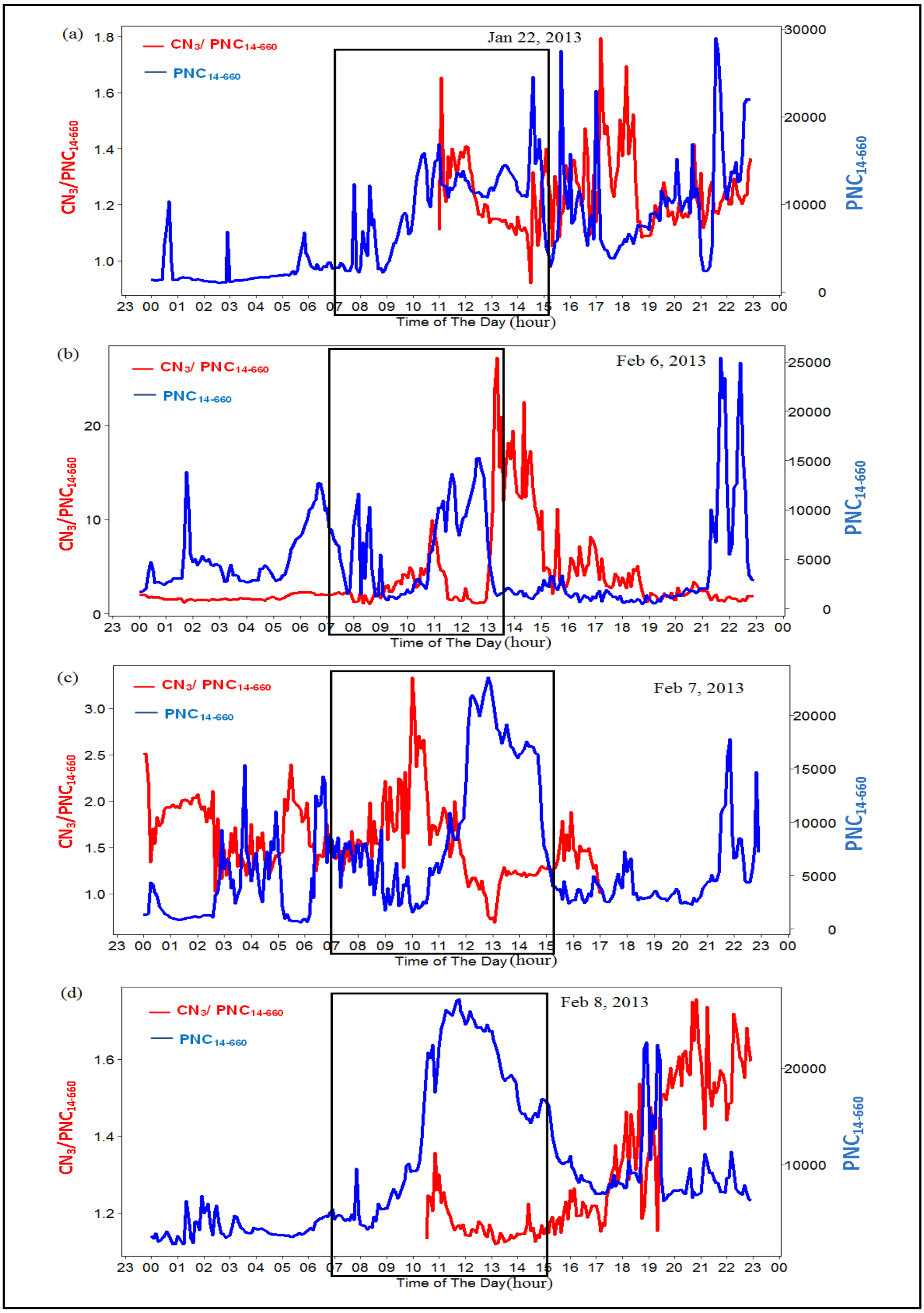

Fig. 4.5: Time series of the total particle number between 14 nm and 660 nm ($PNC_{14nm-660nm}$) and the ratio of total particle concentrations with diameters larger than 3 nm (CN_3) to $PNC_{14nm-660nm}$ (CN_3 / $PNC_{14nm-660nm}$) on the Class I event days. The black rectangular box represents the relevant time of particle populations before, during and after the event. Five-minute averaged data were used in these plots.

4.3.3 Conditions that Favoured Particle Formation on Class I Event days

Local meteorological variables including temperature, relative humidity, wind speed, wind direction and global irradiation were analysed to study their relationship to the particle formation events. Global irradiance was measured at the University of Wollongong, ≈ 2 km southwest of the campaign site (Fig. 2.1 (b)). All the meteorological variables used, excluding global irradiation are in 10-min averaged datasets. Global irradiance was averaged hourly.

Wind direction is one of the important variables that is closely related to air mass sources which influence particle distribution. The 24 hr-backward trajectories produced by HYSPLIT arriving at 10:00 AEST at 100 m above the site indicated that air masses during the Class I events arrived at the sampling point after travelling over the South Pacific Ocean and populated urban areas including Sydney (Fig. 4.6). Air masses from the ocean and urban areas could be one of the factors that contribute with the observed Class I event days. Wind roses were plotted using wind data from the MUMBA campaign obtained on the Class I event days which revealed that the monitoring site experienced air masses from north and northeast directions (Fig. 4.7) which is consistent with the back trajectories.

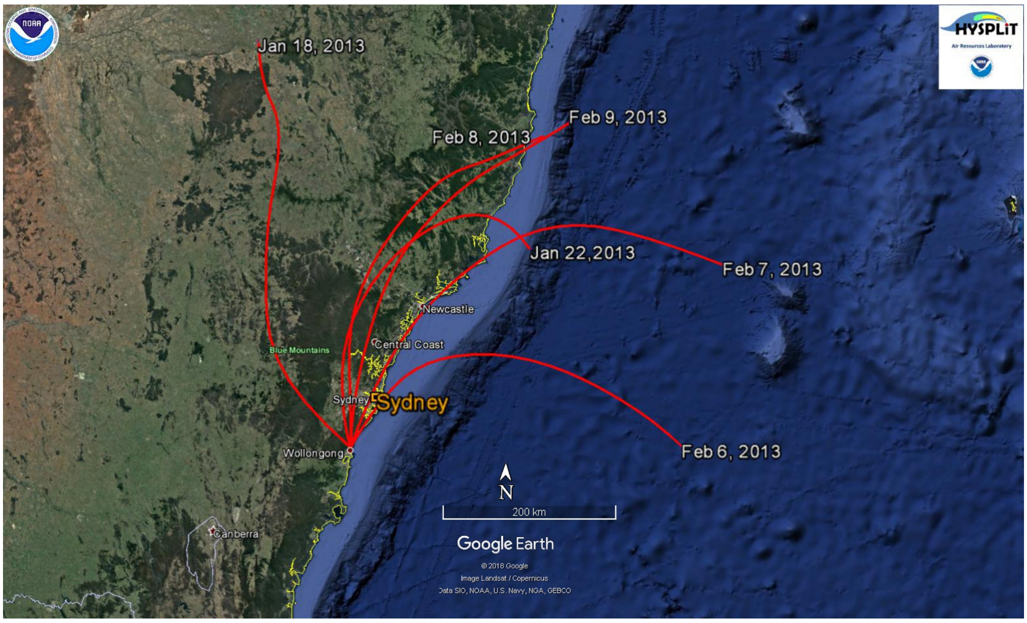

Fig. 4.6: The 24 hr-backward trajectories produced by HYSPLIT at 100 m above the site for Class I event days (Jan 22nd, Feb 6th - 8th, 2013), a Class II event (Feb 9th, 2013) and a hot day (Jan 18th, 2013). The monitoring site received the air masses at 10:00 AEST (+10 UTC). The choice of the Class II event and the hot day are discussed in Section 4.3.4.

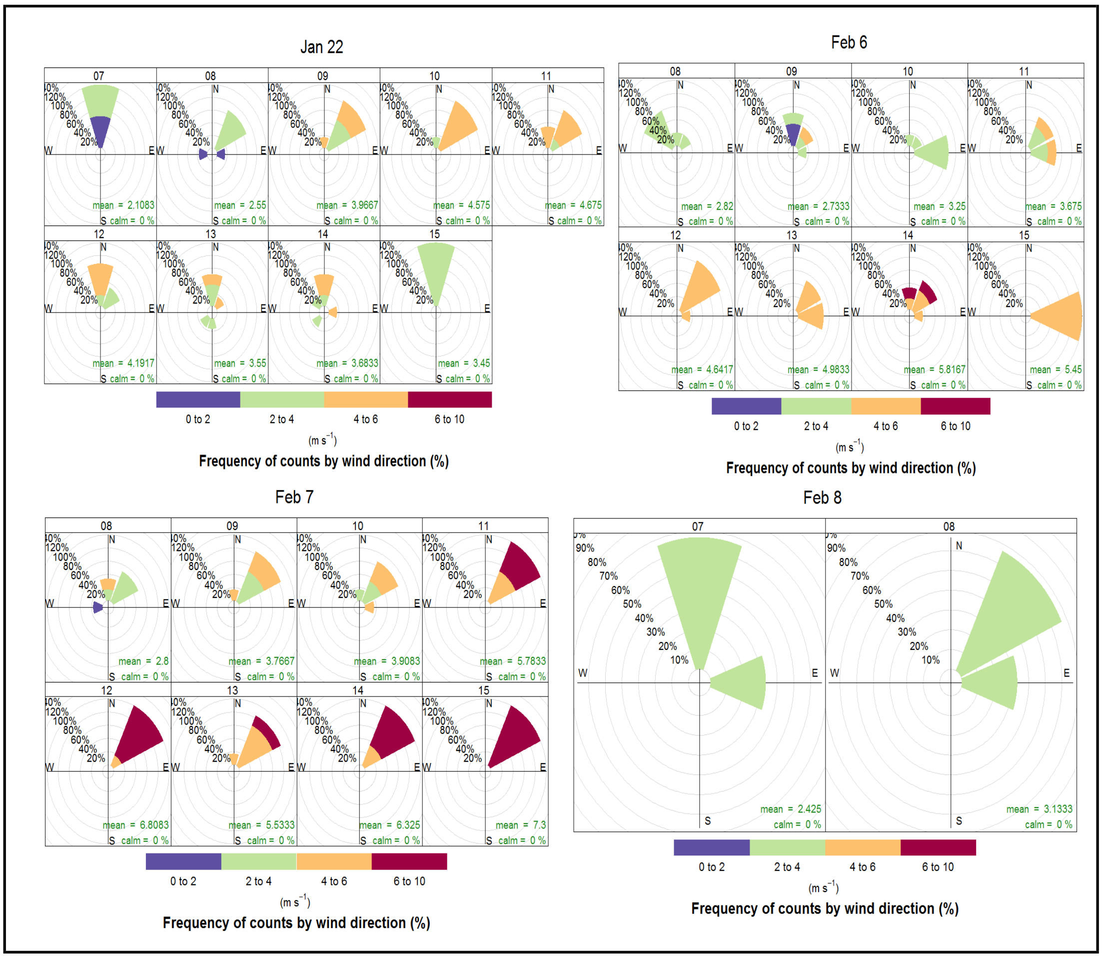

Fig. 4.7: Hourly wind roses during the aerosol measurements on the Class I event days (Jan 22nd, Feb 6th, Feb 7th and Feb 8th, 2013). Only measurements from 7:00 to 15:00 AEST (+ 10 UTC) were plotted. 10-minute averaged data were used in this plot. Note the missing data for Feb 6th, Feb 7th and Feb 8th, 2013. Wind directions are represented by the coloured 'wedge' shape. The percentages of occurrence of the winds are represented by the concentric circles. The strength of the wind speed is represented by the colour bar.

Hierarchical Agglomerative Cluster Analysis (HACA) was applied on the meteorological variables and trace gases measured on the four identified Class I event days. HACA is a useful analysis to group data matrices into clusters with similar characteristics within the groups but with different characteristics between the groups as indicated in Chapter 2. As some meteorological data measured at the MUMBA campaign site was not available on Class I particle formation and growth event days, meteorological variables measured by the Automatic Weather Station operated by the Australian Bureau of Meteorology at Bellambi (34.37°S, 150.93°E) (about 4 km northeast of the MUMBA campaign site) (Fig. 2.1 (a)) were used. Wind direction and global irradiation were not included in this analysis because all four days experienced similar conditions: air masses were from the north and northeast and there was generally sunny weather.

Overall, HACA clustered wind speed of all Class I event days into one group and similar results were observed for temperature (Fig. 4.8(a)). However, relative humidity and CO measurements were clustered into two different groups: 6th February and 7th February 2013 into the first group and 22nd January and 8th February 2013 in the second group. In terms of the other trace gases, no separation was achieved for NO_x and O_3 (Fig. 4.8(b)). These results show that there were dissimilarities in the characteristics of relative humidity and CO measurements during the Class I event day which lead to the separation. Therefore, relative humidity and CO were two of the factors that correlated with the Class I events.

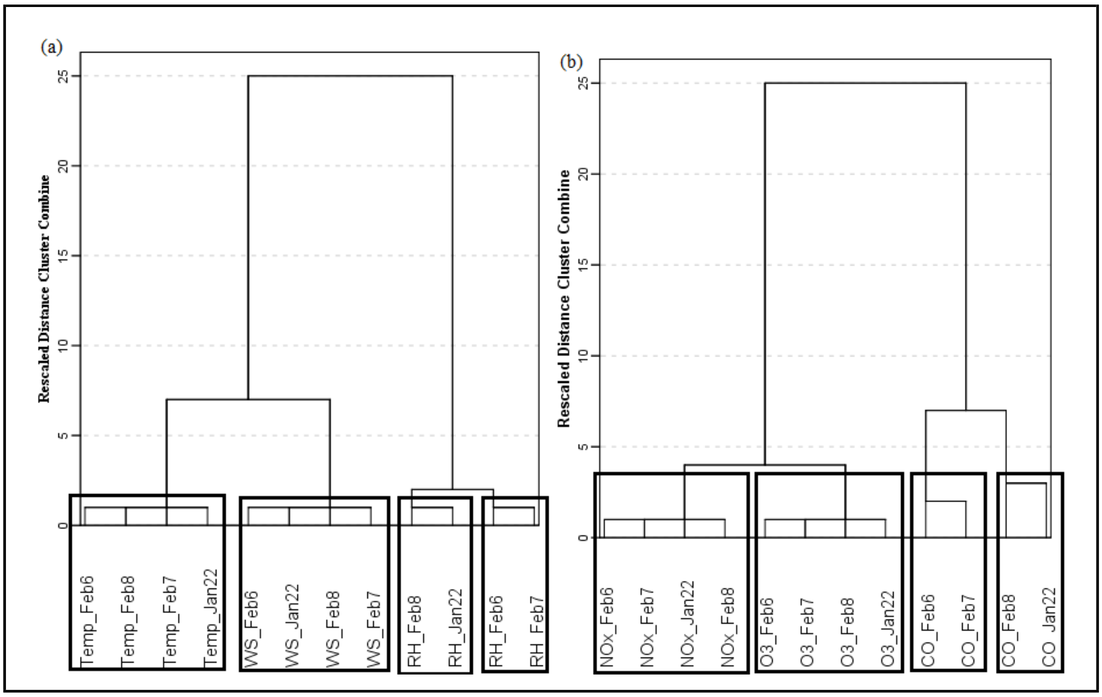

Fig. 4.8: Dendrogram of (a) meteorological variables and (b) gases on the Class I event days (Jan 22nd, Feb 6th, Feb 7th and Feb 8th, 2013) produced by Hierarchical Agglomerative cluster analysis (HACA). Ten-minute averaged data were used in this analysis. Only measurements from 7:00 to 15:00 AEST were plotted.

The time series of meteorological variables (temperature, relative humidity, wind speed, wind direction and global irradiance) (Fig. 4.9) and trace gases (of CO, NO_x and O_3)) (Fig. 4.10) on Class I event days were then analysed to evaluate the factors that drove the groupings obtained from HACA.

Air temperature experienced during the Class I event days ranged from 21 °C to 26 °C with an average of 24 °C. Relative humidity varied between 50% and 86% with average and median values of 70% and 72%, respectively. The average values of wind speed were 6 m s^{-1} with a minimum value of 2 m s^{-1} and a maximum value of 13 m s^{-1}. Generally, it was sunny during the event days except for broken clouds on the 6th February 2013 in the morning and on the 22nd January 2013 in the afternoon. The maximum global irradiance observed during the event days was 1033 W m^{-2} with average and median values of 690 W m^{-2} and 753 W m^{-2}, respectively. The monitoring site experienced air masses from the north and northeast sectors during the event days. On the four event days, relative humidity was higher on 22nd January and the 8th February 2013 than on the 6th February and the 7th February 2013 (Fig. 4.9).

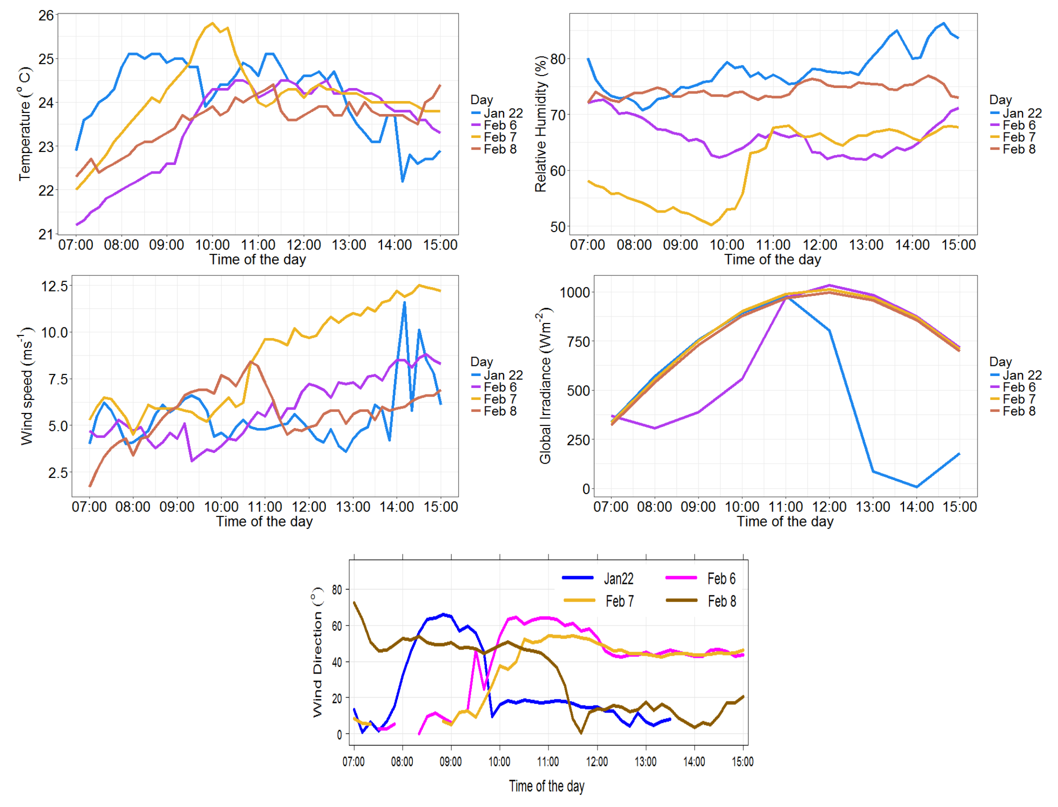

Fig. 4.9: Time series of temperature, relative humidity, wind speed, wind direction and global irradiance on Class I event days (Jan 22nd, Feb 6th, Feb 7th and Feb 8th, 2013). Measurements from 7:00 to 15:00 AEST (+ 10 UTC) were plotted. All the meteorological variables used, excluding global irradiation were in 10-min averaged datasets. Global irradiance was averaged hourly. Measurements from north and east sectors were plotted for wind direction.

The dependence of particle formation events on combustion (markers such as CO and NO$_x$) and formation of secondary pollutants from photochemical reactions (markers such as ozone (O$_3$)) are illustrated in Figure 4.10. Concentrations of CO and NO$_x$ increased before the particle formation and growth events. The concentrations observed for CO and NO$_x$ were lower on the 6th February and 7th February 2013 between 8:00 and 10:00, than for 22nd January and 8th February 2013. The particle formation events on the 22nd January and 8th February 2013 were detected starting at 8:30. On the 6th February and 7th February 2013, they were detected at around 10:00 (Table 4.1). Overall, most of the O$_3$ observations were greater than the median value of observed O_3 in the entire aerosol measurements period (16.4 ppb). On the Class I event days, a steady increase in O_3 concentration was observed from 7:00 which was followed by a slow decrease after 14:00 on average (Fig. 4.10). This observation suggests that photochemical reactions occurred during the campaign and could be one of the factors that favours particle formation events.

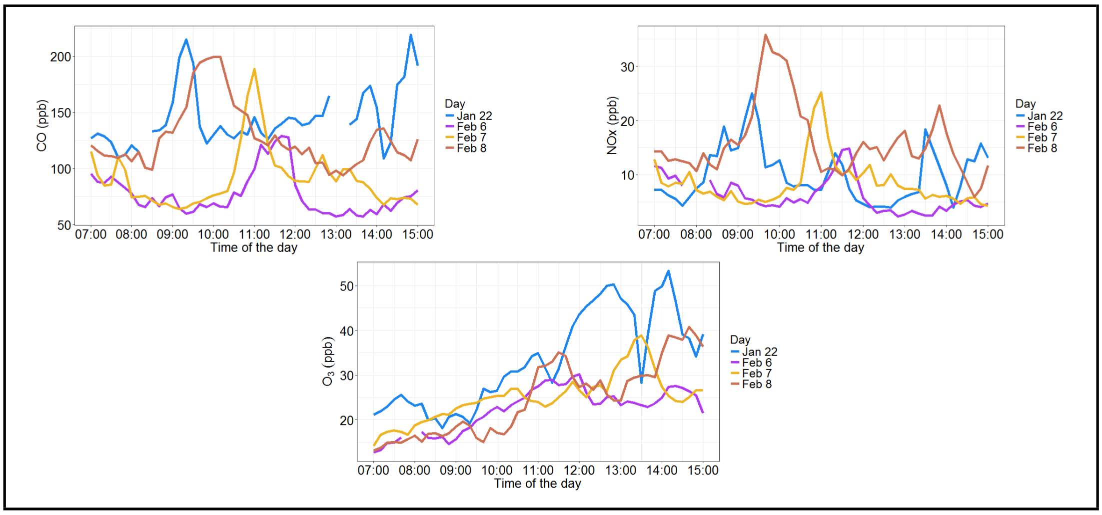

Fig. 4.10: Time series of CO, NO_x and O_3 on Class I event days (Jan 22nd, Feb 6th, Feb 7th and Feb 8th, 2013). 10-minute averaged data were used in these plots. Measurements from 7:00 to 15:00 AEST (+ 10 UTC) were plotted.

Analyses from HACA and the time series revealed that events in the second group (22nd January and 8th February 2013) involved higher CO and NO_x concentrations, and RH, experienced earlier onset and longer event duration times compared to event days mentioned in the first group (6th and 7th February 2013) (Table 4.1). These differences between Class I event days highlight that they are not distinguishing features of Class I events.

4.3.4 Comparison between Class I Event Days and Several Other Cases

This section examines the characteristics of specific cases including:

(i) comparison between event days of Class I and a day where a Class II event occurred;

(ii) comparison between the hottest day in the data series and Class I event days and a day where a Class II event occurred and

(iii) bursts of small particles (nucleation mode) without particle growth events.

The purpose of this analysis is to identify additional factors that contribute to the occurrence of the Class I event. Hourly averaged data of global irradiance and 10-min averaged data of temperature, wind speed, wind direction, relative humidity, trace gases and particles were used in these analyses.

Case 1: Class I Event Days versus a Class II Event Day

As mentioned in Chapter 1, a Class II event is one where particle growth is observed, but due to data fluctuation, the growth and formation rate is questionable. The selected day of Class II event was on the 9^{th} February 2013. On this day, meteorological conditions, particularly wind direction (Fig. 4.7) and global irradiance (Fig. 4.12), were similar to the Class I event days. However, there was no clear Class I particle formation event observed in the contour plot (Fig. 4.11 (d).

Particle number size distributions: To investigate if there is a difference in size distributions between Class I event days and the selected Class II event day, particle number ranging from 3 nm to 100 nm were studied. As illustrated in the contour plots of the Class I event days, particle formation and growth was observed at particle size ranging from 14 nm to 150 nm (Fig. 4.3). Therefore, particle number concentrations for diameters ranging from 14 nm to 30 nm ($\mathrm{PNC}_{14nm-30nm}$) were used to represent smaller size particles while particles ranging from 30 nm to 150 nm ($\mathrm{PNC}_{30nm-150nm}$) were used to represent the larger size particles. A study by *Mejía and Morawska* [2009] also used $\mathrm{PNC}_{14nm-30nm}$ to represent smaller size particles.

Figure 4.11 (a-b) shows the comparison of $\mathrm{PNC}_{14nm-30nm}$ and $\mathrm{PNC}_{30nm-150nm}$ for the Class I event days and the Class II event day (Feb 9^{th}, 2013). Both the Class I event and Class II event days demonstrated a clear peak for $\mathrm{PNC}_{14nm-30nm}$ just after 8:00 and an increase from 9:00 to the middle of the day. The $\mathrm{PNC}_{14nm-30nm}$ recorded for the Class I event days were lower than for the Class II event day. $\mathrm{PNC}_{14nm-30nm}$ on four Class I event days ranged from 2 x 10^2 cm^{-3} to 10 x 10^3 cm^{-3} with median values ranging from 1 x 10^3 cm^{-3} to 3 x 10^3 cm^{-3}. The Class II event day recorded $\mathrm{PNC}_{14nm-30nm}$ ranging from 1 x 10^3 cm^{-3} to 14 x 10^3 cm^{-3} with a median value of 3 x 10^3 cm^{-3} (Fig. 4.11(a)).

The $\mathrm{PNC}_{30nm-150nm}$ on the Class I event days increased at around 10:00 and then began to decrease at around 13:00. Meanwhile, $\mathrm{PNC}_{30nm-150nm}$ for the Class II event did not show a clear trend. Interestingly, there was a sharp peak observed for $\mathrm{PNC}_{30nm-150nm}$ on the Class II event day with a particle number concentration of 13 x 10^3 cm^{-3}. $\mathrm{PNC}_{30nm-150nm}$ recorded just after 8:00 for the Class I event days were ranged from 2.1 x 10^3 cm^{-3} to 4.5 x 10^3 cm^{-3}. The Class II event recorded maximum particle number concentrations for both $\mathrm{PNC}_{14nm-30nm}$ and $\mathrm{PNC}_{30nm-150nm}$ observed just after 8:00 (Fig. 4.11 (b)).

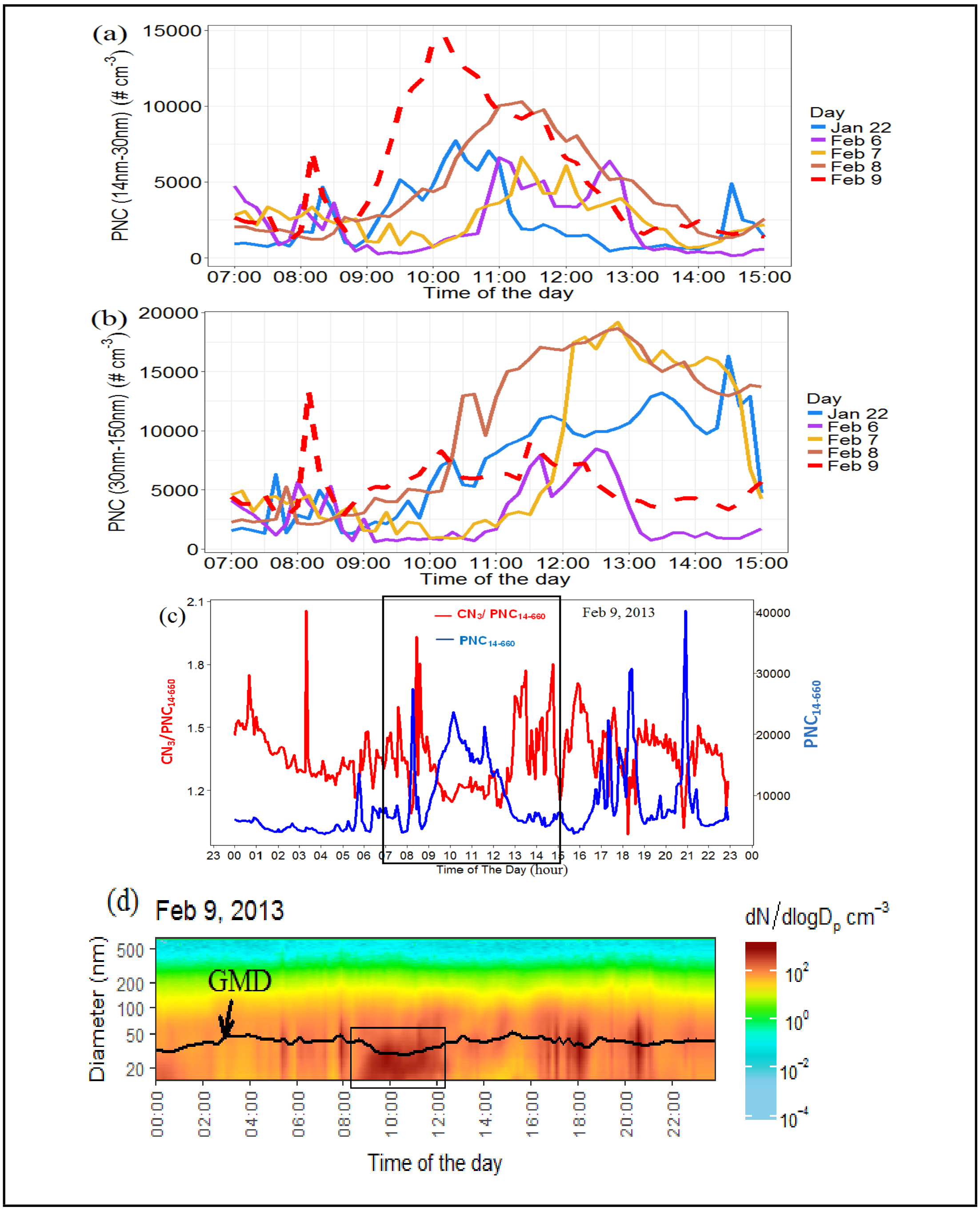

Fig. 4.11: Time series of (a) $\text{PNC}_{14nm-30nm}$ and (b) $\text{PNC}_{30nm-150nm}$ on the Class I event days (Jan 22nd, Feb 6th, Feb 7th and Feb 8th, 2013) and on the Class II event (Feb 9th, 2013). (c) Time series of the total particle number between 14 nm and 660 nm ($\text{PNC}_{14nm-660nm}$) and the ratio of total particle concentrations with diameters larger than 3 nm (CN_3) (CN_3 / $\text{PNC}_{14nm-660nm}$) on 9th February 2013. The black rectangular box represents the relevant time of particle populations before, during and after the Class II event. (d) Contour plot of particle number size distribution on the Class II event. Note that the y-axis is in log format. GMD is geometric mean diameter. The rectangular box (black solid line) represents the Class II events. 10-min averaged data were used for Fig. (a, b and d). Five-min averaged data were used in Fig. (c).

On the Class II event day (9th February, 2013), there was an increase in CN_3 / $PNC_{14nm-660nm}$ ratio just after 8:00 which indicated that the particle number of smaller particles ($>$ 3 nm) was higher than that of larger particles ($PNC_{14nm-660nm}$) (Fig. 4.11 (c)). However, instead of the number of these small size particles decreasing (i.e. decrease in CN_3 / $CN_{14nm-660nm}$ ratio value) and larger size particles increasing (i.e. increase in $PNC_{14nm-660nm}$ value) as observed on Class I event days (at least on the 6th and 8th February, 2013 where observations were complete), both the larger size particles and the smaller size particles continued to increase in number (i.e. increase in both $PNC_{14nm-660nm}$ and CN_3 / $PNC_{14nm-660nm}$). This was followed by an unclear particle growth process in the contour plot from approximately 9:00 (Fig. 4.11 (d)).

Meteorological Conditions: The time series of meteorological variables on the four Class I event days were compared with those of the Class II event (Fig. 4.12). Both Class I event days and the Class II event day experienced increases in temperature and wind speed at around 7:30 to 9:00. Similar observations were made for global irradiance on the 9th February, 2013 and on the 22nd January, 2013 when days were sunny in the morning and there were broken clouds in the afternoon. The Class II day experienced stable relative humidity between 7:30 and 9:00, which was around 80%. Relative humidity experienced on Class I event days ranged from 55% to 75%. The studied meteorological variables therefore are similar during the Class I and Class II measurement periods except for a slightly higher relative humidity on the Class II event day.

Relative humidity can interfere with particle formation and growth processes. Relative humidity is able to increase coagulation, scavenging of smaller or newly formed particles onto pre-existing particles [*Hamed et al.*, 2011] and therefore interfering with the particle growth. Given the small differences in RH observed between Class I and Class II days this does not appear to be a driving factor.

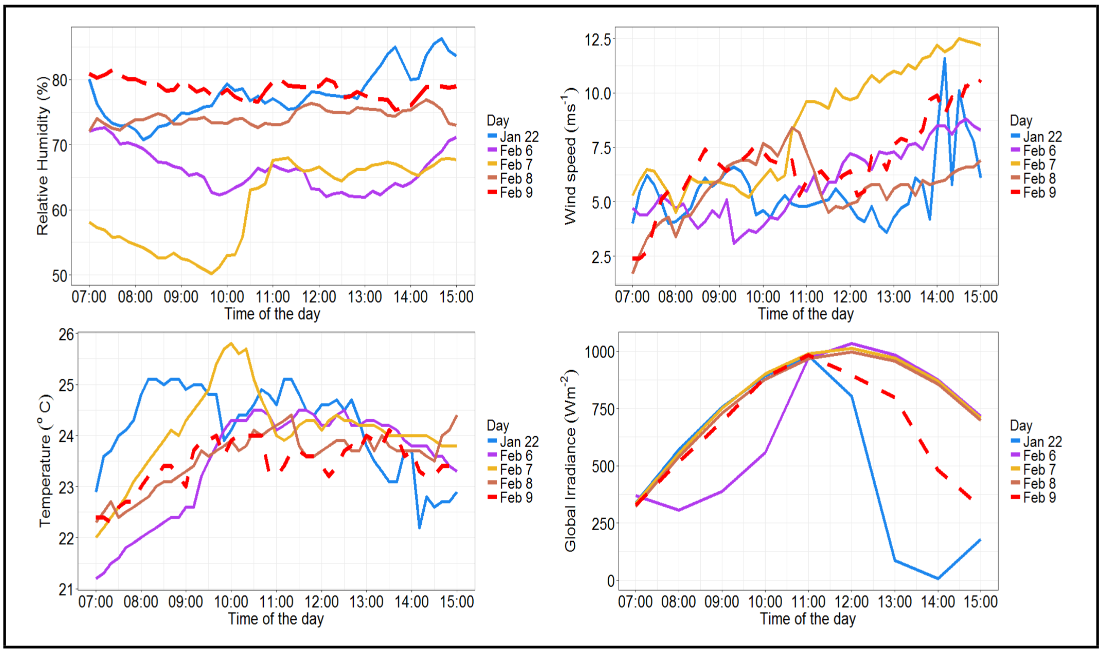

Fig. 4.12: Time series of relative humidity, temperature, wind speed and global irradiance on the Class I event days (Jan 22nd, Feb 6th, Feb 7th and Feb 8th, 2013) and the Class II event (Feb 9th, 2013). Ten-minute averaged data were used in these plots except for global irradiation which was averaged hourly. Measurements from 7:00 to 15:00 AEST were plotted.

Trace gases: Comparison between O_3, CO and NO_x on Class I event days and the Class II event day was also examined (Fig. 4.13). Once again, surface O_3 was used as an indicator of photochemical activity and CO, while and NO_x were combustion markers. The O_3 concentration pattern on these days (Class I and Class II) were very similar to the inference drawn from Section 4.3.3 that photochemical activity occurred during the campaign including on the Class II event day. As mentioned previously in Section 4.3.3, from around 8:30 to 10:30, CO and NO_x observations on Class I event days were split into two categories. The CO and NO_x observation on the Class II event day showed a similar pattern of CO and NO_x concentration on the 22nd January and 8th February 2013 (Fig. 4.13). The increase in the mole fractions of combustion markers (CO and NO_x) before the Class I and Class II event (Fig. 4. 13 (a-b)) indicates that traffic emissions could have initiated the particle formation and growth.

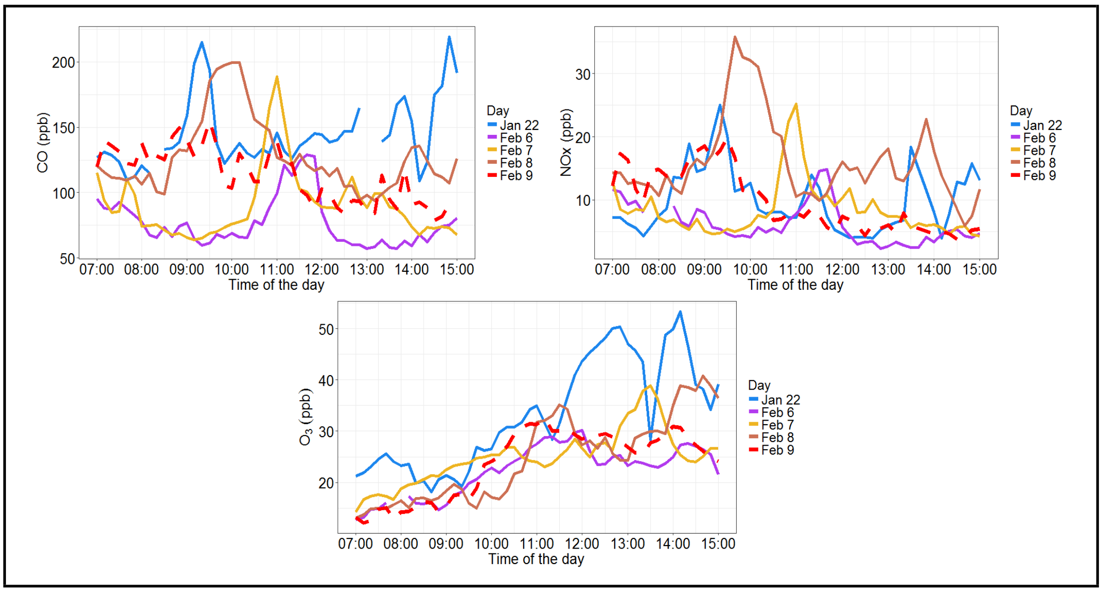

Fig. 4.13: Time series of CO, NO_x and O_3 on the four Class I event days (Jan 22nd, Feb 6th, Feb 7th and Feb 8th, 2013) and the Class II event (Feb 9th, 2013). 10-minute averaged data were used in these plots. Only measurements from 7:00 to 15:00 AEST were plotted.

Results obtained from the comparisons on the available meteorological variables and trace gases between the Class I event days and the Class II event above indicated that the 9th February, 2013 had all necessary conditions for a Class I new particle formation event. However, none of the available information clearly explains the contrasting observation. High relative humidity and its influence on particulate growth could influence the particle population, though the observed difference is small. There results indicate that meteorological parameters do not separate the Class 1 and Class II event days.

Case 2: Hot Day versus Class I Event Days and the Class II Event Day

The 18th of January 2013 was selected as a "Hot day" in this work because the monitoring site experienced very high temperatures and a strong northwesterly wind, which was rare in this campaign (Fig. 4.14). Winds from northwest sector can carry biogenic emissions released from the vegetation on the Illawarra escarpment as mentioned previously. These biogenic emissions have been observed to promote particle formation [*Dall′Osto et al.*, 2018]. Unfortunately, measurements were only obtained until 10:40 on this day because of the high temperatures. The air conditioning could not maintain a safe room temperature and all instruments were shut down to avoid damage. Observations on this hot day were examined and compared with the observations on the Class I event days and the Class II event day (Fig. 4.14).

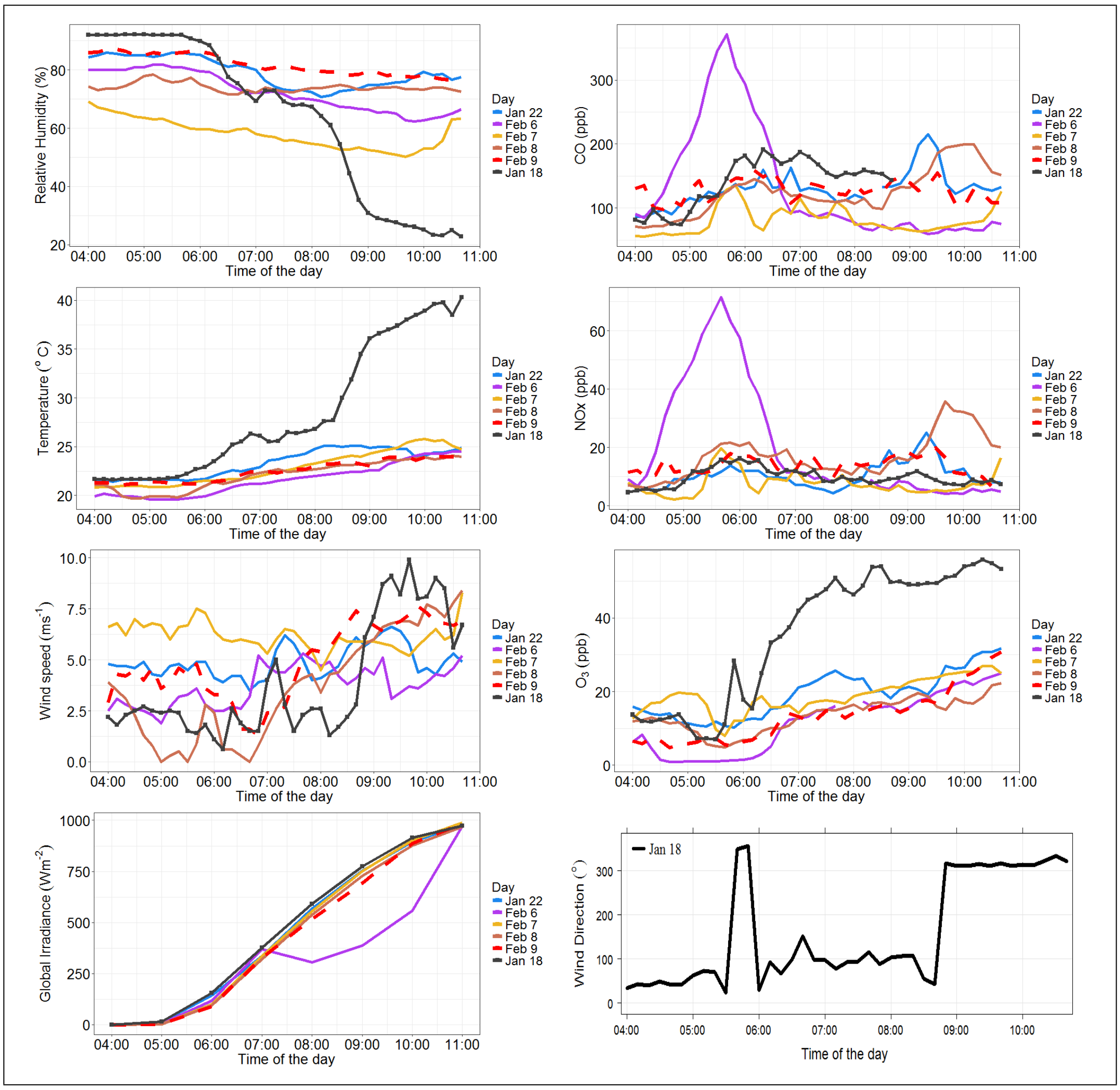

Fig. 4.14: Time series of meteorological variables (temperature, relative humidity, wind speed, wind direction and global irradiance) and trace gases (CO, NO_x and O_3) on the Class I event days (Jan 22nd, Feb 6th, Feb 7th and Feb 8th, 2013), Class II event day (Feb 9th, 2013) and hot day (Jan 18th, 2013). 10-minute averaged data were used in these plots except for global irradiation which was averaged hourly. Measurements from 4:00 to 10:40 AEST were plotted.

The meteorological measurements and trace gases on the hot day (18th January 2013), the Class I event days and the Class II event day (9th of February 2013) are shown in (Fig. 4.14). Temperature ranged from 22 °C to 40 °C with an average of 28 °C. Relative humidity was on average of 64%. Wind speed ranged from 1 m s^{-1} to 10 m s^{-1} with an average of 4 m s^{-1}. By definition, the temperatures on the hot day were higher than those observed on the Class I event days and the Class II event day. For wind speed, there was no obvious pattern observed from 4:00 to 8:00, however there was a steady increase observed after 8:00 with a recorded maximum of 10 m s^{-1} around 10:00. On this hot day, global irradiance steadily increased from around 5:00 and reached a maximum value of 972 W m^{-2} around 10:40.

Morning peaks (around 5:00 to 6:00) were observed in the concentration of CO and NO_x on the 18th of January, as observed on Class I event days and the Class II event day (Fig. 4.14). This observation is presumably attributed to morning traffic (Chapter 3). Oxidation products such as O_3 revealed a steady increase in concentrations from 6:00 for this hot day, with the highest recorded concentration in the campaign observed on the hot day (Fig. 4.14). This indicates that there was greater photochemical activity producing oxidation products and potentially also particulate matter on the 18th of January 2013.

A comparison between smaller particle concentration ($PNC_{14nm-30nm}$, as previously defined) and larger particle concentration ($PNC_{30nm-150nm}$, as previously defined) on the hot day, the Class I event days and the Class II event day is shown in Fig. 4.15 (a-b). Observations on the hot day show that around 4:00 to 5:30, there was a lower number concentration of $PNC_{14nm-30nm}$ compared to $PNC_{30nm-150nm}$. There was an increase in the ratio of CN_3 / $PNC_{14nm-600nm}$ at 5:00 on 18th January, 2013, which indicated the presence of a larger proportion of small particles ($>$ 3 nm) in the particle population (Fig. 4.15 (c)). At around 6:00 the small particles ($>$ 3 nm) decreased in concentration and larger particles ($CN_{14nm-660nm}$) increased in concentration which can be observed in the contour plot (Fig. 4.15(d)). Interestingly, after 8:00, there was another increase in the ratio of CN_3 / $PNC_{14nm-660nm}$ and also the geometric mean diameter (black line) demonstrated a steady increase in the contour plot (Fig. 4.15 (d)). However, the number of particles steadily decreased, which indicated a dilution process, possibly due to a higher boundary layer (larger vertical mixing) and also an increase in wind speed. Wind direction observations on this hot day between 5:00 and 8:00 were from north and east direction (Fig. 4.14). Meanwhile, after 8:00, there was a significant increase in wind speed (Fig. 4.15) and wind direction was from northwest sector (Fig. 4.14). There was no observation of clear particle formation and growth processes on this hot day due to the limited measurement time. However, it is highly probable that a particle formation and growth event on 18th January, 2013 could have been observed if the instruments had been able to continue measurements, triggered by the biogenic emissions.

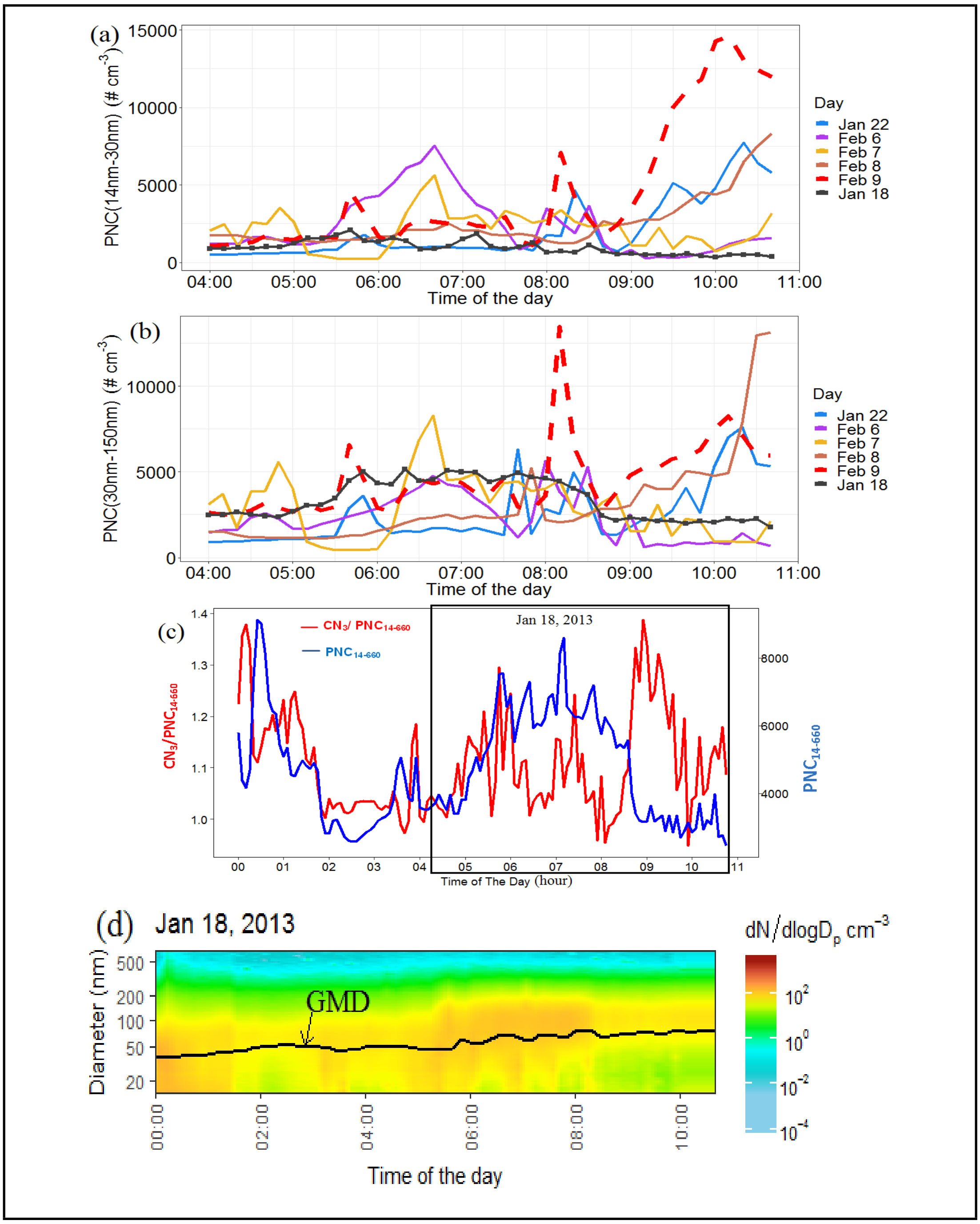

Fig. 4.15: From top panel: Time series of (a) $PNC_{14nm-30nm}$ and (b) $PNC_{30nm-150nm}$ on the Class I event days (Jan 22nd, Feb 6th, Feb 7th and Feb 8th, 2013), the Class II event (Feb 9th, 2013) and the hot day (Jan 18th, 2013). (c) Time series of the total particle number between 14 nm and 660 nm ($PNC_{14nm-660nm}$) and the ratio of total particle concentrations with diameters larger than 3 nm (CN_3) (CN_3 / $PNC_{14nm-660nm}$) on 18th January 2013. The black rectangular box represents the relevant study time of particle populations on Jan 18th, 2013. (d) Contour plots of particle number size distribution on Jan 18th, 2013. GMD is geometric mean diameter. 10-min averaged data were used for (a, b and d). Five-min averaged data were used in (c). Measurements from 4:00 to 10:40 AEST were used to plot for (a and b) while (c and d) used measurements from 0:00 to 10:40 AEST.

Case 3: Burst of Small Particles Size (nucleation mode) Without Particle Growth Events

A study in a sub-tropical urban environment in Brisbane, Australia by *Cheung et al.* [2011] identified an event of this type by observation of the particle populations and the geometric median diameter (noting that this is distinct from geometric mean diameter (GMD) defined earlier) of the particles during the event period. *Cheung et al.* [2011] studied particles ranging from 4 nm to 110 nm where Nucleation and Aitken modes were set as $<$ 30 nm and 30 nm - 110 nm, respectively. A nucleation burst was observed at around 10:00. Particles size in the Nucleation mode increased during the nucleation burst, however, particle size in the Aitken mode did not show any significant variation. *Cheung et al.* [2011] suggests that the possible sources that contribute to the nucleation burst were the emissions of SO_2 and VOCs from industrial sources and aircraft emissions from the Brisbane Airport. The nucleation burst could be also due to local emissions. Such bursts of small particles represent the initial phase of a particle growth event, but the suppression of the particle growth processes was not explained.

The incidence of such particle burst events at MUMBA was therefore investigated. During the aerosol phase of MUMBA campaign, an event of burst of small particles size (nucleation mode) without particle growth events was identified when the ratio between particle number ranging from 3 nm to 14 nm ($\mathrm{PNC}_{3nm-14nm}$) and particle number ranging from 14 nm to 100 nm ($\mathrm{PNC}_{14nm-100nm}$) (Eq. 4.2) was greater or equal to the threshold value. The threshold value used here is 1.0 which is the median value of the $\mathrm{PNC}_{3nm-14nm}$ / $\mathrm{PNC}_{14nm-100nm}$ ratio for the entire dataset. Twelve days of burst of small particles event were identified over the 22 sampling days (Fig. 4.16 and Fig. 4.17).

$$\text{Particle formation without particle growth event} = \frac{PNC_{3nm-14nm}}{PNC_{14nm-100nm}} \geq 1.0 \quad (4.2)$$

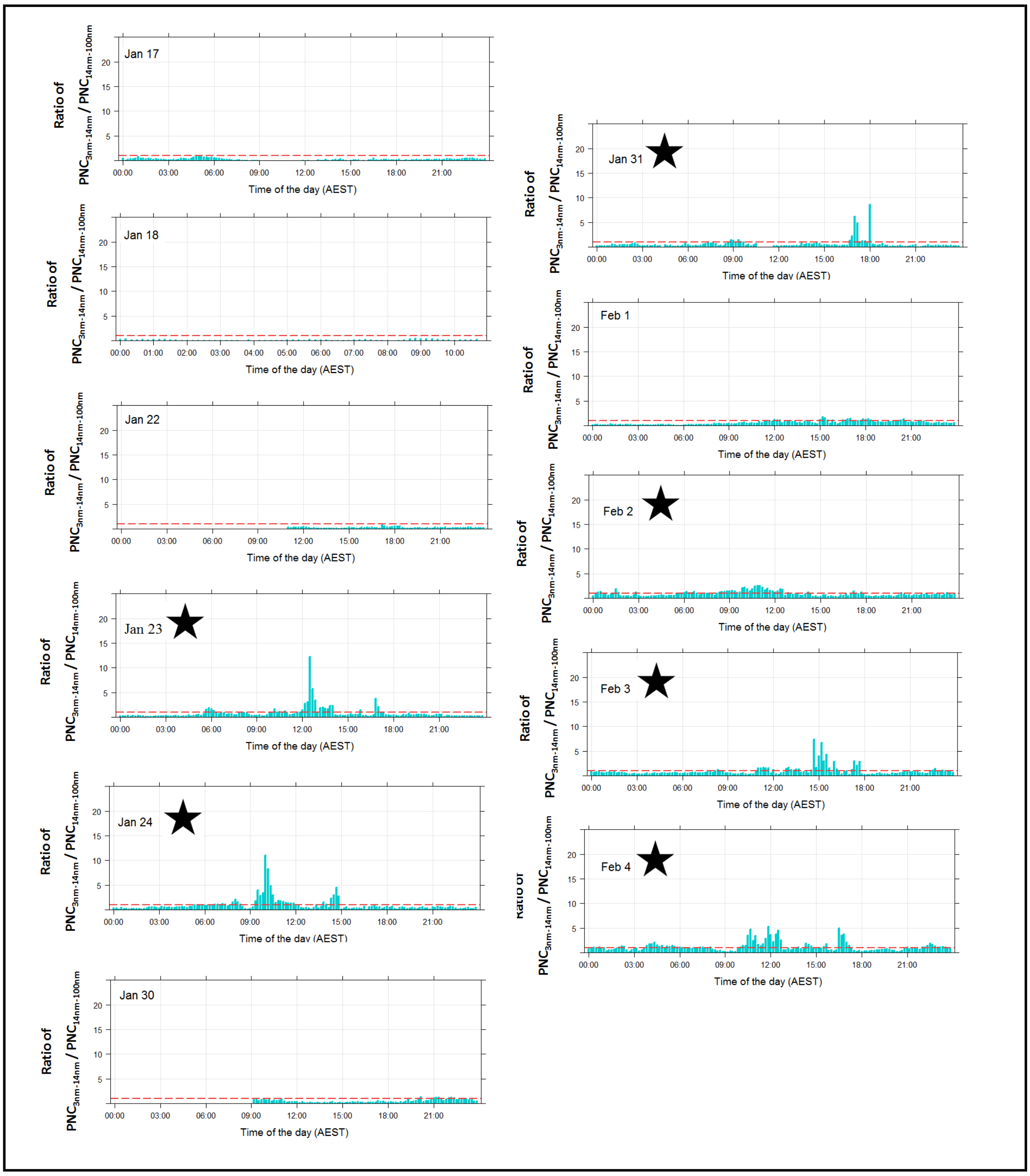

Fig. 4.16: Time series of the PNC$_{3nm-14nm}$ / PNC$_{14nm-100nm}$ ratio during the aerosol measurements. There are gaps in the plots due to the missing data of CN$_{3nm}$. The red dashed line is the threshold value of 1.0. The "black star" symbol represents the particle formation without particle growth event days. Ten-minute averaged data were used.

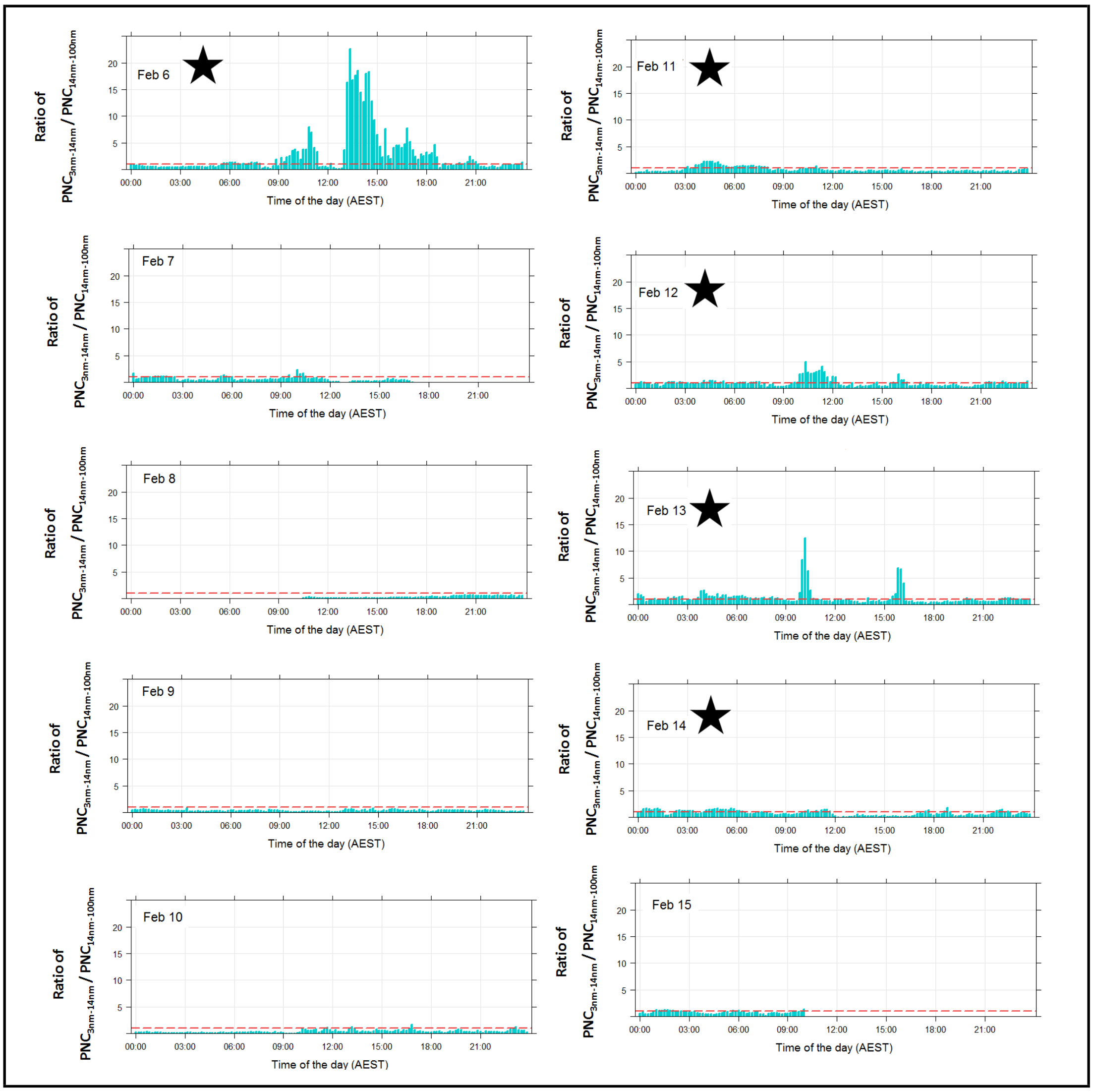

Fig. 4.17: Continued from Fig. 4.16. Time series of the PNC$_{3nm-14nm}$ / PNC$_{14nm-100nm}$ ratio during the aerosol measurements. There are gaps in the plots due to the missing data of CN$_{3nm}$. The red dashed line is the threshold value of 1.0. The "black star" symbol represents the particle formation without particle growth event days. Ten-minute averaged data were used.

The 24th January, 2013 was selected to illustrate this event. As shown in Fig. 4.18 (a), a particle burst was observed at around 10:00 where the ratio values were above the threshold value. The mole fractions of combustion markers (CO and NO$_x$) and O$_3$ (marker for secondary pollutants formed through photochemical reactions) (Fig. 4. 18 (b)) were similar to that observed during the Class I event days (Fig. 4.10). The 24th January, 2013 also experienced similar meteorological conditions (temperature, wind speed, relative humidity) except for wind direction (Fig. 4.18 (c)). In spite of these similarities, the smaller particles (PNC$_{3nm-14nm}$) did not undergo particle growth as evidenced by Fig. 4.1. This could have been due to unfavourable conditions including air masses approaching the site, which were from the open ocean (southeast sector) on this day and at this specific time.

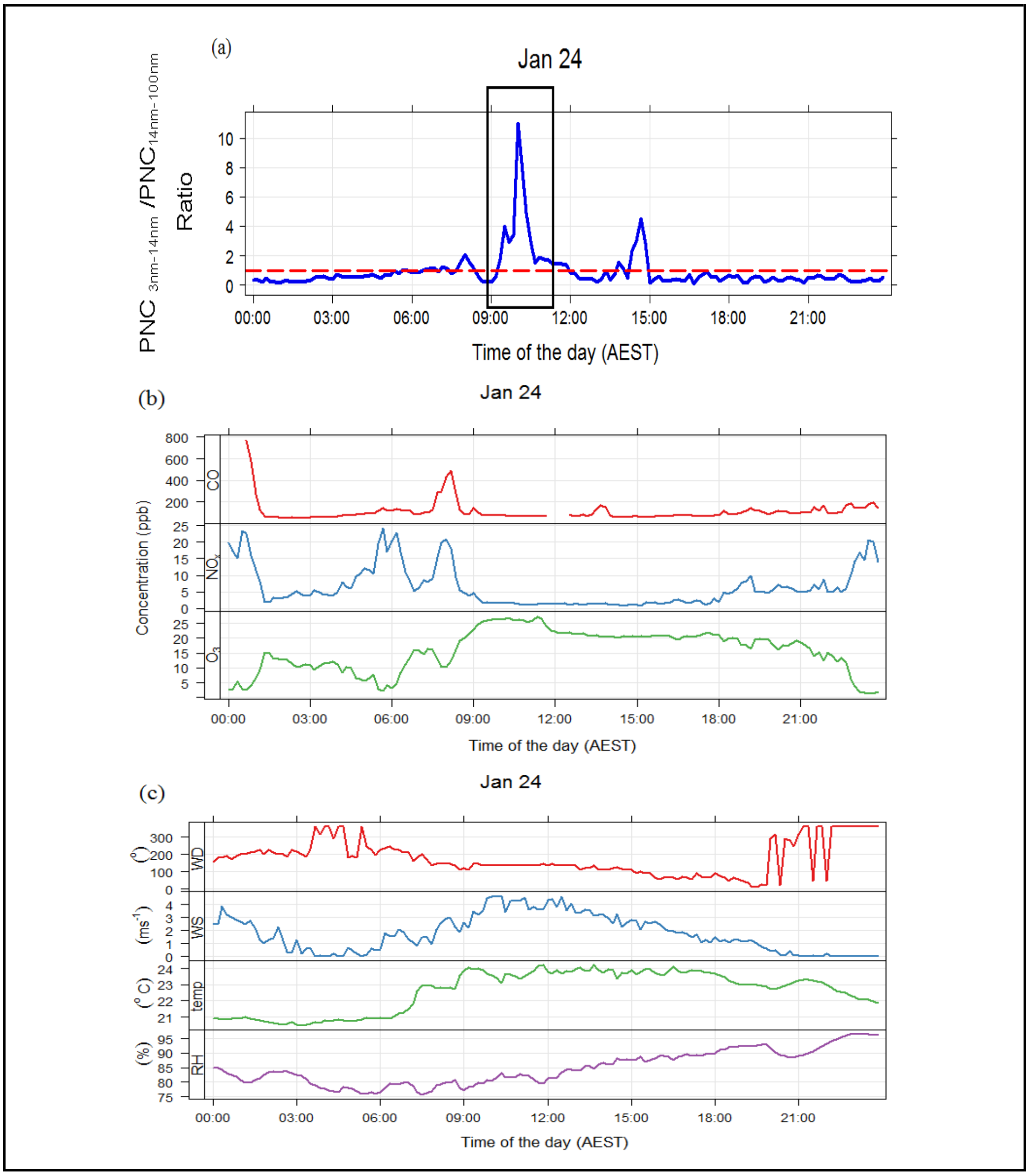

Fig. 4.18: Time series of the (a) $\mathrm{PNC}_{3nm-14nm}$ / $\mathrm{PNC}_{14nm-100nm}$ ratio on the 24th January , 2013. The red dashed line represents the threshold value of 1.0. The rectangular box represents the particle formation without particle growth events. (b) Time series of trace gases (CO, NO_x and O_3) and (c) meteorological variables (wind direction (WD), wind speed (WS), temperature (temp) and relative humidity (RH)) on the 24th January, 2013. Ten-minute averaged data were used.

The increase in the mole fractions of combustion markers (CO and NO_x) before the burst of particle event (Fig. 4. 18(b)) indicates that local traffic emissions could have initiated the particle burst but that these growth conditions were not sufficient to sustain particle growth. This could be due to the chemical atmospheric composition or more likely that the local source does not have a scale large enough that on-going growth can be observed, In other words, the time between release and observation is too short for significant growth to be observed, and small changes in meteorological conditions can change significantly change the influence of the source at the observation site.

4.3.5 Other Possible Factors that Influence Particle Formation

(i) Biogenic sources

Isoprene is one of the VOCs that have the potential to contribute to new particle formation and particle growth. Emission of isoprene is strongly affected by light and temperature [*Khan et al.*, 2018; *Li et al.*, 2011; *Sharkey et al.*, 1996]. As mentioned in Section 3.4, biogenic sources of isoprene dominate in this study and will therefore play a stronger role in the formation of secondary organic aerosol than anthropogenic sources of isoprene. Therefore, isoprene was used as a marker of biogenic emission in this chapter [*Claeys et al.*, 2004]. The hot day (18^{th} of January 2013) recorded the highest concentration of isoprene for the entire aerosol measurements period. Isoprene concentrations increased soon after sunrise (5:45) and reached maximum concentration at 9:00 (Fig. 4.19 (b)). Conversely, isoprene concentrations were low and stable on the Class I event days (Jan 22^{nd}, Feb 6^{th}, Feb 7^{th} and Feb 8^{th}, 2013) and on the Class II event (Feb 9^{th}, 2013) (Fig. 4.19). When considering the time period from 7:00 to 15:00 (Fig. 4.19 (a)), the concentration of isoprene was high before the particle formation and growth event but slowly decreased during the event, (Class I events and the event on the $9^{\text{th}}$of February, 2013 as illustrated in Fig. 4.3 and Fig. 4.11 (d), respectively.) This is consistent with isoprene being one of the factors that is involved in the particle formation and growth process as indicated in Chapter 3. After 8:00 on the 18^{th} of January, air masses were from the northwest sector (Fig. 4.14). There is a good indication that the monitoring site received biogenic emissions from the vegetation on the Illawarra escarpment on the 18^{th} of January.

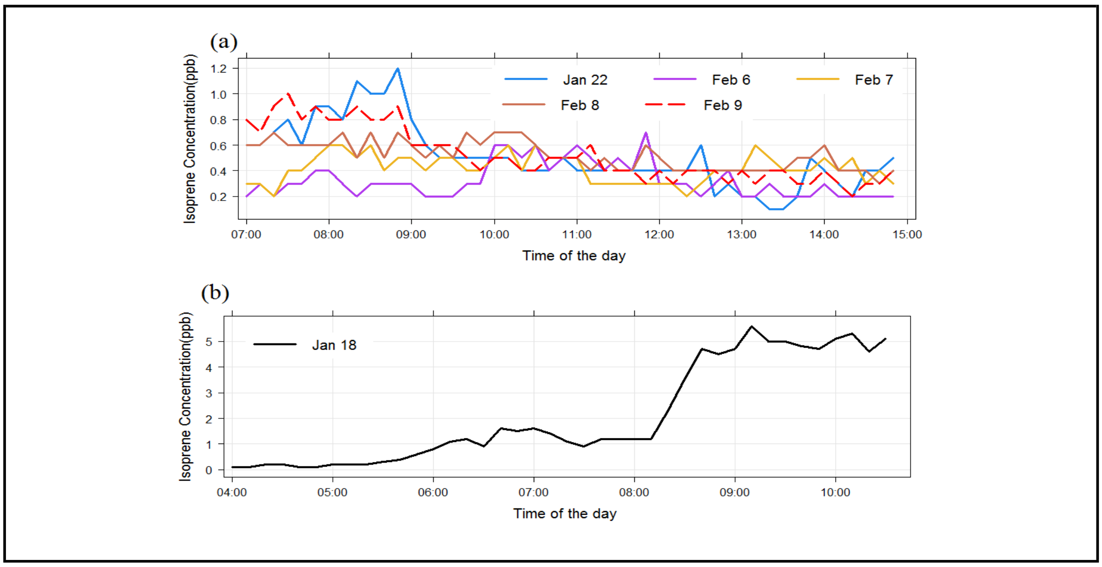

Fig. 4.19: Time series of isoprene on all six studied days: (a) Class I event days (Jan 22nd, Feb 6th, Feb 7th and Feb 8th, 2013), the Class II (Feb 9th, 2013) and (b) hot day (Jan 18th, 2013). Ten-minute averaged data of measurements from 7:00 to 15:00 were used in Fig. (a). and from 4:00 to 10:40 were used in Fig. (b)

(ii) Sulfate ($SO_4{}^{2-}$)

Source of $SO_4{}^{2-}$ one of which is SO_2 was investigated due to the role of this gas in H_2SO_4 production as a particle precursor. SO_2 is emitted into the atmosphere from anthropogenic and natural sources. SO_2 is also produced through the reaction between dimethyl sulphide (DMS) and OH [*Pietikäinen et al.*, 2014; *Seinfeld and Pandis*, 1998], which is associated with sea salt $SO_4{}^{2-}$. Sea salt aerosols were expected to be measured in this work due to the location of the measurement site which was near to the open ocean. *Grythe et al.* [2014] reports that sea salt aerosols are made up of around 33% sodium chloride (NaCl). In addition to NaCl, other chemical ionic species in sea water were found in sea salt aerosols such as $SO_4{}^{2-}$, Ca^{2+} and Mg^{2+}.

The concentration of $SO_4{}^{2-}$ in the aerosol that was attributable to sea salt was investigated by using the method used by *Millero et al.* [2008] for seawater composition. On average, the concentration of salt in seawater (salinity) is about 35 parts per thousand [*NOAA*, 2018]. Sulfate makes up 2.7 g of the 35.2 g salt content in 1000 g of seawater (nearly 8% of sea salt). As the magnesium ion (Mg^{2+}) concentration in seawater is a conservative major element, Mg^{2+} can be used to calculate $SO_4{}^{2-}$(ss) Eq (4.3), where“ss” is sea salt sulfate. The amount of Mg^{2+} of seawater is 1.2 g/kg, as reported by *Millero et al.* [2008].

$$
\begin{aligned}
{SO_4}^{2-}(ss) &= Mg^{2+} \times \frac{Amount\,of\,{SO_4}^{2-}\,in\,g/kg\,of\,seawater}{Amount\,of\,Mg^{2+}\,in\,g/kg\,of\,seawater} \\
{SO_4}^{2-}(ss) &= Mg^{2+} \times \frac{2.7}{1.2}
\end{aligned}
\tag{4.3}
$$

The total of ${SO_4}^{2-}$ can be assumed dominant by three sources: anthropogenic, sea salt and biogenic from the ocean, which is illustrated in Eq. (4.4) where, “Anthro” is anthropogenic sulfate and “BiogenicOceanic” is sulfate from phytoplankton:

$$
\begin{aligned}
{SO_4}^{2-}(total) &= {SO_4}^{2-}(Anthro) + {SO_4}^{2-}(ss) + {SO_4}^{2-}(BiogenicOceanic) \\
{SO_4}^{2-}(Anthro) &= {SO_4}^{2-}(total) - {SO_4}^{2-}(ss) - {SO_4}^{2-}(BiogenicOcenic)
\end{aligned}
\tag{4.4}
$$

The BiogenicOceanic can be estimated using Eq. 4.5 by assuming a ${SO_4}^{2-}$ contribution at a fixed ratio to methane sulfonic acid (MSA) [*Ayers et al.*, 1998].

$$
{SO_4}^{2-}(BiogenicOceanic) = MSA \times 5.1 \tag{4.5}
$$

The MSA concentration is derived from the oxidation of DMS emitted from phytoplankton [*Ayers et al.*, 1998]. The value of 5.1 ng m^{-3} was the average ratio of ${SO_4}^{2-}$(ss) to MSA for PM_{10} at Cape Grim in February over the past 10 years (2002 to 2012) [*CSIRO*, 2017]. February was selected to represent summer in Australia. At Cape Grim during clean air conditions, the primary known source of ${SO_4}^{2-}$(ss) and MSA is from the oxidation of DMS [*Ayers et al.*, 1998]. Therefore, the ratio of MSA to ${SO_4}^{2-}$(ss) from Cape Grim can be used to infer the amount of ${SO_4}^{2-}$(ss) from DMS oxidation (sulfate from phytoplankton) during the MUMBA campaign as illustrated in Eq. 4.5. Total sulfate (${SO_4}^{2-}$(total)) was measured during the campaign using a high-volume sampler (details in *Paton-Walsh et al.* [2017] from Jan 22nd, 2013 to Feb 14th, 2013. On average, 70% of the total sulfate (${SO_4}^{2-}$ (total)) was from anthropogenic sources. A similar value was obtained on the Class I event days.

Hourly concentrations of SO_2 were measured by the Office of Environment and Heritage (OEH) Fig. 2.1 (b)). The hourly average of SO_2 concentration on the available data was 2.4 ppb with a median value of 1.0 ppb. The maximum hourly SO_2 concentration observed was 10 ppb (0.01 ppm) which is well below the hourly maximum allowable concentration specified by the Australian National Environment Protection (Ambient Air Quality) Measure (Air NEPM) of 0.20 ppm (200 ppb). Therefore, from an air quality perspective the region does not contain significant sources of SO_2. A study by *Lee et al.* [2008] that focused on coastal areas found that the SO_2 concentration increases during nucleation events. The concentrations of SO_2 obtained by *Lee et al.* [2008] during event days (Class I and Class II) ranged from 0.5 ppb to 8 ppb. The concentrations of SO_2 during Class I and Class II event days in this study were from 1 ppb to 7 ppb. There were a few occasions when SO_2 concentrations increased during the event days (Class I) for example on the Feb 7th, 2013 at 11:00 to 13:00. There was also an increase in SO_2 concentrations on the Feb 8th, 2013 at 10:00 to 12:00 (Fig. 4.20). Emission of SO_2 from anthropogenic sources (i.e. industrial sources) possibly contributed to the Class I event days. However, due to limited data, further measurements are needed. In particular, for this purpose measurements of SO_2 with greater sensitivity are needed.

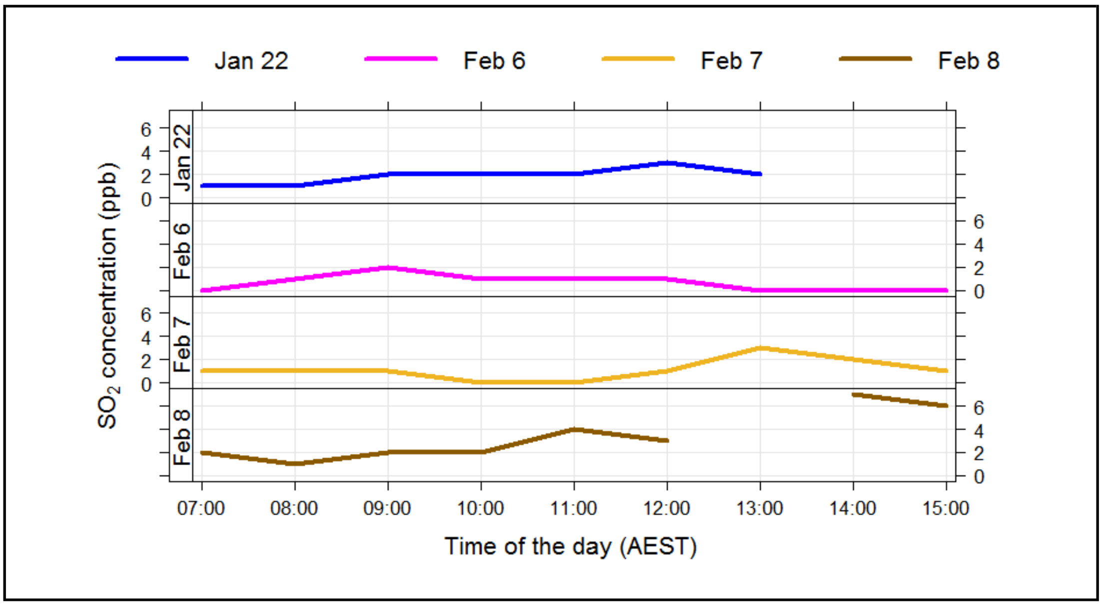

Fig. 4.20: Time series of sulfur dioxide on Class I event days (Jan 22nd, Feb 6th, Feb 7th and Feb 8th, 2013). Hourly averaged data of measurements from 7:00 to 15:00 were used.

(iii) Photochemical Age of Air Masses

Urban atmospheres often include VOCs such as the aromatic hydrocarbons such as benzene, toluene and xylenes that are important precursors for the formation of secondary organic aerosol [*Kalabokas et al.*, 2001; *Molteni et al.*, 2018]. The main sources of benzene, toluene and xylenes are anthropogenic, including industrial activities and traffic emissions [*Tiwari et al.*, 2010]. The ratio of the concentration of the aromatic compounds can provide useful insights into the sources of the aromatics and the photochemical age of an air mass [*Khoder*, 2007; *Miller et al.*, 2011]. The toluene to benzene ratio (T/B) can be used as an indicator of traffic emission [*Miller et al.*, 2010]. T/B ratios that are greater than 4.5 indicate industrial-originated emission sources [*Tiwari et al.*, 2010] whereas T/B ratio values that are within the range of 1.5 to 3.0 indicate traffic-originated emission [*Barletta et al.*, 2005; *Khoder*, 2007]. The xylenes to benzene ratio (X/B) can act as an indicator of the photochemical age of air masses [*Zhang et al.*, 2008]. Ratio values of X/B that are less than 3.0 imply aged plumes [*Tiwari et al.*, 2010].

There were four contiguous days of particle formation and growth events (from 6th to Feb 9th, 2013). Three Class I events were identified on the Feb 6th - Feb 8th, 2013, followed by a Class II event on the Feb 9th, 2013. These four days experienced similar meteorological conditions particularly sources of air masses and global irradiance. Therefore, 9th Feb, 2013 was compared with the observations on the 6th, 7th and 8th Feb, 2013 in order to investigate whether the relative concentrations of benzene, toluene and xylenes provides insight into Class I particle formation and growth. Relevant time frames used in this comparison were from 7:00 till 15:00 to encompass the period both before and after the growth event

Concentrations of benzene for all four days (Feb 6th, 7th, 8th and 9th) (Fig. 4.21 (a)) revealed a similar trend where there were steady increases in concentration in the morning (9:00) and decreases at noon. The concentrations of benzene on Feb 6th and Feb 7th were lower than those on Feb 8th and Feb 9th, especially before 10:30. Concentrations of toluene on these four days (Fig. 4.21 (b)) were usually less than 1.0 ppb, however, there were high toluene concentrations observed between 8:00 to 8:30 on the Feb 6th. High concentrations of xylenes were observed twice on the Feb 7th (9:30-10:00 and 12:30-14:00) and once on Feb 9th (10:30), compared to the xylenes concentrations observed on the Feb 6th and the Feb 8th (Fig. 4.21 (c)).

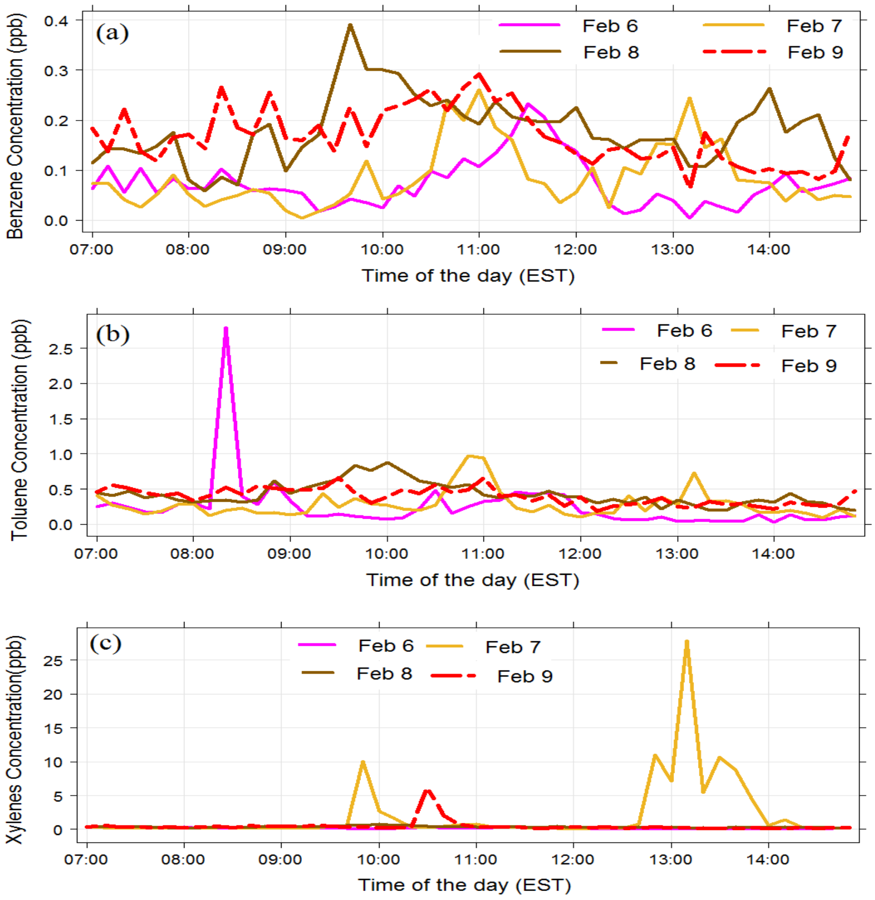

Fig. 4.21: Time series of the (a) benzene, (b) toluene and (c) xylenes concentrations on the four consecutive days (February 6th, 7th, 8th and 9th, 2013). Noted that y-axis were at difference scales. Measurements from 7:00 to 15:00 were plotted. Ten-minute averaged data were used.

Time series of the ratios of the three VOCs are presented in Fig. 4.22. The X/B ratios on Feb 6th and Feb 8th were stable and consistent throughout the day compared to Feb 7th and Feb 9th. There was evidence of fresh plumes (X/B > 3.0) and industrial-originated emissions before the Class I event on the Feb 6th (8:00 to 10:00). Fresh plumes (X/B > 3.0) and a mixture of industrial and traffic-originated emissions were experienced on Feb 8th (6:00 to 8:00). During the relevant time of Class I particle formation and growth on the 6th Feb (10:00 to 13:00) and 8th Feb (after 8:00 to 14:00), the monitoring station experienced emissions from traffic and aged air masses.

On the 7th Feb, the Class I particle formation and growth event was observed from 10:00 till 14:00 (Fig. 4.3). Before the event (just after 9:00), the monitoring site experienced a mixture of fresh plumes (X/B more than 3.0) and industrial-originated emissions (T/B more than 5.0). At 10:00, there were high concentrations of smaller particles observed and the Class I particle formation and growth event was observed (Fig. 4.3). After 10:00, there was a gradual decrease in X/B ratios (less than 3.0), suggesting that the monitoring stations experienced aged air mass. The Class I particle formation and growth event process was continuing. After 12:30, the monitoring site experienced additional fresh plumes (X/B ratio reaching more than 100). The Class I particle formation and growth event process was still continuing but stopped at around 14:00. The campaign site was still undergoing the influence of traffic-originated emissions at this specific time.

On the 9th Feb, the unclear particle formation and growth event observed was just after 8:00 to 12:00 (Fig. 4.11(d)). Before 8:00, the monitoring site experienced aged air masses (X/B were less than 3.0). After 8:00, high concentrations of smaller particles were observed (Fig. 4.11 (a and c)) and the X/B was less than 3.0 (Fig. 4.22). At the same time, the ratios of T/B were less than 5.0 which suggests that the monitoring station experienced traffic-originated emissions and aged air masses. In contrast to the Class I event identified on the 7th Feb, the smaller particles observed on the 9th Feb did not show a clear growth. At around 10:30, the site experienced fresh plumes (X/B greater than 3.0). However, there was still an unclear particle formation and growth observed.

The photochemical age of the air mass could be one of the factors that impeded Class I particle formation and growth on the 9th of Feb, 2013. In this study, the monitoring site experienced an ageing air mass before the Class II particle formation and growth event was observed. However, a different observation was on the 7th of Feb, 2013, where, the monitoring site experienced fresh air mass before the Class I particle formation and growth.

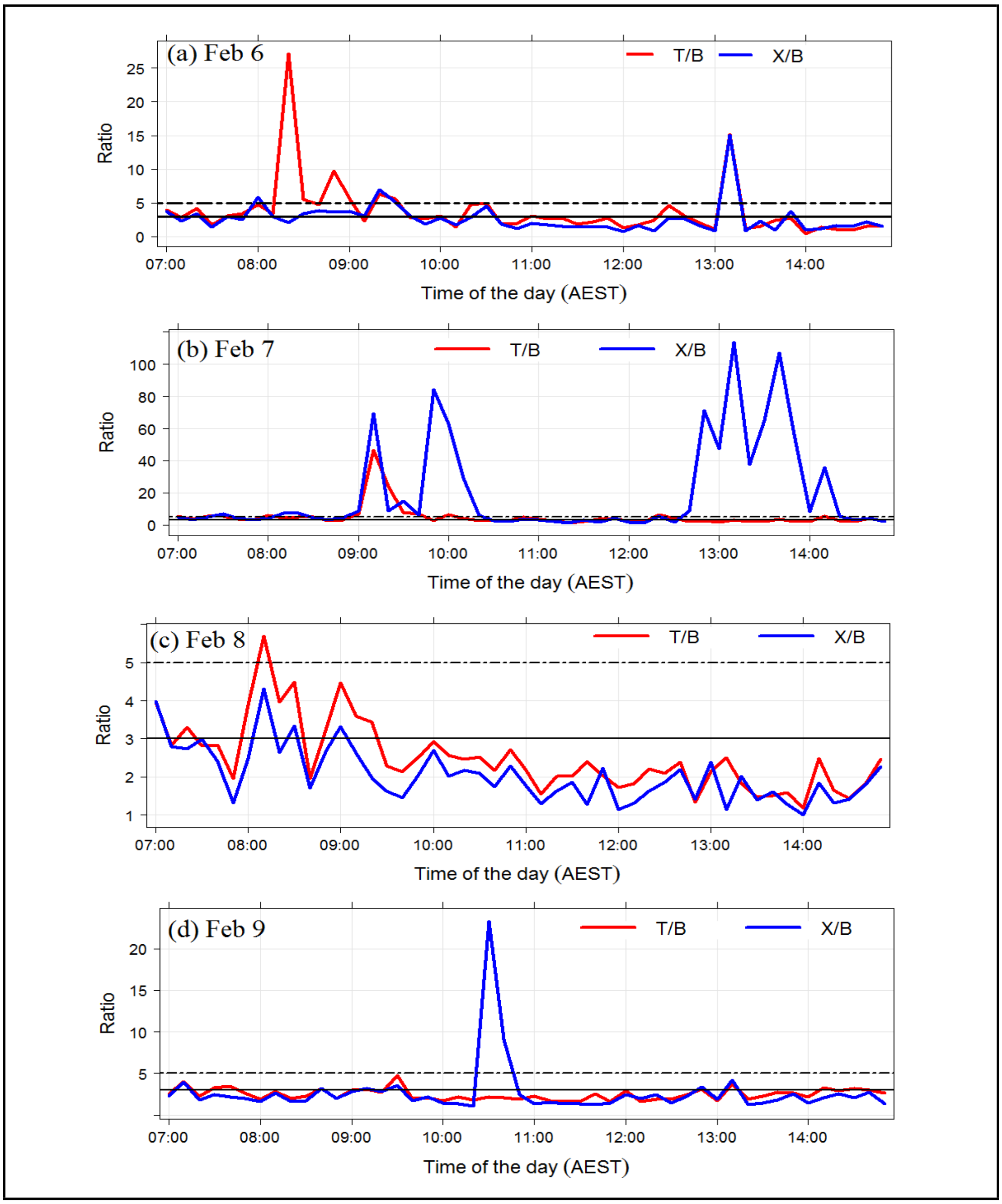

Fig. 4.22: Time plots of the ratios of toluene to benzene (T/B) and xylenes to benzene (X/B) on the four consecutive days (February 6th, 7th, 8th and 9th, 2013). The black dashed black line is toluene to benzene (T/B) ratios that are greater than 5.0 indicate industrial-originated emission sources. The black solid black line is xylenes to benzene (X/B) ratios less than 3.0 imply aged plumes. Noted that y-axis were at difference scales. Ten-minute averaged data were used. Measurements from 7:00 to 15:00 were plotted.

4.4 Summary and Conclusions

This chapter presented a detailed study on new particle formation and growth mechanisms in an urban-marine and forest environment during the Australia summer,

2013. The findings are summarized as follows:

(i) The occurrence of the Class I particle formation and growth events was 13% of the total number of sampling days. All identified Class I events were observed during the day with an average time duration of five hours. At least two out of four Class I event days were classified as "weak" particle formation events;

(ii) Particles with diameter between 50 nm and 100 nm formed during Class I event days were inefficiently activated and contributed to the concentration of cloud condensation nuclei;

(iii) Small particles size (> 3 nm) were formed in the Class I particle formation and growth events before being detected by SMPS instrument;

(iv) Possible factors that could influence Class I particle formation and growth were:

    (a) pollution from urban regions including Sydney
    (b) photochemical reactions and traffic emissions
    (c) relative humidity, photochemical age air mass (although there were insufficient measurements to examine this to a high level of confidence).

Chapter 5

Aerosol Properties by Remote Sensing Techniques

5.1 Introduction

Measurements of aerosol optical properties, including the aerosol extinction coefficient profile and its integral form (aerosol optical depth) provide important information about aerosol vertical distribution. The Intergovernmental Panel on Climate Change (IPCC) has reported that vertical measurements of aerosol optical properties need to be improved in order to properly evaluate aerosol environmental and radiative effects [*Forster et al.*, 2007; *Stocker et al.*, 2013].

Remote sensing is an effective tool for air pollution properties measurements that estimates aerosol vertical distribution [*Irie et al.*, 2011; *Platt and Stutz*, 2008]. Three remote sensing measurements of aerosol properties were employed during the MUMBA campaign namely (a) a sun photometer (b) a Light Detection and Ranging (LIDAR) instrument and (c) a multi-axis differential optical absorption spectroscopy (MAX-DOAS). These three techniques use differing viewing geometry, calibrations and assumptions of aerosol properties.

Sunphotometer: The sun photometer instrument measures the direct beam solar radiation and optical properties of total atmospheric column (i.e. total aerosol extinction). The instrument was calibrated using variation of the Langley method *Langley* [1880] and the measurement was made at a wavelength of 500 nm. The sun photometer instrument was located at the University of Wollongong (Fig. 2.1(b)).

LIDAR: A LIDAR instrument uses a pulsed light source and measures the intensity of the backscattered light as a function of time. The LIDAR instrument was located at the main measurement site (Fig. 2.1(a)) and pointed vertically (Zenith angle of 90°) during MUMBA campaign. Measurements were made at 355 nm. The measurements retrieved by LIDAR can be used to estimate aerosol extinction by using the formula proposed by *Fernald et al.* [1972] as shown in Equation 5.1, where σ is the aerosol extinction, β is the backscatter cross section and S represents the LIDAR ratio.

$$\sigma = S\beta \tag{5.1}$$

The LIDAR ratio (S) depends on aerosol type including their particle size distribution and their chemical composition [*Ackermann*, 1998]. The unit used for LIDAR ratio is the steradian (sr). The LIDAR ratio value is about 20 sr for cloud droplets, 20-26 sr for marine aerosols, 40 sr to 60 sr for mineral dust and can be as high as 80 sr for continental pollution [*Müller et al.*, 2007]. The LIDAR ratio value used in this work was 25 sr which *Müller et al.* [2007] reported as being appropriate for marine particles.

MAX-DOAS: The MAX-DOAS instrument measures the spectra of scattered sunlight. The instrument was located at the second measurements site during the MUMBA campaign (Fig. 2.1(b)) and the MAX-DOAS system was pointed toward the open ocean. Aerosol retrieval was made using the O_4 absorption feature at 361 nm. MAX-DOAS can capture trace gases and aerosol concentrations over the lower troposphere ($<$ 2 km) [*Hönninger et al.*, 2004; *Irie et al.*, 2009; *Lee et al.*, 2009a]. However, the sensitivity of the MAX-DOAS measurements decreases with altitude of the atmosphere which limits the aerosol extinction retrieval from MAX-DOAS at higher altitudes [*Frieß et al.*, 2006].

The aims of this chapter are to describe the retrieval of aerosol properties through MAX-DOAS instrument and to answer the question: “Does the MAX-DOAS instrument provide insight into the aerosol environment at the MUMBA site?” Secondly,what about the other remote sensing techniques?

5.2 Interpretation of MAX-DOAS

Light intensity and the spectra of scattered sunlight measured by MAX-DOAS were used in the colour index (CI) and differential slant column density calculation which are detailed in section 5.2.1 and 5.2.2.

5.2.1 Colour index

The CI retrieved from the MAX-DOAS observation has been applied in this chapter to assess the cloud conditions. The colour index is defined as the ratio of the intensity of two selected wavelengths. This has been used in several studies to identify cloud effects [*Gielen et al.*, 2014; *Takashima et al.*, 2009; *Wagner et al.*, 2016; *Wang et al.*, 2017]. The CI values used in this study were calculated by the ratio of the intensity at wavelength of 330 nm to the intensity at wavelength of 390 nm (Eq. 5.2) *Wagner et al.* [2016]. The principal behind the use of CI observation is, during the day, the colour of the sky changes from blue to white or grey when clouds or aerosols are present. Clear skies therefore have a higher CI value. Broken or scattered cloud conditions as well as a high aerosol loading conditions, have a variable CI value. Elevation at which observations are made also affects the CI observed. A high elevation (close to zenith) gives a high CI value, whereas a lower elevation (near to the horizon) gives a low CI value [*Gielen et al.*, 2014; *Wagner et al.*, 2016].

$$\mathrm{CI} = \frac{Intensity\ at\ 330nm\ (\lambda_{330nm})}{Intensity\ at\ 390nm\ (\lambda_{390nm})} \tag{5.2}$$

5.2.2 Differential Slant Column Density (DSCD)

As mentioned in Chapter 2.4.1, the direct product of the DOAS method is the differential slant column density, which is the difference between the slant column density of atmospheric trace gases and a reference measurement in a specified spectral window. Measurement at 90° was used as the reference angle. The cross section and other fitting parameters are summarised in Table 5.1. The molecular absorption cross-section files were convolved with the spectrometer′s spectral line shape as determined using the measurement of the mercury line at 404 nm [*Kraus*, 2006]. The primary target species in this study is O_4. The wavelength correction was calculated using the wavelength range from 310 nm to 400 nm with eleven sub-windows. For the O_4 retrieval, a shorter fitting interval was used (350 nm - 389 nm) in order to minimise the O_4 root mean square (RMS) value for the residual. A similar method was applied in a study by *Ryan et al.* [2018].

Table 5.1: Summary of the sources of the obstruction cross-section files used in the retrieval of O_4 at the wavelength range from 350 nm to 389 nm.

O_4 (298 K)	*Hermans et al.* [1999]
NO_2 (298 K)	*Vandaele et al.* [1996]
O_3 (293 K)	*Bogumil et al.* [2003]
HCHO (297 K)	*Meller and Moortgat* [2000]
BrO (298 K)	*Wilmouth et al.* [1999]
Ring effect (25 K)	*Grainger and Ring* [1962]
DOAS polynomial	5^{th} order
Offset term	1^{st} order

5.3 Results and Discussion

5.3.1 Differential Slant Column Density (DSCD) and Residual Retrieval

The example of a successful DOAS retrieval for O_4 DSDCs is demonstrated in Fig. 5.1. In this example, the retrieval for O_4 DSDCs at elevation angle of 8° was 3.3 x 10^{43} molec^2 cm^{-5} with a root mean square (RMS) value for the residual of 7.9 x 10^{-4}. The residual shows some unfitted structure which can be caused by errors in the reference spectra, the shift of an absorption feature (due to temperature differences between the actual gas and the reference spectra), the presence of an unidentified atmospheric component or non-linear behaviour of the instrument. A RMS of the residual less than 10^{-3} has been reported as evidence of a reliable fit by other studies, including a study in Melbourne, Australia *Ryan et al.* [2018], in work in the Netherlands *Pinardi et al.* [2013], and in the USA *Ortega et al.* [2016]. The RMS obtained in this study was 10^{-4}, which is within the similar magnitudes.

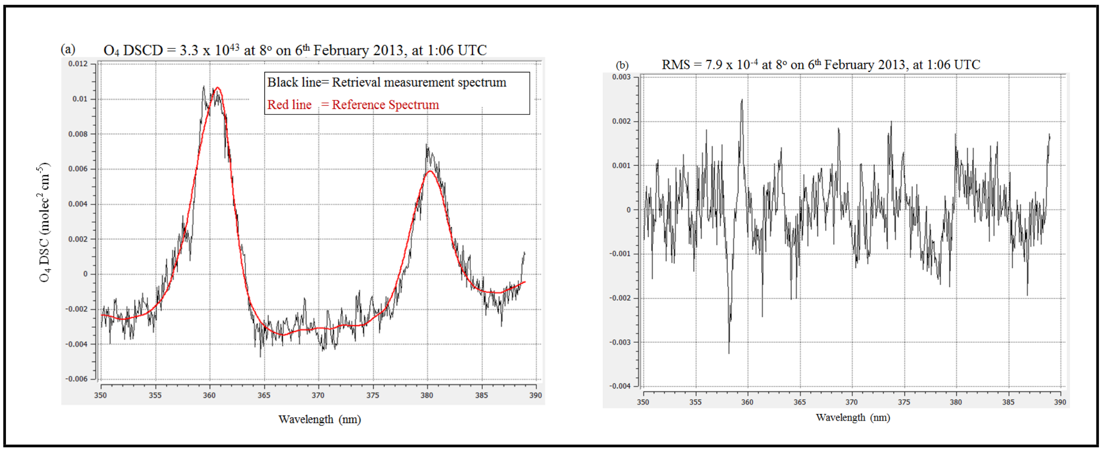

Fig. 5.1: Example of the (a) retrieved O_4 differential slant column densities (DSCDs) and (b) residual at observation angle of 8° on 6^{th} February 2013, at 1:06 UTC (+10 AEST). The O_4 retrieval was conducted at the wavelength range from 350 nm to 389 nm. The root mean square (RMS) is derived from the residual.

The characteristics of the hourly averaged root mean square of the residual at all elevation angles: 1°, 2°, 4°, 8°, 16°, 30° and 60° were studied and are illustrated in the Box-and-whisker plot (Fig. 5.2). The median values of RMS between 16^{th} January 2013 and 10^{th} February 2013 from 7:00 and 17:00 ranged from 0.007 to 0.0024, where the lowest viewing angle (1°) recorded the highest median value of root mean square. The viewing angle of 60° recorded the lowest median value. However, 60° also experienced higher root mean squares values as presented by the circles in Fig. 5.2. These outcomes could be due the signal-to-noise experienced at a lower viewing angle and between 60° and the reference angle used in this study

(90°), respectively. Therefore, only five elevation angles, 2°, 4°, 8°, 16° and 30° were used in this work.

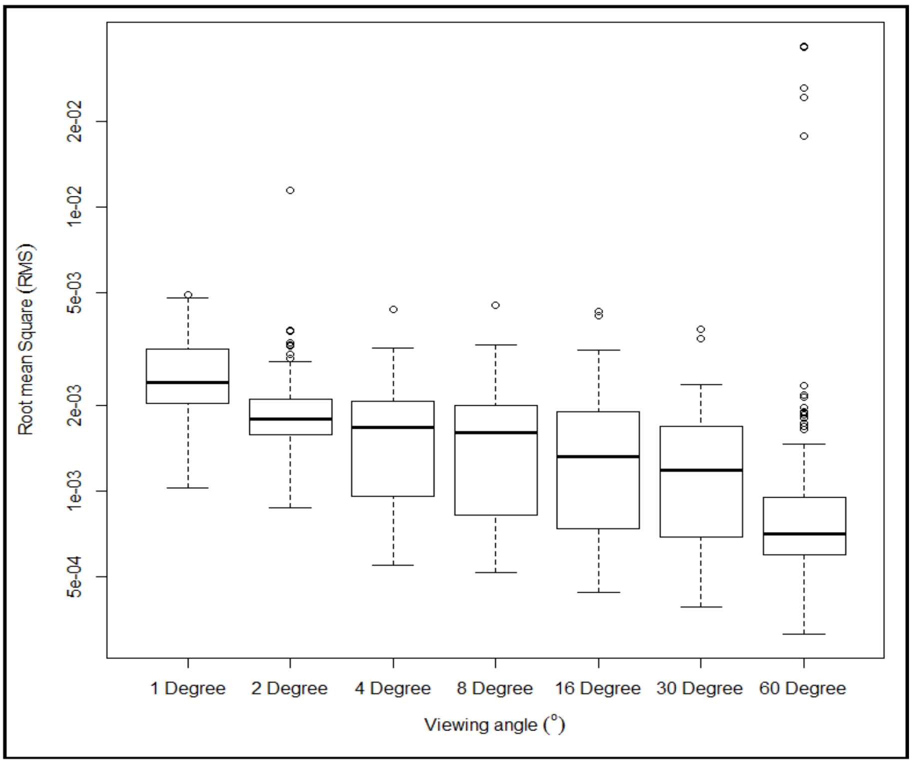

Fig. 5.2: Box-and-whisker plot of root mean square of the residual at all elevation angles (1°, 2°, 4°, 8°, 16° , 30° and 60°). Hourly averaged observations between 7:00 and 17:00 covering the period from 16^{th} January 2013 to 10^{th} February 2013 are shown. The central line of each box is the median and the edges of the box are the lower and upper quartiles (25% and 75%). The whiskers represent the most extreme data points which are no more than 1.5 times the length of the box from either end of the box. The circles are those values beyond the extremes of the whiskers. Note that the log scale used for the y-axis.

5.3.2 Determination of Sky Conditions

Sky conditions in this work were determined from global irradiance measured using a solar radiation sensor located at the University of Wollongong (Fig. 2.1(a)), CI calculated from MAX-DOAS (Fig. 2.1(b)), and the backscatter signal from the LIDAR instrument (Fig. 2.1(a)).

The reference point of global irradiance was 400 W m^{-2}. This is the median value of the global irradiance measured from 16^{th} January 2013 to 10^{th} February 2013 covering the the time period from 7:00 to 17:00. More than half of the sampling days exceeded this reference point at midday. Three days were chosen: 28^{th} January 2013, 9^{th} February 2013 and 5^{th} February 2013 for the determination of “clear” and “cloudy” sky. These three days were chosen because there were periods of time in these three days that were suitable for illustrating the identification of a “clear” and “cloudy’ sky. These three periods are used in Section 5.3.5.

28^{th} January 2013: All three methods showed that on the 28^{th} January 2013, the sky was cloudy (Fig. 5.3). The global irradiance for the whole day was below the reference value (400 W m^{-2}) (Fig. 5.3 (a)). The colour index values were variable (Fig. 5.3 (b)) and laser signal from LIDAR has been scattered lower down as indicated by the intense backscatter signal close to the ground (Fig. 5.3 (c)).

9^{th} February 2013: On the 9^{th} February 2013, the global irradiance for the whole day was above the reference value (400 W m^{-2}) especially from 8:00 to 14:00 (Fig. 5.4 (a)). The LIDAR backscatter signal decreases monotonically with height illustrating that there were clear skies on this day (Fig. 5.4 (c)). The colour index values on this day were similar for the lower observation angles (Fig. 5.4 (b)). Overall, these observations summarised that it was a clear day on the 9^{th} February 2013.

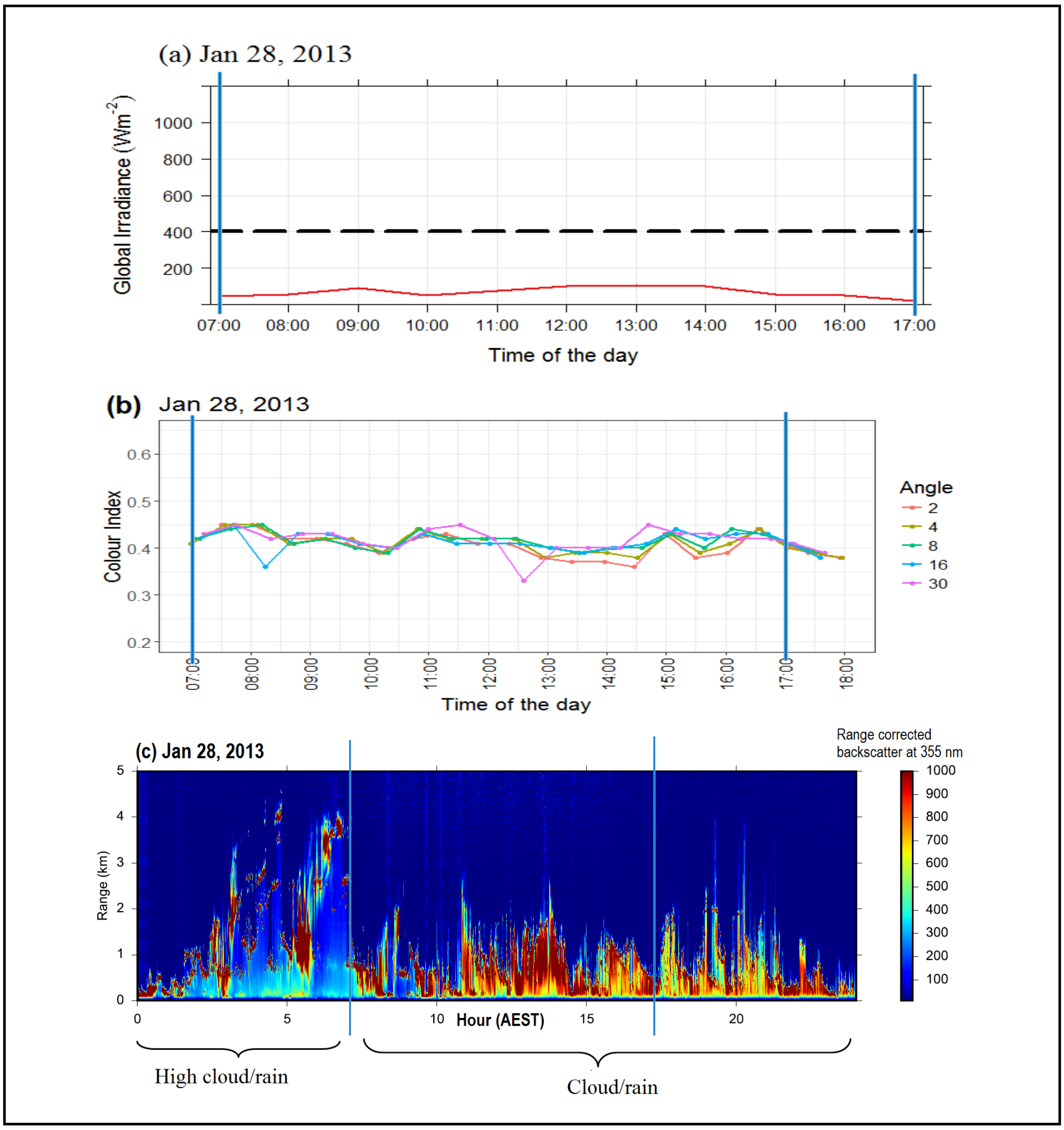

Fig. 5.3: 28th January 2013 (a) Time series of global irradiance. The dashed line represents the median value of the global irrandance from 16th January 2013 to 10th February 2013, from 7:00 and 17:00. (b) Colour index at five observation angles (2°, 4°, 8°, 16° and 30°). (c) LIDAR backscatter signal. Range-normalised backscatter (indicated by the colour scale, red indicates higher backscatter). Colour scale represents the range corrected backscatter at 355 nm. Corrected backscatter refers to correction for the optical geometry. The two solid blue vertical lines represents the time period of interest (7:00 and 17:00).

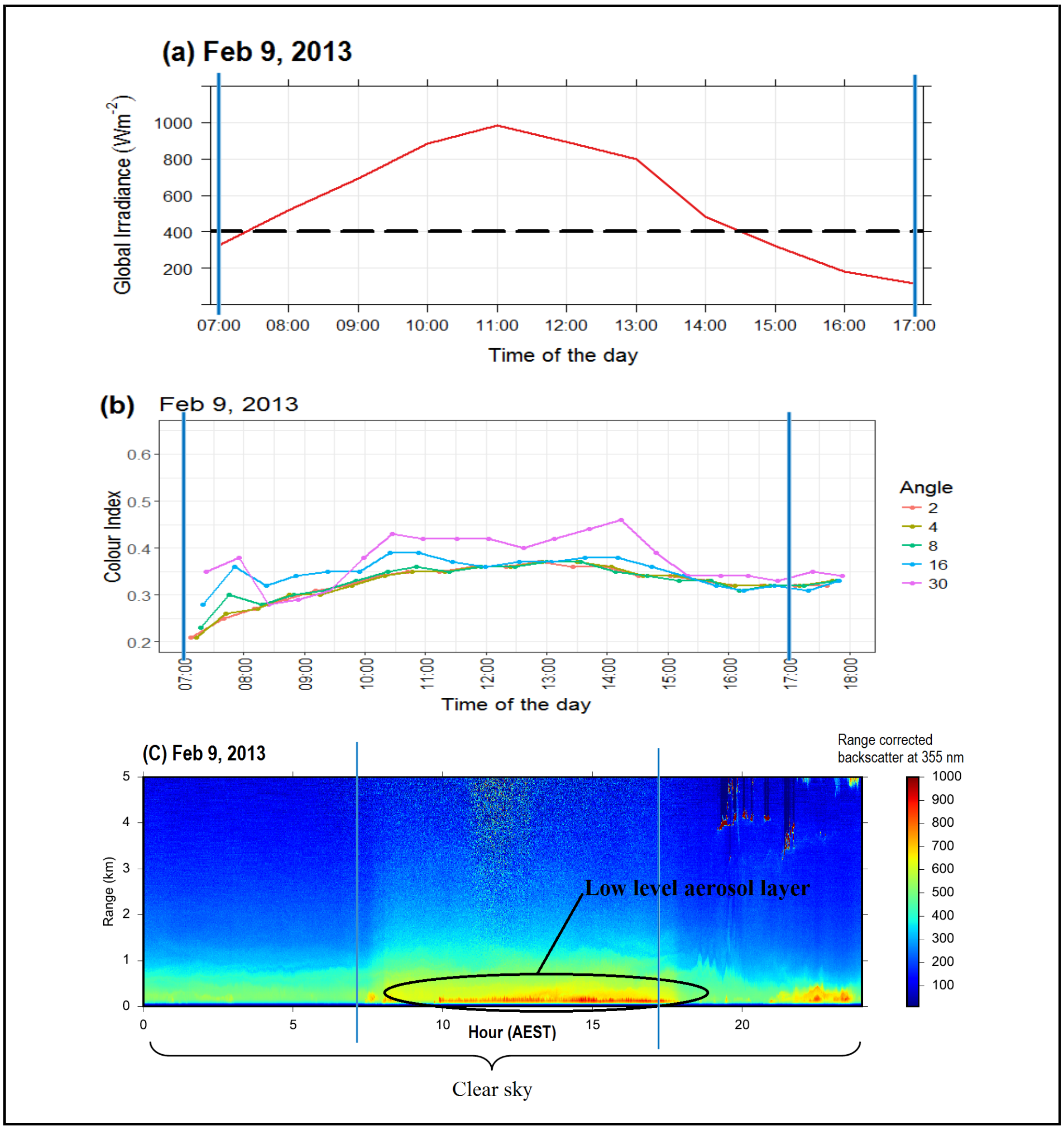

Fig. 5.4: 9th February 2013 (a) Time series of global irradiance. The dashed line represents the median value of the global irrandance from 16th January 2013 to 10th February 2013, from 7:00 and 17:00. (b) Colour index at five observation angles (2°, 4°, 8°, 16° and 30°). (c) LIDAR backscatter signal. Range-normalised backscatter (indicated by the colour scale, red indicates higher backscatter). Colour scale represents the range corrected backscatter at 355 nm. Corrected backscatter refers to correction for the optical geometry. The two solid blue vertical lines represent the time period of interest (7:00 and 17:00).

5th February 2013: The 5th of February 2013 can be separated into two periods which are indicated by (I)AM and (II) PM (Fig. 5.5). For the period (I)AM, prior to 10:30, the global irradiance increased steadily and reached the median value after 8:00 (Fig. 5.5 (a)). Colour index values were inconsistent (Fig. 5.5 (b)) and LIDAR backscatter shows the presence of broken clouds (Fig. 5.5 (c)). The colour index and LIDAR backscatter indicates the presence of broken clouds. However, observations from the global irradiance are consistent with clear skies in the early morning of 5th

February 2013 (period (I) AM). After 11:00 (period (II) PM), the global irradiance observations were above the median value. The colour index values were consistent and LIDAR backscatter signal was strong indicating clear skies. Observation from three instruments show that there were clear skies in this later period on this day (period (II) PM).

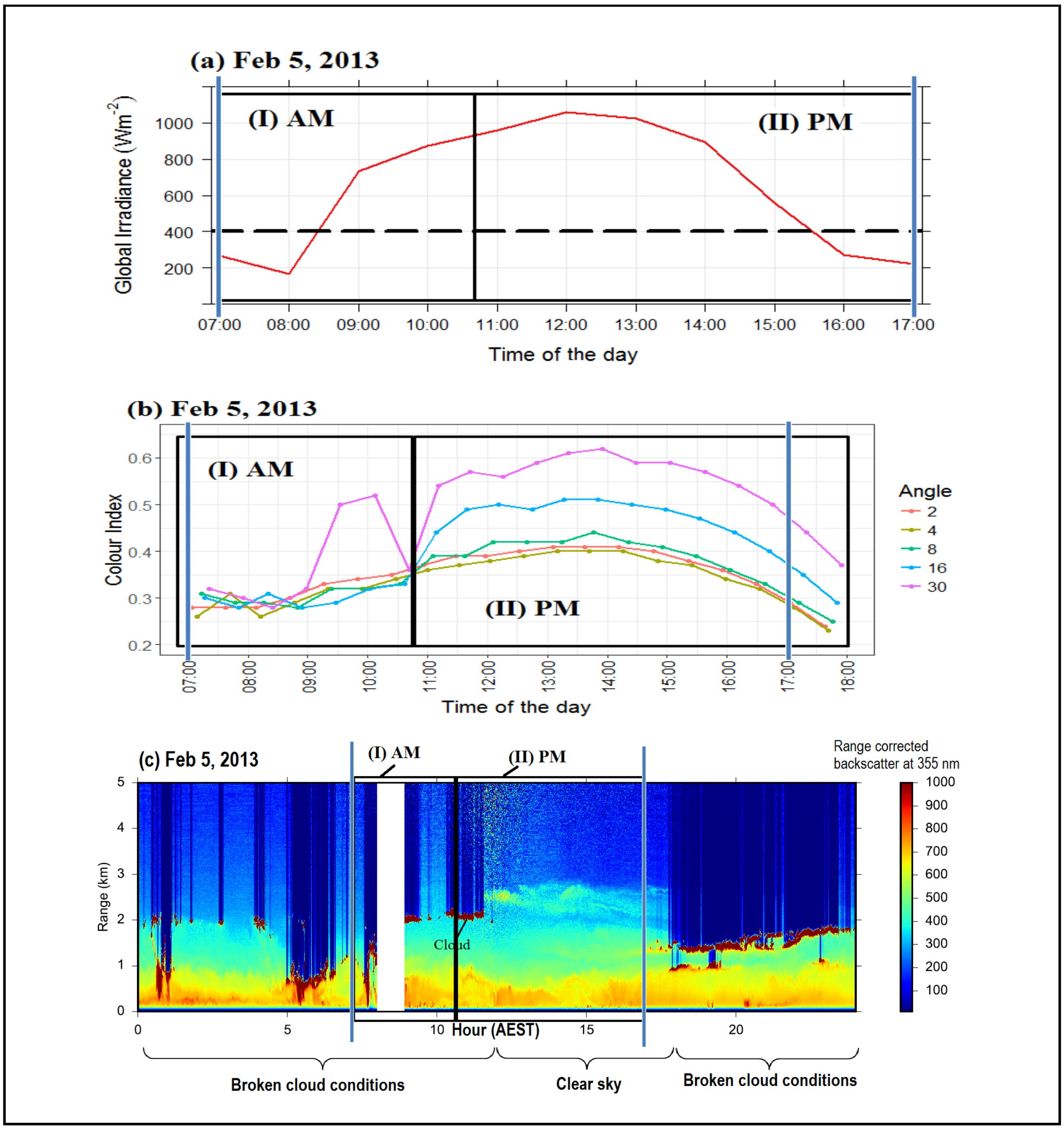

Fig. 5.5: 5th February 2013 (a) Time series of global irradiance. The dashed line represents the median value of the global irradiance from 16th January 2013 to 10th February 2013, from 7:00 and 17:00. (b) Colour index at five observation angles (2°, 4°, 8°, 16° and 30°). (c) LIDAR backscatter signal. Range-normalised backscatter (indicated by the colour scale, red indicates higher backscatter). Colour scale represents the range corrected backscatter at 355 nm. Corrected backscatter refers to correction for the optical geometry. The rectangular black box in Fig. (a) and (b) highlights two periods (I) AM and (II) PM. The two solid blue vertical lines represents the interested time period (7:00 and 17:00).

5.3.3 Determination of Aerosol Loading

Aerosol loading at ground level during MUMBA campaign was determined using the particle number concentration for particles ranging in size from 14 nm to 660 nm ($PNC_{14nm-660nm}$) and the fine particle mass (with an aerodynamic diameter of less than 2.5 µm, $PM_{2.5}$). Both measurement were made at the main measurements site during the MUMBA campaign (Fig. 2.1(a)). The median value of the concentration of $PNC_{14nm-660nm}$ (3500 cm^{-3}) and $PM_{2.5}$ (5 $\mu g\, m^{-3}$) were used as cut-off values. A "high" or "low" aerosol loading is when both the concentrations of $PNC_{14nm-660nm}$ and $PM_{2.5}$ were greater or lower than the cut-off value, respectively. Example of days that experienced "high" aerosol loading include the 28^{th} January 2013 and 9^{th} February 2013, whereas 5^{th} February 2013 experienced "low" aerosol loading (Fig. 5. 6). These three days are used in the discussion in Section 5.3.5.

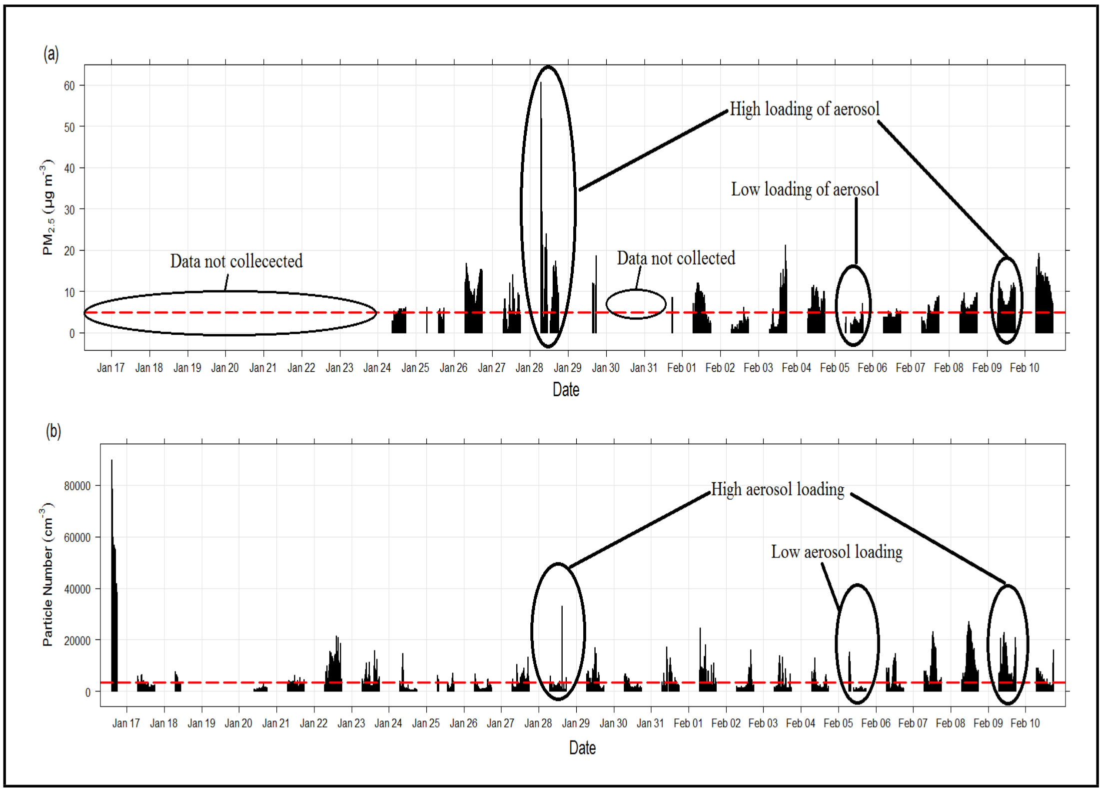

Fig. 5.6: Hourly time series of (a) $PM_{2.5}$ and (b) $PNC_{14nm-660nm}$ during MUMBA campaign. $PM_{2.5}$ measured from 24^{th} January 2013 to 15^{th} February 2013. $PNC_{14nm-660nm}$ measured from 16^{th} January 2013 to 10^{th} February 2013. The red dashed line represents the median value of $PM_{2.5}$ (5 $\mu g\, m^{-3}$) and $PNC_{14nm-660nm}$ (3500 cm^{-3}).

5.3.4 Overview on Differential Slant Column Density (DSCD)

The DSCDs from MAX-DOAS followed the general rule that the lower observation angles give a higher observation signal for trace gases in the lower troposphere [*Lee* *et al.*, 2009b; *Sinreich et al.*, 2013; *Wang et al.*, 2016b]. Therefore, in this work, observations at 2° and 4° were more sensitive to conditions in the lower layer of the atmosphere (close to the ground surface). Meanwhile, observations at 16° and 30° were more sensitive to measurements at higher layers of the atmosphere (above the ground surface). The characteristics of O_4 DSCDs at five elevation angles were studied and are illustrated in the Box-and-whisker plot (Fig. 5.7). Hourly averaged O_4 observations between 7:00 and 17:00 covering the period from 16th January 2013 to 10th February 2013 demonstrated higher values of O_4 DSCDs at lower viewing angles compared to the higher angles (Fig. 5.7). The O_4 DSCD values measured at 2° were approximately double the O_4 DSCD values measured at 30°. Similar observations were reported in a study by *Gratsea et al.* [2016], which focused on slant column measurements in the urban environment of Athens.

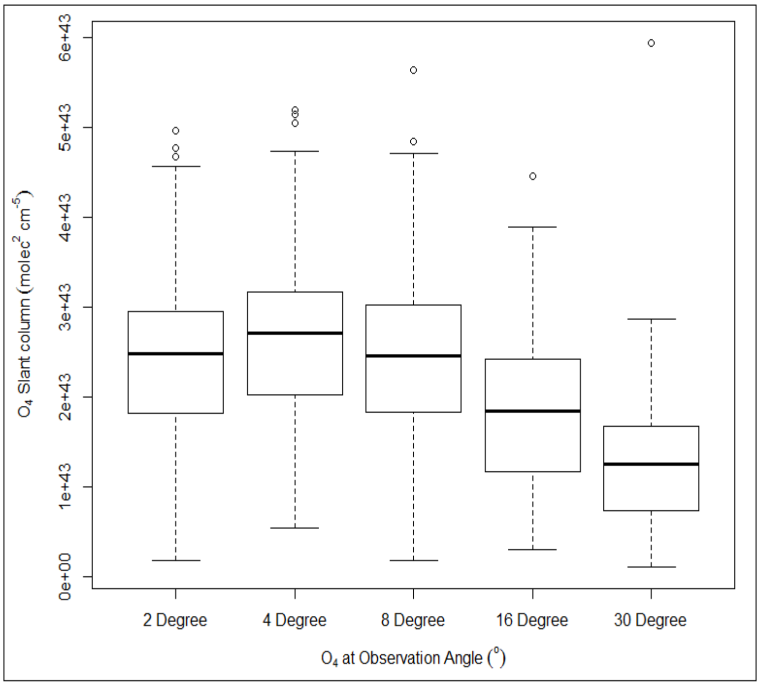

Fig. 5.7: Box-and-whisker plot of O_4 DSCD at five observation angles of 2°, 4°, 8°, 16° and 30°. Hourly averaged observations between 7:00 and 17:00 covering the period from 16th January 2013 to 10th February 2013 are shown. The central line of each box is the median and the edges of the box are the lower and upper quartiles (25% and 75%). The whiskers represent the most extreme data points which are no more than 1.5 times the length of the box from either end of the box. The circles are those values beyond the extremes of the whiskers.

5.3.5 Daily Average of O_4 DSCDs

Daily averages of O_4 DSCDs were plotted (Fig. 5.8) to asses how the O_4 DSCDs pattern depends on viewing conditions. O_4 DSCDs at lower viewing angles (2° and 4°) show an apparent separation from the O_4 DSCDs observed at higher viewing angles (16° and 30°) (Fig. 5.8). However, on some days the average retrievals converge. This can be caused by effects of aerosol loading and cloud conditions [*Gratsea et al.*, 2016]. Both high aerosol loadings and clouds decrease the path length of the scattered sunlight on average and therefore, decrease the O_4 DSCDs [*Heckel et al.*, 2005; *Sinreich et al.*, 2013; *Wagner et al.*, 2004].

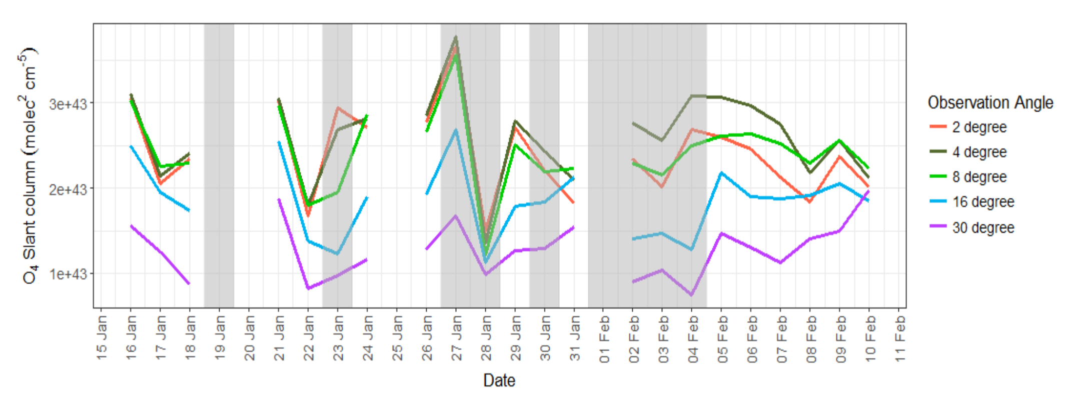

Fig. 5.8: Daily averages of O_4 DSCDs at five observation angles (i.e. 2°, 4°, 8°, 16° and 30°). Daily averaged observations between 7:00 and 17:00 covering the period from 16^{th} January 2013 to 10^{th} February 2013 are shown. The shaded areas refer to cloudy days as determined by the methods discussed in Section 5.3.2.

The characteristics of daily averaged O_4 DSCDs observations from MAX-DOAS were then categorised visually into four situations in order to study the influence of aerosol loading and clouds on the behaviour of the O_4 DSCDs measurements at different observation angles. Determination on the "cloudy" or "clear" and "high" or "low" aerosol loading periods have been discussed in Section 5.3.2 and Section 5.3.3, respectively. The four situations were as follows:

(i) high aerosol loading and a cloudy period (28^{th} January 2013);

(ii) high aerosol loading and a clear period (9^{th} February 2013);

(iii) low aerosol loading and a cloudy period (5^{th} February 2013) and

(iv) low aerosol loading and a clear period (5^{th} February 2013).

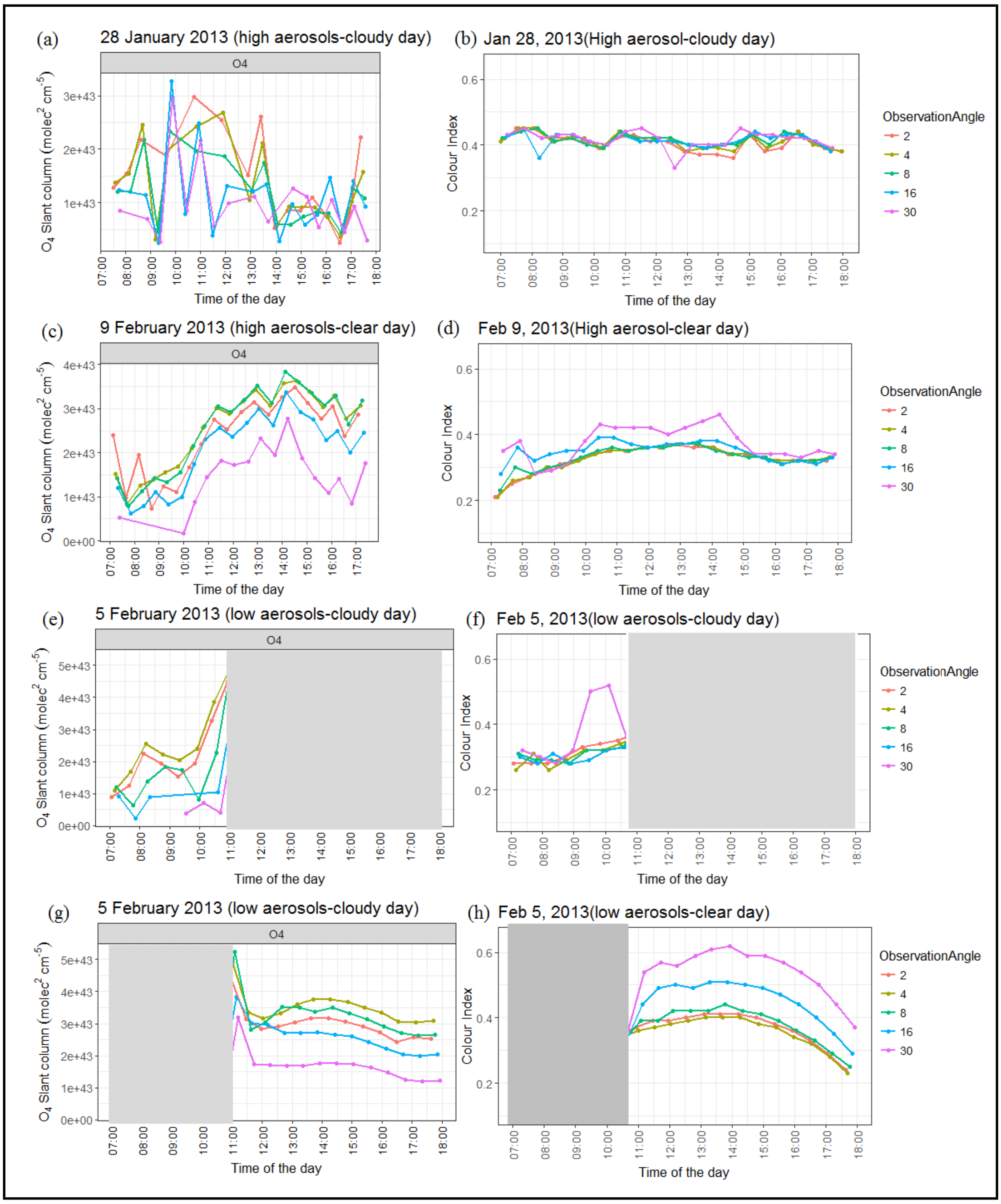

Fig. 5.9: Time series of O_4 DSCD observations and colour Index at five observation angles (2°, 4°, 8°, 16° and 30°) on the 28th January, 2013, 9th February, 2013 and 5th February, 2013. The rectangular shaded areas on the 5th February, 2013 highlight two situations chosen :Fig. (e) and (f) are observations for “low aerosol loading and cloudy day”, Fig. (g) and (h) are observations for “low aerosol loading and clear day”. Measurement data from 7:00 to 17:00 were used in these plots.

Retrievals of O_4 DSCDs observed on the 28th January 2013 were similar at all angles Fig. 5.9(a)) as was the colour index (Fig. 5.9(b)). This observation can be caused by the high population of aerosols and the presence of clouds which increase the scattered sunlight on average and caused the variability in the observed O_4

DSCDs at different viewing angles. O_4 DSCDs observed on the 9^{th} Feb 2013 shows two behaviours, where O_4 DSCDs at lower anglesat lower angles (2° and 4°) were close together but separated from observations at higher viewing angles (16° and 30°)(Fig. 5.9(c)). This was also observed in the time series of the colour index (Fig. 5.9(d)).

The colour index values observed in the morning of the 5^{th} February were variable (Fig. 5.9(f)) with no clear pattern relating O_4 DSCDs to observation angles (Fig. 5.9(e)). This outcome is due to the presence of broken clouds which causes inconsistency in the observed signals and therefore produces inconsistent O_4 DSCDs at different viewing angles and times. In contrast, retrievals of O_4 DSCDs and colour index values at all viewing angles were well separated in the afternoon (Fig. 5.9(g, h)). This is due to the clear sky and low aerosol population during this period.Similar observations were obtained by *Ortega et al.* [2016] on the east coast of North America (over Cape Cod, MA, U.S.) and also by *Heckel et al.* [2005] in the Po-Valley in northern Italy.

5.3.6 Diurnal Variation of O_4 DSCDs and Surface Aerosol Extinction

Daily pattern of O_4 DSCDs retrieval at all observation angles were compared with the surface aerosol extinction retrieved by HEIPRO in this section in order to answer the question "is it possible to use DSCD′s to infer aerosol properties?" Surface aerosol extinction used here refers to the aerosol extinction at 200 m and below as retrieved from the HEIPRO analysis. Retrieval of O_4 DSCDs revealed a diurnal pattern at all viewing angles, with low values in the morning that steadily increased until mid-afternoon and then decreased (Fig. 5.10 (a) to (e)). O_4 DSCD observations are negatively correlated to aerosol population. Therefore, high O_4 DSCD accompanies a low aerosol loading. The surface aerosol extinction shows an inverse pattern (Fig. 5. 11 (b)) compared with O_4 DSCD. The daily variation of total particle number concentration (N_T) and the possible sources of aerosols such as combustion markers CO and NO_x that are shown in Chapter 3. Generally, there were low concentrations of total particle number concentration (N_T), CO and NO_x observed in the middle of the day (Fig. 3.3 (a), and Fig. 3.7). Meanwhile, both diurnal variation pattern of particle mass ($PM_{2.5}$) measured *in-situ* (Fig. 5.11(a)) and surface aerosol extinction (Fig. 5.11(b)) from 24^{th} January to 10^{th} February 2013 show that there were high aerosol concentrations in the morning and low concentrations in the middle of the day. This indicates that DSCD′s can be used to infer aerosol properties during the MUMBA campaign.

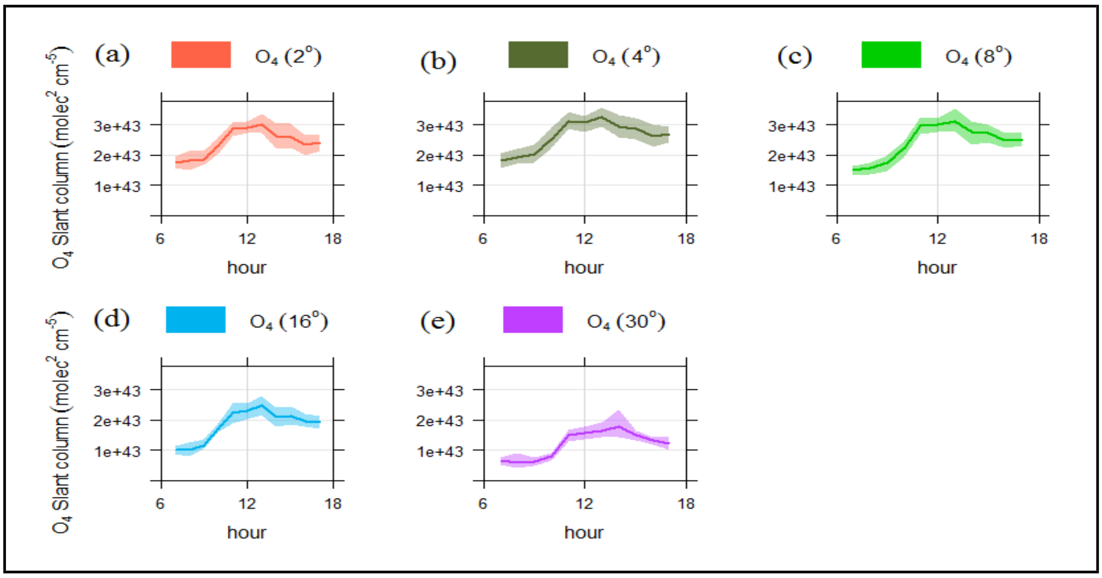

Fig. 5.10: Fig. (a) to (e) are the diurnal variations of O_4 DSCD observations at five elevation angles (2°, 4°, 8°, 16° and 30°). Observations from 7:00 to 17:00 were used to interpret the result. Hourly averaged data from 16^{th} January to 10^{th} February 2013 are used in these plots.The shaded area is the 95 % confidence interval.

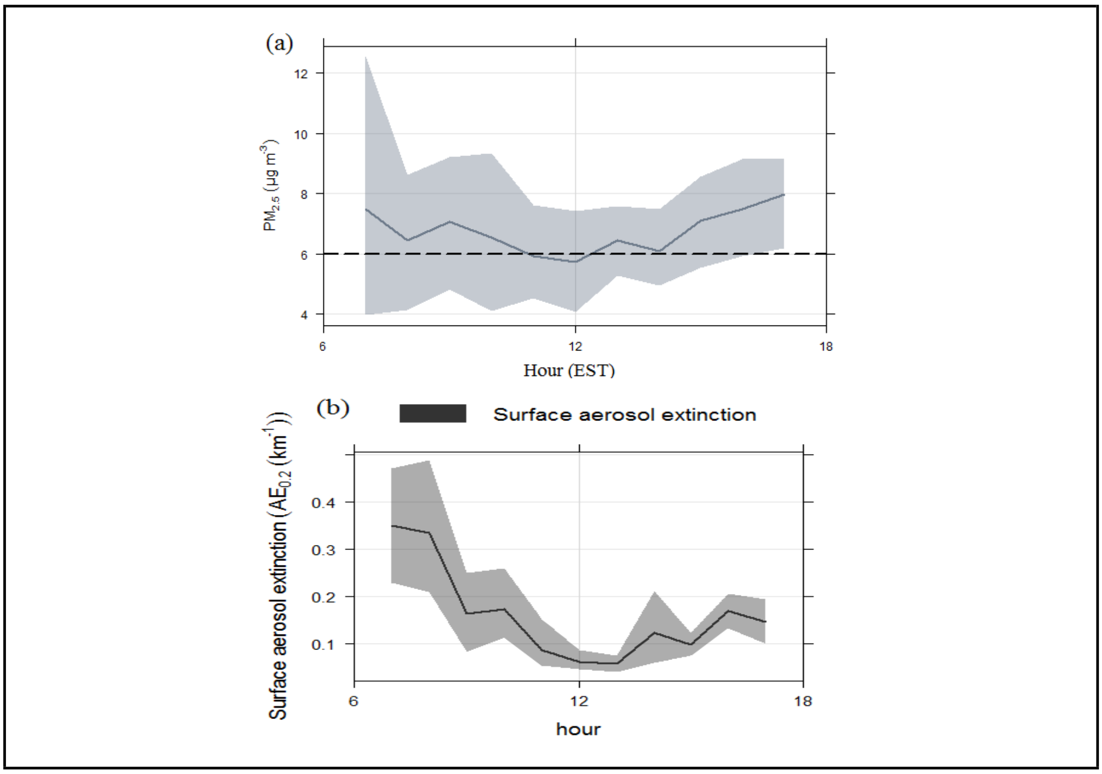

Fig. 5.11: Diurnal variations of (a) in-situ measurements of $PM_{2.5}$ and (b) surface aerosol extinction at 200 m and below retrieved from the HEIPRO analysis. Hourly averaged data from 24th January to 10th February 2013 from 7:00 to 17:00 are used for these plots. The black horizontal dashed line is the average value of the $PM_{2.5}$ from 7:00 to 17:00 over the measurement period. The shaded area is the 95 % confidence level.

5.3.7 Characteristics of Aerosol Extinction Coefficients

AOD information was retrieved by using the O_4 DSCDs information obtained from the QDOAS analysis into the aerosol inversion algorithm (HEIPRO) as discussed in Chapter 2. The aerosol optical depth information retrieved by HEIPRO was compared with measurements by the sun photometer and the LIDAR to investigate the correlation between them.

(a) Relationship of aerosol optical depth from MAX-DOAS and the sun photometer

The sun photometer produced an estimate of aerosol optical depth at one minute resolutions. Cloud filter analysis was applied on the dataset using the method described by *Harrison and Michalsky* [1994]. Overall, there was a poor correlation between hourly averaged AOD from the MAX-DOAS and the sun photometer (R^2= 0.03, number of points = 199) (Fig. 5.12 (a)). Observation of the available data from both instruments illustrated that the AOD retrieved were predominantly less than 0.2. A study in Madrid, Spain by *Wang et al.* [2016b] reported a good agreement between hourly retrieved AODs and MAX-DOAS and the sun photometer in the Aerosol Robotic Network (AERONET) with $R^2 = 0.87$ (number of data points = 618). Aerosol optical depths retrieved by *Wang et al.* [2016b] were predominantly less than 0.6. Madrid is the third largest city in the European Union and experiences severe levels of air pollution by nitrogen dioxide, suspended particulates and ozone *Council* [2012]. In contrast to the air pollution level experienced during the duration of study by *Wang et al.* [2016b], the MUMBA sampling site experienced clean air [*Paton-Walsh et al.*, 2017] with low daily average and always below the the Australian National Environment Protection (Ambient Air Quality) Measure (Air NEPM) recommended daily average value of 25 $\mu g\, m^{-3}$.

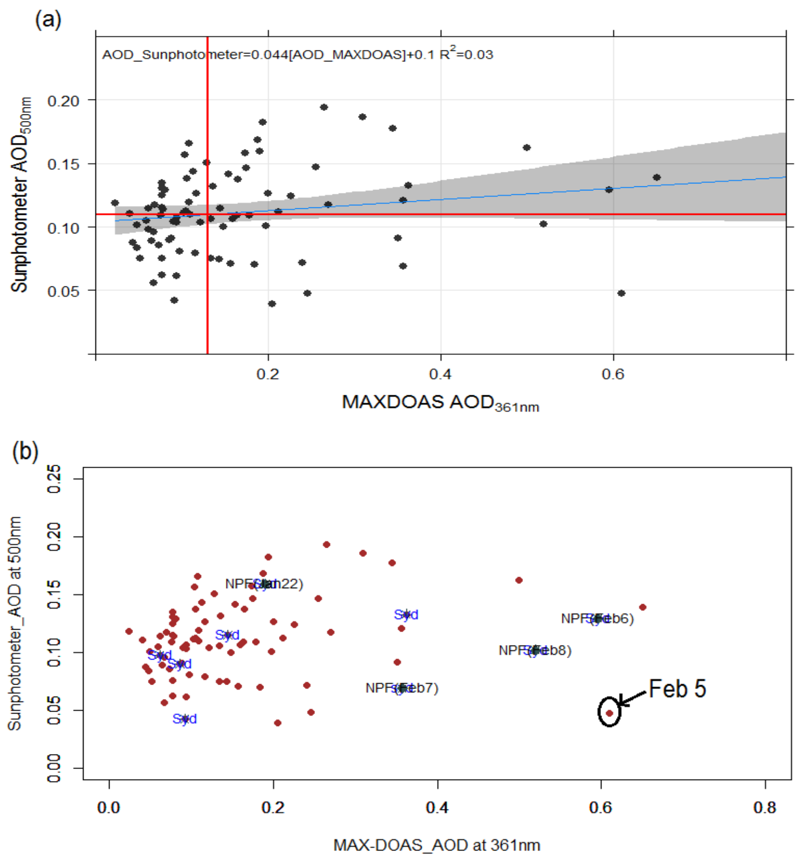

Fig. 5.12: (a) Relationship between aerosol optical depth (AOD) obtained from the MAX-DOAS and the sun photometer. The shaded area is the 95 % confidence level. The solid horizontal and vertical lines are the median value of AOD measured by the sun photometer (0.11) and AOD measured by MAX-DOAS (0.13), respectively. (b) The AOD obtained from MAX-DOAS and the sun photometer in relation to "Sydney air mass" (presented as "Syd") and particle formation and growth events (presented as "NPF"). Hourly averaged data from 7:00 to 17:00 from 16^th^ January to 10^th^ February 2013 were used.

One of the factors that can contribute to the weak correlations is the different location and viewing geometry of the MAX-DOAS and the sun photometer instruments. As mentioned earlier (Section 5.1), the MAX-DOAS was located at the second monitoring site (Fig. 2.1(b)) and the sun photometer instrument was located at the University of Wollongong (Fig. 2.1(b)). Therefore, AOD retrieved from the MAX-DOAS can be more readily affected by the marine environments.

Another factor that can contribute to the poor correlation of AOD from the MAX-DOAS and the sun photometer is the different wavelength used in the MAX-DOAS and the sun photometer measurement. AOD values from the MAX-DOAS were retrieved at 361 nm whereas sun photometer AOD measurements were made at 500 nm. $\mathring{A}$ngstrom turbidity coefficient (β) described by *Iqbal* [1983] and *Ångström* [1929] have describes the AOD dependence on wavelength as (Eq. 5.3):

$$\tau = \beta\lambda^{-\alpha} \tag{5.3}$$

where $\tau=$ aerosol optical depth for wavelength, λ (in micrometers) and $\alpha=$ corresponding $\mathring{A}$ngstrom exponent value. *Iqbal* [1983] reported the typical range of α is from 0.5 to 2.5. By using equation 5.4, when $\alpha = 0.5$, the ratio is 0.85 and for when $\alpha = 1$, the ratio is 0.72. This effect could be large but not large enough to contribute to a poor correlation of AOD from the MAX-DOAS and the sun photometer observed in this work.

$$(\frac{\tau_{500nm}}{\tau_{361nm}}) = (\frac{500nm}{361nm})^{-\alpha} \tag{5.4}$$

Wind direction was then studied to investigate the potential for an impact of pollution at the monitoring site, by running 24-hr backward trajectories. Here, air masses that arrived at the monitoring site at 10:00 AEST from the north and north-east sectors are labelled with “Syd” to represent Sydney air mass (Fig. 5.12(b)), as air from this sector is likely to have traversed Sydney prior to reaching the monitoring site. 10:00 AEST was chosen because the particle formation and growth event days (Class I and Class II) were observed at this time. Overall, observations of the “Sydney Air Mass” varied over a wide range.

In relation to the particle formation and growth events, all the Class I particle formation and growth events were observed when AOD values measured from MAX-DOAS were ≥ 0.2 (as “NPF” in Fig. 5.12(b)). MAX-DOAS also retrieved high AOD values (AOD > 0.5) when the monitoring site experienced air masses from Sydney (Fig. 5.8(b)). One of these AOD >0.5 observations was on the 5^{th} February 2013 at 10:00 AEST. Interestingly, this was not apparent in the sun photometer measurements (Fig. 5.12(b)). At this time, the 24-hr backward trajectories demonstrated that wind direction was from the southeast sector. To investigate the cause of this observation, the cloud conditions on the 5^{th} February 2013 was studied (Fig. 5.5). As discussed in section 5.3.2, the global irradiance measurements obtained from the sun photometer indicate it was a clear period at 10:00 AEST. However, colour index and values which were calculated from the intensity measured by MAX-DOAS indicate the presence of broken clouds at 10:00 AEST and similar observation showed by LIDAR backscatter. The higher value of AOD retrieved from MAX-DOAS compared with the AOD retrieved from the sun photometer may have been caused by cloud effects at this time of the day.

(b) Aerosol Optical Depth retrieval on a clear day

The relationship between AOD retrievals from the MAX-DOAS, the LIDAR and the sun photometer instruments on a “clear day” (7^{th} of February 2013) were examined. The “clear day” was selected based on the analysis as discussed in Section 5.3.2. Hourly averaged data from 7:00 to 17:00 were chosen due to the different time scales, location and the principles of the measurement used in the three instruments.

There was a good correlation between the AOD obtained from LIDAR (measurement made at 335 nm) and the sun photometer (measurements made at 500 nm) instruments with a R^2 of 0.96 (Fig. 5. 13 (a)). The slope of 1.1 in the linear regression between the LIDAR and the sun photometer indicates that the LIDAR ratio value (25 sr) used in this study (as mentioned in Section 5.1) worked well for the marine environments during the MUMBA campaign. In contrast, there was poor correlation between the AOD obtained from the MAX-DOAS retrievals at 361 nm and the other two instruments (LIDAR and sun photometer) (Fig. 5.13(b) and (c)). This poor correlation could be attributed to the difference in the principles of the viewing geometry of these three instruments. Another factor that could have caused this result is the sensitivity of MAX-DOAS measurements decrease significantly with altitude [*Frieß et al.*, 2006].

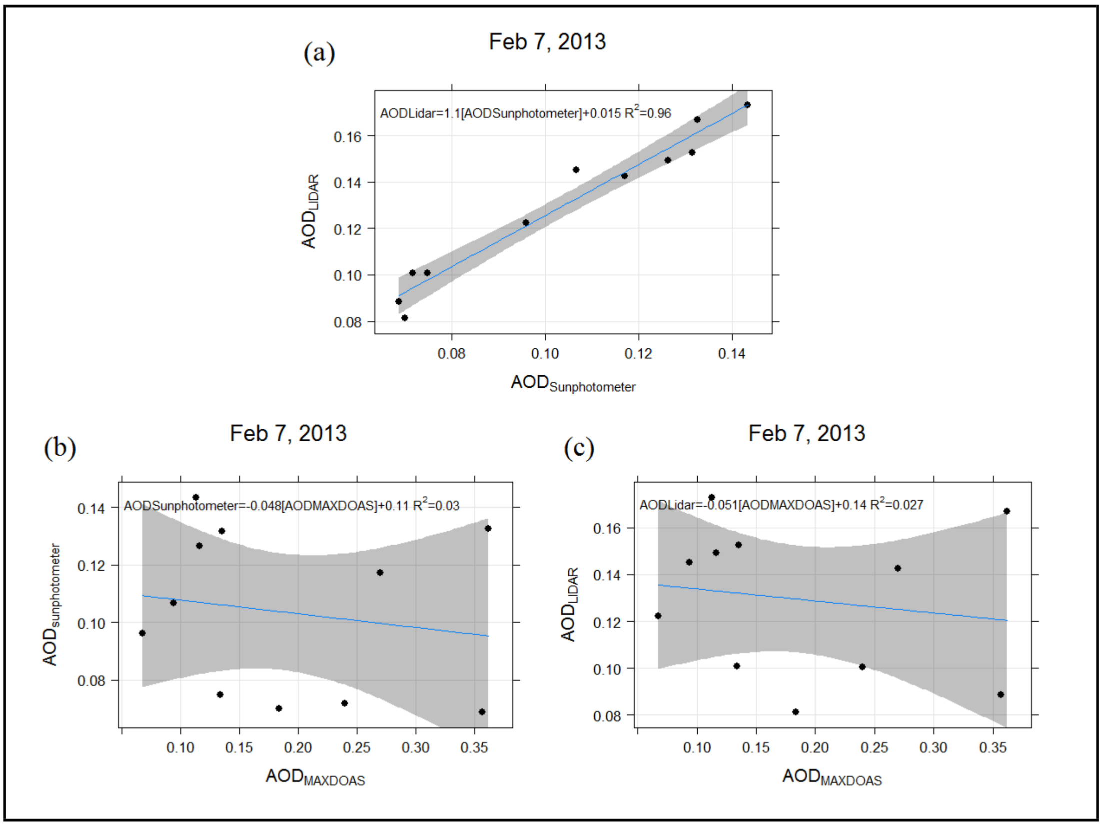

Fig. 5.13: Relationship between AOD from the (a) LIDAR and sun photometer, (b) sun photometer and MAX-DOAS and (c) LIDAR and MAX-DOAS instruments on the 7^{th} February, 2013. The 7^{th} February, 2013 is used to present the "clear day". Hourly averaged data from 7:00 to 17:00 were used in these plots.

The vertical profile of aerosol extinction retrieved from MAX-DOAS and the backscatter aerosol extinction from LIDAR were plotted in order to investigate the reproducibility of the aerosol vertical distribution on the 7^{th} February 2013 at around 8:00 AES when the sky was clear (Fig. 5.14 (a)). A strong correlation (R^2= 0.77) was obtained between the estimates of the vertical resolved aerosol extinction from the MAX-DOAS and LIDAR. Both instruments recorded the strongest extinction at approximately 300 m height (the brown line) (Fig. 5.14 (b)). However, there was a large difference in the magnitude of the extinction. This might be caused by the viewing angle which makes a difference in the the sampling area/environment measured by the MAX-DOAS and LIDAR instruments as discussed in Section 5.3.7 (a). Another factor that can cause the large different in magnitude is the sensitivity of MAX-DOAS retrieval decreasing with higher altitudes in the atmosphere. MAX-DOAS is sensitive to trace gases and aerosol concentration over the 2-3 km of the atmosphere. The presence of clouds at lower altitudes out the sea (< 2 km) during the measurements can lead to an overestimation of MAX-DOAS aerosol extinction due to a multiple scattering effect [*Irie et al.*, 2008; *Wagner et al.*, 2004]. The type of *a priori* used in aerosol retrieval in this work can also contribute significantly to the results [*Ryan et al.*, 2018; *Xing et al.*, 2017].

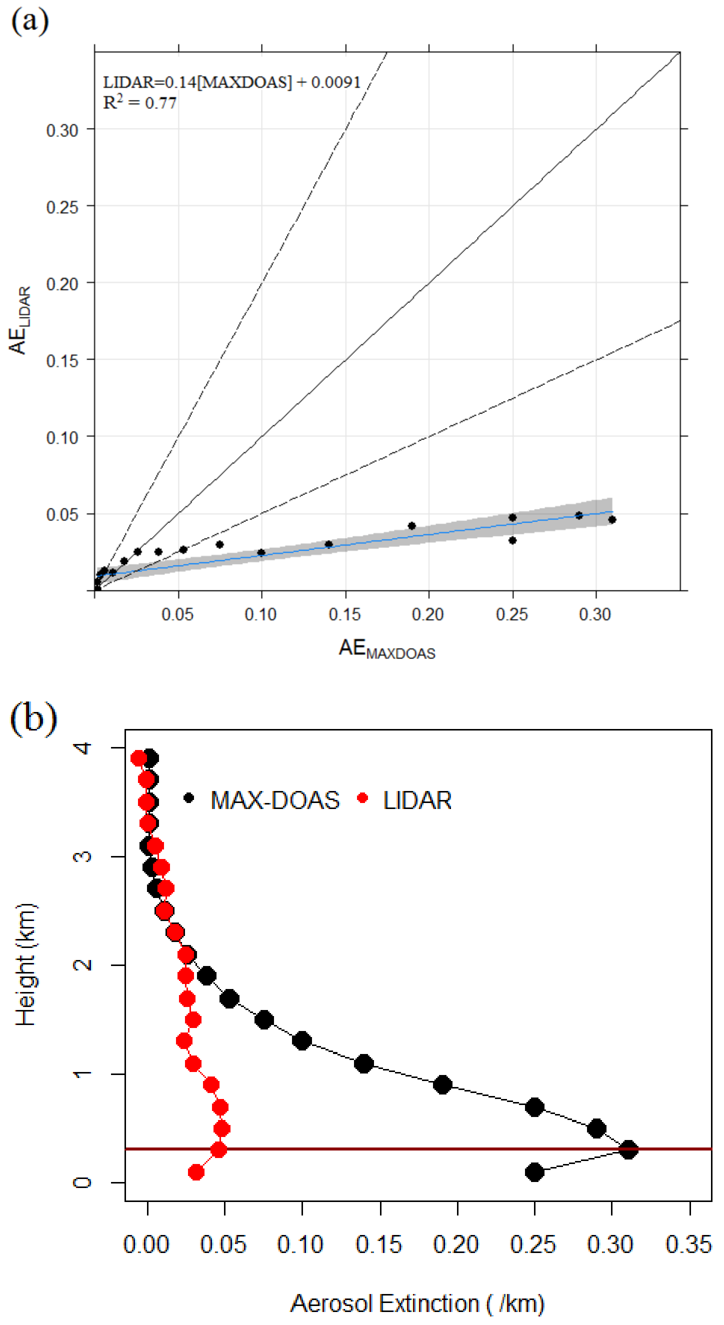

Fig. 5.14: (a) Relationship between aerosol extinction (AE) from the MAX-DOAS and the LIDAR instruments. The 1:1 line is represented by a solid black line. The dashed black line above and below the 1:1 line are the 1:2 and 1:0.5 lines, respectively. (b) Comparison of vertical aerosol distribution profiles from the MAX-DOAS and the LIDAR instruments. The brown line is the strongest extinction at 300 m. Data on the 7th February 2013 at around 8:00 were used in these plots.

5.3.8 Relationship between MAX-DOAS Retrieval and *In-situ* Measurements

(a) Surface Aerosol Extinction

In this section, the aerosol extinction retrieved by MAX-DOAS for the lowest levels of the atmosphere (surface aerosol extinction) is compared to the particle mass concentration ($PM_{2.5}$) to investigate whether MAX-DOAS measurements reflect the observed *in-situ* ground surface aerosol loading, similar to a study conducted in Madrid, Spain ([*Wang et al.*, 2016b]).

The particle mass concentration ($PM_{2.5}$) used by *Wang et al.* [2016b] was obtained from six in-situ air quality stations over Madrid city from 15th March, 2015 to 15th September, 2015. The surface aerosol extinction used by *Wang et al.* [2016b] refers to the aerosol extinction at 100 m and below as returned from the HEIPRO analysis. There was a good correlation (R= 0.89, number of days = 134) obtained between daily averaged data of $PM_{2.5}$ and surface aerosol extinction. The surface aerosol extinctions in this study refers to the aerosol extinction at 200 m and below as returned from the HEIPRO analysis. There was not a good correlation (R^2= 0.12, number of days=16) obtained between daily averaged data of $PM_{2.5}$ and surface aerosol extinction (Fig. 5.15).

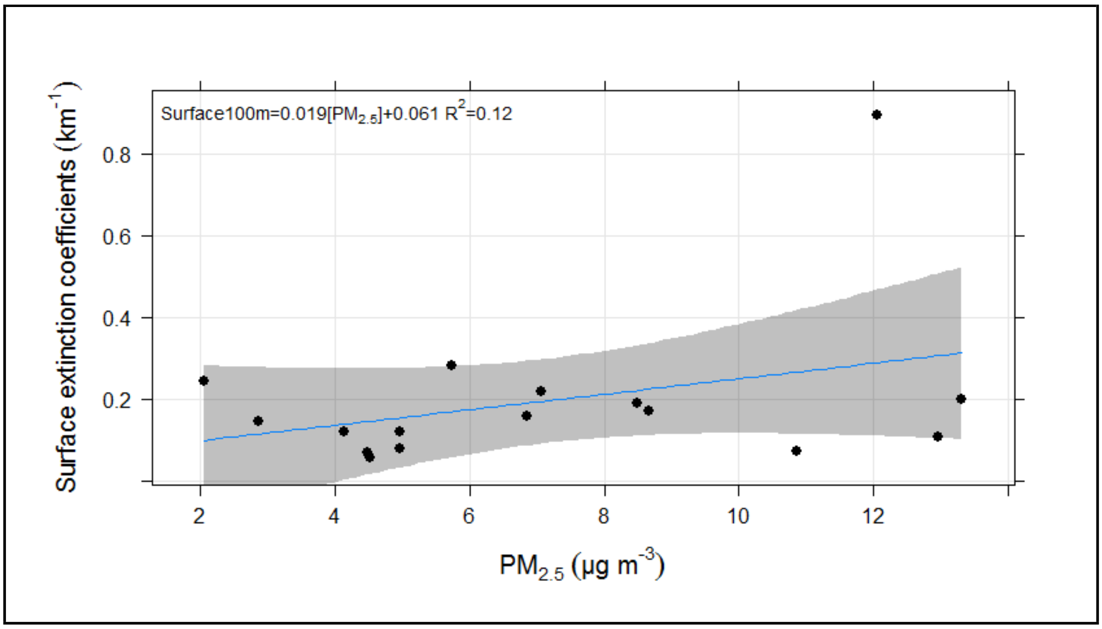

Fig. 5.15: (a) Relationship between surface aerosol extinction coefficients and particle mass concentration ($PM_{2.5}$). Daily averaged data from 24th January to 10th February 2013 were used in this plot.

Several factors can cause this poor correlation obtained during the MUMBA campaign. The $PM_{2.5}$ mass concentrations during MUMBA were low, where the daily average of $PM_{2.5}$ mass concentration ranged from 1.0 $\mu g\,m^{-3}$ to 22.1 $\mu g\,m^{-3}$ with a median value of 5.0 $\mu g\,m^{-3}$. In contrast, the $PM_{2.5}$ mass concentrations measured by *Wang et al.* [2016b] ranged from 5.0 $\mu g\,m^{-3}$ to 30.0 $\mu g\,m^{-3}$.

The poor correlation between surface aerosol extinction retrieved by MAX-DOAS and *in-situ* $PM_{2.5}$ mass concentration can also be caused by the observation area. During the MUMBA campaign, the MAX-DOAS and the eSampler instruments were not exposed to identical air masses. The MAX-DOAS instrument was pointed over the open ocean, while the eSampler was based on direct measurements at the ground surface. Therefore, aerosol retrievals from MAX-DOAS included information from marine sources such as sea salt aerosols. For *Wang et al.* [2016b], the MAX-DOAS instrument was pointer over the city of Madrid and the *in-situ* $PM_{2.5}$ mass concentrations were obtained from six *in-situ* automatic measuring stations which were located around the urban area of Madrid. Therefore, the MAX-DOAS and six *in-situ* automatic stations were exposed to similar air masses.

(b) Aerosol extinction on the Class I Particle formation growth events

The variation of aerosol extinction coefficients and particle number size distribution on the Class I particle formation and growth event days (discussed in Chapter 4) was also compared. This comparison could provide information on aerosol populations during the events. Backscatter aerosol distribution on the 7^{th} February, 2013 and the 8^{th} February, 2013 obtained from LIDAR were then compared visually with the aerosol extinction variability (Fig. 5.17 and Fig. 5.18). The events on 22^{nd} January, 2013 and 6^{th} February, 2013 were not included in this comparison because there were broken cloud conditions in the afternoon and in the morning, respectively which are likely to affect both the MAX-DOAS and LIDAR measurements. The time series of global irradiation and colour index on the 7^{th} February, 2013 and the 8^{th} February, 2013 are presented in Fig. 4.7 and Fig. 5.16, respectively.

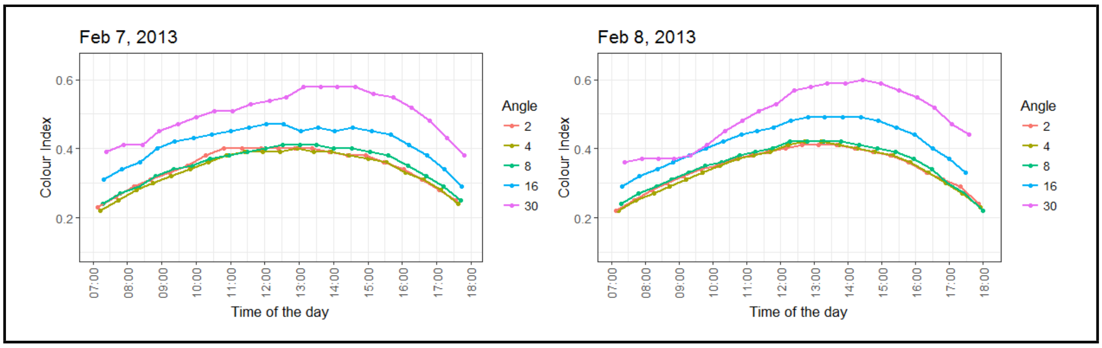

Fig. 5.16: Colour index variability at five observation angles (i.e. 2°, 4°, 8°, 16° and 30°) on the 7^{th} February, 2013 and the 8^{th} February, 2013. Measurements from 7:00 to 17:00 were used in these plots.

Contour plots of vertical aerosol extinction and backscatter aerosol distribution on the 7th February, 2013 and the 8th February, 2013 are illustrated in Fig. 5.17 and Fig. 5.18, respectively. In general, both instruments show the presence of an aerosol layer close to the ground but little other structure.

The Class I event days were observed when the monitoring station experienced particles with diameters less than 150 nm (Chapter 4) which explains the weak-moderate signal. Ultrafine particles (particles with diameter less than 100 nm) scatter ultraviolet radiation weakly by remote sensing techniques[*Junkermann and Hacker*, 2018]. Therefore, neither technique is very sensitive to small particles.

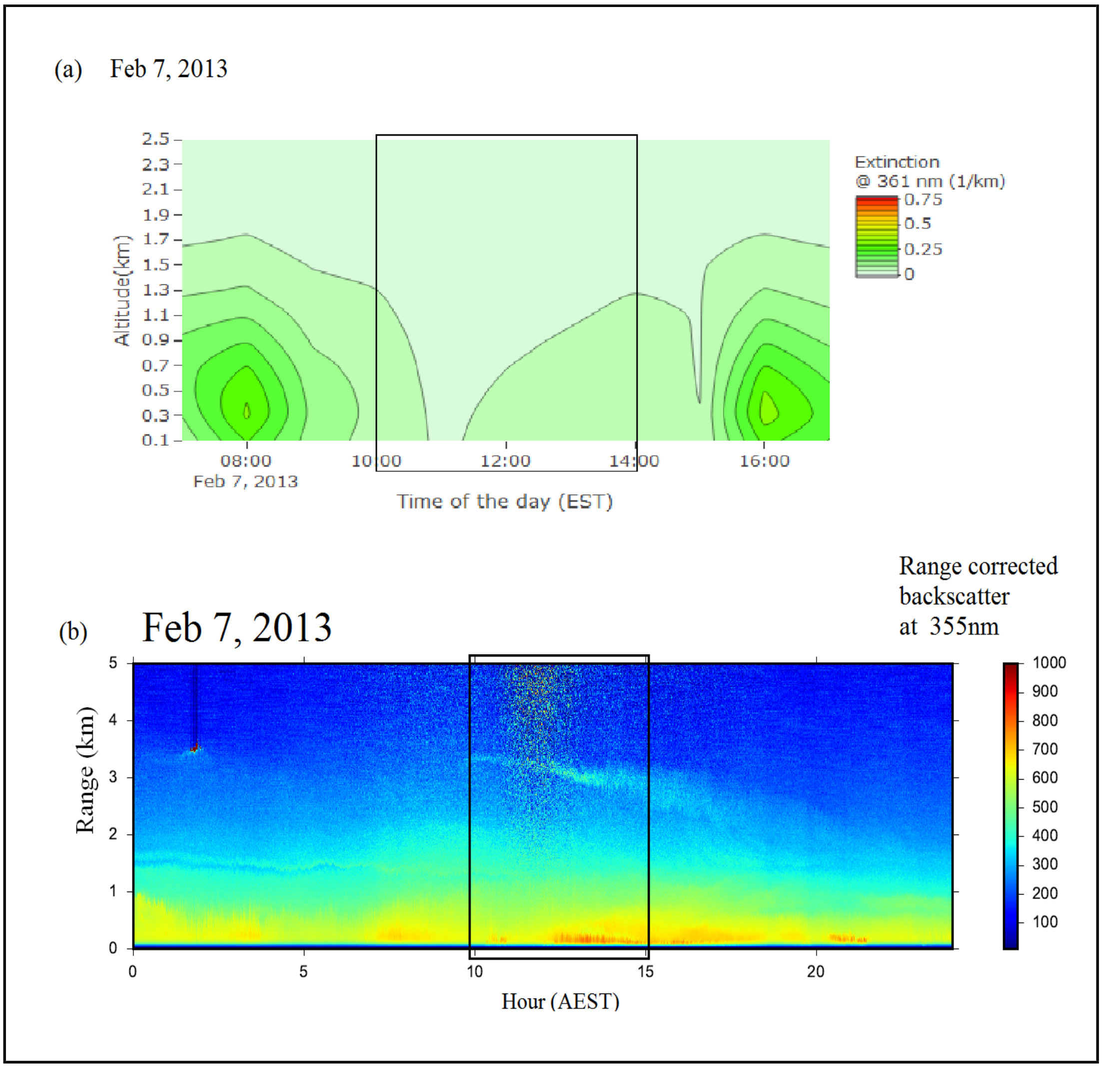

Fig. 5.17: Feb 7th, 2013 (a) variability of vertical aerosol extinction over time retrieved by HEIPRO at 361 nm. (b) Range-normalised backscatter measured by LIDAR at 355 nm. The colour scale represents the range of the signals (indicated by colour scale, red indicates higher signal). The rectangular boxes with black lines represent the relevant time of particle formation events.

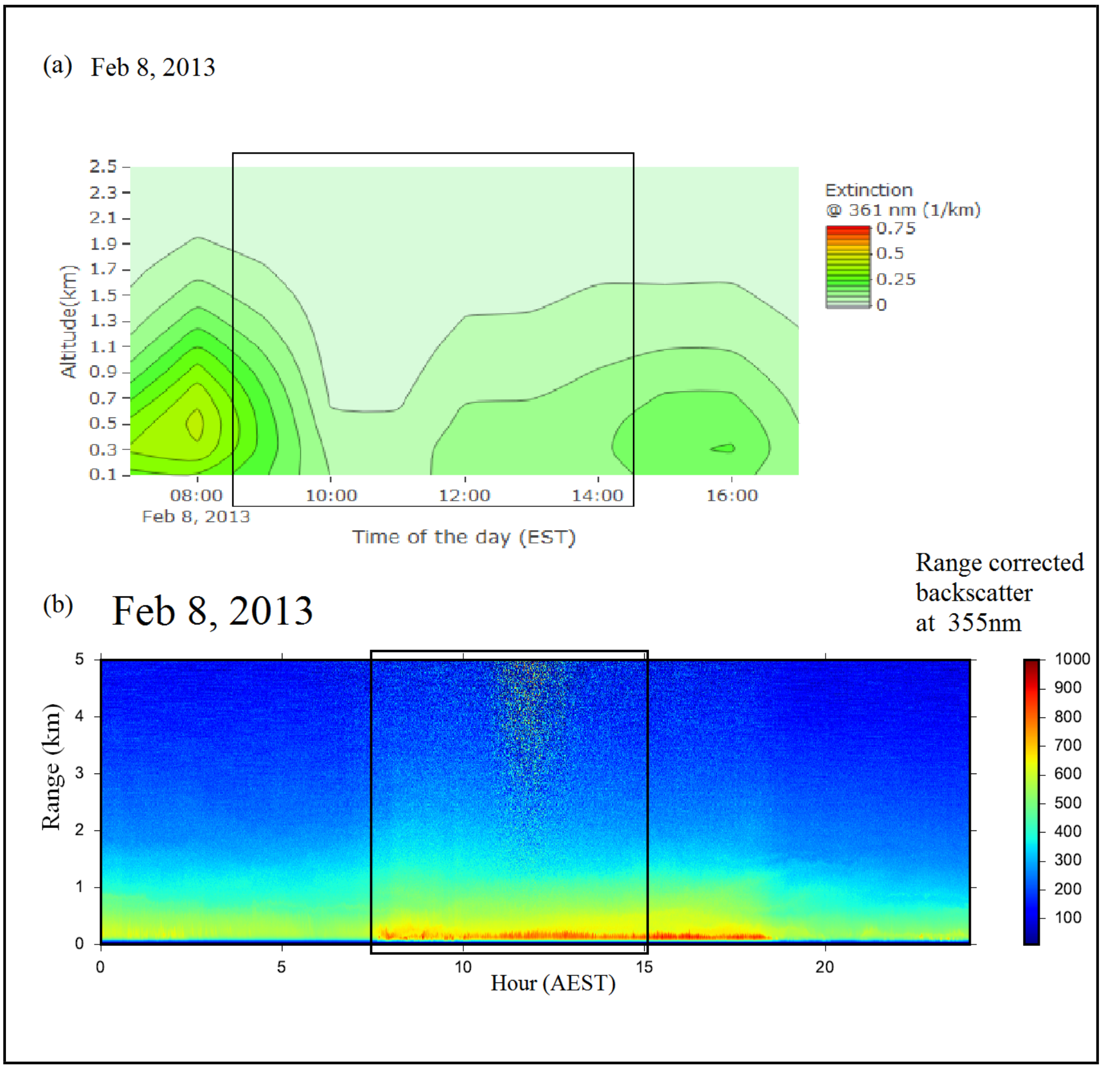

Fig. 5.18: Feb 8th, 2013 (a) variability of vertical aerosol extinction over time retrieved by HEIPRO at 361 nm. (b) Range-normalised backscatter measured by LIDAR at 355 nm. The colour scale represents the range of the signals (indicated by colour scale, red indicates higher signal). The rectangular boxes with black lines represent the relevant time of particle formation events.

5.4 Summary and Conclusions

This chapter presented a detailed study of the application of remote sensing techniques on aerosol properties during the aerosol measurements period of the MUMBA campaign. The following conclusions can be made:

(i) The MAX-DOAS instrument successfully retrieved aerosol properties, representing the first such retrievals by the research group and the first deployment of this instrument;

(ii) Differential slant column density (DSCD) can be used to infer changes in aerosol properties;

(iii) Aerosol optical depth retrieved from the MAX-DOAS and the sun photometer were weakly correlated. This is probably due to the difference in location and observation conditions;

(iv) Reproducibility of the LIDAR derived aerosol vertical distribution by the MAX-DOAS instrument was demonstrated on a clear day; and

(v) Surface aerosol extinctions (200 m height and below) retrieved from MAX-DOAS has a poor correlation with the in-situ $PM_{2.5}$ mass concentrations. This result is due in part to the low $PM_{2.5}$ concentrations observed during the aerosol measurement period.

Chapter 6

Summary and Conclusion

Aerosol measurements were conducted over the period of 16th January 2013 to 15th February 2013 in the coastal city of Wollongong, Australia during a campaign known as the Measurements of Urban, Marine and Biogenic Air (MUMBA). During the measurement period, the particle population as measured by number concentration was dominated by ultrafine particles ($\mathrm{PNC}_{3nm-100nm}$) with an average and median value of 7.0 x 10^3 cm^{-3} and 5.2 x 10^3 cm^{-3}, respectively. The average value of particle number concentration of the size of 14 nm to 660 nm ($\mathrm{PNC}_{14nm-660nm}$) was 5.2 x 10^3 cm^{-3} with a median value of 3.1 x 10^3 cm^{-3}. The daily average mass concentration of fine particles ($\mathrm{PM}_{2.5}$) was low (6.1 $\mu\mathrm{g\,m}^{-3}$) and always below the maximum daily average recommended by the Australian National Environment Protection (Ambient Air Quality) Measure (Air NEPM).

The results highlight that the distinct sources of particle number identified were traffic emissions, industrial activities and marine aerosols. Traffic emissions dominated in the morning, whereas photochemical reactions, marine aerosols and local source particles dominated in the afternoon. Emissions from industrial activities and central business district activities dominated at night. Similar to previous studies, particles of diameter < 1 µm were influenced by vehicle emissions. Particle number concentrations were strongly influenced by sea breezes that carry particles from sources in and around Sydney (north easterly winds) as well as from Port Kembla Steel Works and the urban areas (winds from the south). A weak correlation between organic carbon and elemental carbon suggests that the population of carbonaceous aerosols were influenced by multiple sources.

The evolution of particle number size distribution in the range of 14 nm to 600 nm was analysed in order to determine the occurrence frequency of particle formation during the one month period of aerosol measurements of the MUMBA campaign. Eight particle formation and growth events (four Class I and four Class II) were observed in this study which is equivalent to 25% of the total observation days. The Class I events took place in the sunny periods, starting after 8:00 and lasting till 14:30 with an average duration of five hours. These events were classified as "weak" particle formation events. This observation is likely to be related to the meteorological conditions, especially wind speed and wind direction experienced at the monitoring site. Particles formed during the Class I events increased and/or decreased the cloud condensation nuclei number. However, there was no clear indication that particles of a diameter equal to or larger than 50 nm were activated as cloud condensation nuclei. There were high concentrations of isoprene, CO and NO_x observed before the events. An increased of surface O_3 concentrations during the events was also observed. This suggests that the events were influenced by photochemical reactions, as well as biogenic and traffic emissions. A mix of oceanic and anthropogenic air masses was also one of the factors that influenced these events. Particle formation and growth events were only observed when air masses originated from the north and northeast sectors. These air masses had travelled from the ocean and passed through populated areas including Sydney. While many factors have been looked at, there was no clear single set of factors that caused the Class I events. Relative humidity, SO_2 and the photochemical age of air masses had potentially played a role in the particle formation and growth events although there were insufficient measurements to determine this to a high level of confidence.

Aerosol vertical properties were studied using a remote sensing technique. The Multi-Axis Differential Optical Absorption Spectroscopy (MAX-DOAS) instrument successfully retrieved aerosol properties during the aerosol measurement phase of the MUMBA campaign. This was the first achievement by the Centre for Atmospheric Chemistry at the University of Wollongong on these retrievals. Differential slant column density can be used to infer changes in aerosol properties. Aerosol optical depth derived from the MAX-DOAS and the sun photometer were uncorrelated ($R^2 = 0.03$). This could be due to the different location and viewing geometry of the instruments. Aerosol optical depth retrieved by the MAX-DOAS was affected readily by the marine environment compared to the sun photometer. Aerosol optical depth measured by the Light Detection and Ranging (LIDAR) was successfully compared to measurements from the MAX-DOAS on a selected "clear day" with a strong level of agreement ($R^2 = 0.77$). Both MAX-DOAS and LIDAR instruments demonstrated a significant scattering layer at approximately 300 m above ground level. The MAX-DOAS retrieved surface aerosol extinction coefficient (200 m height and below) was also compared with the *in-situ* measurements of fine particle mass concentration ($PM_{2.5}$). A poor correlation was obtained from this two datasets ($R^2 = 0.12$) relative to the study observed by [*Wang et al.*, 2016b]. This observation was probably due in part to the low $PM_{2.5}$ populations experienced during the aerosol measurement period. Both the aerosol extinction coefficient derived from MAX-DOAS and the backscatter aerosol distribution derived from LIDAR were capable of capturing the presence of aerosol layer close to ground surface during the Class I particle formation and growth event days.

The characteristics of particle populations are complex in Wollongong, due to the background of the Illawarra area. This study shows that local and transported sources together with meteorological conditions have a definite influence on the particle population. The area experiences mixed and complex pollution sources which present challenges to air quality management of the sources. Nevertheless, listed below are recommendations that would improve our knowledge of the characteristics of particle populations:

1. Information on elemental concentrations is needed to understand the aerosol sources and their formation. The elemental concentration data obtained during the MUMBA campaign were restricted to the detection limit of the instruments.

2. Previous studies have shown that the detectable size range of the newly formed particles was from 1 nm to 10 nm. This study was limited to particle size range from 14 nm to 660 nm. Having an instrument covering the particle number size distribution less than 14 nm ($Dp < 14$ nm) would be an advantage.

3. There was limited information on the traffic data. There was no available information on the type of vehicles at the study area. This information would have been an advantage in explaining the sources of particle number concentrations.

4. Previous studies have shown the advantages of using sky cameras which support and provide more information on cloud conditions during the sampling days. It is also worthwhile comparing the MAX-DOAS instrument used in this study with other MAX-DOAS instruments. A longer observation period covering different environments is needed to further test the performance of the MAX-DOAS instrument.

Output from This Study

Work presented here contributes to a greater understanding of the characteristics of aerosols that affect Australian air quality, particularly in Wollongong, Illawarra, NSW. The aerosol measurements during the MUMBA campaign have already provided a better understanding on the overall characteristics of aerosol populations and their sources at the coastal-urban environment. Work on this has been published in the Atmospheric Environment journal:

Dominick, D., S. R. Wilson, C. Paton-Walsh, R. Humphries, E.-A. Guérette, M. Keywood, D. Kubistin, and B. Marwick (2018), Characteristics of airborne particle number size distributions in a coastal-urban environment, Atmos. Environ., 186, 256265, doi:10.1016/j.atmosenv.2018.05.031.

A manuscript on the particle formation mechanisms has been submitted for publication in Atmosphere, in the special issue "Air quality in New South Wales, Australia". At this stage, this manuscript is under revision. Results obtained in this study have also contributed to the published work by *Paton-Walsh et al.* [2017], *Guérette et al.* [2017] and *Paton-Walsh et al.* [2018]. A manuscript on the comparison of MAX-DOAS retrieval from several other campaigns is also planned which include the collaborative research of a PhD student, Robert George Ryan of the University of Melbourne.

This thesis has presented a complex study on the characterisation of atmospheric aerosol and has successfully provided information on the atmospheric composition during the MUMBA campaign. This thesis also provides a useful stepping stone towards our understanding of a complex mixed atmospheric environment with coastal, biogenic and urban influences. Atmospheric processes described in this study are likely to be replicated in many other coastal cities worldwide.

Bibliography

Ackermann, J. (1998), The extinction-to-backscatter ratio of tropospheric aerosol: A numerical study, *Journal of atmospheric and oceanic technology*, *15*(4), 1043–1050.

Adam, M., T. Schikowski, A. E. Carsin, Y. Cai, B. Jacquemin, M. Sanchez, A. Vierkötter, A. Marcon, D. Keidel, D. Sugiri, et al. (2015), Adult lung function and long-term air pollution exposure. ESCAPE: a multicentre cohort study and meta-analysis, *Eur. Respir. J.*, *45*(1), 38–50, doi:10.1183/09031936.00130014.

Ångström, A. (1929), On the atmospheric transmission of sun radiation and on dust in the air, *Geografiska Annaler*, *11*(2), 156–166.

Ansmann, A., and D. Muller (2005), *Lidar and Atmospheric Aerosol Particles, in Lidar: Range-Resolved Optical Remote Sensing of the Atmosphere, Vol.102*, edited by C. Weitkamp, Springer, New York.

Ayers, G., J. Cainey, and R. Gillett (1998), Sulfur dioxide and dimethyl sulfide in marine air at Cape Grim, Tasmania, *Oceanographic Literature Review*, *1*(45), 49.

Barletta, B., S. Meinardi, F. S. Rowland, C.-Y. Chan, X. Wang, S. Zou, L. Y. Chan, and D. R. Blake (2005), Volatile organic compounds in 43 Chinese cities, *Atmos. Environ.*, *39*(32), 5979–5990, doi:10.1016/j.atmosenv.2005.06.029.

Barry, R. G., and E. A. Hall-McKim (2014), *Essentials of the Earth's climate system*, Cambridge University Press.

Begg, S., T. Vos, B. Barker, C. Stevenson, L. Stanley, and A. D. Lopez (2007), The burden of disease and injury in Australia 2003, *Tech. rep.*, Australian Institute of Health and Welfare, Retrieved from http://hdl.handle.net/10536/DRO/DU:30046702.

Birmili, W., K. Heinke, M. Pitz, J. Matschullat, A. Wiedensohler, J. Cyrys, H.-E. Wichmann, and A. Peters (2010), Particle number size distributions in urban air before and after volatilisation, *Atmos. Chem. Phys.*, *10*(10), 4643–4660, doi:10.5194/acp-10-4643-2010.

Bogumil, K., J. Orphal, T. Homann, S. Voigt, P. Spietz, O. Fleischmann, A. Vogel, M. Hartmann, H. Kromminga, H. Bovensmann, et al. (2003), Measurements of molecular absorption spectra with the SCIAMACHY pre-flight model: instrument characterization and reference data for atmospheric remote-sensing in the 230–2380 nm region, *J. Photochem. Photobiol. A: Chem*, *157*(2), 167–184, doi:10.1016/S1010-6030(03)00062-5.

BOM (2009), Learn about Meteorology Climate Education: Climate of Australia, Retrieved from http://pandora.nla.gov.au/pan/96122/20090317-1643/www.bom.gov.au/lam/climate/levelthree/ausclim/ausclim.html.

BOM (2018), Climate statistics for Australian locations:Monthly climate statistics, Retrieved from http://www.bom.gov.au/climate.

Borbon, A., H. Fontaine, M. Veillerot, N. Locoge, J. Galloo, and R. Guillermo (2001), An investigation into the traffic-related fraction of isoprene at an urban location, *Atmos. Environ.*, *35*(22), 3749–3760, doi:10.1016/S1352-2310(01)00170-4.

Boucher, O. (2015), *Atmospheric aerosols: Properties and climate impacts*, Springer, doi:10.1007/978-94-017-9649-1.

Boucher, O., D. Randall, P. Artaxo, C. Bretherton, G. Feingold, P. Forster, V.-M. Kerminen, Y. Kondo, H. Liao, U. Lohmann, et al. (2013), Clouds and aerosols, in *Climate change 2013: the physical science basis. Contribution of Working Group I to the Fifth Assessment Report of the Intergovernmental Panel on Climate Change.[Stocker, T.F., D. Qin, G.-K. Plattner, M. Tignor, S.K. Allen, J. Boschung, A. Nauels, Y. Xia, V. Bex and P.M. Midgley (eds.)]*, pp. 571–657, Cambridge University Press, Cambridge, United Kingdom and New York, NY, USA.

Brasseur, G. P., and D. J. Jacob (2017), *Modeling of Atmospheric Chemistry*, Cambridge University Press.

Brauer, M., M. Amann, R. T. Burnett, A. Cohen, F. Dentener, M. Ezzati, S. B. Henderson, M. Krzyzanowski, R. V. Martin, R. Van Dingenen, et al. (2012), Exposure assessment for estimation of the global burden of disease attributable to outdoor air pollution, *Environ. Sci. Technol.*, *46*(2), 652–660, doi:10.1021/es2025752.

Brimblecombe, P. (2015), *Urban Pollution and Changes to Materials and Building Surfaces*, vol. 5, World Scientific.

Broome, R. A., N. Fann, T. J. N. Cristina, C. Fulcher, H. Duc, and G. G. Morgan (2015), The health benefits of reducing air pollution in Sydney, Australia, *Environ. Res.*, *143*, 19–25, doi:10.1016/j.envres.2015.09.007.

Brus, D., L. Škrabalová, E. Herrmann, T. Olenius, T. Trávničková, U. Makkonen, and J. Merikanto (2017), Temperature-Dependent Diffusion of H_2SO_4 in Air at Atmospherically Relevant Conditions: Laboratory Measurements Using Laminar Flow Technique, *Atmosphere*, *8*(7), 132, doi:10.3390/atmos8070132.

Butler, C. D., and J. Whelan (2018), Air pollution and climate change in Australia: A triple burden, in *Climate Change and Air Pollution*, pp. 131–149, Springer, doi:10.1007/978-3-319-61346-8_9.

Cainey, J. M., M. Keywood, M. R. Grose, P. Krummel, I. E. Galbally, P. Johnston, R. W. Gillett, M. Meyer, P. Fraser, P. Steele, et al. (2007), Precursors to particles P2P at Cape Grim 2006: campaign overview, *Environ. Chem.*, *4*(3), 143–150, doi:10.1071/EN07041.

Cao, J., S. Lee, J. C. Chow, J. G. Watson, K. Ho, R. Zhang, Z. Jin, Z. Shen, G. Chen, Y. Kang, et al. (2007), Spatial and seasonal distributions of carbonaceous aerosols over China, *J. Geophys. Res. Atmos.*, *112*(D22S11), doi:10.1029/2006JD008205.

Carlton, A. G., B. J. Turpin, H.-J. Lim, K. E. Altieri, and S. Seitzinger (2006), Link between isoprene and secondary organic aerosol (soa): Pyruvic acid oxidation yields low volatility organic acids in clouds, *Geophys. Res. Lett.*, *33*(L06822), doi:10.1029/2005GL025374.

Carslaw, D. C., and K. Ropkins (2012), Openair —an R package for air quality data analysis, *Environ. Modell. Softw.*, *27*, 52–61, doi:10.1016/j.envsoft.2011.09.008.

Cesaroni, G., F. Forastiere, M. Stafoggia, Z. J. Andersen, C. Badaloni, R. Beelen, B. Caracciolo, U. de Faire, R. Erbel, K. T. Eriksen, et al. (2014), Long term exposure to ambient air pollution and incidence of acute coronary events: prospective cohort study and meta-analysis in 11 european cohorts from the escape project, *Bmj*, *348*, f7412, doi:10.1136/bmj.f7412.

Chan, K., M. Wiegner, M. Wenig, and D. Pöhler (2018), Observations of tropospheric aerosols and NO_2 in Hong Kong over 5 years using ground based MAX-DOAS, *Sci.Total Environ.*, *619*, 1545–1556, doi:10.1016/j.scitotenv.2017.10.153.

Chance, K. V., and R. J. Spurr (1997), Ring effect studies: Rayleigh scattering, including molecular parameters for rotational Raman scattering, and the Fraunhofer spectrum, *Applied Optics*, *36*(21), 5224–5230, doi:10.1364/AO.36.005224.

Chang, M.-C. O., J. C. Chow, J. G. Watson, P. K. Hopke, S.-M. Yi, and G. C. England (2004), Measurement of ultrafine particle size distributions from coal-, oil-, and gas-fired stationary combustion sources, *J Air Waste Manag. Assoc.*, *54*(12), 1494–1505, doi:10.1080/10473289.2004.10471010.

Charron, A., W. Birmili, and R. M. Harrison (2008), Fingerprinting particle origins according to their size distribution at a UK rural site, *J. Geophys. Res. Atmos.*, *113*(D7), doi:10.1029/2007JD008562.

Cheung, J., L. Morawska, and Z. Ristovski (2011), Observation of new particle formation in subtropical urban environment, *Atmos. Chem. Phys.*, *11*, 3823–3833, doi:10.5194/acp-11-3823-2011.

Claeys, M., B. Graham, G. Vas, W. Wang, R. Vermeylen, V. Pashynska, J. Cafmeyer, P. Guyon, M. O. Andreae, P. Artaxo, et al. (2004), Formation of secondary organic aerosols through photooxidation of isoprene, *Science*, *303*(5661), 1173–1176, doi:10.1126/science.1092805.

Cohen, A. J., M. Brauer, R. Burnett, H. R. Anderson, J. Frostad, K. Estep, K. Balakrishnan, B. Brunekreef, L. Dandona, R. Dandona, et al. (2017), Estimates and 25-year trends of the global burden of disease attributable to ambient air pollution: an analysis of data from the Global Burden of Diseases Study 2015, *The Lancet*, *389*(10082), 1907–1918, doi:10.1016/S0140-6736(17)30505-6.

Collins, D., M. Parsons, and C. Zinyemba (2014), Air quality at outdoor community events: findings from fine particulate ($PM_{2.5}$) sampling at festivals in Edmonton, Alberta, *Int. J. Environ. Health. Res.*, *24*(3), 215–225, doi:10.1080/09603123.2013.807328.

Cope, M., M. Keywood, K. Emmerson, I. Galbally, K. Boast, S. Chambers, M. Cheng, S. Crumeyrolle, E. Dunne, R. Fedele, et al. (2014), Sydney particle study–Stage II, *The Centre for Australian Weather and Climate Research.*

Council, M. C. (2012), Madrid's air quality plan 2011-2015. approved by the governing board of madrid city council on april 26, 2012. general directorate of sustainability, government division of environment, safety and mobility, madrid city council.

CSIRO (2017), Cape Grim Baseline Air Pollution Station data, Retrieved from https://research.csiro.au/acc/capabilities/cape-grim-baseline-air-pollution-station/cgbaps/.

Dada, L., P. Paasonen, T. Nieminen, S. Buenrostro Mazon, J. Kontkanen, O. Peräkylä, K. Lehtipalo, T. Hussein, T. Petäjä, V.-M. Kerminen, et al. (2017), Long-term analysis of clear-sky new particle formation events and nonevents in Hyytiälä, *Atmos. Chem. Phys.*, *17*(10), 6227–6241, doi:10.5194/acp-17-6227-2017.

Dadvand, P., J. Parker, M. L. Bell, M. Bonzini, M. Brauer, L. A. Darrow, U. Gehring, S. V. Glinianaia, N. Gouveia, E.-h. Ha, et al. (2013), Maternal exposure to particulate air pollution and term birth weight: a multi-country evaluation of effect and heterogeneity, *Environ. Health Perspect.*, *121*(3), 267–373, doi:10.1289/ehp.1205575.

Dal Maso, M., M. Kulmala, I. Riipinen, R. Wagner, T. Hussein, P. P. Aalto, and K. E. Lehtinen (2005), Formation and growth of fresh atmospheric aerosols: eight years of aerosol size distribution data from SMEAR II, Hyytiälä), Finland, *Boreal Environment Research*, *10*(5), 323–336.

Dall ´Osto, M., D. Beddows, A. Asmi, L. Poulain, L. Hao, E. Freney, J. Allan, M. Canagaratna, M. Crippa, F. Bianchi, et al. (2018), Novel insights on new particle formation derived from a pan-european observing system, *Scientific reports*, *8*(1), 1482, doi:10.1038/s41598-017-17343-9.

Danckaert, T., C. Fayt, and M. Van Roozendael (2014), QDOAS software user manual 2.108, IASB/BIRA, Uccle, Belgium, 2014.

de España, C. D., A. Wonaschütz, G. Steiner, B. Rosati, A. Demattio, H. Schuh, and R. Hitzenberger (2017), Long-term quantitative field study of New Particle Formation (NPF) events as a source of Cloud Condensation Nuclei (CCN) in the urban background of Vienna, *Atmos. Environ.*, *164*, 289–298, doi:10.1016/j.atmosenv.2017.06.001.

de Leeuw, G., C. Guieu, A. Arneth, N. Bellouin, L. Bopp, P. Boyd, H. Denier van der Gon, K. Desboeufs, F. Dulac, M. Facchini, B. Gantt, B. Langmann, N. Mahowald, E. Maranon, C. O'Dowd, N. Olgun, E. Pulido-Villena, M. Rinaldi, E. Stephanou, and T. Wagener (2014), *Ocean - Atmosphere Interactions of Particles*, 171-246 pp., Springer Earth System Sciences, doi:10.1007/978-3-642-25643-1_4.

Ding, X., Q.-F. He, R.-Q. Shen, Q.-Q. Yu, Y.-Q. Zhang, J.-Y. Xin, T.-X. Wen, and X.-M. Wang (2016), Spatial and seasonal variations of isoprene secondary organic aerosol in China: Significant impact of biomass burning during winter, *Scientific reports*, *6*, 20,411, doi:10.1038/srep20411.

Dinoi, A., D. Cesari, A. Marinoni, P. Bonasoni, A. Riccio, E. Chianese, G. Tirimberio, A. Naccarato, F. Sprovieri, V. Andreoli, et al. (2017), Inter-comparison of carbon content in $PM_{2.5}$ and PM_{10} collected at five measurement sites in Southern Italy, *Atmosphere*, *8*(12), 243, doi:10.3390/atmos8120243.

Dominick, D., S. R. Wilson, C. Paton-Walsh, R. Humphries, E.-A. Guérette, M. Keywood, D. Kubistin, and B. Marwick (2018), Characteristics of airborne particle number size distributions in a coastal-urban environment, *Atmos. Environ.*, *186*, 256–265, doi:10.1016/j.atmosenv.2018.05.031.

Draxler, R. R., and G. Rolph (2003), Hysplit (hybrid single-particle lagrangian integrated trajectory) model access via NOAA website (http://www. arl. noaa. gov/ready/hysplit4. html). NOAA Air Resources Laboratory, Silver Spring.

Draxler, R. R., B. Stunder, G. Rolph, A. Stein, and A. Taylor (2018), *HYSPLIT 4 user's guide, Version 4, report. NOAA Air Resources Laboratory, Silver Spring*, Last Revised: February 2018.

Duane, M., B. Poma, D. Rembges, C. Astorga, and B. Larsen (2002), Isoprene and its degradation products as strong ozone precursors in Insubria, Northern Italy, *Atmos. Environ.*, *36*(24), 3867–3879, doi:10.1016/S1352-2310(02)00359-X.

Duh, J.-D., V. Shandas, H. Chang, and L. A. George (2008), Rates of urbanisation and the resiliency of air and water quality, *Sci. Total Environ.*, *400*(1-3), 238–256, doi:10.1016/j.scitotenv.2008.05.002.

Duplissy, J., J. Merikanto, A. Franchin, G. Tsagkogeorgas, J. Kangasluoma, D. Wimmer, H. Vuollekoski, S. Schobesberger, K. Lehtipalo, R. Flagan, et al. (2016), Effect of ions on sulfuric acid-water binary particle formation: 2. experimental data and comparison with QC-normalized classical nucleation theory, *J. Geophys. Res. Atmos.*, *121*(4), 1752–1775, doi:doi:10.1002/2015JD023538.

Dusek, U., G. Frank, L. Hildebrandt, J. Curtius, J. Schneider, S. Walter, D. Chand, F. Drewnick, S. Hings, D. Jung, et al. (2006), Size matters more than chemistry for cloud-nucleating ability of aerosol particles, *Science*, *312*(5778), 1375–1378, doi:10.1126/science.1125261.

Emmerson, K. M., I. E. Galbally, A. B. Guenther, C. Paton-Walsh, E.-A. Guerette, M. E. Cope, M. D. Keywood, S. J. Lawson, S. B. Molloy, E. Dunne, et al. (2016), Current estimates of biogenic emissions from eucalypts uncertain for southeast Australia, *Atmos. Chem. Phys.*, *16*(11), 6997–7011, doi: 10.5194/acp-16-6997-2016.

Emmerson, K. M., M. E. Cope, I. E. Galbally, S. Lee, and P. F. Nelson (2018), Isoprene and monoterpene emissions in south-east australia: comparison of a multi-layer canopy model with megan and with atmospheric observations, *Atmos. Chem. Phys*, *18*(10), 7539–7556, doi:10.5194/acp-18-7539-2018.

Fernald, F. G., B. M. Herman, and J. A. Reagan (1972), Determination of aerosol height distributions by lidar, *J Appl. Meteorol.*, *11*(3), 482–489, doi:10.1175/1520-0450(1972)011⟨0482:DOAHDB⟩2.0.CO;2.

Fleming, Z. L., P. S. Monks, and A. J. Manning (2012), Untangling the influence of air-mass history in interpreting observed atmospheric composition, *Atmos. Res.*, *104*, 1–39, doi:10.1016/j.atmosres.2011.09.009.

Forouzanfar, M. H., et al. (2016), Global, regional, and national comparative risk assessment of 79 behavioural, environmental and occupational, and metabolic risks or clusters of risks, 19902015: a systematic analysis for the Global Burden of Disease Study 2015, *The Lancet*, *388(10053)*, 1659–1724, doi:10.1016/S0140-6736(16)31679-8.

Forster, P., V. Ramaswamy, P. Artaxo, T. Berntsen, R. Betts, D. W. Fahey, J. Haywood, J. Lean, D. C. Lowe, G. Myhre, et al. (2007), Changes in atmospheric constituents and in radiative forcing Chapter 2, in *Climate Change 2007. The Physical Science Basis*, United Kingdom: Cambridge University Press.

Frieß, U., P. Monks, J. Remedios, A. Rozanov, R. Sinreich, T. Wagner, and U. Platt (2006), MAX-DOAS O_4 measurements: A new technique to derive information on atmospheric aerosols: 2. modeling studies, *J. Geophys. Res*, *111*(D14203), doi:10.1029/2005JD006618.

Frieß, U., H. Sihler, R. Sander, D. Pöhler, S. Yilmaz, and U. Platt (2011), The vertical distribution of BrO and aerosols in the Arctic: Measurements by active and passive differential optical absorption spectroscopy, *J. Geophys. Res*, *116*(D00R04), doi:10.1029/2011JD015938.

Frieß, U., H. K. Baltink, S. Beirle, K. Clémer, F. Hendrick, B. Henzing, H. Irie, G. de Leeuw, A. Li, M. Moerman, et al. (2016), Intercomparison of aerosol extinction profiles retrieved from MAX-DOAS measurements, *Atmos. Meas. Tech.*, *9*(7), 3205–3222, doi:10.5194/amt-9-3205-2016.

Fuchs, N. (1963), On the stationary charge distribution on aerosol particles in a bipolar ionic atmosphere, *Geofisica pura e applicata*, *56*(1), 185–193, doi:10.1007/BF01993343.

Fuzzi, S., U. Baltensperger, K. Carslaw, S. Decesari, H. Denier Van Der Gon, M. Facchini, D. Fowler, I. Koren, B. Langford, U. Lohmann, et al. (2015), Particulate matter, air quality and climate: lessons learned and future needs, *Atmos. Chem. Phys.*, *15*(14), 8217–8299, doi:10.5194/acp-15-8217-2015.

Garcia-Nieto, D., N. Benavent, and A. Saiz-Lopez (2018), Measurements of atmospheric HONO vertical distribution and temporal evolution in Madrid (Spain) using the MAX-DOAS technique, *Sci. Total Environ.*, *643*, 957–966, doi:10.1016/j.scitotenv.2018.06.180.

Gehring, U., O. Gruzieva, R. M. Agius, R. Beelen, A. Custovic, J. Cyrys, M. Eeftens, C. Flexeder, E. Fuertes, J. Heinrich, et al. (2013), Air pollution exposure and lung function in children: the ESCAPE project, *Environ. Health Perspect.*, *121*(11-12), 1357–1364, doi:10.1289/ehp.1306770.

Gielen, C., M. Van Roozendael, F. Hendrick, G. Pinardi, T. Vlemmix, V. De Bock, H. De Backer, C. Fayt, C. Hermans, D. Gillotay, et al. (2014), A simple and versatile cloud-screening method for MAX-DOAS retrievals, *Atmos. Meas. Tech.*, *7*(10), 3509–3527, doi:10.5194/amt-7-3509-2014.

Grainger, J., and J. Ring (1962), Anomalous fraunhofer line profiles, *Nature*, *193*(4817), 762–762, doi:10.1038/193762a0.

Gratsea, M., M. Vrekoussis, A. Richter, F. Wittrock, A. Schönhardt, J. Burrows, S. Kazadzis, N. Mihalopoulos, and E. Gerasopoulos (2016), Slant column MAX-DOAS measurements of nitrogen dioxide, formaldehyde, glyoxal and oxygen dimer in the urban environment of Athens, *Atmos. Environ.*, *135*, 118–131, doi:10.1016/j.atmosenv.2016.03.048.

Grythe, H., J. Ström, R. Krejci, P. Quinn, and A. Stohl (2014), A review of sea-spray aerosol source functions using a large global set of sea salt aerosol concentration measurements, *Atmos. Chem. Phys.*, *14*(3), 1277–1297, doi:10.5194/acp-14-1277-2014.

Guenther, A., T. Karl, P. Harley, C. Wiedinmyer, P. Palmer, and C. Geron (2006), Estimates of global terrestrial isoprene emissions using MEGAN (Model of Emissions of Gases and Aerosols from Nature), *Atmos. Chem. Phys.*, *6*(11), 3181–3210, doi:10.5194/acp-6-3181-2006.

Guérette, E.-A. (2016), Measurements of volatile organic compound sources and ambient concentrations in south-east australia, Ph.D. thesis, School of Chemistry, University of Wollongong.

Guérette, E.-A., C. Paton-Walsh, D. Kubistin, R. Humphries, M. Bhujel, R. R. Buchholz, S. Chambers, M. Cheng, P. Davy, D. Dominick, I. Galbally, D. W. T. Griffith, A. Griffiths, M. Keywood, S. Lawson, S. Molloy, P. Selleck, J. Simmons, and S. R. Wilson (2017), Measurements of Urban, Marine and Biogenic Air (MUMBA): characterisation of trace gases and aerosol at the urban, marine and biogenic interface in summer in Wollongong, Australia, doi: 10.1594/PANGAEA.871982.

Guo, C., Z. Zhang, A. K. Lau, C. Q. Lin, Y. C. Chuang, J. Chan, W. K. Jiang, T. Tam, E.-K. Yeoh, T.-C. Chan, et al. (2018), Effect of long-term exposure to fine particulate matter on lung function decline and risk of chronic obstructive pulmonary disease in Taiwan: a longitudinal, cohort study, *Lancet Planetary Health*, *2*(3), e114–e125, doi:10.1016/S2542-5196(18)30028-7.

Guo, H., A. Ding, L. Morawska, C. He, G. Ayoko, Y.-s. Li, and W.-t. Hung (2008), Size distribution and new particle formation in subtropical eastern Australia, *Environ. Chem.*, *5*(6), 382–390, doi:10.1071/EN08058.

Hamed, A., H. Korhonen, S.-L. Sihto, J. Joutsensaari, H. Järvinen, T. Petäjä, F. Arnold, T. Nieminen, M. Kulmala, J. N. Smith, et al. (2011), The role of relative humidity in continental new particle formation, *J. Geophys. Res.*, *116*(D03202), doi:10.1029/2010JD014186.

Harris, S. J., and M. M. Maricq (2001), Signature size distributions for diesel and gasoline engine exhaust particulate matter, *J. Aerosol Sci.*, *32*(6), 749–764, doi: 10.1016/S0021-8502(00)00111-7.

Harrison, L., and J. Michalsky (1994), Objective algorithms for the retrieval of optical depths from ground-based measurements, *Applied optics*, *33*(22), 5126–5132, doi:10.1364/AO.33.005126.

Harrison, R. M., and J. Yin (2000), Particulate matter in the atmosphere: which particle properties are important for its effects on health?, *Sci. Total Environ.*, *249*(1-3), 85–101, doi:10.1016/S0048-9697(99)00513-6.

Harrison, R. M., D. C. Beddows, and M. Dall ′Osto (2011), PMF analysis of wide-range particle size spectra collected on a major highway, *Environ. Sci. Techno.*, *45*(13), 5522–5528, doi:10.1021/es2006622.

Hawkins, L. N., and L. M. Russell (2010), Oxidation of ketone groups in transported biomass burning aerosol from the 2008 Northern California Lightning Series fires, *Atmos. Environ.*, *44*(34), 4142–4154, doi:10.1016/j.atmosenv.2010.07.036.

Heckel, A., A. Richter, T. Tarsu, F. Wittrock, C. Hak, I. Pundt, W. Junkermann, and J. Burrows (2005), MAX-DOAS measurements of formaldehyde in the Po-Valley, *Atmos. Chem. Phys.*, *5*(4), 909–918, doi:10.5194/acp-5-909-2005.

Hendrick, F., J.-F. Müller, K. Clémer, P. Wang, M. D. Mazière, C. Fayt, C. Gielen, C. Hermans, J. Ma, G. Pinardi, et al. (2014), Four years of ground-based MAX-DOAS observations of HONO and NO_2 in the Beijing area, *Atmos. Chem. Phys.*, *14*(2), 765–781, doi:10.5194/acp-14-765-2014.

Hendricks, J., M. Righi, and V. Aquila (2012), Global atmospheric aerosol modeling, in *Atmospheric Physics*, pp. 561–576, Springer, doi:10.1007/978-3-642-30183-4_34.

Hermans, C., A. C. Vandaele, M. Carleer, S. Fally, R. Colin, A. Jenouvrier, B. Coquart, and M.-F. Mérienne (1999), Absorption cross-sections of atmospheric constituents: NO_2, O_2, and H_2O, *Environ. Sci. Pollut. Res.*, *6*(3), 151–158, doi: 10.1007/BF02987620.

Hinds, W. C. (1999), *Properties Behavior and Measurement of Airborne Particles, Aerosol Technology*, John Wiley & Sons.

Hinds, W. C. (2011), *Physical and chemical processes in aerosol systems*, John Wiley & Sons.

Hinds, W. C. (2012), *Aerosol technology: properties, behavior, and measurement of airborne particles*, John Wiley & Sons.

Holzinger, R., D. Millet, B. Williams, A. Lee, N. Kreisberg, S. Hering, J. Jimenez, J. Allan, D. Worsnop, and A. Goldstein (2007), Emission, oxidation, and secondary organic aerosol formation of volatile organic compounds as observed at Chebogue Point, Nova Scotia, *J. Geophys. Res.*, *112*(D10S24), doi:10.1029/2006JD007599.

Hönninger, G., and U. Platt (2002), Observations of BrO and its vertical distribution during surface ozone depletion at Alert, *Atmos. Environ.*, *36*(15), 2481–2489, doi: 10.1016/S1352-2310(02)00104-8.

Hönninger, G., C. v. Friedeburg, and U. Platt (2004), Multi axis differential optical absorption spectroscopy (MAX-DOAS), *Atmos.Chem. Phys.*, *4*(1), 231–254, doi: 10.5194/acp-4-231-2004.

Hoy, W. E., et al. (2016), Australian burden of disease study: impact and causes of illness and death in Australia 2011, *Tech. rep.*, Australian Institute of Health and Welfare.

Humphries, R. S., R. Schofield, M. Keywood, J. Ward, J. Pierce, C. Gionfriddo, M. Tate, D. Krabbenhoft, I. Galbally, S. Molloy, et al. (2015), Boundary layer new particle formation over East Antarctic sea ice–possible Hg-driven nucleation?, *Atmos. Chem. Phys.*, *15*(23), 13,339–13,364, doi:10.5194/acp-15-13339-2015.

Ibarra-Berastegi, G., J. Sáenz, A. Ezcurra, U. Ganzedo, J. D. de Argandoña, I. Errasti, A. Fernandez-Ferrero, and J. Polanco-Martínez (2009), Assessing spatial variability of SO_2 field as detected by an air quality network using self-organizing maps, cluster, and principal component analysis, *Atmos. Environ.*, *43*(25), 3829–3836, doi:10.1016/j.atmosenv.2009.05.010.

IPCC (2013), Summary for policymakers, in *Climate Change 2013: The Physical Science Basis. Contribution of Working Group I to the Fifth Assessment Report of the Intergovernmental Panel on Climate Change*, edited by T. Stocker, D. Qin, G.-K. Plattner, M. Tignor, S. Allen, J. Boschung, A. Nauels, Y. Xia, V. Bex, and P. Midgley, chap. SPM, p. 130, Cambridge University Press, Cambridge, United Kingdom, doi:10.1017/CBO9781107415324.004.

IPCC, et al. (2014), Annex II: Glossary [Mach, K.J., S. Planton and C. von Stechow (eds.)], in *Climate change 2014: Synthesis Report. Contribution of Working Groups I, II and III to the Fifth Assessment Report of the Intergovernmental Panel on Climate Change [Core Writing Team, R.K. Pachauri and L.A. Meyer (eds.)]*, pp. 117–130, IPCC Geneva, Switzerland.

Iqbal, M. (1983), *An introduction to solar radiation*, Elsevier Science.

Irie, H., Y. Kanaya, H. Akimoto, H. Iwabuchi, A. Shimizu, and K. Aoki (2008), First retrieval of tropospheric aerosol profiles using MAX-DOAS and comparison with lidar and sky radiometer measurements, *Atmos. Chem. Phys.*, *8*(2), 341–350, doi:10.5194/acp-8-341-2008.

Irie, H., Y. Kanaya, H. Akimoto, H. Iwabuchi, A. Shimizu, and K. Aoki (2009), Dual-wavelength aerosol vertical profile measurements by MAX-DOAS at Tsukuba, Japan, *Atmos. Chem. Phys.*, *9*(8), 2741–2749, doi:10.5194/acpd-8-19357-2008.

Irie, H., H. Takashima, Y. Kanaya, K. Boersma, L. Gast, F. Wittrock, D. Brunner, Y. Zhou, and M. V. Roozendael (2011), Eight-component retrievals from ground-based MAX-DOAS observations, *Atmos. Meas. Tech.*, *4*(6), 1027–1044, doi:10.5194/amt-4-1027-2011.

Junkermann, W., and J. M. Hacker (2018), Ultrafine particles in the lower troposphere: major sources, invisible plumes and meteorological transport processes, *Bulletin of the American Meteorological Society*, (2018), doi:10.1175/BAMS-D-18-0075.1.

Kalabokas, P., J. Hatzianestis, J. Bartzis, and P. Papagiannakopoulos (2001), Atmospheric concentrations of saturated and aromatic hydrocarbons around a greek oil refinery, *Atmos. Environ.*, *35*(14), 2545–2555, doi:10.1016/S1352-2310(00)00423-4.

Kansal, A. (2009), Sources and reactivity of NMHCs and VOCs in the atmosphere: A review, *Journal of hazardous materials*, *166*(1), 17–26, doi:10.1016/j.jhazmat.2008.11.048.

Kaushik, S. (2016), An introduction to clustering and different methods of clustering.

Kerminen, V.-M., X. Chen, V. Vakkari, T. Petj, M. Kulmala, and F. Bianchi (2018), Atmospheric new particle formation and growth: review of field observations, *Environ. Res. Lett.*, *13*(10), 103,003.

Keywood, M., H. Guyes, P. Selleck, and R. Gillett (2011), Quantification of secondary organic aerosol in an Australian urban location, *Environ. Chem.*, *8*(2), 115–126, doi:10.1071/EN10100.

Khan, M., B.-L. Schlich, M. Jenkin, B. Shallcross, K. Moseley, C. Walker, W. Morris, R. Derwent, C. Percival, and D. Shallcross (2018), A two-decade anthropogenic and biogenic isoprene emissions study in a London urban background and a London urban traffic site, *Atmosphere*, *9*(10), 387, doi:10.3390/atmos9100387.

Khoder, M. I. (2007), Ambient levels of volatile organic compounds in the atmosphere of Greater Cairo, *Atmos. Environ.*, *41*(3), 554–566, doi:10.1016/j.atmosenv.2006.08.051.

Khor, W. Y., W. S. Hee, F. Tan, H. San Lim, M. Z. M. Jafri, and B. Holben (2014), Comparison of Aerosol optical depth (AOD) derived from AERONET sunphotometer and lidar system, in *IOP Conf. Ser.: Earth Environ. Sci*, p. 012058, IOP Publishing, doi:10.1088/1755-1315/20/1/012058.

Kim, J.-O., and C. W. Mueller (1987), Introduction to factor analysis: what it is and how to do it. Quantitative applications in the social sciences series.

Kim, K.-H., S. A. Jahan, and E. Kabir (2013), A review on human health perspective of air pollution with respect to allergies and asthma, *Environ. Int.*, *59*, 41–52, doi:10.1016/j.envint.2013.05.007.

Kim, K.-H., E. Kabir, and S. Kabir (2015), A review on the human health impact of airborne particulate matter, *Environ. Int.*, *74*, 136–143, doi:10.1016/j.envint.2014.10.005.

Kinney, P. L. (2008), Climate change, air quality, and human health, *Am. J. Prev. Med.*, *35*(5), 459–467, doi:10.1016/j.amepre.2008.08.025.

Kirkby, J., J. Curtius, J. Almeida, E. Dunne, J. Duplissy, S. Ehrhart, A. Franchin, S. Gagné, L. Ickes, A. Kürten, et al. (2011), Role of sulphuric acid, ammonia and galactic cosmic rays in atmospheric aerosol nucleation, *Nature*, *476*(7361), 429, doi:10.1038/nature10343.

Kittelson, D., J. Johnson, W. Watts, Q. Wei, M. Drayton, D. Paulsen, and N. Bukowiecki (2000), Diesel aerosol sampling in the atmosphere, *Tech. rep.*, SAE Technical Paper, doi:10.4271/2000-01-2212.

Klett, J. D. (1985), Lidar inversion with variable backscatter/extinction ratios, *Applied Optics*, *24*(11), 1638–1643, doi:10.1364/AO.24.001638.

Kraus, S. (2006), *DOASIS: A framework design for DOAS*, Shaker.

Kristensson, A., M. Dal Maso, E. Swietlicki, T. Hussein, J. Zhou, V.-M. KERMINEN, and M. Kulmala (2008), Characterization of new particle formation events at a background site in Southern Sweden: relation to air mass history, *Tellus B*, *60*(3), 330–344, doi:10.1111/j.1600-0889.2008.00345.x.

Kulmala, M., and V.-M. Kerminen (2008), On the formation and growth of atmospheric nanoparticles, *Atmos. Res.*, *90*(2), 132–150, doi:10.1016/j.atmosres.2008.01.005.

Kulmala, M., H. Vehkamäki, T. Petäjä, M. Dal Maso, A. Lauri, V.-M. Kerminen, W. Birmili, and P. H. McMurry (2004), Formation and growth rates of ultrafine atmospheric particles: a review of observations, *J. Aerosol Sci.*, *35*(2), 143–176, doi:10.1016/j.jaerosci.2003.10.003.

Kulmala, M., J. Kontkanen, H. Junninen, K. Lehtipalo, H. E. Manninen, T. Nieminen, T. Petäjä, M. Sipilä, S. Schobesberger, P. Rantala, et al. (2013), Direct observations of atmospheric aerosol nucleation, *Science*, *339*(6122), 943–946, doi:10.1126/science.1227385.

Kulmala, M., T. Petäjä, M. Ehn, J. Thornton, M. Sipilä, D. Worsnop, and V.-M. Kerminen (2014), Chemistry of atmospheric nucleation: on the recent advances on precursor characterization and atmospheric cluster composition in connection with atmospheric new particle formation, *Annu. Rev. Phys. Chem.*, *65*, 21–37, doi:10.1146/annurev-physchem-040412-110014.

Kumar, P., A. Robins, S. Vardoulakis, and R. Britter (2010), A review of the characteristics of nanoparticles in the urban atmosphere and the prospects for developing regulatory controls, *Atmos. Environ.*, *44*(39), 5035–5052, doi:10.1016/j.atmosenv.2010.08.016.

Kürten, A., T. Jokinen, M. Simon, M. Sipilä, N. Sarnela, H. Junninen, A. Adamov, J. Almeida, A. Amorim, F. Bianchi, et al. (2014), Neutral molecular cluster formation of sulfuric acid–dimethylamine observed in real time under atmospheric conditions, *Proc. Natl. Acad. Sci. U.S.A.*, *111*(42), 15,019–15,024, doi:10.1073/pnas.1404853111.

Kürten, A., S. Münch, L. Rondo, F. Bianchi, J. Duplissy, T. Jokinen, H. Junninen, N. Sarnela, S. Schobesberger, M. Simon, et al. (2015), Thermodynamics of the formation of sulfuric acid dimers in the binary (h_2so_4–h_2o) and ternary (h_2so_4–h_2o–nh_3) system, *Atmos. Chem. Phys.*, *15*(18), 10,701–10,721, doi:10.5194/acp-15-10701-2015.

Langley, S. P. (1880), The bolometer and radiant energy, in *Proceedings of the American Academy of Arts and Sciences*, vol. 16, pp. 342–358, JSTOR.

Lau, J., W. Hung, and C. Cheung (2009), Interpretation of air quality in relation to monitoring station's surroundings, *Atmos. Environ.*, *43*(4), 769–777, doi:10.1016/j.atmosenv.2008.11.008.

Lee, H., H. Irie, Y. J. Kim, Y. Noh, C. Lee, Y. Kim, and K. J. Chun (2009a), Retrieval of aerosol extinction in the lower troposphere based on UV MAX-DOAS measurements, *Aerosol Sci. Tech.*, *43*(5), 502–509, doi:10.1080/02786820902769691.

Lee, H., H. Irie, J. Ryu, Y. Kanaya, Y. Noh, Y. J. Kim, S. Kwon, M. Trail, and A. G. Russell (2009b), Lower tropospheric aerosol measurements by MAX-DOAS during Severe Asian dust period, *Aerosol Sci. Tech.*, *43*(12), 1208–1217, doi:10.1080/02786820903307665.

Lee, K. K., M. R. Miller, and A. S. Shah (2018), Air pollution and stroke, *J.Stroke*, *20*(1), 2–11, doi:10.5853/jos.2017.02894.

Lee, Y.-G., H.-W. Lee, M.-S. Kim, C. Y. Choi, and J. Kim (2008), Characteristics of particle formation events in the coastal region of Korea in 2005, *Atmos. Environ.*, *42*(16), 3729–3739, doi:10.1016/j.atmosenv.2007.12.064.

Leppä, J., T. Anttila, V.-M. Kerminen, M. Kulmala, and K. Lehtinen (2011), Atmospheric new particle formation: real and apparent growth of neutral and charged particles, *Atmos. Chem. Phys.*, *11*(10), 4939–4955, doi:10.5194/acp-11-4939-2011.

Li, Z., E. A. Ratliff, and T. D. Sharkey (2011), Effect of temperature on postillumination isoprene emission in oak and poplar, *Plant Physiology*, *155*(2), 1037–1046, doi:10.1104/pp.110.167551.

Lihavainen, H., V.-M. Kerminen, M. Komppula, J. Hatakka, V. Aaltonen, M. Kulmala, and Y. Viisanen (2003), Production of "potential" cloud condensation nuclei associated with atmospheric new-particle formation in northern Finland, *J. Geophys. Res.*, *108*(D24), 4782, doi:10.1029/2003JD003887.

Lim, H.-J., B. J. Turpin, L. Russell, and T. Bates (2003), Organic and elemental carbon measurements during ACE-Asia suggest a longer atmospheric lifetime for elemental carbon, *Environ. Sci. Technol.*, *37*(14), 3055–3061, doi:10.1021/es020988s.

Lim, S. S., et al. (2012), A comparative risk assessment of burden of disease and injury attributable to 67 risk factors and risk factor clusters in 21 regions, 1990–2010: a systematic analysis for the Global Burden of Disease Study 2010, *The lancet*, *380*(9859), 2224–2260, doi:10.1016/S0140-6736(12)61766-8.

Lin, Y. C., M. T. Cheng, C. P. Chio, and C. Y. Kuo (2009), Carbonaceous aerosol measurements at coastal, urban, and inland sites in central Taiwan, *Environ. Forensics*, *10*(1), 7–17, doi:10.1080/15275920802660188.

Liu, C.-W., K.-H. Lin, and Y.-M. Kuo (2003), Application of factor analysis in the assessment of groundwater quality in a blackfoot disease area in Taiwan, *Sci. Total Environ.*, *313*(1), 77–89, doi:10.1016/S0048-9697(02)00683-6.

Lohmann, U., and J. Feichter (2005), Global indirect aerosol effects: a review, *Atmos. Chem. Phys.*, *5*(3), 715–737, doi:10.5194/acp-5-715-2005.

MacCartney, E. J. (1976), *Optics of the Atmosphere*, John Wiley & Sons.

MacIntyre, E. A., U. Gehring, A. Mölter, E. Fuertes, C. Klümper, U. Krämer, U. Quass, B. Hoffmann, M. Gascon, B. Brunekreef, et al. (2013), Air pollution and respiratory infections during early childhood: an analysis of 10 European birth cohorts within the ESCAPE Project, *Environ. Health Perspects*, *122*(1), 107–113, doi:10.1289/ehp.1306755.

Madhulatha, T. S. (2012), An overview on clustering methods, *J Eng*, *2*(4), 719–725, url:http://arxiv.org/abs/1205.1117.

Malley, C. S., D. K. Henze, J. C. Kuylenstierna, H. W. Vallack, Y. Davila, S. C. Anenberg, M. C. Turner, and M. R. Ashmore (2017), Updated Global Estimates of Respiratory Mortality in Adults $\geq$ 30 Years of Age Attributable to Long-Term Ozone Exposure, *Environ. Health Perspect.*, *125*(8), doi:10.1289/EHP1390.

Mattis, I., G. D'Amico, H. Baars, A. Amodeo, F. Madonna, and M. Iarlori (2016), EARLINET single calculus chain–technical–part 2: Calculation of optical products, *Atmos. Meas. Tech.*, *9*(7), 3009–3029, doi:10.5194/amt-9-3009-2016.

McKenna, J. (2003), An enhanced cluster analysis program with bootstrap significance testing for ecological community analysis, *Environ. Model Softw.*, *18*(3), 205–220, doi:10.1016/S1364-8152(02)00094-4.

Mejia, J., D. Wraith, K. Mengersen, and L. Morawska (2007), Trends in size classified particle number concentration in subtropical Brisbane, Australia, based on a 5 year study, *Atmos. Environ.*, *41*(5), 1064–1079, doi:10.1016/j.atmosenv.2006.09.020.

Mejía, J. F., and L. Morawska (2009), An investigation of nucleation events in a coastal urban environment in the Southern Hemisphere, *Atmos. Chem. Phys.*, *9*(20), 7877–7888, doi:10.5194/acp-9-7877-2009.

Meller, R., and G. K. Moortgat (2000), Temperature dependence of the absorption cross sections of formaldehyde between 223 and 323 K in the wavelength range 225–375 nm, *J. Geophys. Res.*, *105*(D6), 7089–7101, doi:10.1029/1999JD901074.

Merikanto, J., I. Napari, H. Vehkamäki, T. Anttila, and M. Kulmala (2007), New parameterization of sulfuric acid-ammonia-water ternary nucleation rates at tropospheric conditions, *J. Geophys. Res. Atmos.*, *112*(D15207), doi:doi.org/10.1029/2006JD007977.

Miller, L., L. D. Lemke, X. Xu, S. M. Molaroni, H. You, A. J. Wheeler, J. Booza, A. Grgicak-Mannion, R. Krajenta, P. Graniero, et al. (2010), Intra-urban correlation and spatial variability of air toxics across an international airshed in Detroit, Michigan (USA) and Windsor, Ontario (Canada), *Atmos. Environ.*, *44*(9), 1162–1174, doi:10.1016/j.atmosenv.2009.12.030.

Miller, L., X. Xu, A. Wheeler, D. O. Atari, A. Grgicak-Mannion, and I. Luginaah (2011), Spatial variability and application of ratios between BTEX in two Canadian cities, *The scientific world journal*, *11*, 2536–2549, doi:10.1100/2011/167973.

Millero, F. J., R. Feistel, D. G. Wright, and T. J. McDougall (2008), The composition of standard seawater and the definition of the reference-composition salinity scale, *Deep Sea Research Part I: Oceanographic Research Papers*, *55*(1), 50–72, doi:10.1016/j.dsr.2007.10.001.

Mitchell, R. M., B. W. Forgan, and S. K. Campbell (2017), The climatology of Australian aerosol, *Atmos. Chem. Phys.*, *17*(8), 5131–5154, doi:10.5194/acp-17-5131-2017.

Modini, R. L., Z. Ristovski, G. R. Johnson, C. He, N. Surawski, L. Morawska, T. Suni, and M. Kulmala (2009), New particle formation and growth at a remote, sub-tropical coastal location, *Atmos. Chem. Phys.*, *9*(19), 7607–7621, doi:10.5194/acp-9-7607-2009.

Mohan, S. M. (2016), An overview of particulate dry deposition: measuring methods, deposition velocity and controlling factors, *Int. J. Environ. Sci. Technol.*, *13*(1), 387–402, doi:10.1007/s13762-015-0898-7.

Mohr, C., F. D. Lopez-Hilfiker, T. Yli-Juuti, A. Heitto, A. Lutz, M. Hallquist, E. L. D'Ambro, M. P. Rissanen, L. Hao, S. Schobesberger, et al. (2017), Ambient observations of dimers from terpene oxidation in the gas phase: Implications for new particle formation and growth, *Geophys. Res. Lett.*, *44*(6), 2958–2966, doi:10.1002/2017GL072718.

Molteni, U., F. Bianchi, F. Klein, I. E. Haddad, C. Frege, M. J. Rossi, J. Dommen, and U. Baltensperger (2018), Formation of highly oxygenated organic molecules from aromatic compounds, *Atmos. Chem. Phys.*, *18*(3), 1909–1921, doi:10.5194/acp-18-1909-2018.

Morawska, L., Z. Ristovski, E. Jayaratne, D. U. Keogh, and X. Ling (2008), Ambient nano and ultrafine particles from motor vehicle emissions: Characteristics, ambient processing and implications on human exposure, *Atmos. Environ.*, *42*(35), 8113–8138, doi:10.1016/j.atmosenv.2008.07.050.

Müller, D., A. Ansmann, I. Mattis, M. Tesche, U. Wandinger, D. Althausen, and G. Pisani (2007), Aerosol-type-dependent lidar ratios observed with raman lidar, *J Geophys. Res.*, *112*(D16202), doi:10.1029/2006JD008292.

Na, K., A. A. Sawant, C. Song, and D. R. Cocker (2004), Primary and secondary carbonaceous species in the atmosphere of Western Riverside County, California, *Atmos. Environ.*, *38*(9), 1345–1355, doi:10.1016/j.atmosenv.2003.11.023.

Németh, Z., B. Rosati, N. Zíková, I. Salma, L. Bozó, C. D. de España, J. Schwarz, V. Ždímal, and A. Wonaschütz (2018), Comparison of atmospheric new particle formation events in three Central European cities, *Atmos. Environ.*, *178*, 191–197, doi:10.1016/j.atmosenv.2018.01.035.

NOAA (2018), Why is the ocean salty?, Retrieved from https://oceanservice.noaa.gov/facts/whysalty.html, accessed on 5/5/2019.

NSW (2017), NSW National Parks and Wildlife Service, Retrieved from https://www.nationalparks.nsw.gov.au.

O'Dowd, C., Y. Yoon, W. Junkerman, P. Aalto, M. Kulmala, H. Lihavainen, and Y. Viisanen (2007), Airborne measurements of nucleation mode particles i: coastal nucleation and growth rates, *Atmos. Chem. Phys.*, *7*(6), 1491–1501, doi:10.5194/acp-7-1491-2007.

O'Dowd, C. D., M. Geever, M. K. Hill, M. H. Smith, and S. G. Jennings (1998), New particle formation: Nucleation rates and spatial scales in the clean marine coastal environment, *Geophys. Res. Lett.*, *25*(10), 1661–1664, doi:10.1029/98GL01005.

O'Dowd, C. D., K. Hämeri, J. Mäkelä, M. Väkeva, P. Aalto, G. de Leeuw, G. J. Kunz, E. Becker, H.-C. Hansson, A. G. Allen, et al. (2002), Coastal new particle formation: Environmental conditions and aerosol physicochemical characteristics during nucleation bursts, *J. Geophys. Res.*, *107*(D19), 8107, doi:10.1029/2000JD000206.

OEH (2005), Air quality fact sheet:Particles, Retrieved from https://www.environment.gov.au/resource/particles.

OEH (2015), Air Quality Trends in the Illawarra, *Tech. rep.*, Office of Environment and Heritage NSW.

OEH (2016), Towards Cleaner Air. NSW Air Quality Statement 2016, *Tech. rep.*, Office of Environment and Heritage NSW.

OEH (2017), Air Quality in NSW, *Tech. rep.*, Office of Environment and Heritage NSW.

Ortega, I., L. K. Berg, R. A. Ferrare, J. W. Hair, C. A. Hostetler, and R. Volkamer (2016), Elevated aerosol layers modify the O_2 - O_2 absorption measured by ground-based MAX-DOAS, *J Quant. Spectrosc. Radiat. Transf.*, *176*, 34–49, doi:10.1016/j.jqsrt.2016.02.021.

Pachauri, T., A. Satsangi, V. Singla, A. Lakhani, and K. M. Kumari (2013), Characteristics and sources of carbonaceous aerosols in $PM_{2.5}$ during wintertime in Agra, India, *Aerosol Air Qual. Res.*, *13*(3), 977–991, doi:10.4209/aaqr.2012.10.0263.

Pani, S. K., C.-T. Lee, C. C.-K. Chou, K. Shimada, S. Hatakeyama, A. Takami, S.-H. Wang, and N.-H. Lin (2017), Chemical Characterization of Wintertime Aerosols over Islands and Mountains in East Asia: Impacts of the Continental Asian Outflow, *Aerosol Air Qual. Res.*, *17*(12), 3006–3036, doi:10.4209/aaqr.2017.03.0097.

Parker, J. D., N. Kravets, and A. Vaidyanathan (2018), Particulate matter air pollution exposure and heart disease mortality risks by race and ethnicity in the United States: 1997 to 2009 National Health Interview Survey with mortality follow-up through 2011, *Circulation*, *137*(16), 1688–1697, doi:10.1161/CIRCULATIONAHA.117.029376.

Paton-Walsh, C., É.-A. Guérette, D. Kubistin, R. Humphries, S. R. Wilson, D. Dominick, I. Galbally, R. Buchholz, M. Bhujel, S. Chambers, et al. (2017), The MUMBA campaign: measurements of urban, marine and biogenic air, *Earth System Science Data*, *9*(1), 349–362, doi:10.5194/essd-9-349-2017.

Paton-Walsh, C., É.-A. Guérette, K. Emmerson, M. Cope, D. Kubistin, R. Humphries, S. Wilson, R. Buchholz, N. Jones, D. Griffith, et al. (2018), Urban air quality in a coastal city: Wollongong during the MUMBA campaign, *Atmosphere*, *9*(12), 500, doi:10.3390/atmos9120500.

Pedersen, M., L. Giorgis-Allemand, C. Bernard, I. Aguilera, A.-M. N. Andersen, F. Ballester, R. M. Beelen, L. Chatzi, M. Cirach, A. Danileviciute, et al. (2013), Ambient air pollution and low birthweight: a European cohort study (ESCAPE), *Lancet Respir*, *1*(9), 695–704, doi:10.1016/S2213-2600(13)70192-9.

Peng, J., M. Hu, Z. Wang, X. Huang, P. Kumar, Z. Wu, S. Guo, D. Yue, D. Shang, Z. Zheng, et al. (2014), Submicron aerosols at thirteen diversified sites in China: size distribution, new particle formation and corresponding contribution to cloud condensation nuclei production, *Atmos. Chem. Phys.*, *14*(18), 10,249–10,265, doi:10.5194/acp-14-10249-2014.

Peng, Y., Y. Dong, X. Li, X. Liu, J. Dai, C. Chen, Z. Dong, C. Du, and Z. Wang (2017), Different characteristics of new particle formation events at two suburban sites in northern China, *Atmosphere*, *8*(12), 258, doi:10.3390/atmos8120258.

Petäjä, T., G. Mordas, H. Manninen, P. Aalto, K. Hämeri, and M. Kulmala (2006), Detection efficiency of a water-based TSI condensation particle counter 3785, *Aerosol Sci. Technol.*, *40*(12), 1090–1097, doi:10.1080/02786820600979139.

Petters, M., and S. Kreidenweis (2007), A single parameter representation of hygroscopic growth and cloud condensation nucleus activity, *Atmos. Chem. Phys.*, *7*(8), 1961–1971, doi:10.5194/acp-7-1961-2007.

Pettibone, A. J. (2009), Toward a better understanding of new particle formation, Ph.D. thesis, University of Iowa.

Pey, J., S. Rodríguez, X. Querol, A. Alastuey, T. Moreno, J. P. Putaud, and R. Van Dingenen (2008), Variations of urban aerosols in the western Mediterranean, *Atmos. Environ.*, *42*(40), 9052–9062, doi:10.1016/j.atmosenv.2008.09.049.

Pietikäinen, J.-P., S. Mikkonen, A. Hamed, A. Hienola, W. Birmili, M. Kulmala, and A. Laaksonen (2014), Analysis of nucleation events in the European boundary layer using the regional aerosol–climate model REMO-HAM with a solar radiation-driven OH-proxy, *Atmos. Chem. Phys.*, *14*(21), 11,711–11,729, doi:10.5194/acp-14-11711-2014.

Pinardi, G., M. Van Roozendael, N. Abuhassan, C. Adams, A. Cede, K. Clémer, C. Fayt, U. Frieß, M. Gil, J. Herman, et al. (2013), MAX-DOAS formaldehyde slant column measurements during CINDI: intercomparison and analysis improvement., *Atmos. Meas. Tech.*, *6*(1), doi:10.5194/amt-6-167-2013.

Platt, U., and J. Stutz (2008), Differential absorption spectroscopy, in *Differential Optical Absorption Spectroscopy. Physics of Earth and Space Environments.*, pp. 135–174, Springer, Berlin, Heidelberg, doi:10.1007/978-3-540-75776-4_6.

Pope III, C. A., and D. W. Dockery (2006), Health effects of fine particulate air pollution: lines that connect, *J. Air Waste Manage. Assoc.*, *56*(6), 709–742, doi:10.1080/10473289.2006.10464485.

Pöschl, U. (2005), Atmospheric aerosols: composition, transformation, climate and health effects, *Angewandte Chemie International Edition*, *44*(46), 7520–7540, doi:10.1002/anie.200501122.

Pushpawela, B., R. Jayaratne, and L. Morawska (2018), Temporal distribution and other characteristics of new particle formation events in an urban environment, *Environ. Pollut.*, *233*, 552–560, doi:10.1016/j.envpol.2017.10.102.

R Core Team (2016), *R: A Language and Environment for Statistical Computing*, R Foundation for Statistical Computing, Vienna, Austria, url:https://www.R-project.org/.

Raaschou-Nielsen, O., Z. J. Andersen, R. Beelen, E. Samoli, M. Stafoggia, G. Weinmayr, B. Hoffmann, P. Fischer, M. J. Nieuwenhuijsen, B. Brunekreef, et al. (2013), Air pollution and lung cancer incidence in 17 European cohorts: prospective analyses from the European Study of Cohorts for Air Pollution Effects (ESCAPE), *Lancet Oncol*, *14*(9), 813–822, doi:10.1016/S1470-2045(13)70279-1.

Rasool, S. (2012), *Chemistry of the lower atmosphere*, Springer Science & Business Media.

Ristovski, Z., E. Jayaratne, M. Lim, G. A. Ayoko, and L. Morawska (2006), Influence of diesel fuel sulfur on nanoparticle emissions from city buses, *Environ. Sci. Technol.*, *40*(4), 1314–1320, doi:10.1021/es050094i.

Ristovski, Z., T. Suni, M. Kulmala, M. Boy, N. K. Meyer, J. Duplissy, A. Turnipseed, L. Morawska, and U. Baltensperger (2010), The role of sulphates and organic vapours in growth of newly formed particles in a eucalypt forest, *Atmos. Chem. Phys.*, *10*(6), 2919–2926, doi:10.5194/acp-10-2919-2010.

Rodgers, C. D. (2000), *Inverse methods for atmospheric sounding: theory and practice*, vol. 2, World scientific.

Rosenfeld, D., U. Lohmann, G. B. Raga, C. D. O'Dowd, M. Kulmala, S. Fuzzi, A. Reissell, and M. O. Andreae (2008), Flood or drought: How do aerosols affect precipitation?, *science*, *321*(5894), 1309–1313, doi:10.1126/science.1160606.

Rotstayn, L., M. Collier, A. Chrastansky, S. Jeffrey, and J.-J. Luo (2013), Projected effects of declining aerosols in RCP4. 5: unmasking global warming?, *Atmos. Chem. Phys.*, *13*(21), 10,883–10,905, doi:10.5194/acp-13-10883-2013.

Rozanov, A., H. Bovensmann, A. Bracher, S. Hrechanyy, V. Rozanov, M. Sinnhuber, F. Stroh, and J. Burrows (2005), NO_2 and BrO vertical profile retrieval from SCIAMACHY limb measurements: Sensitivity studies, *Adv. Space Res.*, *36*(5), 846–854, doi:10.1016/j.asr.2005.03.013.

Ryan, R. G., S. Rhodes, M. Tully, S. Wilson, N. Jones, U. Frieß, and R. Schofield (2018), Daytime HONO, NO_2 and aerosol distributions from MAX-DOAS observations in Melbourne, *Atmos. Chem. Phys*, *18*(19), 13,969–13,985, doi:10.5194/acp-18-13969-2018.

Salimi, F., M. Rahman, S. Clifford, Z. Ristovski, L. Morawska, et al. (2017), Nocturnal new particle formation events in urban environments, *Atmos. Chem. Phys*, *17*(1), 521–530, doi:10.5194/acp-17-521-2017.

Schobesberger, S., A. Franchin, F. Bianchi, L. Rondo, J. Duplissy, A. Kürten, I. Ortega, A. Metzger, R. Schnitzhofer, J. Almeida, et al. (2015), On the composition of ammonia–sulfuric-acid ion clusters during aerosol particle formation, *Atmos. Chem. Phys.*, *15*(1), 55–78, doi:10.5194/acp-15-55-2015.

Seinfeld, J. H., and S. N. Pandis (1998), Atmospheric chemistry and physics: from air pollution to climate change.

Seinfeld, J. H., and S. N. Pandis (2012), *Atmospheric chemistry and physics:from air pollution to climate change (2nd Edition)*, John Wiley & Sons.

Seinfeld, J. H., and S. N. Pandis (2016), *Atmospheric chemistry and physics: from air pollution to climate change (3rd edition)*, John Wiley & Sons.

Seinfeld, J. H., et al. (2016), Improving our fundamental understanding of the role of aerosol- cloud interactions in the climate system, *Proceedings of the National Academy of Sciences*, *113*(21), 5781–5790, doi:10.1073/pnas.1514043113.

Selvam, A. M. (2010), Universal spectrum for atmospheric suspended particulates: comparison with observations, *arXiv preprint arXiv:1005.1336*.

Sharkey, T. D., E. L. Singsaas, P. J. Vanderveer, and C. Geron (1996), Field measurements of isoprene emission from trees in response to temperature and light, *Tree physiology*, *16*(7), 649–654.

Shen, X., J. Sun, Y. Zhang, B. Wehner, A. Nowak, T. Tuch, X. Zhang, T. Wang, H. Zhou, X. Zhang, et al. (2011), First long-term study of particle number size distributions and new particle formation events of regional aerosol in the North China Plain, *Atmos. Chem. Phys.*, *11*(4), 1565–1580, doi:10.5194/acp-11-1565-2011.

Siakavaras, D., C. Samara, M. Petrakakis, and G. Biskos (2016), Nucleation events at a coastal city during the warm period: Kerbside versus urban background measurements, *Atmos. Environ.*, *140*, 60–68, doi:10.1016/j.atmosenv.2016.05.054.

Sinreich, R. (2007), Multi-axis differential optical absorption spectroscopy measurements in polluted environments, Ph.D. thesis, Heidelberg University.

Sinreich, R., A. Merten, L. Molina, and R. Volkamer (2013), Parameterizing radiative transfer to convert MAX-DOAS dSCDs into near-surface box-averaged mixing ratios, *Atmos. Meas. Tech.*, *6*(6), 1521–1532, doi:10.5194/amt-6-1521-2013.

Sorribas, M., B. De la Morena, B. Wehner, J. López, N. Prats, S. Mogo, A. Wiedensohler, and V. Cachorro (2011), On the sub-micron aerosol size distribution in a coastal-rural site at El Arenosillo Station (SW–Spain), *Atmos. Chem. Phys.*, *11*(21), 11,185–11,206, doi:10.5194/acp-11-11185-2011.

Sorribas, M., J. Adame, F. Olmo, J. Vilaplana, M. Gil-Ojeda, and L. Alados-Arboledas (2015), A long-term study of new particle formation in a coastal environment: meteorology, gas phase and solar radiation implications, *Sci. Total Environ.*, *511*, 723–737, doi:10.1016/j.scitotenv.2014.12.011.

Spracklen, D., K. Carslaw, M. Kulmala, V.-M. Kerminen, G. Mann, and S.-L. Sihto (2006), The contribution of boundary layer nucleation events to total particle concentrations on regional and global scales, *Atmos. Chem. Phys.*, *6*(4), 5631–5648, doi:10.5194/acp-6-5631-2006.

Stafoggia, M., G. Cesaroni, A. Peters, Z. J. Andersen, C. Badaloni, R. Beelen, B. Caracciolo, J. Cyrys, U. de Faire, K. de Hoogh, et al. (2014), Long-term exposure to ambient air pollution and incidence of cerebrovascular events: results from 11 European cohorts within the ESCAPE project, *Environ. Health Perspect.*, *122*(9), 919–925, doi:10.1289/ehp.1307301.

Stein, A., R. R. Draxler, G. D. Rolph, B. J. Stunder, M. Cohen, and F. Ngan (2015), NOAAs HYSPLIT atmospheric transport and dispersion modeling system, *Bull. Amer. Meteor. Soc.*, *96*(12), 2059–2077, doi:10.1175/BAMS-D-14-00110.1.

Stocker, T., F. Qin, G. Plattner, L. Alexander, S. Allen, N. Bindoff, S. Xie, et al. (2013), Technical summary: The physical science basis. contribution of working group i to the fifth assessment report of the intergovernmental panel on climate change [stocker, t.f., d. qin, g.-k. plattner, m. tignor, s.k. allen, j. boschung, a. nauels, y. xia, v. bex and p.m. midgley (eds.)].

Suni, T., M. Kulmala, A. Hirsikko, T. Bergman, L. Laakso, P. Aalto, R. Leuning, H. Cleugh, S. Zegelin, D. Hughes, et al. (2008), Formation and characteristics of ions and charged aerosol particles in a native Australian Eucalypt forest, *Atmos. Chem. Phys.*, *8*(1), 129–139, doi:10.5194/acp-8-129-2008.

Takashima, H., H. Irie, Y. Kanaya, A. Shimizu, K. Aoki, and H. Akimoto (2009), Atmospheric aerosol variations at Okinawa Island in Japan observed by MAX-DOAS using a new cloud-screening method, *J Geophys. Res.*, *114*(D18213), doi: 10.1029/2009JD011939.

Tian, Y.-Z., Z.-M. Xiao, B. Han, G.-L. Shi, W. Wang, H.-Z. Hao, X. Li, Y.-C. Feng, and T. Zhu (2013), Seasonal study of primary and secondary sources of carbonaceous species in PM_{10} from Five Northern Chinese Cities, *Aerosol Air Qual. Res*, *13*, 148–161, doi:10.4209/aaqr.2012.01.0010.

Tiwari, V., Y. Hanai, and S. Masunaga (2010), Ambient levels of volatile organic compounds in the vicinity of petrochemical industrial area of Yokohama, Japan, *Air. Qual. Atmos. Health*, *3*(2), 65–75.

Tomasi, C., and A. Lupi (2017), *Primary and Secondary Sources of Atmospheric Aerosol*, Wiley-VCH Verlag GmbH & Co. KGaA: Weinheim, Germany, doi:10.1002/9783527336449.ch1.

Toon, O. B., and J. B. Pollack (1980), Atmospheric aerosols and climate: Small particles in the earth's atmosphere interact with visible and infrared light, altering the radiation balance and the climate, *American Scientist*, *68*(3), 268–278, url:http://www.jstor.org/stable/27849822.

TSI (2010), Model 3936 scanning mobility particle sizer^{TM} (smps^{TM}) spectrometer, *Tech. rep.*, TSI Incorporated.

TSI (2012), Aerosol statistics lognormal distributionsand dN/dlogDp, *Tech. rep.*, TSI Incorporated.

TSI (2014), Fundamentals of condensation particle counters (CPC) and scanning mobility particle sizer (SMPS) spectrometers, *Tech. rep.*, TSI Incorporated.

Turpin, B. J., and J. J. Huntzicker (1995), Identification of secondary organic aerosol episodes and quantitation of primary and secondary organic aerosol concentrations during SCAQS, *Atmos. Environ.*, *29*(23), 3527–3544, doi:10.1016/1352-2310(94)00276-Q.

Uria-Tellaetxe, I., and D. C. Carslaw (2014), Conditional bivariate probability function for source identification, *Environ. Model. Softw.*, *59*, 1–9, doi:10.1016/j.envsoft.2014.05.002.

USEPA (2004), Air quality criteria for particulate matter, *US Environmental Protection Agency, Research Triangle Park.*

Vandaele, A., C. Hermans, P. Simon, M. Van Roozendael, J. Guilmot, M. Carleer, and R. Colin (1996), Fourier transform measurement of NO_2 absorption cross-section in the visible range at room temperature, *J. Atmos. Chem.*, *25*(3), 289–305, doi:10.1007/BF00053797.

Vehkamäki, H., M. D. Maso, T. Hussein, R. Flanagan, A. Hyvärinen, J. Lauros, P. Merikanto, M. Mönkkönen, K. Pihlatie, K. Salminen, et al. (2004), Atmospheric particle formation events at Värriö measurement station in Finnish Lapland 1998-2002, *Atmos. Chem. Phys.*, *4*(7), 2015–2023, doi:10.5194/acp-4-2015-2004.

Voiland, A. (2010), Aerosols: Tiny Particles, Big Impact, Retrieved from https://earthobservatory.nasa.gov/Features/Aerosols/page1.php.

Wagner, T., B. v. Dix, C. v. Friedeburg, U. Frieß, S. Sanghavi, R. Sinreich, and U. Platt (2004), MAX-DOAS O_4 measurements: A new technique to derive information on atmospheric aerosolsprinciples and information content, *J. Geophys. Res.*, *109*(D22205), doi:10.1029/2004JD004904.

Wagner, T., S. Beirle, J. Remmers, R. Shaiganfar, and Y. Wang (2016), Absolute calibration of the colour index and O_4 absorption derived from multi axis (MAX-DOAS) measurements and their application to a standardised cloud classification algorithm, *Atmos. Meas. Tech.*, *9*(9), 4803–4823, doi:10.5194/amt-9-4803-2016.

Wahlina, P., F. Palmgren, and R. Van Dingenen (2001), Experimental studies of ultrafine particles in streets and the relationship to traffic, *Atmos.Environ.*, *35*, S63–S69, doi:10.1016/S1352-2310(00)00500-8.

Wang, D., B. Zhou, Q. Fu, Q. Zhao, Q. Zhang, J. Chen, X. Yang, Y. Duan, and J. Li (2016a), Intense secondary aerosol formation due to strong atmospheric photochemical reactions in summer: observations at a rural site in eastern Yangtze River Delta of China, *Sci. Total Environ.*, *571*, 1454–1466, doi:10.1016/j.scitotenv.2016.06.212.

Wang, S., C. A. Cuevas, U. Frieß, and A. Saiz-Lopez (2016b), MAX-DOAS retrieval of aerosol extinction properties in Madrid, Spain, *Atmos. Meas. Tech.*, *9*(10), 5089, doi:10.5194/amt-9-5089-2016.

Wang, Y., A. Li, P. Xie, T. Wagner, H. Chen, W. Liu, and J. Liu (2014), A rapid method to derive horizontal distributions of trace gases and aerosols near the surface using multi-axis differential optical absorption spectroscopy, *Atmos. Meas. Tech.*, *7*(6), 1663–1680, doi:10.5194/amt-7-1663-2014.

Wang, Y., J. Lampel, P. Xie, S. Beirle, L. Ang, D. Wu, and T. Wagner (2017), Ground-based MAX-DOAS observations of tropospheric aerosols, NO_2, SO_2 and HCHO in Wuxi, China, from 2011 to 2014, *Atmos. Chem. Phys.*, *17*(3), 2189, doi:10.5194/acp-17-2189-2017.

Weijers, E., and M. Schaap (2013), Anthropogenic and natural constituents in PM_{10} at urban and rural sites in North-Western Europe: Concentrations, Chemical composition and Sources, in *Urban Air Quality in Europe*, pp. 239–258, Springer, doi:10.1007/698_2012_207.

WHO (2018), Air pollution, url:http://www.who.int/airpollution/en/.

WHO, et al. (2013), Review of evidence on health aspects of air pollution–REVIHAAP project, *World Health Organization, Copenhagen, Denmark.*

WHO, et al. (2016), Ambient air pollution: A global assessment of exposure and burden of disease, *Tech. rep.*, World Health Organization, Copenhagen, Denmark.

Wilks, D. S. (2011), Cluster analysis, in *International geophysics*, vol. 100, pp. 603–616, Elsevier, doi:10.1016/B978-0-12-385022-5.00015-4.

Wilmouth, D. M., T. F. Hanisco, N. M. Donahue, and J. G. Anderson (1999), Fourier transform ultraviolet spectroscopy of the a $2\pi3/2$ x $2\pi3/2$ transition of BrO, *J. Phys. Chem.*, *103*(45), 8935–8945, doi:10.1021/jp991651o.

Wilson, W. E., and H. H. Suh (1997), Fine particles and coarse particles: concentration relationships relevant to epidemiologic studies, *J Air Waste Manage. Assoc.*, *47*(12), 1238–1249, doi:10.1080/10473289.1997.10464074.

Winters, A. J., M. A. Adams, T. M. Bleby, H. Rennenberg, D. Steigner, R. Steinbrecher, and J. Kreuzwieser (2009), Emissions of isoprene, monoterpene and short-chained carbonyl compounds from Eucalyptus spp. in Southern Australia, *Atmos. Environ.*, *43*(19), 3035–3043, doi:10.1016/j.atmosenv.2009.03.026.

Xing, C., C. Liu, S. Wang, K. L. Chan, Y. Gao, X. Huang, W. Su, C. Zhang, Y. Dong, G. Fan, et al. (2017), Observations of the vertical distributions of summertime atmospheric pollutants and the corresponding ozone production in Shanghai, China, *Atmos. Chem. Phys.*, *17*(23), 14,275, doi:10.5194/acp-17-14275-2017.

Xing, Y.-F., Y.-H. Xu, M.-H. Shi, and Y.-X. Lian (2016), The impact of $PM_{2.5}$ on the human respiratory system, *J. Thorac, Dis.*, *8*(1), E69–E74, doi:10.3978/j.issn.2072-1439.2016.01.19.

Zhang, J., T. Wang, W. Chameides, C. Cardelino, D. Blake, and D. Streets (2008), Source characteristics of volatile organic compounds during high ozone episodes in Hong Kong, Southern China, *Atmos. Chem. Phys.*, *8*(16), 4983–4996, doi:10.5194/acp-8-4983-2008.

Zhang, Q., C. O. Stanier, M. R. Canagaratna, J. T. Jayne, D. R. Worsnop, S. N. Pandis, and J. L. Jimenez (2004), Insights into the chemistry of new particle formation and growth events in Pittsburgh based on aerosol mass spectrometry, *Environ. Sci. Technol.*, *38*(18), 4797–4809, doi:10.1021/es035417u.